Evaluation of the pi0 background for the nu_e appearance search in the T2K experiment. First study of the leptonic CP violation phase.

João Pedro Athayde Marcondes de André

École Polytechnique
École doctorale de l'X
Laboratoire Leprince-Ringuet

Evaluation of the π^0 background for the ν_e appearance search in the T2K experiment. First study of the leptonic CP violation phase.

Neutrino oscillation

PHD Thesis

dissertation submitted and defended in public the 22nd October 2012 for the degree of

Doctorat de l'École Polytechnique
Spécialité physique des particules

by

João Pedro Athayde Marcondes de André

Dissertation comitee :

Jury president	:	Alain Blondel
Thesis referee	:	David Lhuillier
Thesis referee	:	Thomas Patzak
Examiner	:	Yorick Blumenfeld
Examiner	:	Pascal Paganini
Thesis director	:	Michel Gonin

Abstract

The T2K experiment is an off-axis long baseline neutrino flavour oscillation experiment. In T2K, the neutrino beam produced by an accelerator at J-PARC, Tokai, is detected using the Super Kamiokande (SK) detector, Kamioka, located 295 km away from Tokai. The accelerator produces a very pure ν_μ beam. During the propagation of neutrinos between their production point and SK they may change flavour. This effect is the neutrino flavour oscillation.

The main objective of T2K is to measure some parameters describing the neutrino flavour oscillation, in particular of θ_{13} and eventually δ_{CP}. This determination is performed by measuring the $\nu_\mu \rightarrow \nu_e$ oscillation probability, via the ν_e appearance search. In 2011, T2K was the first experiment to observe ν_e appearance and published a 2.5 σ evidence that θ_{13} is not null.

In this thesis we present the work done on the evaluation of the systematic error on the π^0 background reconstruction efficiency. The π^0 background is one of the main background sources affecting the ν_e appearance search through the detection of ν_e charged current quasi-elastic events at SK. Two different and complementary approaches have been developed. First, we have started developing a new device that partially reproduces the topology of physics events. Second, we have created a specific sample to estimate the systematic uncertainty of π^0 events reconstruction efficiency. This result was used in the official 2011 ν_e search. Furthermore, results from this sample will be used in future extended oscillation analysis.

We also present the first study of the leptonic CP violation phase (δ_{CP}) using T2K ν_e data, using the recently measured value of θ_{13} by reactor experiments.

Keywords : T2K, Super Kamiokande, neutrino flavour oscillation, θ_{13} mixing angle, CP violation phase, π^0 background, oscillation analysis

---

Résumé

L'expérience T2K est une expérience de recherche d'oscillation de saveur de neutrinos utilisant une base longue avec la technique du faisceau hors axe. Dans T2K, un faisceau de neutrinos est produit dans l'accélérateur J-PARC à Tokai pour être détecté ensuite dans le détecteur Super Kamiokande (SK) à Kamioka qui se situe à 295 km de Tokai. Cet accélérateur produit un faisceau très pur de ν_μ. Au cours de la propagation des neutrinos entre leur point de production et SK, ils peuvent changer de saveur, phénomène que l'on appelle oscillation quantique de saveur des neutrinos.

L'objectif principal de T2K est de mesurer certains paramètres décrivant l'oscillation de saveur des neutrinos, et plus particulièrement les paramètres θ_{13} et éventuellement δ_{CP}. Cette estimation est réalisée, via la mesure de la probabilité d'oscillation $\nu_\mu \rightarrow \nu_e$, avec la recherche d'apparition de ν_e. En 2011, l'expérience T2K a été la première à observer l'apparition de ν_e et ainsi exclu, à 2.5 σ, une valeur nulle de θ_{13}.

Cette thèse présente le travail réalisé pour estimer l'erreur systématique de l'efficacité de reconstruction du bruit de fond π^0. Celui-ci est l'une des principales sources d'erreur affectant la recherche d'apparition de ν_e par la détection d'événements quasi élastiques à courant chargé à SK. Deux méthodes différentes et complémentaires ont été développées. Dans un premier temps, nous avons développé un nouvel outil expérimental qui reproduit partiellement la topologie des événements physiques, et en parallèle crée avec des simulations et données un échantillon spécifique pour estimer l'incertitude systématique de l'efficacité de reconstruction des événements π^0. Ce dernier résultat a été utilisé dans l'analyse officielle d'apparition de ν_e publiée en 2011. Le nouvel échantillon produit sera également utilisé dans les futures analyses d'oscillation.

En tenant compte de la valeur récemment mesurée de θ_{13} par des expériences faites auprès de réacteurs, nous présentons dans cette thèse une première étude de la phase de violation CP dans le secteur leptonique (δ_{CP}) en utilisant les données ν_e de T2K.

Mots-clés : T2K, Super Kamiokande, oscillation de saveur de neutrinos, angle de mélange θ_{13}, phase de violation CP, bruit de fond π^0, analyse d'oscillation

Acknowledgements

Even though I have written this manuscript in English, I feel that, for the acknowledgements part, it would be more appropriate that I write it in different languages, taking into account the typically the mother language of the people concerned by them, in the case I do know their language.

Eu gostaria, primeiramente, de agradecer o suporte que me foi dado pela minha família, especialmente meus pais Lino e Maria Elizabeth, e minha irmã Beatriz. Sem tal apoio eu jamais teria conseguido chegar enfrentar essa jornada e obter o meu doutorado.

Eu também gostaria de agradecer aos meus amigos e professores com quem eu pude discutir em vários momentos a respeito do que desejava fazer no futuro. Tais discussões foram de uma importância fundamental, e sem elas eu provavelmente não teria seguido o caminho que eu segui e do qual eu estou satisfeito.

Eu não poderia deixar de agradecer a todos que colaboraram para a introdução à física, que me foi dada no Instituto de Física da Universidade de São Paulo. Tal introdução, eu tenho certeza, foi fundamental para que eu decidisse fazer um trabalho de doutorado no campo da física experimental. Particularmente eu gostaria de agradecer ao meu primeiro professor de física experimental, Zwinglio, e aos pesquisadores do grupo de espectroscopia nuclear com íons leves, Thereza, Márcia, Lighia e Luciano, com quem eu trabalhei pela primeira vez em um projeto experimental, interrompendo-o para concluir minha graduação na École Polytechnique na França.

Je voudrais ensuite remercier l'École Polytechnique de m'avoir permis de venir en France compléter mes études, ce que m'a permis avoir un premier contact avec la physique de particules expérimentale, qui m'a assez rapidement fasciné, ce que m'a amené a faire des stages dans le domaine, encadrés déjà par Michel, et de finalement avoir poursuivi avec une thèse, conclusion de laquelle vous avez ici entre vos mains maintenant.

Je voudrais aussi remercier tous mes amis en France pour le support moral qui m'a été donné pendant tout mon séjour en France, sans lesquels je ne serais probablement pas resté pour faire une thèse ou celle ci ne se serait pas aussi bien passé. Dans ce cadre je voudrais remercier spécialement mes colocataires, Bernardo et Emmanuel, avec qui j'ai partagé un appartement pendant les trois années de ma thèse.

Je voudrais également remercier les physiciens, les services mécanique, électronique et informatique, ainsi que l'admnistration du Laboratoire Leprince-Ringuet pour l'accueil que j'ai eu lors que je suis arrivé et pour avoir fourni un cadre amical et sympathique pendant les trois ans où j'étais en thèse. Je tiendrais toujours à cœur les discussions pendant le déjeuner et les pauses café, ainsi que les équipes de foot et basket du laboratoire qui m'ont permis d'avoir des moments d'épanouissement pendant la thèse.

Je voudrais spécialement remercier les personnes avec qui j'ai partagé mon bureau et avec qui j'ai pu discuté à des nombreuses occasions sur les détails et l'avance de mon travail, au départ Christophe et Magali, et ensuite avec Thomas et Benjamin, sans compter les stagiaires que sont passés par le groupe T2K pendant que j'étais là. Je voudrais égale-

ment remercier fortement les autres membres du groupe T2K avec qui je n'ai pas partagé le bureau, nominalement Michel et Olivier, pour leur soutien et les idées qu'ils ont proposé pour la solution de plusieurs problèmes trouvés pendant le cours de la thèse. Je voudrais remercier en particulier Thomas et Michel encore une fois pour leur aide indispensable à la relecture et clarification de ce manuscrit. Je tiens également à remercier les membres de mon jury de thèse que l'on pris le temps de lire et commenter ce manuscrit.

I would also like to thank the T2K and Super Kamiokande collaborations for having welcomed me to work on different groups. I specially would like to thank the Super Kamiokande collaboration that has allowed me to use their full data set even though I was not a Super Kamiokande collaborator myself to perform the studies presented in this thesis which were performed in collaboration with Mine, who also helped me at several occasions during my PhD. I would also like to thank all the T2K and SK collaborators which have given me useful inputs and comments at several occasions and which I will not name here to avoid forgetting someone. I would like equally to thank the administration offices of the Kamioka Observatory and of J-PARC and Kyoto University for their help at several occasion, specially when I needed invitation letters to be able to go work in Japan on several different projects. I would also like to thank the University of California Irvine for having housed me while I was in Japan to work on Super Kamiokande at several occasions.

Finally, I would also like to thank the several computing centers, namely the IN2P3, Kamioka, KEK and LLR, which I have used to process data and generate the Monte-Carlo samples, as well as the authors of several public software, languages and libraries which I have used frequently during my PhD, such as Linux (and more specially Gentoo and Archlinux maintainers and developers), vim, xfig, LaTeX 2_ε, C/C++, Fortran, ROOT, GEANT4.

Contents

Introduction

After the discovery of radiation in 1896 by Becquerel [1], Chadwick observed in 1914 a continuous electron spectrum from a β-decay [2], therefore the law of conservation of energy, momentum, spin and associated statistics seemed to be violated by the β-decay. In 1930 Pauli postulated the existence of a new particle, which he called neutron, produced in the β-decay along with the electron to avoid violating the conservation laws previously mentioned [3]. At this moment there was no perspective for any possible measurement of the existence of such particle, which needed to interact weakly, be neutral, have spin 1/2 and have a mass much smaller than the proton mass. In 1934 Fermi incorporated this newly postulated particle in the β-decay theory [4] and renamed it as neutrino, given the experimental discovery of the neutron by Chadwick [5].

The first experimental observation of the neutrino happened many years after its postulate and integration to the β-decay theory by the detection of anti-neutrinos produced by the nuclear reactor at Savannah River [6] in 1956 by Reines and Cowan. For this experimental discovery Reines was attributed the Nobel prize in 1995. In 1962 the existence of two flavours of neutrinos [7], which correspond to electron neutrinos (ν_e) and muon neutrinos (ν_μ), was experimentally discovered. For such discovery the Nobel prize was attributed in 1988 to Lederman, Schwartz and Steinberger. Later on, in 2000, the DONUT experiment discovered a third flavour of neutrino [8], called tau neutrino (ν_τ), which completed the third family of fundamental fermions. In 2006, the LEP showed that there are only three flavours of neutrinos produced by Z^0 decay [9], which are the already mentioned ν_e, ν_μ and ν_τ.

After the discovery of neutrinos, several experiments were performed to measure their properties and to use neutrinos to measure the properties of other objects. It was through the measurement of the neutrino flux produced at the Sun and at the Earth's atmosphere that neutrino oscillations were discovered, which awarded the Nobel prize to Davis in 2002. At first, in late 1960s it was observed at Homestake a deficit of the number of electron neutrinos observed from the Sun in relation to what was expected from the Standard Solar Model [10]. Such findings were later confirmed by other experiments and named the "Solar neutrino problem". One solution for such problem was the neutrino flavour oscillation, in which case a part of the electron neutrinos produced at the Sun would not be detected on the Earth's surface because they oscillated during their propagation and, at the same time the detector was only able to detect electron neutrinos. At the same time the rate of electron and muon neutrinos produced at the Earth's atmosphere was measured and it was also not compatible with the expected value, and which could also be explained through neutrino flavour oscillation. In 1998, the Super Kamiokande collaboration has proven the oscillation of neutrinos produced in the Earth's atmosphere [11] and in 2001, the SNO collaboration has proven the oscillation of neutrinos produced at the Sun [12].

The neutrino flavour oscillation is parametrized by six quantities : three mixing angles (θ_{12}, θ_{13}, θ_{23}), two squared mass differences (Δm^2_{32}, Δm^2_{21}) and one CP violation phase

(δ_{CP}). Studies with solar, atmospheric, reactor and accelerator neutrinos had measured the value of θ_{12}, θ_{23}, $|\Delta m^2_{32}|$ and Δm^2_{21} and found an upper bound for θ_{13} by the beginning of this thesis. The natural continuation of such measurements was to obtain the value of θ_{13}, the sign of Δm^2_{32} and the value of δ_{CP}, the latter term only exists if $\theta_{13} \neq 0$. The estimation of the value of these parameters has fundamental consequences in physics, since through the CP violation in the lepton sector, we could expect to open the path for an explanation of the observed matter-antimatter asymmetry in the universe.

The theoretical aspects of neutrino physics and neutrino oscillations as well as the current status of the estimation of the parameters describing the neutrino flavour oscillations is presented in *chapter 1*.

The measurement of the remaining parameters describing the neutrino flavour oscillation is currently being performed by experiments using neutrinos produced in reactors or in accelerators. The experiments based on reactor neutrinos are able to measure only the value of θ_{13}, via ν_e disappearance. On the other hand, those based on accelerator neutrinos have the potential to measure at the same time θ_{13}, δ_{CP} and the sign of Δm^2_{32}, though these quantities are slightly correlated, via ν_e appearance, considering matter effects, and also improve the precision of θ_{23}, via ν_μ disappearance. In this context the Tokai to Kamioka (T2K) experiment was designed to measure neutrino flavour oscillation using a neutrino beam generated at J-PARC, at Tokai, and measured at Super Kamiokande (SK), at Kamioka. T2K was tuned to have an excellent resolution for θ_{13} being the first experiment to use the off-axis neutrino beam technique which produces neutrino beams with narrow energy spectrum which allows T2K to perform its measurement at first oscillation maximum. The T2K experiment and its goals is presented in detail in *chapter 2*.

In order to measure θ_{13} and δ_{CP} using T2K data it is essential to observe $\nu_\mu \rightarrow \nu_e$ oscillation, and calculate its probability. This measurement can only be achieved with small statistical and systematic uncertainties, that is, it is not enough to measure the $\nu_\mu \rightarrow \nu_e$ oscillation during a long period but it is essential to constrain the experimental uncertainties related to the production and detection of neutrinos.

One of the main backgrounds for the ν_e search at SK are π^0 events, that are misreconstructed as if they were events produced from ν_e CCQE interaction, and for which there is no natural control sample. In order to estimate the systematic error on the event reconstruction we have started developing a new device, called Cone Generator, that is a multi-ring light source which partly reproduces the topology of physics events at SK *chapter 3*. We have created, in parallel to the development of the Cone Generator, a sample composed by mixing data and Monte-Carlo to estimate the reconstruction efficiency systematic error of π^0 events *chapter 4*. The estimation of this systematic error using this hybrid sample was used in the official 2011 ν_e search [13]. An extension of the 2011 analysis using this hybrid sample has also been made for the official 2012 ν_e search which is currently in progress.

Finally, given the recent measurements of θ_{13} by reactor experiments, we performed the first study of the CP violation phase on the lepton sector using T2K ν_e data *chapter 5*.

Chapter 1

Physics background

Contents

1.1 Neutrinos in the Standard Model

In this section we will present briefly the neutrino in the Standard Model as well as some recent areas of research in neutrino physics.

1.1.1 Standard Model

The Standard Model is a theory describing the strong, weak and electromagnetic interaction between the elementary particles that constitute matter, within the framework of the Quantum Field Theory that combines Special Relativity and Quantum Mechanics. Even though the Standard Model is not a complete theory[1], its results agree well with most of the experimental data concerning the interaction between elementary particles through these three forces. There are however a few observations that cannot be understood in the framework of the Standard Model, such as neutrino masses (which will be further discussed in section 1.1.2), the observation by astrophysicists of dark matter and energy

[1]The Standard Model is not a complete theory as it does not explain every observed phenomena, as for example the gravitational interaction.

in the universe and the predominance of matter in our universe with no traces of natural anti-matter [14].

The elementary particles in the Standard Model are classified in fermions and bosons. The 12 fermions are further divided between quarks and leptons depending on whether they interact through strong interaction or not, respectively. The quarks and leptons are further grouped depending on their electrical charge, which results in groups of three particles each. To further categorize these particles they are also grouped in generations that consist of one particle that had previously been classified in a different category using the strong interaction and electrical charge. The fermions of the Standard Model and their classification is shown in table 1.1. The gauge bosons of the Standard Model, which have the role of vectors of the interactions, are four gauge bosons vectors of the Electroweak interaction (γ, $W^{\pm}$ and Z^0,), and eight gauge bosons vectors of the Strong interaction (gluons). In addition to the gauge bosons, in the Standard Model is included a scalar boson (Higgs) to explain why particles are massive. The Higgs is the only fundamental particle of the Standard Model which had not been measured by the beginning of this thesis, and this year we have finally measured a boson that is compatible with the predicted Higgs boson [15, 16].

Table 1.1: Generations of fermions in the Standard Model and their classification.

	quarks		leptons	
charge	$+\frac{2}{3}$	$-\frac{1}{3}$	-1	0
First generation	u	d	e	ν_e
Second generation	c	s	μ	ν_μ
Third generation	t	b	τ	ν_τ

In this thesis we will not describe in details the Standard Model but we will focus on the leptons, among which are neutrinos, and their interactions. This means that we will not discuss the Quantum Chromodynamics since leptons do not interact via the strong interaction.

We will also describe here this model for the first generation of particles only. The other two families require only a simple extension of the model by adding new particles coupling to the electroweak bosons in the same way the first generation particles couple to the electroweak bosons.

Symmetry group of the electroweak theory

The symmetry group used to describe the electroweak theory is the group product :

$$SU(2) \times U_Y(1)$$

The $SU(2)$ group generates three W bosons (the "weak isospin") and the $U_Y(1)$ group generates one A^0 boson (the "weak hypercharge").

In this description, the W and A^0 bosons are naturally massless. In order to give a mass to some of these particles and obtain the $U_{em}(1)$ group corresponding to the electromagnetic interactions it is necessary to spontaneously break the electroweak symmetry with the Higgs mechanism. This spontaneous symmetry breaking leads to a mixing of the W^0 and A^0 bosons that generate the Z^0 and γ bosons.

In this formalism, the γ boson is defined as being generated by the $U_{em}(1)$ group, thus it is associated with the electromagnetic interaction. As the γ boson couples only with charged particles and the neutrinos have no charge [14] there is no interaction between γ and neutrinos. Their properties will not be discussed in this thesis.

The remaining bosons Z^0 and $W^{\pm}$ are vectors of the weak interaction, and therefore interact with neutrinos.

Chirality and representation of the leptons

The chirality is an intrinsic property of particles that can be defined on two different states : left handed (L) and right handed (R). In the electroweak theory, each of the these two different chiralities behave differently which leads to two different representations used to describe the left and right handed particles.

In the case where the particles are massless the chirality and helicity (λ), the sign of the projection of the spin in the direction of the movement (see equation (1.1)), are equivalent operators. This gives us a simple interpretation of what is the chirality in this case, where the left chirality state corresponds to the spin of the particle being in the direction opposed to the movement direction. However there is no correspondence between chirality and helicity with massive particles as it is possible to change the helicity of a particle by choosing a different referential while the chirality, which is an intrinsic property of the particle and therefore a Lorentz invariant, cannot be changed by changing the referential. The physical processes do not change by changing the referential used to observe it.

$$\lambda = \frac{\boldsymbol{p} \cdot \boldsymbol{s}}{|\boldsymbol{p}|}, \text{ with } \boldsymbol{p} \text{ the momenta and } \boldsymbol{s} \text{ the spin of the particle.} \tag{1.1}$$

In the electroweak theory we have two leptons states : the electron (e) and neutrino (ν). We have observed with the study of the β decay that only left handed leptons interact with each other through a charged current weak interaction [17]. In order to take into account this observation we introduce the left handed leptons as a doublet of $SU(2)$ and the right handed leptons as a singlet of $SU(2)$, that would be written for the first generation of particles :

$$l_L = \begin{pmatrix} (\nu_e)_L \\ e_L \end{pmatrix} \qquad l_R = ((\nu_e)_R), (e_R)$$

We should note that, as far as we have observed, right handed leptons do not interact through the $W^{\pm}$ boson and right handed neutrinos are not produced through the decay of the Z^0 boson. In addition to that, given that the neutrino are neutral particles, the (ν_R) singlet is not expected to interact through this theory and is removed from the theory by the Occam's razor[2]. Furthermore there is no experimental evidence of a right handed neutrino which supports the validity of this theory and further reduces the need to introduce a right handed neutrino.

In the Standard Model we have then a doublet and a singlet to describe the leptons of each family as follows for the first generation of particles of the Standard Model[3] :

$$\begin{pmatrix} (\nu_e)_L \\ e_L \end{pmatrix} \qquad (e_R)$$

[2]The Occam's razor is the principle to remove from a theory anything that is not strictly needed, that is if two theories predict the same results we should pick the one with the smaller number of parameters. [18]

[3]The structure is the same for the second and third generations of particles in the Standard Model.

As we have described, the leptons are chiral fermions. We can add to the model a Dirac mass term with Lagrangian $\mathcal{L}_m = -m\overline{\Psi_e}\Psi_e$ where $\Psi_e = P_L\Psi_e + P_R\Psi_e = e_L + e_R$ is the spinor representing electrons, and P_L and P_R are the operators that project the state in the left and right chirality, respectively. This leads to $\mathcal{L}_m = -m\left(\overline{e_L}e_R + \overline{e_R}e_L\right)$, given that since $\overline{e_L} = \overline{e}P_R$, $\overline{e_R} = \overline{e}P_L$ and $P_LP_R = 0$ we have that $\overline{e_L}e_L = 0$ and $\overline{e_R}e_R = 0$.

Since the neutrinos described by this model are only left handed we cannot write the mass Lagrangian for the neutrinos as it was done for the electrons. For this reason the neutrinos are massless particles in the Standard Model, as such possibility was also allowed by the low limits on the neutrino mass given by the experiments at the moment, as will be described in subsection 1.1.2.

Types of neutrino interaction in the Standard Model

As it was mentioned previously the bosons Z^0 and $W^\pm$ are associated with the weak interaction and couple with neutrinos. This implies that we have two different types of neutrino interactions possible in function of with which boson the neutrino interacts.

If the neutrino interacts with the boson Z^0 one call the interaction "neutral current" (NC) and the Feynman diagram representing it is :

If the neutrino interacts with the boson $W^\pm$ one call the interaction "charged current" (CC) and the Feynman diagram representing it is :

where l is the lepton associated with the neutrino ν_l. In this diagram, as in the previous one, we have drawn only half the particles present in this interaction, which is why the charge of the input particle (ν_l or $\overline{\nu_l}$) is not the same as the charge of the output particles (l^- or l^+).

From the experimental point of view, the distinction between NC and CC interactions is that in order to be able to observe the NC interaction it is needed to observe the nuclear recoil or by-products (for example, π^0) of the interaction from the nuclei, while in order to observe the CC interaction it is only needed to observe the lepton associated with the ν that interacted. We should also note that by measuring the NC interaction we cannot distinguish between neutrino flavors, while by measuring the CC interaction each interaction can be distinguished.

1.1.2 Neutrino mass

As it was described previously the neutrinos are massless particles in the Standard Model. However in 1998 the Super Kamiokande collaboration has shown [11] that the neutrinos produced at the Earth's atmosphere disappeared as function of the zenith angle, and in

2001 the SNO collaboration has shown [12] that the neutrino flux from the Sun measured using NC interactions with deuterium was compatible with the neutrino flux expected from the Standard Solar Models, while the same neutrino flux measured using CC interaction with deuterium or electron scattering (which is composed of NC and CC interactions with the electrons) was not compatible with the expected neutrino flux produced at the Sun, as shown in figure 1.1. All these observations were however compatible between themselves and with the expected neutrino flux from the Sun given by the Standard Solar Model when we assume the neutrinos oscillate as proposed by [19].

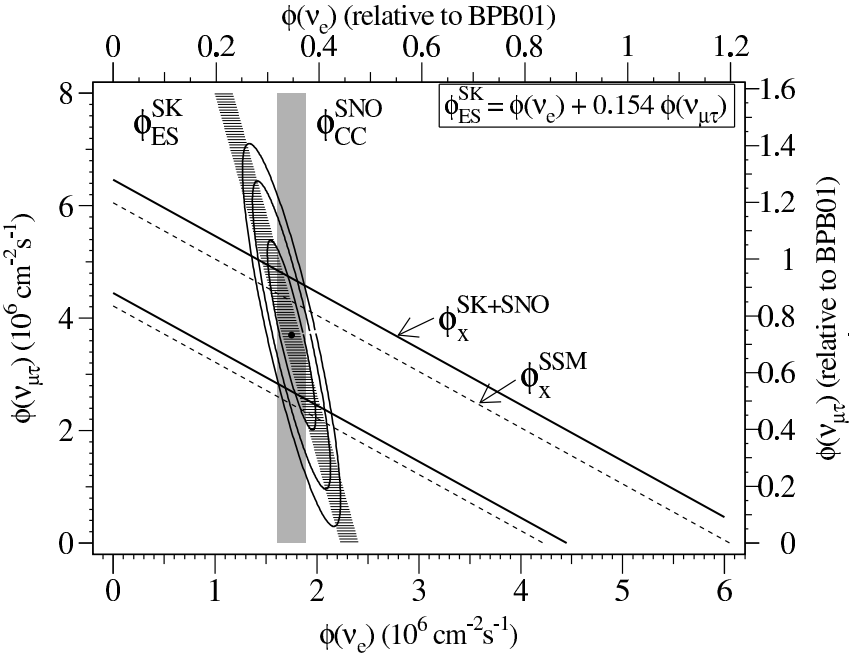

Figure 1.1: Fluxes of ^{8}B solar neutrinos for electron neutrinos (ϕ_e) and muon and tau neutrinos ($\phi_{\mu\tau}$) deduced from SNO and Super Kamiokande measurements of the CC interaction (only sensitive to ν_e), of the NC interaction (sensitive to all ν flavours) and of the ES, that is electron scattering (sensitive mostly to ν_e, but with some contribution from the other neutrino flavours). In dashed lines is shown the Standard Solar Model (SSM) prediction for the total neutrino flux. Figure extracted from [12].

As will be discussed on the section 1.2 in more details, the observation of neutrino oscillation implies that the neutrino masses are not degenerate, thus cannot all be zero as was assumed in the Standard Model. The neutrino oscillations allow only to measure the difference between the square of neutrino masses, not their absolute value, as shown in equation (1.5). For the moment we have only measured upper bounds for the neutrino masses using different assumptions as will be discussed further on.

The observation that neutrinos are massive particles is the first evidence of physics beyond the Standard Model. Even though there is a possible simple extension to the Standard Model that give masses to the neutrinos using the same mechanism that was used for the other particles (the Higgs mechanism) this solution requires the existence of ν_{R} that we cannot observe, as discussed previously. In this case neutrinos are Dirac particles.

Another way to introduce a mass Lagrangian to neutrinos is to extend the Standard Model by assuming the neutrino is a Majorana particle [20]. In this case we

can create a mass term without adding a right handed neutrino that has the form $\mathcal{L}_{M_L} = -m_L \left(\overline{\nu_L}\,(\nu_L)^c + (\overline{\nu_L})^c\,\nu_L\right)$. It is also possible to add a right handed neutrino which would also be related to another mass Lagrangian with the same format (by changing the L fields to R fields in the previous expression), and in this case this right handed Majorana mass Lagrangian could be added to the left handed Majorana mass Lagrangian and to the Dirac Lagrangian to create a more general mass Lagrangian. It is however important to notice that it has not yet been experimentally observed that neutrinos are Majorana particles [14], because the principal measurements to observe the neutrino Majorana nature, that is the search for neutrino-less double β decay, has only set upper limits to their existence, as will be discussed in section 1.1.4.

1.1.3 Majorana particles and the seesaw mechanism

Majorana particles are particles which are their own anti-particles. In order for this to be possible it is needed that these particles have null charge, therefore in the Standard Model only neutrinos are candidates to be Majorana particles.

If the neutrinos are Majorana particles, that is if they are their own antiparticles, there can no longer be conservation of the lepton number by interactions and therefore it should be possible to observe processes violating the lepton number, such as a neutrino-less double beta decay, where the two neutrinos that are usually produced by a double beta decay annihilate during the interaction :

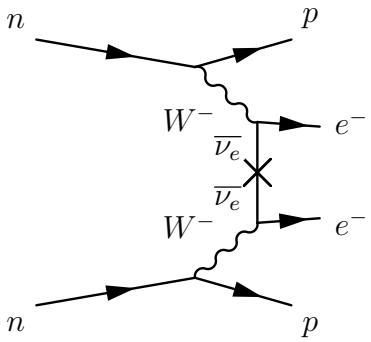

Furthermore, if the neutrinos are Majorana particles with also a Dirac mass term, it is also possible to justify the smallness of the neutrinos masses in relation to the masses of other fermions from the Standard Model using the seesaw mechanism[4], in which the neutrinos masses are $\frac{m_D^2}{m_R}$ and m_R, where m_D is the Dirac mass of the neutrinos and m_R is the Majorana mass of the right-handed neutrinos. In this context usually the Dirac mass is assumed to be of the same order of magnitude as the mass of the other fermions, and the Majorana mass m_R could be as large as required to explain the observed neutrino mass[5]. One could argue that in this case the problem of the smallness of neutrino masses was only transfered to the bigness of m_R compared to the other masses, however since the process that engenders the other fermion masses is the Higgs mechanism it corresponds only to the m_D mass and has no relation whatsoever with the m_R mass specific to neutrinos.

[4]To have the seesaw mechanism it is required that $m_D \ll m_R$ and $m_L = 0$, m_L is the Majorana mass of the left-handed neutrinos. More precisely these are the required conditions for type I seesaw. In the case of type II seesaw the $m_L = 0$ constraint is softened to $m_L \ll m_D$ and the expression of the neutrinos masses is slightly changed from the given ones.

[5]Usually the Majorana mass m_R is assumed to be at the Grand Unification Theory scale.

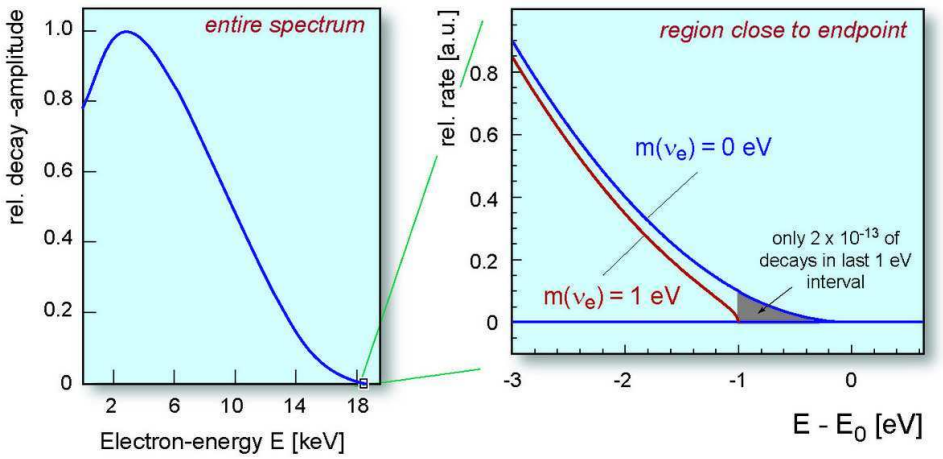

Figure 1.2: β-decay spectra of the electron. The right figure is a zoom-in of the end of the left figure in order to show explicitly the effect of the neutrino mass at the end point of the spectrum (E_0). Figure extracted from `http://www.katrin.kit.edu/`.

Finally we should note that the Dirac or Majorana characteristic of the neutrinos do not change the flavour oscillation probabilities, therefore it will not be further discussed in the section 1.2.

1.1.4 Measurement and estimation of neutrino masses

There are actually several different methods to determine the neutrino masses using different data sets and assumptions, such as :

- measure of the end point of the beta spectrum;
- measure of the time of flight of neutrinos from a supernovae;
- observation of the cosmological formation of structures;
- measure of the neutrino-less double beta decay.

Measure of the end point of the beta spectrum

This method is based on the fact that in a three body decay the maximum energy each particle can have is smaller than the total energy released subtracted to the mass energy of each of the particles. Therefore if the electron spectrum from a beta decay is precisely measured it is possible to measure the neutrino mass as the difference between the end point of this spectrum and the energy difference between the two different nuclei, given that we know well the mass of the other particles involved in the beta decay, as shown in figure 1.2.

The current best results for the measurement of the ν_e mass were obtained from tritium decay by the experiments Mainz and Troisk which lead to a superior limit on the neutrino electron mass of 2 eV/c^2 at 95% confidence level [14, 21, 22].

There is also an ongoing experiment, KATRIN, which intends to measure the neutrino electron mass with this method using tritium beta decay. The expected sensitivity for this experiment is 0.2 eV/c^2 at 90% confidence level [23].

Measure of the time of flight of neutrinos from a supernovae

By measuring the time a neutrino generated from a supernovae takes to arrive to Earth, the distance from the supernovae and it's energy it is possible to measure the neutrino mass. Using the 1987A supernovae it was determined that the neutrino electron mass is lower than 5.7-5.8 eV/c^2 at 95% confidence level [24, 25].

Observation of the cosmological formation of structures

In the current models that explain the formation of our universe the neutrino mass is one of the parameters that need to be implemented. From simulations of these models it is possible to evaluate the type of structure formation would be observed for different neutrino masses. These estimations depend strongly in the models used for the simulations, and therefore do not provide a robust estimative for the neutrino masses. From the observation of formation of structures and other cosmological observations it is possible to obtain an upper limit for the neutrino masses of 0.44 eV/c^2 [26] using 7 years of WMAP CMB data, halo power spectrum (HPS) and the Hubble constant (HST). The best limit quoted in [14] for the sum of neutrino masses is 0.17 eV/c^2 [27] obtained using 3 years of WMAP CMB data, large scale structure (LSS), Lyman-alpha forest power spectrum (Ly-α) and Supernovae type 1a (SN1a) data.

Measure of the neutrino-less double beta decay

As was discussed previously, if the neutrinos are Majorana particles we can observe a neutrino-less double beta decay. The branching ratio of this decay depends on the mass of the neutrinos. It is this possible to measure in this case the effective weighted sum of Majorana neutrino mass $< m_\nu >= |\sum U_{1j}^2 m_{\nu_j}|$ with the measure of the neutrino-less double beta decay branching ratio. As we have not yet observed this signature we can only obtain a superior limit to the case the neutrino is a Majorana particle. The limits are given as function of the isotope used for the measurement and are usually in the order of the eV/c^2, with limits that can be as low as 0.26-1.1 eV/c^2 90% CL, which was quoted by the KamLAND-Zen collaboration for ^{136}Xe [28]. The mass range given reflects spread of nuclear matrix elements considered in the given work. The current best limits for each studied isotope, as reported by [14] is shown in figure 1.3.

The Heilderberg-Moscow collaboration has claimed a measurement of neutrino-less double beta decay with 6σ significance level, leading to a neutrino effective Majorana mass of about 0.32$\pm$0.03 eV/c^2 (however the uncertainty quoted here does not take into account uncertainties due to nuclear matrix elements) [37]. This claim is not widely accepted by the physics community and was not verified by other independent measurements [14].

Currently several experiments are running, such as KamLAND-Zen (^{136}Xe), EXO (^{136}Xe), CUORE 0 (^{130}Te, upgrade from CUORICINO); and several others are under construction and R&D, such as SuperNEMO (upgrade from NEMO 3), CUORE (continuation of upgrade from CUORE 0), GERDA and Majorana (that use Ge as isotopes to directly confirm or refute the Heilderberg-Moscow claim).

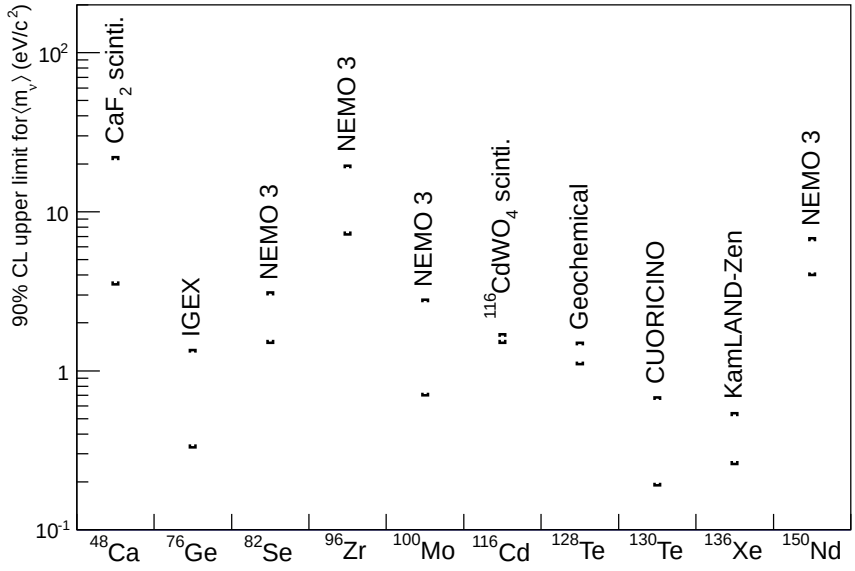

Figure 1.3: Upper limit of $< m_\nu >$ given for different isotopes. Above each limit is shown which collaboration or technique was used for this measurement. The results shown here were obtained by IGEX [29], NEMO 3 [30–32], CUORICINO [33] and KamLAND-Zen [28] collaborations or using CaF_2 scintillators [34], $^{116}CdWO_4$ scintillators [35] and a geochemical method [36].

Current limits obtained from different searches

The current best knowledge of the neutrino masses is summarized on table 1.2 and on figure 1.4 where is also shown the constraints on each neutrino mass from the known oscillation parameters. The best limit currently accepted for the neutrino masses come from the measure of the end point of tritium spectrum and is of 2 eV/c^2 [14].

The more precise estimations given by the cosmological limits are currently not quoted as the best limits on neutrinos masses since it is not yet clear how much these estimations are dependent on the used models [14]. Likewise the estimations of neutrino masses from neutrino-less double beta decay measurements is not quoted as the current limits for the neutrino mass given that for this limit to be valid it is required that the neutrino is a Majorana particle, which was not yet measured to be the case.

Table 1.2: Best limits on the neutrino mass from several different searches

	measured mass	actual limit (eV/c^2)	
end point of beta spectrum	$m_{\overline{\nu_e}}$	<2	(95% CL)
time of flight of neutrinos from supernovae	$m_{\overline{\nu_e}}$	<5.8	(95% CL)
cosmological formation of structures	$\sum_i m_{\nu_i}$	<0.17,0.44	(95% CL)
neutrino-less double beta decay	$< m_\nu >$	<0.26-1.1	(90% CL)

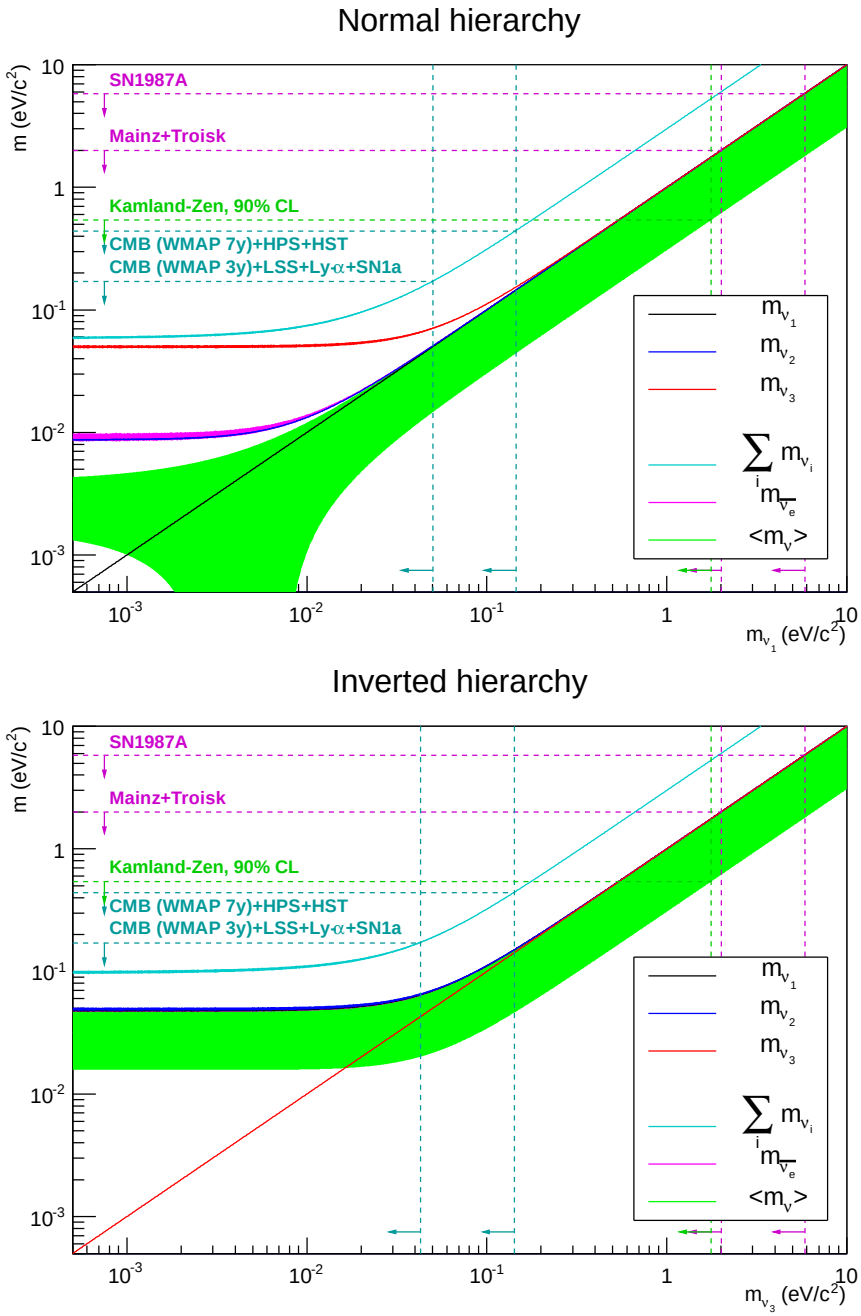

Figure 1.4: Mass of neutrinos in function of the mass of the lightest neutrino for normal (top) and inverted (bottom) hierarchy. It is also shown in the total sum of the three neutrino masses, the $\overline{\nu_e}$ mass and the effective Majorana mass ($< m_\nu >$). The line width represents the $\pm 1\sigma$ region obtained from current knowledge of the oscillation parameters given in table 1.3 for all calculated masses, expect for the effective Majorana mass where we only consider the differences coming from the phase space produced from the unknown Majorana phases. We should note that in normal hierarchy $m_{\overline{\nu_e}}$ and m_{ν_2} are quasi-degenerates and in inverted hierarchy $m_{\overline{\nu_e}}$, m_{ν_1} and m_{ν_2} are quasi-degenerates, therefore they are not clearly visible in the figure. The current limits on the neutrino mass shown in table 1.2 are also shown in the same color as the mass they constrain. These limits are given for 95% CL when not stated otherwise. In the case of $< m_\nu >$ we show the worst value of the current limit given in table 1.2 given that the given range correspond to uncertainties in the knowledge of nuclear matrix elements.

1.2 Neutrinos oscillations

In 1957 B. Pontecorvo proposed that neutrinos could oscillate between $\nu \leftrightarrow \overline{\nu}$ [38]. A few years later, in 1962, it was observed the existence of two kinds of neutrinos [39] and in the same year Z. Maki, M. Nakagawa and S. Sakata proposed neutrino flavour oscillation [19], a bit earlier than the publication of [39]. Even though the neutrino flavour oscillation formalized in reference [19] was described using as base a different model for the composition of matter than the currently accepted Standard Model, the basis for neutrino mixing and oscillation are the same with both models.

As will be explained neutrino oscillation can only happen if the neutrinos are massive particles, with mass eigenstates different from flavour eigenstates. In this case neutrinos are produced via weak interaction in a flavour eigenstate, a linear composition of the different mass eigenstates. These states are propagated separately and, after some time, measured through weak interaction in a different flavour eigenstate. In this section this property will be studied.

1.2.1 Eigenstates

For each generation in the Standard Model we have different neutrino mass eigenstates defined as $|\nu_i\rangle = \{|\nu_1\rangle, |\nu_2\rangle, |\nu_3\rangle\}$.

Likewise we define the neutrino flavour eigenstates from which of the charged leptons interact with the neutrinos through charged current : $|\nu_\alpha\rangle = \{|\nu_e\rangle, |\nu_\mu\rangle, |\nu_\tau\rangle\}$. Each of these states is a different linear composition of the $|\nu_i\rangle$ eigenstates. We can thus write :

$$|\nu_\alpha\rangle = \sum_i U^*_{\alpha i} |\nu_i\rangle \tag{1.2}$$

where U is an unitary matrix ($UU^\dagger = \mathbb{1}$).

This matrix, which is defined from the transformation between neutrino flavour and mass states, is called Pontecorvo-Maki-Nakagawa-Sakata (PMNS) matrix[6].

1.2.2 Oscillation probability in the vacuum

If not mentioned otherwise we will consider neutrino oscillations in the vacuum where there is no interaction probability with matter during propagation. We will later discuss the validity of this approximation for T2K.

If at given time ($t = 0$) a neutrino with flavour $|\nu_\alpha\rangle$ is produced, we obtain at time t the new $|\nu_\alpha, t\rangle$ is given by :

$$|\nu_\alpha, t\rangle = \sum_j U^*_{\alpha j} e^{-iE_j t} |\nu_j\rangle \tag{1.3}$$

The probability that we measure after t a neutrino with flavour $|\nu_\beta\rangle$ is given by :

$$P(\nu_\alpha \to \nu_\beta, t) = ||\langle \nu_\beta | \nu_\alpha, t\rangle||^2 = \sum_{j,k} U_{\beta j} U^*_{\alpha j} U^*_{\beta k} U_{\alpha k} e^{-i(E_j - E_k)t} \tag{1.4}$$

[6]The PMNS matrix is named after the first physicists that have proposed neutrino oscillation. Given that some physicists do not consider B. Pontecorvo as one of the parents of neutrino oscillations the PMNS matrix is also called MNS matrix. The PMNS matrix is also referred to as lepton mixing matrix or neutrino mixing matrix given its function.

We can note here that for $t = 0$:

$$P(\nu_\alpha \to \nu_\beta, 0) = \sum_{j,k} U_{\beta j} U^*_{\alpha j} U^*_{\beta k} U_{\alpha k} = (UU^\dagger)_{\beta\alpha}(UU^\dagger)_{\alpha\beta} = \delta_{\alpha\beta}$$

that is as we would have expected.

As $E_i = \sqrt{m_i^2 + p^2} \approx p + \frac{1}{2}\frac{m_i^2}{p}$ where m_i is the mass of the $|\nu_i\rangle$ and p its momentum for $p \gg m_i$ and $t \cong L$ we obtain that

$$(E_j - E_k)t \approx (m_j^2 - m_k^2)\frac{L}{2p} = \Delta m^2_{jk}\frac{L}{2p}$$

$$\Rightarrow P(\nu_\alpha \to \nu_\beta) = \sum_{j,k} U_{\beta j} U^*_{\alpha j} U^*_{\beta k} U_{\alpha k} e^{-i\Delta m^2_{jk}\frac{L}{2p}} \tag{1.5}$$

This relation shows that with same degenerate mass eigenstates there would be no neutrino oscillations as $\Delta m^2_{jk} = 0$, thus all neutrino masses cannot be 0 as assumed in the Standard Model.

If we consider the case of anti-neutrinos rather than neutrinos we obtain in the same way

$$P(\overline{\nu_\alpha} \to \overline{\nu_\beta}) = \sum_{j,k} U^*_{\beta j} U_{\alpha j} U_{\beta k} U^*_{\alpha k} e^{-i\Delta m^2_{jk}\frac{L}{2p}} \tag{1.6}$$

If the CP symmetry is conserved we should have $P(\overline{\nu_\alpha} \to \overline{\nu_\beta}, t) = P(\nu_\alpha \to \nu_\beta, t)$, true if U is a real matrix.

2-flavour case

In this case the matrix U can be written generically as a 2×2 rotation matrix :

$$U = \begin{pmatrix} \cos\theta & \sin\theta \\ -\sin\theta & \cos\theta \end{pmatrix}$$

where θ is the mixing angle between the two flavours. Using the explicit formula for U in (1.5) we can easily calculate the oscillation probability as

$$P(\nu_\alpha \to \nu_\beta) = \frac{\sin^2 2\theta}{2}\left(1 - \cos\Delta m^2_{jk}\frac{L}{2p}\right) \qquad (\alpha \neq \beta) \tag{1.7}$$

$$P(\nu_\alpha \to \nu_\alpha) = 1 - \frac{\sin^2 2\theta}{2}\left(1 - \cos\Delta m^2_{jk}\frac{L}{2p}\right) \tag{1.8}$$

Note that we cannot in this case add a CP violating phase in the 2-flavour U matrix : if we considered a complex U matrix with the required properties (see A.3) :

$$U = \begin{pmatrix} \cos\theta & \sin\theta e^{-i\delta} \\ -\sin\theta e^{i\delta} & \cos\theta \end{pmatrix}$$

the oscillation probability would not depend on δ as $\forall \alpha, \beta, j, k$ the $U_{\beta j} U^*_{\alpha j} U^*_{\beta k} U_{\alpha k}$ do not depend on δ, thus we cannot have CP violation in neutrino oscillations.

3-flavour case

In this case we can write generically a rotation matrix U as the product of 3 rotations matrix :

$$\begin{aligned} U &= \begin{pmatrix} 1 & 0 & 0 \\ 0 & c_{23} & s_{23} \\ 0 & -s_{23} & c_{23} \end{pmatrix} \times \begin{pmatrix} c_{13} & 0 & s_{13}e^{-i\delta} \\ 0 & 1 & 0 \\ -s_{13}e^{i\delta} & 0 & c_{13} \end{pmatrix} \times \begin{pmatrix} c_{12} & s_{12} & 0 \\ -s_{12} & c_{12} & 0 \\ 0 & 0 & 1 \end{pmatrix} \\ &= \begin{pmatrix} c_{12}c_{13} & s_{12}c_{13} & s_{13}e^{-i\delta} \\ -s_{12}c_{23} - c_{12}s_{23}s_{13}e^{i\delta} & c_{12}c_{23} - s_{12}s_{23}s_{13}e^{i\delta} & s_{23}c_{13} \\ s_{12}s_{23} - c_{12}c_{23}s_{13}e^{i\delta} & -c_{12}s_{23} - s_{12}c_{23}s_{13}e^{i\delta} & c_{23}c_{13} \end{pmatrix} \end{aligned}$$

where $c_{ij} = \cos\theta_{ij}$ and $s_{ij} = \sin\theta_{ij}$, with θ_{ij} mixing angles and δ is a CP violating phase.

We should note that if we had written each rotation matrix with a complex phase the obtained oscillation probability would have the same expression as the result obtained with the given U matrix with only one complex phase. This is demonstrated in the appendix A.4.

As was briefly discussed previously in the 2-flavour section we use a complex rotation matrix in order to be able to violate the CP symmetry. A very weak CP violation has already been observed in the quark sector. Furthermore, we expect there is CP violation in the universe because currently we observe the universe to be composed mainly of matter, while in the absence of CP violation we would expect to observe the same quantity of matter and antimatter. In order to violate the CP symmetry in the lepton sector it is necessary that all 3 θ_{ij} angles be different from 0.

We can then use the U matrix to calculate the oscillation probability between any two given neutrino types as previously. The results from this calculation have a complicated expression[7], thus we usually use a 2-flavour approximation to calculate these probabilities as will be discussed further on.

In the 3-flavour oscillation probability there are 6 free parameters :

- 3 mixing angles : θ_{12}, θ_{23} and θ_{13};
- 2 squared mass differences[8] : Δm^2_{21} and Δm^2_{32};
- 1 CP violation phase : δ (or δ_{CP}).

Even though the full expression of the oscillation probability in the 3-flavour case cannot be easily written, given the current knowledge of the oscillation parameters, it is composed by a long oscillation (defined by the Δm^2_{21} term) and shorter oscillations (defined by the $\Delta m^2_{32} \approx \Delta m^2_{31}$) that will be superposed to one another as shown in figure 1.5 for $P(\nu_\mu \to \nu_X)$ in function of L/E. In this figure we assume the value of the oscillations parameters to be the currently best measured values for the 3 mixing angles and 2 squared mass differences assuming normal hierarchy and $\delta_{CP} = 0°$.

The effect of different δ_{CP} phase on $P(\nu_\mu \to \nu_e)$ is shown in figure 1.6 for four different δ_{CP} values. For the typical T2K L/E of about 500 km/GeV (see chapter 2) it is possible to distinguish well the $\delta_{CP} = 90°$ (lowest oscillation probability), $\delta_{CP} = 270°$ (highest oscillation probability) and $\delta_{CP} = 0°$, however it is much harder to distinguish between $\delta_{CP} = 0°$ and $\delta_{CP} = 180°$ which have similar oscillation probability, though with slightly different position for the maximum L/E.

[7] The full 3-flavour calculation is developed in the appendix A.5 for the U matrix given previously.

[8] Note that the third squared mass difference can be written in function of the other two squared mass differences as $\Delta m^2_{31} = \Delta m^2_{32} + \Delta m^2_{21}$.

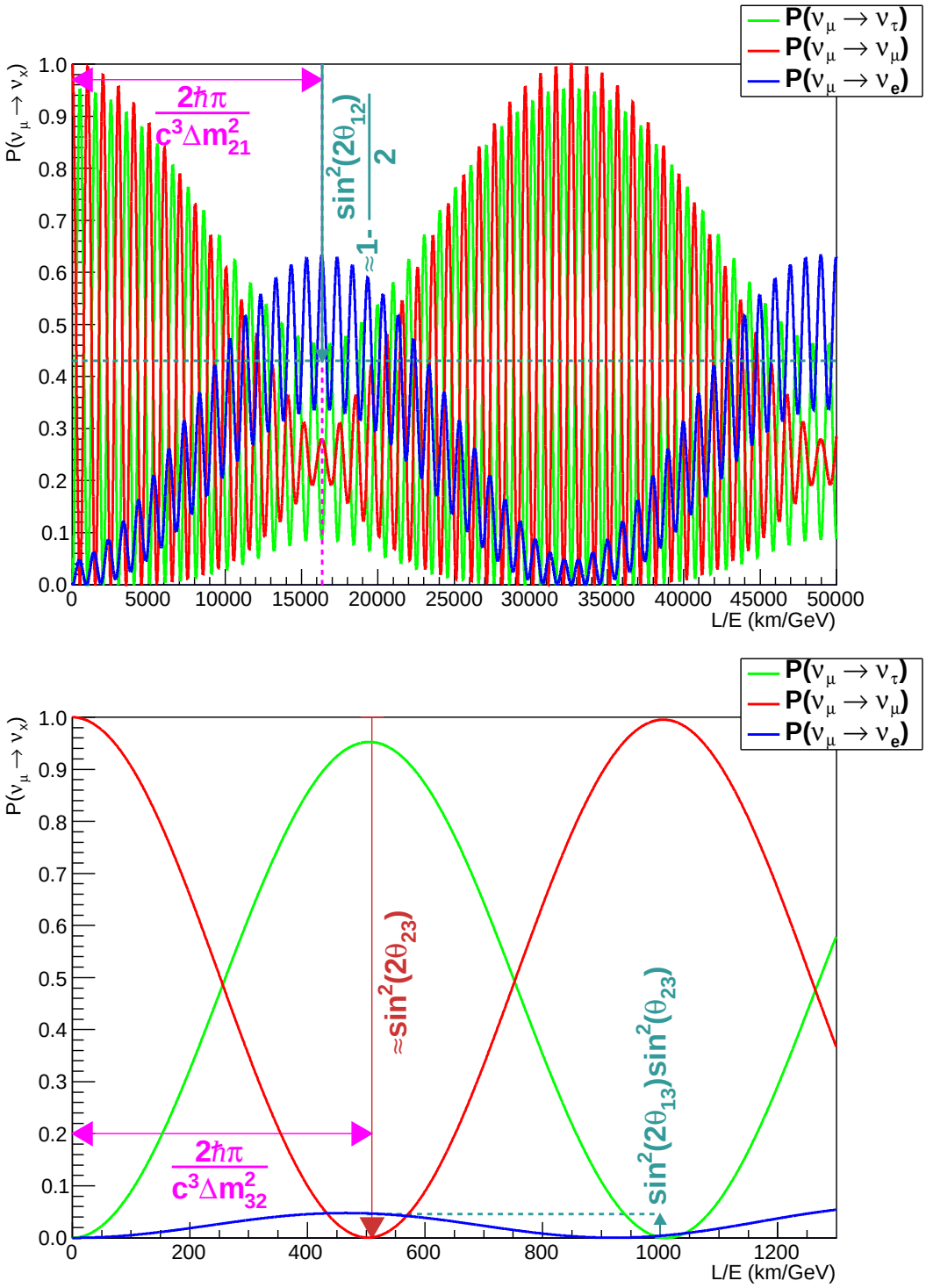

Figure 1.5: Oscillation probability of $\nu_\mu \to \nu_e$ (blue), $\nu_\mu \to \nu_\mu$ (red) and $\nu_\mu \to \nu_\tau$ (green) as function of L/E. In the top plot the full effect of the 3-flavour oscillation is shown, where we can clearly distinguish two oscillation frequencies related to Δm^2_{21} (slow oscillation) and Δm^2_{32} (fast oscillation). In the bottom plot the L/E region is zoomed in near the first oscillation peak. Oscillation probabilities were calculated using Prob3++ [40] with $\sin^2(2\theta_{12}) = 0.861$, $\sin^2(2\theta_{13}) = 0.092$, $\sin^2(2\theta_{23}) = 1$, $\Delta m^2_{21} = 7.59 \cdot 10^{-5}$ eV^2/c^4 , $\Delta m^2_{32} = 2.43 \cdot 10^{-3}$ eV^2/c^4 (normal hierarchy) and $\delta_{CP} = 0$. In the figure are also shown to which oscillation periods each Δm^2 corresponds, as well as to which amplitudes each θ corresponds. The T2K experiment has L/E between about 300 and 600 km/GeV, with maximum at about 500 km/GeV, as will be presented in chapter 2.

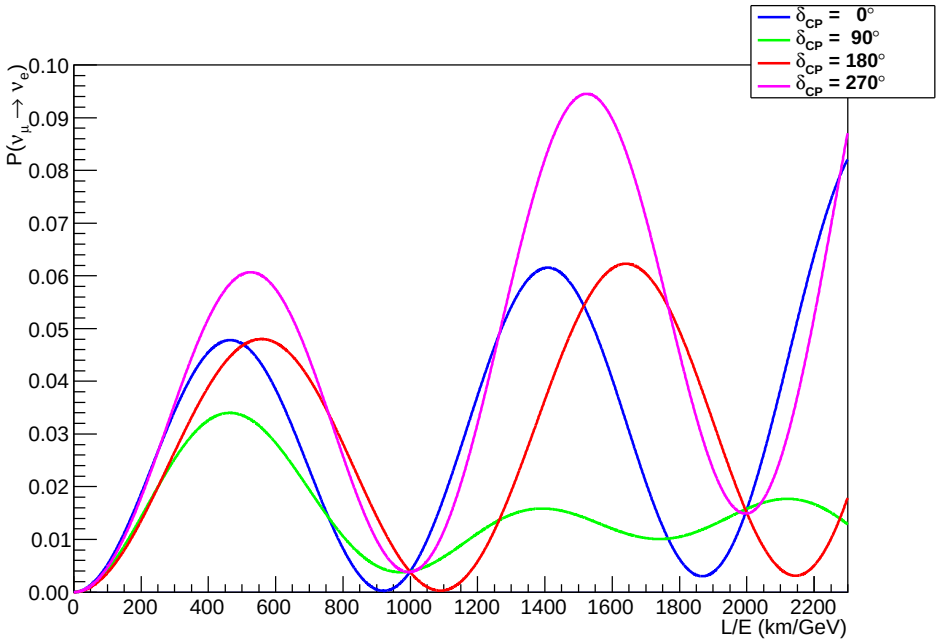

Figure 1.6: Oscillation probability of $\nu_\mu \to \nu_e$ as function of L/E assuming $\delta_{CP} = 0°$ (blue), $\delta_{CP} = 90°$ (green), $\delta_{CP} = 180°$ (red) and $\delta_{CP} = 270°$ (magenta). Oscillation probabilities were calculated using Prob3++ [40] with $\sin^2(2\theta_{12}) = 0.861$, $\sin^2(2\theta_{13}) = 0.092$, $\sin^2(2\theta_{23}) = 1$, $\Delta m^2_{21} = 7.59 \cdot 10^{-5}$ eV^2/c^4 and $\Delta m^2_{32} = 2.43 \cdot 10^{-3}$ eV^2/c^4 (normal hierarchy). The T2K experiment has L/E between about 300 and 600 km/GeV, with maximum at about 500 km/GeV, as will be presented in chapter 2.

Validity of 2-flavour approximation of 3-flavour case

The 2-flavour approximation for the 3-flavour oscillation can be used when the two Δm^2_{jk} have large differences. In this case this approximation can be used when $e^{i\Delta m^2 L/2p} \approx 1$, Δm^2 being the smallest mass difference.

Let's suppose that $|\Delta m^2_{21}| \ll |\Delta m^2_{32}|$. We have then that $|\Delta m^2| := |\Delta m^2_{32}| \approx |\Delta m^2_{31}|$. As it is shown at the appendix A.6 the oscillation probability in the considered case is :

$$\begin{cases} P(\nu_\alpha \to \nu_\alpha) &= 1 - 4|U_{\alpha 3}|^2 \left(1 - |U_{\alpha 3}|^2\right) \sin^2\left(\frac{c^3}{4\hbar}\Delta m^2 \frac{L}{E}\right) \\ P(\nu_\alpha \to \nu_\beta) &= 4|U_{\alpha 3} U_{\beta 3}|^2 \sin^2\left(\frac{c^3}{4\hbar}\Delta m^2 \frac{L}{E}\right) \end{cases}$$

As these oscillation probabilities depend only on $|U_{\alpha 3}|$ they do not depend on the value of θ_{12}. This occurs since in the condition this approximation is valid $|\nu_1\rangle$ and $|\nu_2\rangle$ are two degenerate mass states, which means that we can choose a $|\nu_1\rangle$ and $|\nu_2\rangle$ with any given θ_{12} angle without changing our result.

We should note that using this approximation it is not possible to measure the CP violation phase as $|U_{\alpha 3}|$ do not depend on δ_{CP}. Therefore this approximation will not be used in the oscillation analysis performed in this thesis, using the full 3-flavour oscillation probability instead.

This same formalism can be used also to study neutrino oscillations when θ_{13} is small at long distances [14]. In this case the oscillation from the Δm^2_{32} is rapid and will average to zero as our detector has a finite resolution. This approximation allows us to study directly Δm^2_{21} and θ_{12} directly, as shown in the top part of the figure 1.5.

Sterile neutrinos

Even though we know from the LEP's measurement of the Z^0 width [9] that there are only 3 light neutrino[9] flavours coupling to the Z boson, as shown in figure 1.7. We could, on the other hand, suppose that there are more than 3 neutrinos and that the additional neutrinos simply do not interact with the Z boson, therefore do not change the Z width. The supplementary neutrinos that we can introduce in this way are called sterile neutrinos, given that they do not have an ordinary weak interaction except those induced by mixing with other neutrinos [41].

The existence of sterile neutrinos requires that there are more than 3 neutrino mass eigenstates ν_i, which means that the PMNS matrix has a dimension higher than 3 and therefore a part of the usual neutrinos would be from another $|\nu_i\rangle$ with $i > 3$. The effect of this change in the PMNS matrix is that the oscillation probabilities, in this case, have no longer the given formula and we should be able to observe a different ν disappearance or ν appearance rate than what would be expected by the 3-dimensional PMNS matrix. Another implication of having sterile neutrinos is that the 3×3 PMNS matrix usually considered no longer needs to be unitary because it would be in fact part of a larger PMNS matrix.

For the moment there is no conclusive evidence of the existence of sterile neutrinos, even though there are hints at a 3 σ level from experiments such as LSND [42] and MiniBooNE [43], or from the reactor anomaly [44]. There are, on the other hand, other measurements that do not favour the existence of sterile neutrinos, such as Karmen [45] where it puts restrictions to the phase space allowed by LSND as shown in figure 1.8, or

[9]Here light neutrinos refer to neutrinos lighter than $m_Z/2 \approx 45$ GeV/c^2.

that are even in some tension with the mentioned hints in the case of the simplest scenario for sterile neutrinos [41].

Given that at present there is no conclusive evidence of sterile neutrinos, we will consider in this thesis that they do not exist and will describe neutrino oscillation using only 3 ν flavours.

1.2.3 Neutrino propagation through matter

In the previous section we have discussed how the neutrino oscillates when it propagates in the vacuum. However, usually the neutrino will propagate through matter before arriving at the detection point, typically it will travel through the Earth's crust or mantle, or leave the Sun core.

As was previously explained neutrinos can interact either via neutral current or via charged current. The effect of matter in the neutrino oscillation is engendered by the coherent forward scattering of neutrinos in matter that is given by the following Feynman diagrams :

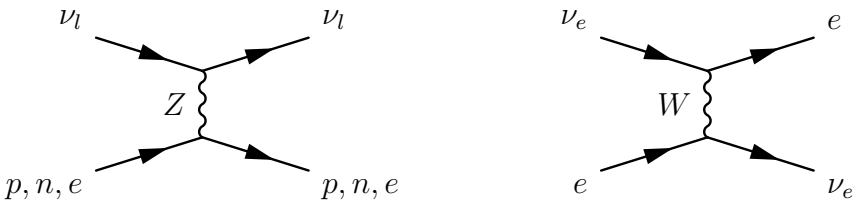

We should note that the NC scatterings do not distinguish between neutrinos flavours, therefore it will not change the oscillation probability. However the CC scattering happens only for electron neutrinos since matter is mainly composed by protons, neutrons and electrons. No μ and τ are naturally present to allow CC scattering for ν_μ and ν_τ, respectively. This effect is called the Mikheyev–Smirnov–Wolfenstein (MSW) effect [46, 47].

The MSW effect changes the oscillation probability increasing the ν effective mass in matter by adding a potential of $\sqrt{2}G_F(N_e\delta_{\alpha e} + \frac{N_n}{2})$ for ultrarelativistic left-handed neutrinos, where G_F is the Fermi constant, N_e the electron density of the medium, N_n the neutron density of the medium and $\delta_{\alpha e}$ is 1 for ν_e and 0 for ν_μ and ν_τ [48]. It should also be noted that in addition to changing the effective mass the angular decomposition of the PMNS matrix in θ_{12}, θ_{13} and θ_{23} is also changed by this potential.

In figure 1.9 is shown how the $\nu_\mu \to \nu_e$ oscillation probabilities change due to the MSW effect for matter with uniform density of 2.6 g/cm^3 and 3.2 g/cm^3, values that correspond the Earth's crust mean density of the T2K baseline and the Earth's mantle density [49], respectively. As shown there is no strong MSW change in the shape of the ν_e appearance probability for L/E of about 500 km/GeV which corresponds to the typical value of L/E of T2K. For the oscillation analysis presented in chapter 5 we will assume that neutrinos propagate through the Earth's crust with constant density of 2.6 g/cm^3.

The MSW effect is essential to explain the oscillation of the neutrinos produced in the Sun and to measure the sign of Δm^2_{21}. In effect, the large oscillation from ν_e to other neutrino flavours in the Sun cannot be explained simply by the vacuum oscillation of neutrinos and to explain such oscillation rate it is needed to consider the case of the MSW effect being applied to neutrinos being propagated through a medium with decreasing electron density[10]. In this case, there a critical value for the electron density

[10]It is also required that the electron density at the production point be higher than the electron density at the "resonance" point, which is the case in the Sun.

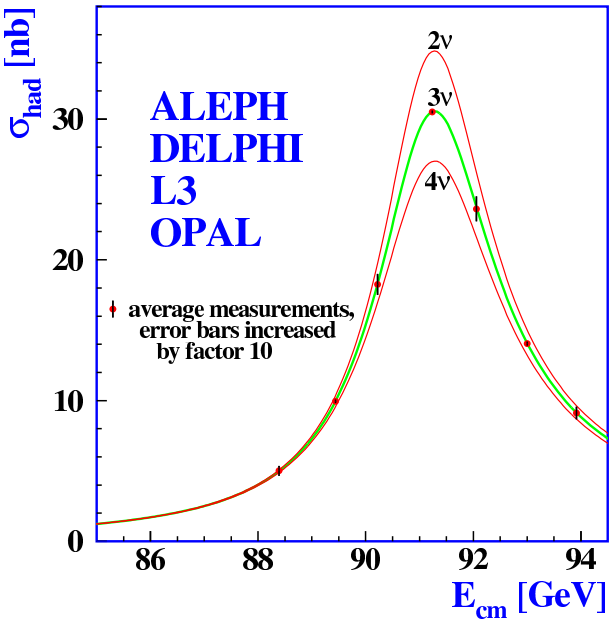

Figure 1.7: Measurement of the hadron production cross-section around the Z resonance at the LEP. The curves indicate the predicted cross-section for 2ν, 3ν and 4ν species interacting with the Z boson, assuming Standard Model couplings and having a negligible mass. Figure extracted from [9].

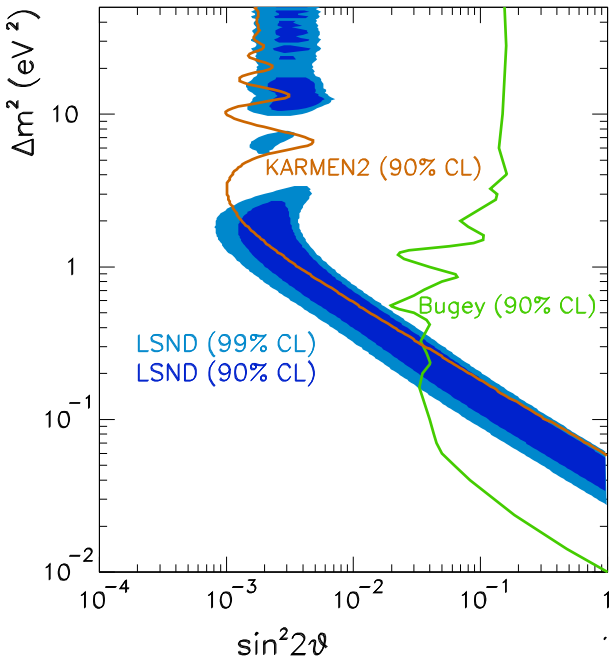

Figure 1.8: $(\Delta m^2, \sin^2 2\theta)$ phase space allowed from fit to LSND data (blue). Here are also shown exclusion limits at 90% CL from KARMEN 2 (red) and Bugey 4 (green) data. Figure extracted from [41].

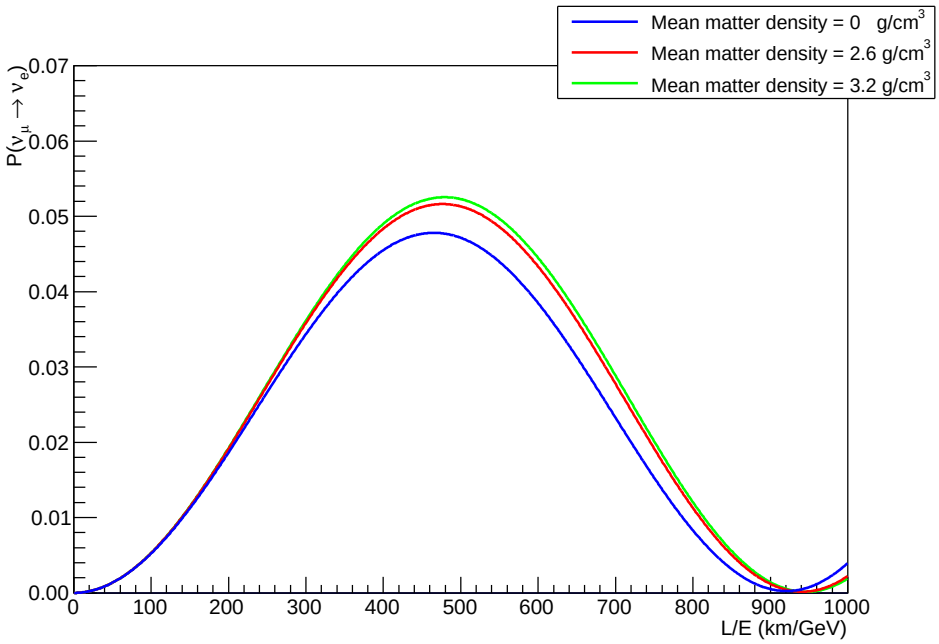

Figure 1.9: Oscillation probability of $\nu_\mu \rightarrow \nu_e$ as function of L/E for mean matter densities during neutrino propagation corresponding to vacuum (blue), the crust of the Earth (red) and mantle of the Earth (green). Oscillation probabilities were calculated using Prob3++ [40] with $\sin^2(2\theta_{12}) = 0.861$, $\sin^2(2\theta_{13}) = 0.092$, $\sin^2(2\theta_{23}) = 1$, $\Delta m^2_{21} = 7.59 \cdot 10^{-5}$ eV^2/c^4, $\Delta m^2_{32} = 2.43 \cdot 10^{-3}$ eV^2/c^4 (normal hierarchy) and $\delta_{CP} = 0$ calculated for ν_μ at L=295 km. The T2K experiment has L/E between about 300 and 600 km/GeV, with maximum at about 500 km/GeV, as will be presented in chapter 2.

at which the flavour content of the neutrino "jump" to another state. This critical point is called "resonance condition" and then it is possible to have large flavour oscillation rates. This "resonance condition" can only happen if $\Delta m^2_{21} > 0$. Since such "jump" is required to explain the amount of ν_e measured at Earth in relation to the amount of ν_e produced at the Sun it was determined that Δm^2_{21} is positive [14].

It would be possible to measure the sign of Δm^2_{32} using the MSW effect in the same way, using another neutrino source, however we have not yet achieved the required precision to perform such measurement.

1.2.4 Usual decomposition of the PMNS matrix and currently known values and experiments

The PMNS matrix presented earlier is usually decomposed with the parts depending on each of the θ_{jk} angles separately. Historically θ_{12} and Δm^2_{21} were called $\theta_\odot$ and $\Delta m^2_\odot$, respectively, because their values was measured via the neutrino oscillation observed for solar neutrinos, therefore the part of the PMNS matrix depending on the θ_{12} parameter was called "solar sector". Also, historically θ_{23} and Δm^2_{32} were called[11] θ_{atm} and Δm^2_{atm}, respectively, because their values was measured via neutrino oscillation observed for neutrinos produced in the Earth's atmosphere, and therefore the part of the PMNS matrix depending on the θ_{23} parameter was called "atmospheric sector". Finally, since the first experiences to measure and set limits on the θ_{13} parameter were reactor-based experiments this remaining sector was called "reactor sector".

$$\text{PMNS matrix} : U = \underbrace{\begin{pmatrix} 1 & 0 & 0 \\ 0 & c_{23} & s_{23} \\ 0 & -s_{23} & c_{23} \end{pmatrix}}_{\text{"atmospheric sector"}} \times \underbrace{\begin{pmatrix} c_{13} & 0 & s_{13}e^{-i\delta} \\ 0 & 1 & 0 \\ -s_{13}e^{i\delta} & 0 & c_{13} \end{pmatrix}}_{\text{"reactor sector"}} \times \underbrace{\begin{pmatrix} c_{12} & s_{12} & 0 \\ -s_{12} & c_{12} & 0 \\ 0 & 0 & 1 \end{pmatrix}}_{\text{"solar sector"}}$$

Even though historically each sector was named after the first neutrino source that was used to study them, it is usual to study each sector with more than one source. Typically there are and have been experiences using a neutrino beams produced in an accelerator complex, such as the T2K beam that will be described in section 2.3, that were used to verify the measurement with "natural" neutrinos and for example improve the measured precision of the parameter Δm^2_{32}.

In the following subsections we will describe the current best knowledge of the measurement of each of the parameters of the neutrino oscillation matrix as it is quoted in the PDG [14] for Δm^2_{21}, Δm^2_{32}, θ_{12} and θ_{23}. For the θ_{13} parameter we will describe the Daya-Bay measurement which was not yet included in the PDG[12].

Measure of Δm^2_{21} and θ_{12}

As mentioned previously the Δm^2_{21} and θ_{12} parameters were measured first via neutrino oscillations from the Sun. Several experiences have contributed to the current measurement

[11] In this context the Δm^2 parameter is given for a 2-flavour oscillation probability, therefore the difference between Δm^2_{32} and Δm^2_{31} is neglected.

[12] The 2012 version of the PDG already contains the measured value of θ_{13} obtained by combining the results from reactor experiments Daya-Bay, Reno and Double-Chooz. However, the 2012 PDG was not available at the moment the oscillation analysis in chapter 5 was performed.

given their different energy thresholds and resolutions which were therefore sensitive to different reactions producing neutrinos that take place in the Sun, as shown in figure 1.10, yielding results that were at first deemed incompatible with the Standard Solar Model, as shown in figure 1.11, which resulted in the discovery of the neutrino oscillation with solar neutrinos by SNO, which as already mentioned in the beginning of this section.

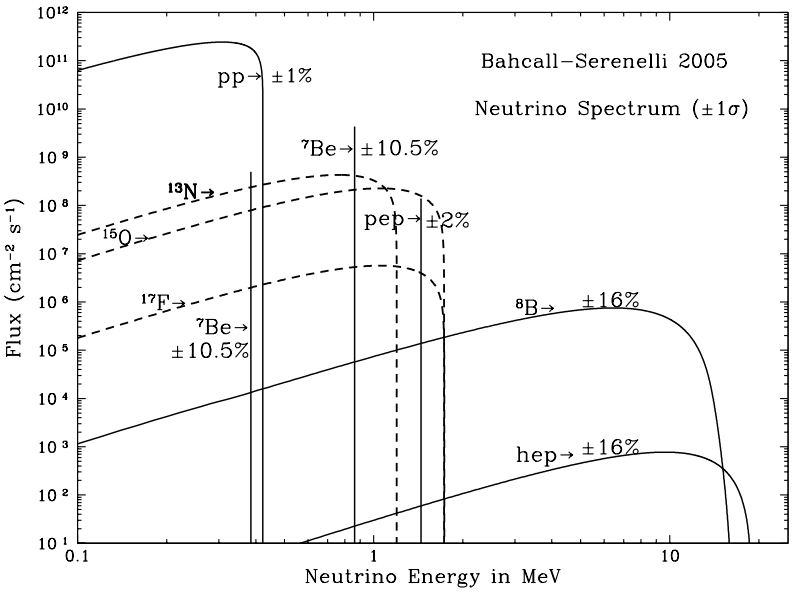

Figure 1.10: Neutrino solar flux in function the reaction that generated it. Neutrino fluxes are given in units of $\mathrm{cm}^{-2}\mathrm{s}^{-1}\mathrm{MeV}^{-1}$ for continuous spectra and $\mathrm{cm}^{-2}\mathrm{s}^{-1}$ for line spectra. Typically the energy threshold of Super Kamiokande and SNO is of a few MeV (in [50] the threshold in SNO is lowered to 3.5 MeV); of Gallium experiments is of 0.233 MeV and of Chlorine experiments if of 0.814 MeV [14]. Figure extracted from `http://www.sns.ias.edu/~jnb/` based on [51].

In addition to solar neutrino measurements these parameters were also measured by the disappearance of $\overline{\nu_e}$ produced in reactors in Japan located in average about 180 km of the detector where it is possible to observe more clearly the dependency of the oscillation probability to L/E by KamLAND [52], as shown in figure 1.12.

The article [50] presents a new analysis done using SNO data, for global results for Δm^2_{21} and θ_{12} by taking into account several measurements of solar neutrino oscillations and results from KamLAND. The result of this analysis is shown in figure 1.13. It is useful to note in this figure that the result from KamLAND is used mainly to determine the value of Δm^2_{21}, while the global fit of solar data is used mainly to determine the value of $\tan^2\theta_{12}$.

The values of Δm^2_{21} and $\tan^2\theta_{12}$ quoted by [50] are $(7.59 \pm 0.21)10^{-5}$ $\mathrm{eV}^2/\mathrm{c}^4$ and $0.468^{+0.042}_{-0.033}$, respectively, giving $\theta_{12} = (34.1^{+1.2}_{-0.8})^\circ$. Furthermore from figure 1.13 it is shown that these measurements are not correlated to each other.

Measure of Δm^2_{32} and θ_{23}

As mentioned previously, the Δm^2_{32} and θ_{23} parameters were measured first via neutrino oscillations from neutrinos produced at Earth's atmosphere in function of the zenith angle,

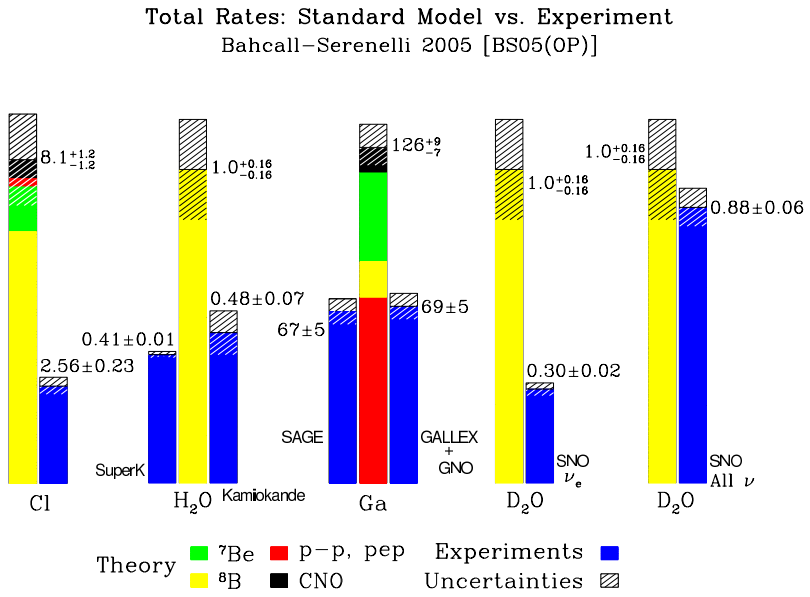

Figure 1.11: Neutrino solar flux measured by several different experiments in comparison with the expected flux from the Standard Solar Model. Currently the differences between the measurements and the Standard Solar Model is explained via neutrino oscillations. Figure extracted from `http://www.sns.ias.edu/~jnb/`.

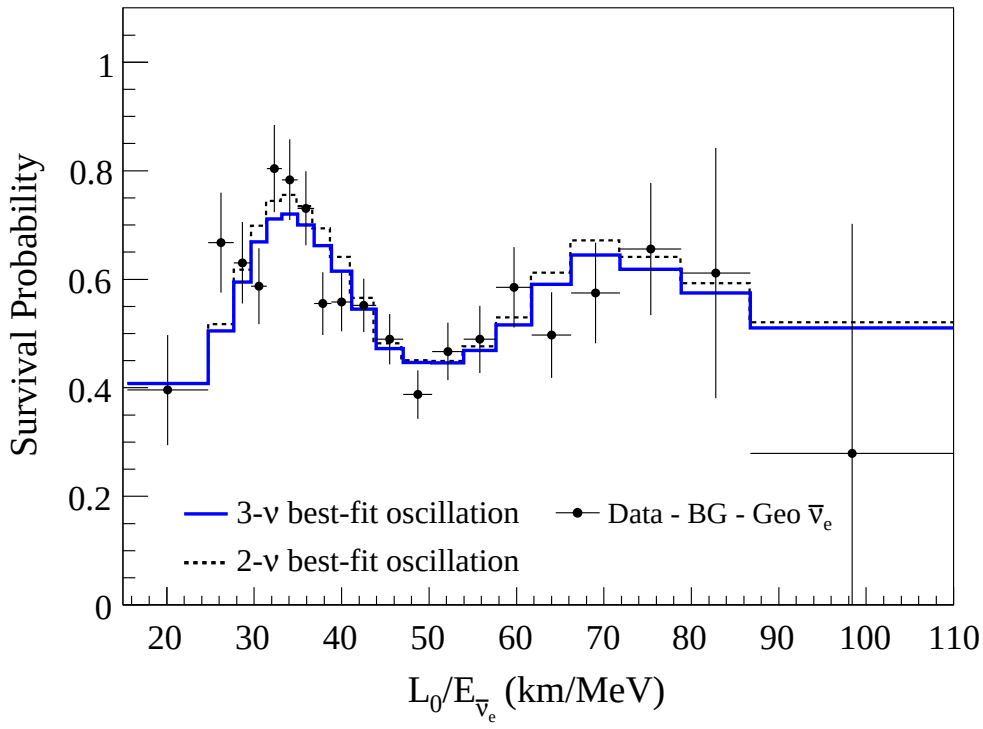

Figure 1.12: Survival probability of $\overline{\nu_e}$ emitted by nuclear power plants in Japan in function of the L_0/E ($L_0 = 180$ km) for KamLAND. The best fit for 2 and 3 neutrino oscillation fits is also shown. Figure extracted from [52].

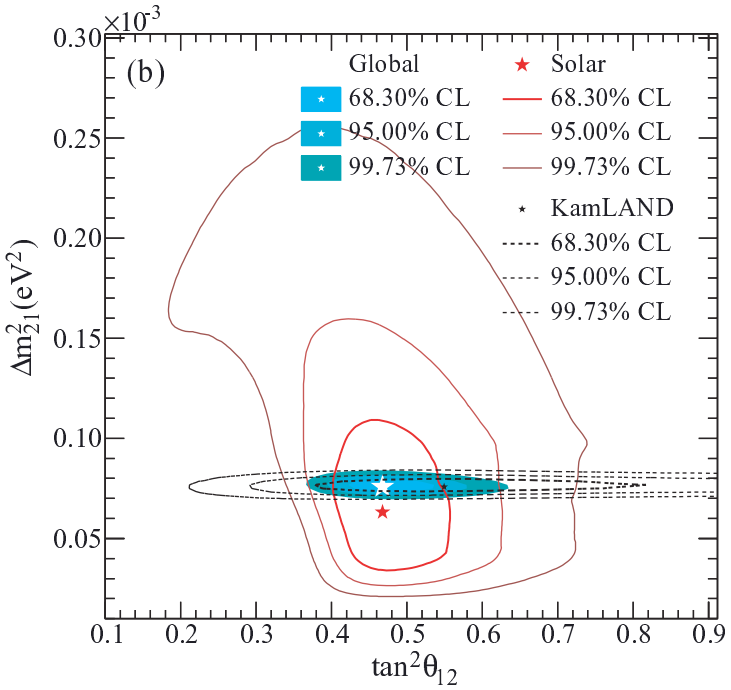

Figure 1.13: Solar and KamLAND oscillation parameter analysis for a three-flavor oscillation hypothesis. The solar data include SNO's LETA survival probability day/night curves, SNO Phase III integral rates, Cl, SAGE, Gallex/GNO, Borexino, SK-I zenith and SK-II day/night spectra. The χ^2 was minimized with respect to all undisplayed parameters. Figure extracted from reference [50].

which represents the distance the neutrino had to travel between its production point at the Earth's atmosphere and the detection point. In figure 1.14 are shown the number of neutrino events measured in function of the zenith angle for ν_e and ν_μ of different energies.

In addition to those measurements of atmospheric neutrinos these parameters were also measured by the disappearance of ν_μ from a ν_μ beam produced in accelerators.

The current limit for $\sin^2(2\theta_{23})$ is $\sin^2(2\theta_{23}) > 0.92$ with 90% confidence level, given in reference [53], as shown in figure 1.15. In this reference Super Kamiokande measured the atmospheric ν_μ and ν_e flux in function of the distance between the detector and the production point at Earth's atmosphere. This measurement corresponds to $36.8° < \theta_{23} < 53.2°$ at 90% confidence level.

The current limit for $|\Delta m^2_{32}|$ is $(2.43 \pm 0.13)10^{-3}$ eV^2/c^4, given in reference [54], as shown in figure 1.16. In this reference MINOS measured the disappearance of ν_μ in a neutrino beam produced at Fermilab.

Measure of θ_{13}

For a long period, an upper limit for the value of θ_{13} was only available. Until recently the best upper limit had been measured by the CHOOZ experiment [55] in which $\overline{\nu_e}$ produced at a nuclear power plant were measured at a detector situated at roughly 1 km of the nuclear reactors.

The new generation of experiments built to measure θ_{13} are composed mainly of two kinds. The first kind intended to measure disappearance of $\overline{\nu_e}$ from the $\overline{\nu_e}$ produced in

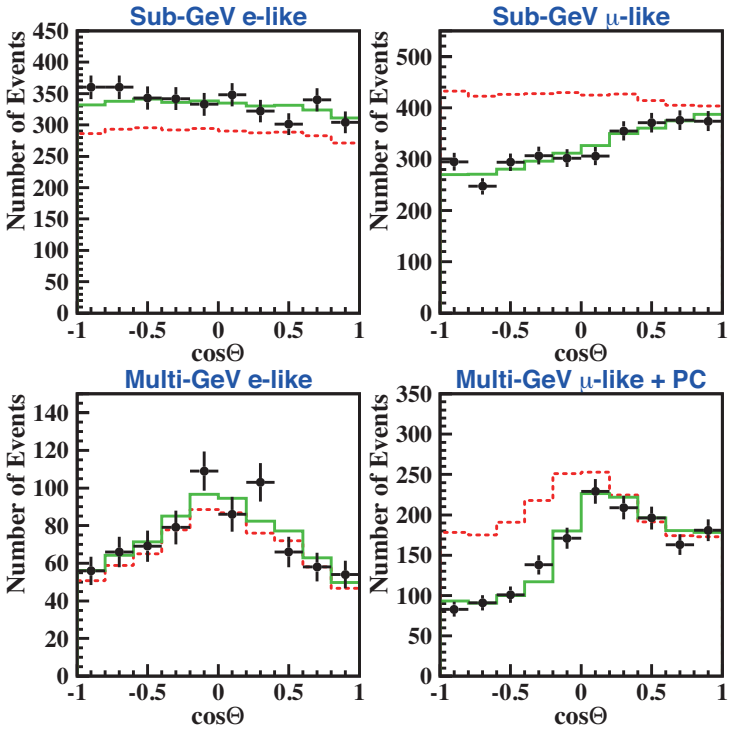

Figure 1.14: Zenith angle distribution of fully contained 1-ring e-like and μ-like events with visible energy below or above 1.33 GeV, corresponding to the Sub-GeV and Multi-GeV samples. For the "Multi-GeV μ-like events" distribution were also include partially contained (PC) events. The dashed curves show non-oscillated expected flux and solid curves show the best fit for $\nu_\mu \leftrightarrow \nu_\tau$ oscillation. Figure extracted from reference [14], provided by the Super Kamiokande Collaboration.

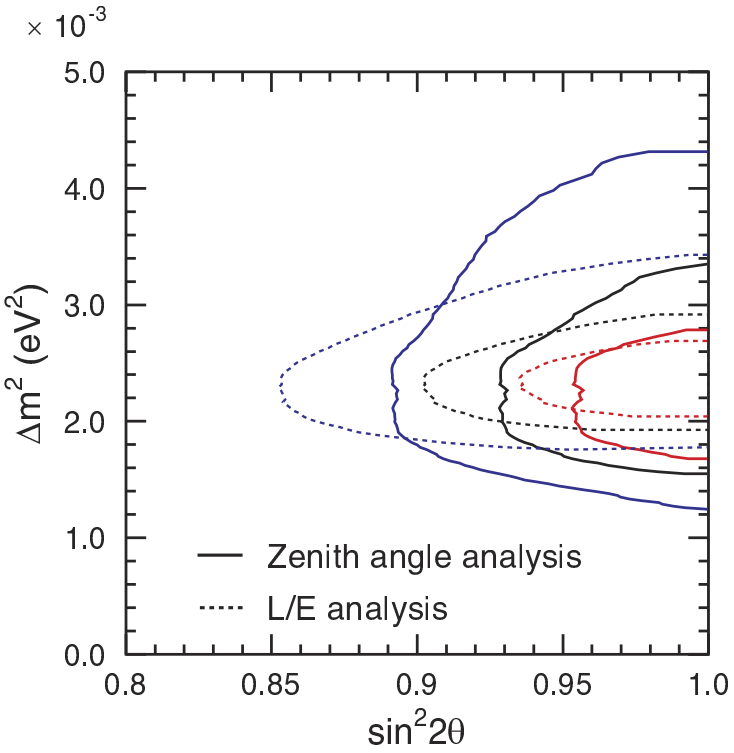

Figure 1.15: Measure of $\sin^2 2\theta_{23}$ and $|\Delta m^2_{32}|$ using Super Kamiokande I data using L/E and Zenith angle analyses. The 68% (red), 90% (black) and 99% (blue) contours are shown for each analysis. Figure extracted from reference [53].

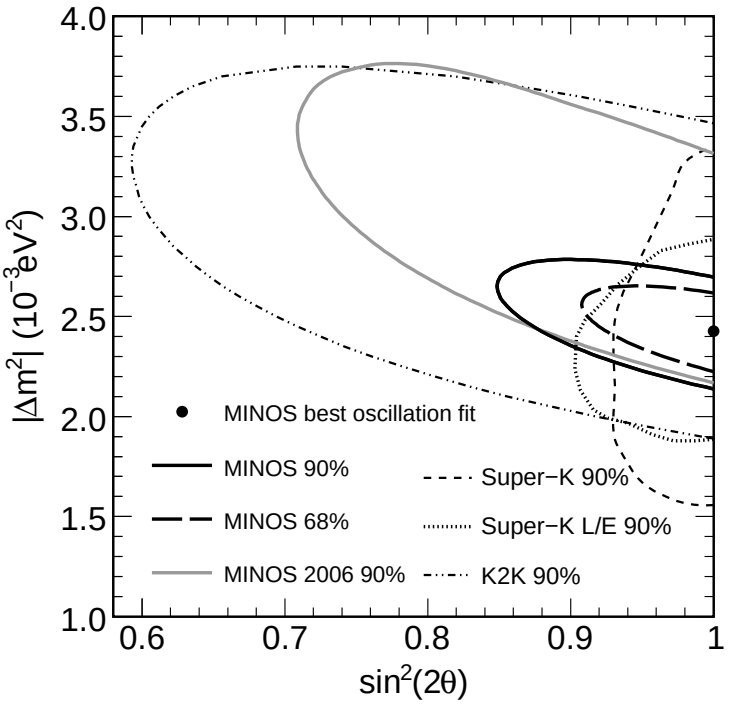

Figure 1.16: Contours for the oscillation fit to the MINOS data, including systematic errors for the $\sin^2 2\theta_{23}$ and $|\Delta m^2_{32}|$ parameters. Contours from others experiments are also shown. Figure extracted from reference [54].

reactors, such as Double-CHOOZ, RENO and Daya-Bay [56]. The second kind intended to measure the appearance of ν_e from a ν_μ beam produced in an accelerator complex, such as T2K and Nova. These two techniques are complementary because the first kind of experience uses $\overline{\nu}$ and is only sensitive to θ_{13} while the second kind of experience can use both ν and $\overline{\nu}$ and is sensitive to θ_{13} and δ_{CP}.

In July 2011 the T2K Collaboration published for the first time a result for $\sin^2(2\theta_{13})$ that was about 2.5 σ from 0 [13], that is a strong indication of non zero θ_{13}. In December the Double-Chooz Collaboration published their first results [57] which increases the difference between the value of $\sin^2(2\theta_{13})$ and 0 to about 3 σ, in combination with results from T2K and MINOS. By April 2012 a measurement of $\sin^2(2\theta_{13}) = 0.092 \pm 0.016(\text{stat}) \pm 0.005(\text{syst})$ was performed by Daya-Bay Collaboration [58], as shown in figure 1.17, verifying that $\theta_{13} \neq 0$ at more than 5 σ level. This corresponds to $\theta_{13} = (8.8 \pm 0.8)°$. After this result was published it was sequentially followed by an independent measurement of the same angle by the RENO collaboration of $\sin^2(2\theta_{13}) = 0.113 \pm 0.013(\text{stat}) \pm 0.019(\text{syst})$ [59] which is compatible with the quoted result from Daya-Bay.

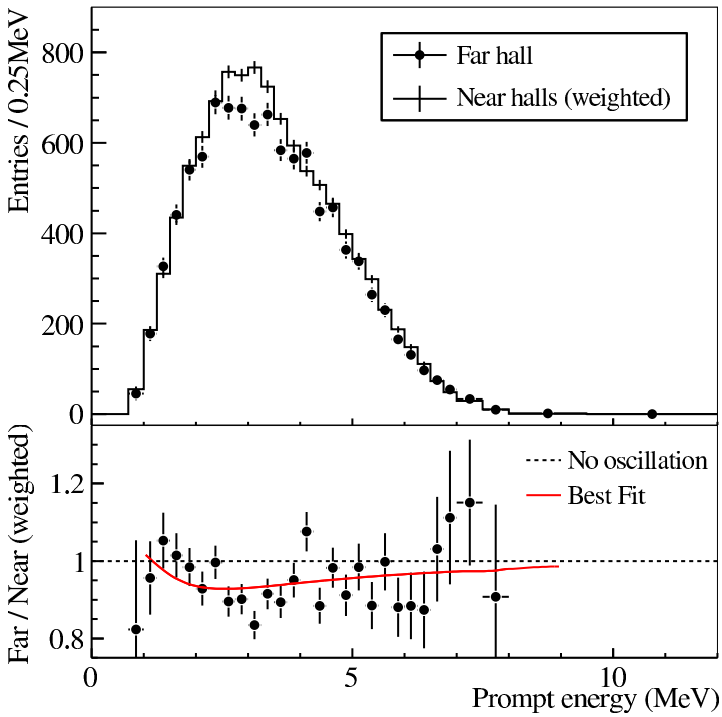

Figure 1.17: Measured prompt energy spectrum in the Far hall compared to extrapolation of the Near halls detected flux assuming no oscillation (top) and their ratio (bottom). If there were no oscillation the Far/Near ratio should always be 1 (dashed line in the bottom plot). The red line shows the best ν_e disappearance fit. Only statistical errors are shown. Figure extracted from [58].

For the moment we will quote use only the Daya-Bay result since it is the one with smallest uncertainty and we would like to avoid evaluating whether there are correlations between both experiments.

Summary of the current best knowledge of the oscillation parameters and assumptions for their use in oscillation analysis described in chapter 5

In the reference [50] the θ_{12} angle is quoted as a value of $\tan^2\theta_{12}$, for the oscillation analysis it is more useful to have the value of $\sin^2(2\theta_{12})$. Since the PDG quotes the value of reference [50] as $\sin^2(2\theta_{12}) = 0.861^{+0.026}_{-0.022}$ these is the value we will be using later on.

For the moment we have only a lower bound measured for $\sin^2(2\theta_{23})$, it is useful for the oscillation analysis to quote the current knowledge as $\sin^2(2\theta_{23}) = 1.000^{+0.000}_{-0.045}$, where we explicitly show the current knowledge for this value, that is : best fit of θ_{23} is 45°; the 68% lower limit $\sin^2(2\theta_{23})$ given the $|\Delta m^2_{32}|$ from reference [54] is for $\sin^2(2\theta_{23}) = 0.955$ as shown in figure 1.15; and the upper limit for $\sin^2(2\theta_{23})$ is 1 because the $\sin^2$ function is bound between 0 and 1.

In the reference [58] the uncertainty for $\sin^2(2\theta_{13})$ was quoted with systematical and statistical errors separated. For the purpose of the oscillation analysis, and to summarise better the current knowledge of the mixing angles, it is useful to combine both errors to obtain one global error. This was done by adding both errors in quadrature as they are independent errors, therefore $\sin^2(2\theta_{13}) = 0.092 \pm 0.017$.

Finally, we will assume that there is no correlation between any of these five quantities because each of these quantities was determined by a different experience and are quoted separately.

In table 1.3 are summarized all values given previously in the form they will be used for the oscillation analysis.

Table 1.3: Summary of current best knowledge of the neutrino oscillation parameters that will be used to perform an oscillation analysis using T2K data in chapter 5

$\sin^2(2\theta_{12})$	$= 0.861^{+0.026}_{-0.022}$
$\sin^2(2\theta_{23})$	$= 1.000^{+0.000}_{-0.045}$
$\sin^2(2\theta_{13})$	$= 0.092 \pm 0.017$
Δm^2_{21}	$= (7.59 \pm 0.21)10^{-5}$ eV^2/c^4
$\lvert\Delta m^2_{32}\rvert$	$= (2.43 \pm 0.13)10^{-3}$ eV^2/c^4

Finally, we should note that in the Neutrino 2012 conference updates for the values of these parameters were reported by several collaborations, however such updates will not be quoted here because they have not been used for the oscillation analysis presented in chapter 5 and they change the current the results shown in table 1.3 only slightly.

Chapter 2

T2K experiment

Contents

2.1 Motivations

The T2K experiment was designed to achieve three different, though complementary, objectives :

1. Measure θ_{13}
2. Improve measurement of "atmospheric sector"
3. First study of δ_{CP} once θ_{13} is measured

We should note that in the moment the T2K experiment was designed, only an upper limit to the value of θ_{13} was measured. At the same period where T2K was designed and built other projects, such as Double-Chooz, Reno, Daya-Bay and Noνa were also being prepared. T2K was the first of these experiments to start data taking, however because of differences on the technique used to measure θ_{13} it was Daya-Bay which achieved the first measurement that has shown this angle to be not zero. By June 2011 the value of θ_{13} measured by T2K already excluded the zero value with more than 90% confidence level as was reported in [13] using all the data taken until the "2011 Tōhoku earthquake" that has forced T2K to temporally stop data taking for about one year.

Even though currently the value of θ_{13} has been measured with the disappearance of $\overline{\nu_e}$ produced from nuclear reactors, it will still be an important verification to measure this angle using neutrinos instead of anti-neutrinos and using a different technique, that is appearance of ν_e from a ν_μ beam.

The T2K collaboration has also published a measurement of θ_{23} and $|\Delta m^2_{32}|$ using all the data taken until the "2011 Tōhoku earthquake" as was reported in [60]. For this result, instead of the apparition of ν_e from the ν_μ beam, the ν_μ survival probability between the production and detection points was measured. It should be noted that even though in this article there is no improvement of the currently known values of θ_{23} and $|\Delta m^2_{32}|$ it shows the potential of T2K to measure parameters in the atmospheric sector of the mixing matrix.

The goal for T2K given in its letter of intent [61], for systematic errors within 10%:

- sensitivity for $\sin^2 2\theta_{13} = 0.006$ with 90% confidence level
- uncertainty for $\sin^2 2\theta_{23} < 0.01$
- uncertainty for $|\Delta m^2_{32}| < 10^{-4}$ eV^2/c^4

By comparing these values with the current knowledge of these parameters it is shown that T2K should be able to reduce the measured uncertainty of the $\sin^2 2\theta_{23}$ angle by a factor 5, with at the same time a measure of $|\Delta m^2_{32}|$ with the same precision of the currently achieved result.

Finally, even though T2K did not expect to measure the δ_{CP} phase at the early stage of the experiment, the large value of θ_{13} measured very recently means that it will be possible to start using T2K data to study this phase.

2.2 Overview

T2K is a long-baseline neutrino experiment built to study neutrino oscillations near the first maxima of the oscillations due to the squared mass difference Δm^2_{32}. In T2K, neutrinos are produced by the accelerator complex J-PARC (situated at Tokai, Japan), mostly in the ν_μ flavour. In order to understand the neutrino flux produced at J-PARC there are several neutrino detectors placed about 280 meters from the target. T2K will measure the neutrino flux produced by J-PARC at the Super Kamiokande detector (situated at Mozumi) situated 295 kilometers from J-PARC and compare with the expected neutrino flux given the constraints in the neutrino flux from the measurements done at J-PARC. A scheme of the T2K experiment and its detectors is shown in figure 2.1.

In the following sections we will present in more details the accelerator used to produce the neutrino beam (section 2.3), the detectors placed at about 280 meters also called Near Detectors (section 2.4) and the Super Kamiokande detector (section 2.5). In this thesis we will detail more the Super Kamiokande detector because most of the work presented here is related to.

As it was explained, the T2K experiment intends to measure the probability of oscillations $\nu_\mu \to \nu_e$ and $\nu_\mu \to \nu_\mu$, therefore it is required to produce a ν_μ neutrino beam with as little of other neutrino flavours as possible. However the current methods used to produce neutrino beams using the decay of pions and kaons will always produce some fraction of ν_e that will be present on the neutrino beam, which should be reduced as much as possible.

In addition to the ν_e contamination of the produced ν_μ beam, the ν_μ beam that can oscillate to ν_e or ν_τ has some contamination of ν_μ in the incorrect energy range for oscillation at $L = 295$ km.

The solution proposed by T2K to reduce the impact of each of these contaminations just described was to use a "off-axis beam", that is, not pointing the beam direction towards the Super Kamiokande detector. The angle between the on-axis beam direction and the Super Kamiokande detector direction chosen to be used at the T2K experiment is 2.5°.

The "off-axis beam" reduces the contamination of the ν_μ beam from other ν_μ with the incorrect energy due to the kinematics of the decays which produce the neutrinos (see appendix B.1), this effect reduces the spread of the ν_μ energy distribution and increases the number of neutrinos produced in the required energy range for oscillation, as shown in figure 2.2.

Furthermore, the "off-axis angle" increase of the ν_μ beam flux at the energies of interest for the oscillation analysis also have the effect to reduce the ν_e beam contamination. For T2K, the ν_e beam flux contamination is 0.5%, as shown in figure 2.3, while at the beam axis direction such contamination is of 1%. In appendix B.2, the reduction of ν_e contamination in an "off-axis beam" is justified.

2.3 The accelerator complex to produce neutrino beam

The accelerator complex used by the T2K experiment to produce the neutrino beam is J-PARC (Japan Proton Accelerator Research Complex), situated at Tokai. This accelerator complex was built by KEK (The High Energy Accelerator Research Organization) and JAEA (Japan Atomic Energy Agency) to provide a beam for several different experiments, as shown in figure 2.4.

The J-PARC accelerator complex is composed of three proton accelerators, which are shown in figure 2.4, which accelerate the protons one after the other until they reach the desired energy.

The first of the proton accelerators is a standard linear accelerator (LINAC) meant to accelerate protons up to 400 MeV and then inject these protons in the second accelerator. Currently the LINAC is accelerating protons up to 180 MeV with a maximum beam power of 30 kW [62].

The second accelerator is a 3 GeV synchrotron (called RCS or "Rapid Cycling Synchroton") which as the name indicates accelerate the protons up to 3 GeV. These protons will be sent either to the "Materials and Life Science Experimental Facility" (MLF), or to the third proton accelerator. The average beam power of the RCS is 200 kW.

The third accelerator of the chain is a 50 GeV synchrotron (called MR or "Main Ring") which was designed to accelerate protons up to 50 GeV. Currently however the protons in the MR are accelerated only up to 30 GeV, with average beam power of 150 kW. From the MR the protons can be sent either to the "Hadron Experimental Facility", or to the "Neutrino Beam Line".

In this thesis we will only describe the extraction to the "Neutrino Beam Line", as well as how the neutrino beam is produced, two relevant parts of J-PARC for T2K. In figure 2.5 is shown a schema of the "Neutrino Beam Line" after the MR up to the near detectors site.

The beam is extracted from the MR to the "Neutrino Beam Line" by "fast extraction", that is, all the proton beam is sent to the "Neutrino Beam Line" at the same time.

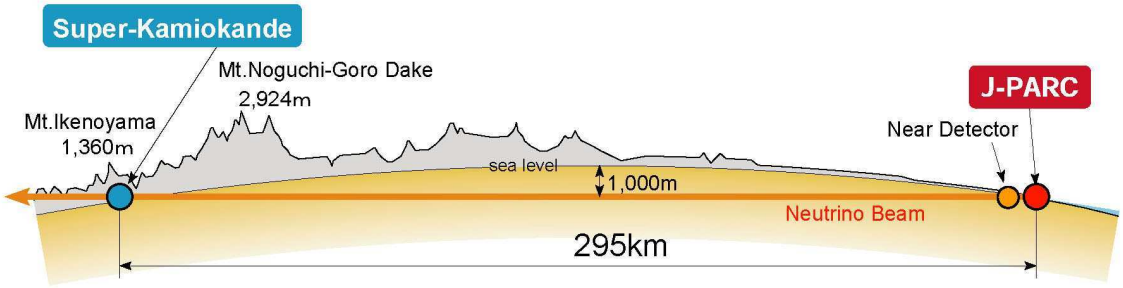

Figure 2.1: Schematic view of the neutrino propagation (orange arrow) in the T2K experiment : the neutrino is produced at J-PARC (red dot), goes through the near detectors (orange dot) that are placed at 280 m from the target, and then further 295 km away goes through the Super Kamiokande detector (blue dot).

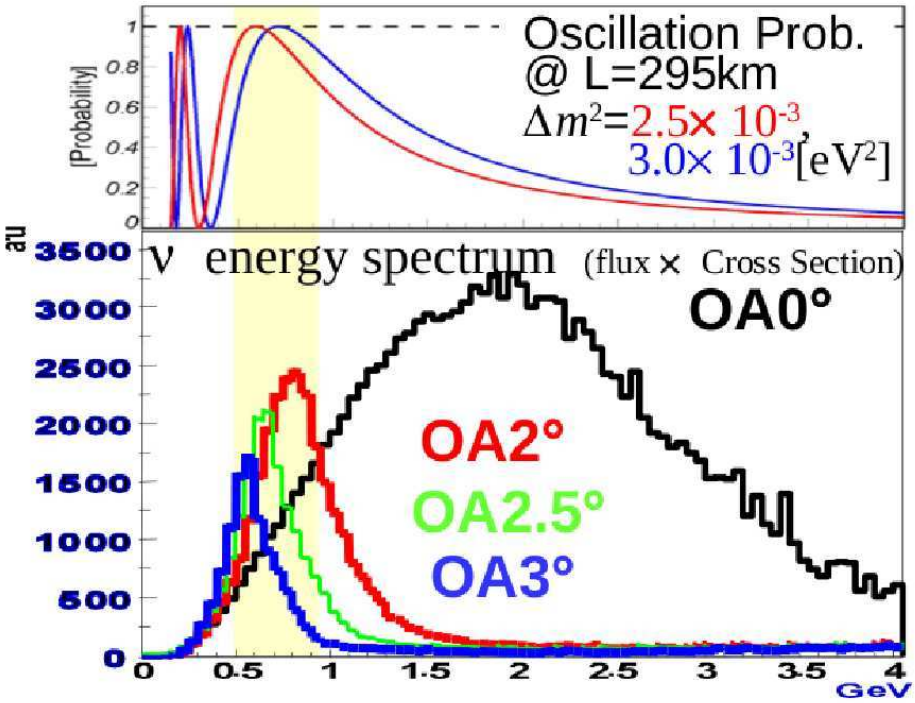

Figure 2.2: Neutrino energy spectrum as function of several different "off-axis angle". It is also shown the oscillation probability at Super Kamiokande as function of the neutrino energy. It is shown that for $|\Delta m^2_{32}| \sim 2.5 \cdot 10^{-3}$ the first oscillation maxima is at about 0.7 GeV. To maximize the flux of neutrinos with this energy, while at the same time reducing as much as possible the spread of the neutrino energy spectrum, the "off-axis angle" is chosen as 2.5° (the green curve).

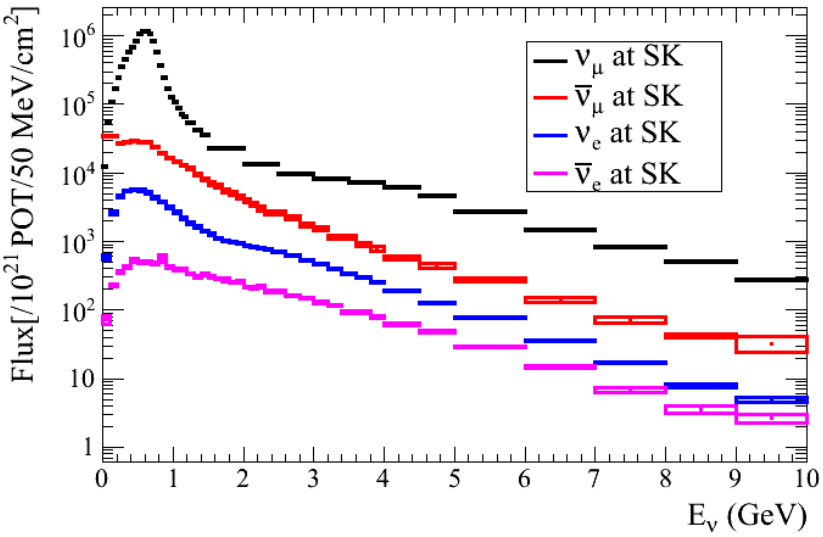

Figure 2.3: Neutrino flux at Super Kamiokande (SK) as function of the neutrino energy assuming no neutrino oscillation. For neutrino energies of about 800 MeV the ν_e contamination of the beam is about 0.5%. These spectra were obtained from the simulation T2K JNUBEAM, 10d version.

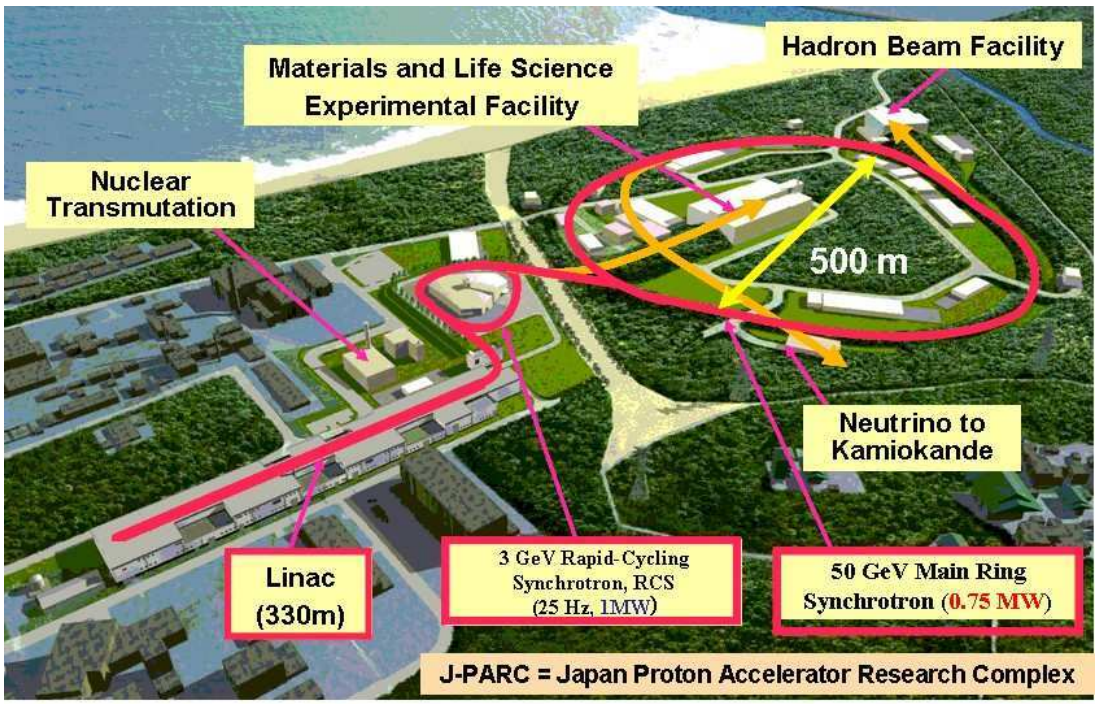

Figure 2.4: Schema of the different structures in J-PARC. Extracted from `http://www.teilchen.at/news/334`.

The period required for the accelerator components to be ready to perform another "fast extraction" is 2 s, therefore the proton injection in the "Neutrino Beam Line" will happen every 2 s, with duration of 5 μs.

The "Neutrino Beam Line" has in fact two different functions. Its first function is to tune the beam so that its direction is 2.5° from the Super Kamiokande direction, as explained previously. Its second function is to focus the beam to a target, at which it will be produced pions and kaons through the target interaction with the proton beam. The neutrino beam will be generated by the decay of these pions and kaons in the decay tunnel.

The proton beam is focused on the T2K beam target in the "Neutrino Beam Line". The T2K beam target is composed of carbon graphite. This material has been chosen because it will heat less when exposed to an intense proton beam than other materials with larger atomic numbers, while at the same time it has a high fusion and sublimation point. Furthermore, the target needs to be large enough to encompass all the proton beam, and not being too thick to allow the particles produced by the proton beam interaction to leave the target. The T2K target was constructed as a cylindrical rod with diameter of 26 mm and length of 90 cm (which corresponds to about 2 radiation lengths), and to further control the target temperature it is refrigerated by helium gas. The target is placed inside the first horn which start the selection of which particles produced by the proton beam on the carbon target will be kept, that is π^+ and K^+ when we want to produce a ν_μ beam or π^- and K^- when we want to produce a $\overline{\nu_\mu}$ beam, and their focusing. A picture of the target being inserted in the first horn is shown in figure 2.6.

The focusing of the pions and kaons in the required direction is made by a set of three horns. Each horn produces a toroidal magnetic field that will focus particles with a given charge and defocus particles with the opposite charge, as mentioned previously. The use of horns is imperative because it increases the intensity of the mesons flux in the decay tunnel, therefore increasing the intensity of the neutrino beam itself. Typically a horn will reduce the angular distribution of the particles composing the "decay beam" by a factor of 2, however in the case of the T2K horns the first two horns are close together and will have the effect equivalent to the usual effect of one horn. A scheme of the position of the three horns is shown in figure 2.7.

After the horns the "decay beam" composed of pions and kaons will go through the decay tunnel (or decay volume), where these particles will decay producing neutrinos. The decay tunnel in T2K is about 100 meters long and filled with helium to reduce the meson absorption. At the end of the decay volume the remaining hadrons are stopped at the "beam dump" composed of graphite, iron and copper. The beam dump will also stop

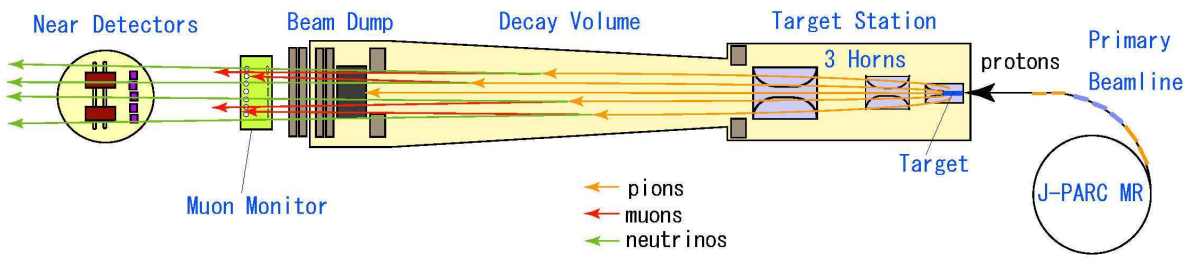

Figure 2.5: Schema the "Neutrino Beam Line" up to the near detector site. This schema is not in scale.

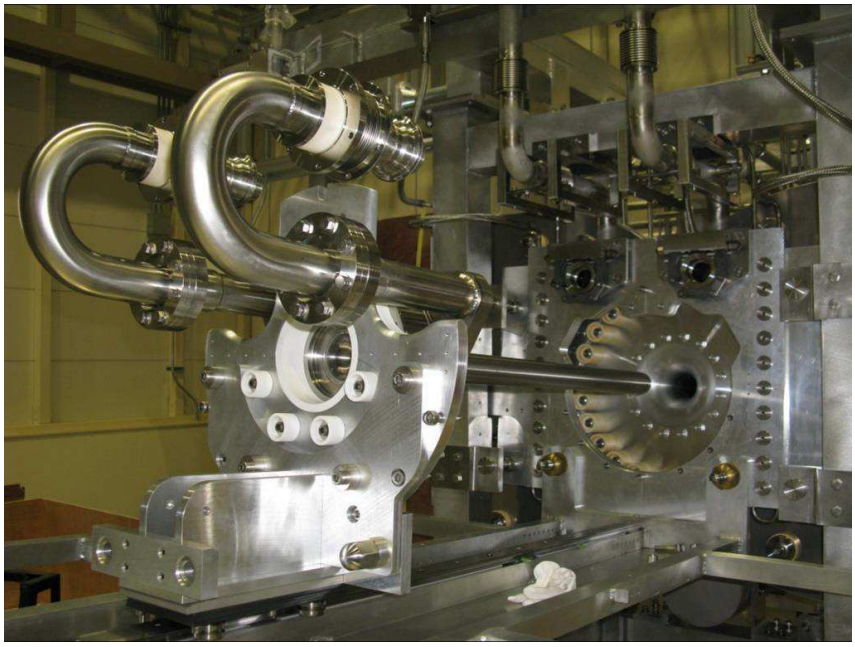

Figure 2.6: Picture of the T2K target being inserted in the first horn.

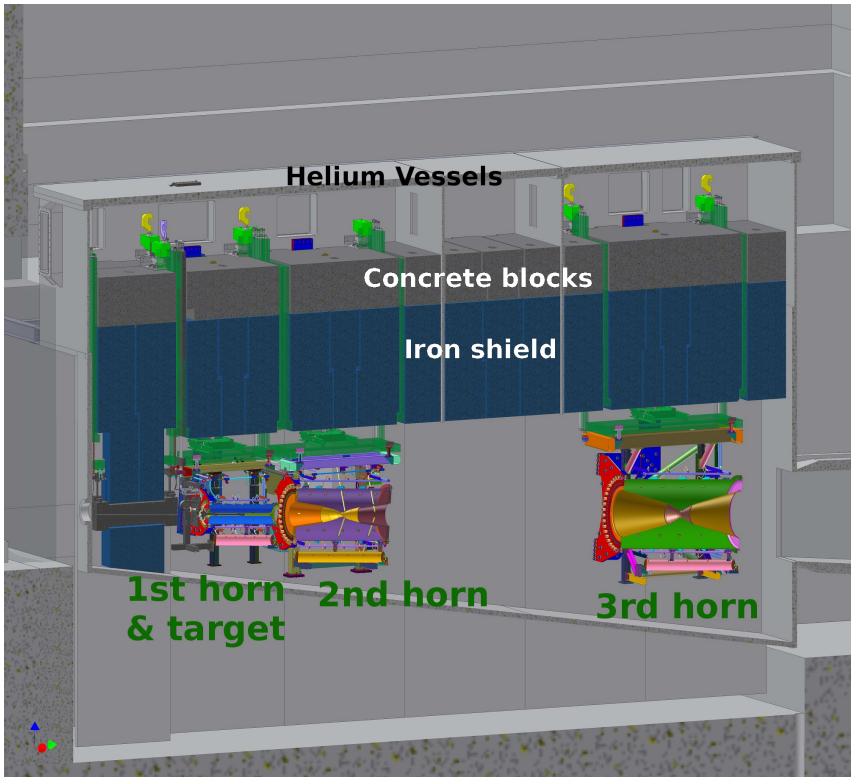

Figure 2.7: Schema of the setup around the horn area. The proton beam arrives from the left of the figure and interacts in the target (inside the first horn). The mesons produced are focused by the three horns shown and will proceed to the decay tunnel at the right of the figure. Note that the proton beam line, horns and decay tunnel are slightly pointed downwards with and angle of of 3.64° from the horizontal direction due to the off-axis angle from Super Kamiokande and to the Earth's curvature.

Table 2.1: Decay modes that will lead to neutrino production in a conventional neutrino beam. Typically, these beams are composed of pions and kaons, and the positive mesons are focused to produce a neutrino beam. For simplicity, only decay modes with more than 0.01% branching ratio (BR) are shown. We should note that the K^+ decay modes where a π^+ is produced are also shown here, as well as μ^+, because it could produce neutrinos. These values were extracted from [14].

Decay mode	Branching ratio
$\pi^+ \to \mu^+ + \nu_\mu$	99.988%
$\pi^+ \to e^+ + \nu_e$	0.012%
$K^+ \to \mu^+ + \nu_\mu$	63.55%
$K^+ \to \pi^+ + n\pi^0$ ($n = 1$ or 2)	22.42%
$K^+ \to 2\pi^+ + \pi^-$	5.59%
$K^+ \to \pi^0 + e^+ + \nu_e$	5.07%
$K^+ \to \pi^0 + \mu^+ + \nu_\mu$	3.35%
$K^0_L \to \pi^- + e^+ + \nu_e$	40.55%
$K^0_L \to \pi^- + \mu^+ + \nu_\mu$	27.04%
$\mu^+ \to e^+ + \nu_e + \overline{\nu_\mu}$	100%

muons with energy below 5 GeV, those with energy larger than 5 GeV will be detected by the "muon monitor" behind the "beam dump". The "muon monitor" is one of the tools used to monitor the beam direction and its time structure.

The neutrinos produced by pions and kaons decays will then be detected at the Near Detectors and at Super Kamiokande. The neutrino beams produced using this technique will be mostly composed by ν_μ (or $\overline{\nu_\mu}$) because pions and kaons will mostly produce ν_μ when decaying as shown in table 2.1. We should note, however, that the neutrino beam will be mainly created by pion decays, and not kaon decays, and therefore the "off-axis angle" chosen for the beam direction in relation to the Super Kamiokande direction takes into account mainly the kinematics of the π^+ decay in ν_μ. That having been considered, we should also note that the intrinsic ν_e contamination of the neutrino beam will have been generated by the μ^+ from π^+ decays mainly, with a contribution from K^+ and K^0_L, and not by the π^+ decays directly.

In order for T2K to accurately determine the neutrino production, it is necessary to know the amount of pions and kaons produced at the interaction of the proton beam with the T2K carbon target, as well as their momenta. We have therefore collaborated with the NA61 experiment which measure the particles produced by interaction of the proton beam with a replica target from T2K using an independent setup. Their measurements (for example [63]) are used as constraint to improve the current neutrino beam simulations.

The neutrino beam produced is not a continuous neutrino beam in time, but a pulsed beam : each pulse of the proton beam will generate a corresponding pulse of neutrinos that will compose the neutrino beam. These pulses of neutrinos are called "spills". At nominal operation, the "spills" have duration of 4.2 μs and the time between spills is of about 3.5 s. During a spill, about $3.3 \cdot 10^{14}$ protons are fired in the target, which corresponds to a power of 0.75 MW. To be more precise each "spill" is composed of 8 bunches, at nominal configuration or 6 bunches during the beginning of T2K runs, of about 60 ns each. The time between two bunches is of the order of 580 ns.

2.4 Near Detectors

The near detectors have the role of controlling the neutrino beam properties before oscillation in order to predict the neutrino flux expected at the far detector. As explained previously the near detectors are placed 280 meters downstream from the target position, and are in fact composed of two different detectors. A scheme of these detectors is shown in figure 2.8 inside the near detector pit.

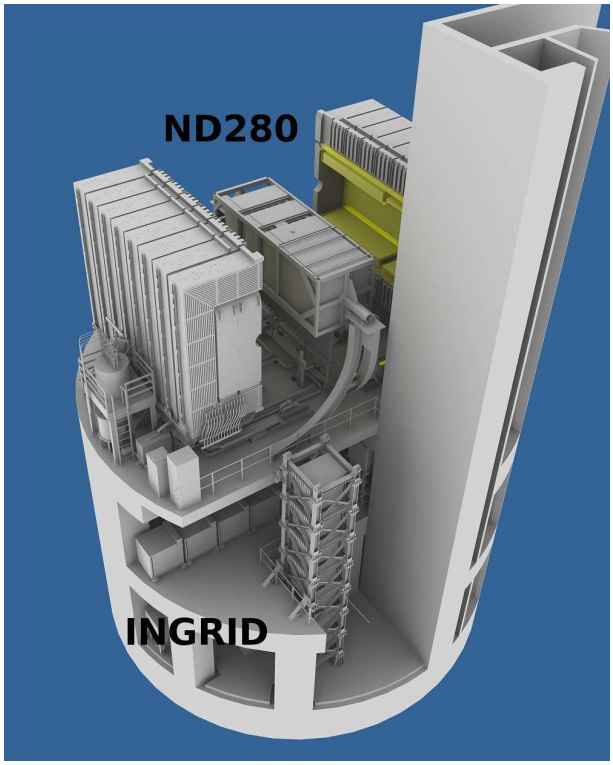

Figure 2.8: Schema of the Near Detector pit including the two near detectors. In this figure the "off-axis" near detector (ND280) is shown with the magnet open and the components inside the magnet are visible. In this figure are not present the "on-axis" near detector (INGRID) modules that were added after the first T2K run, namely the "off-cross modules" and the "proton module".

One of these detectors is placed in the beam direction and is used to monitor the beam direction mainly and compare the beam profile with the one predicted by the simulation. This detector is called "Interactive Neutrino GRID" (INGRID) and will be described in section 2.4.1.

The other detector is placed in the same direction as the Super Kamiokande direction, therefore it is specially useful to measure the composition, energy distribution and flux of the neutrino beam sent to Super Kamiokande. This detector is called simply ND280 because it is a near detector placed at 280 meters from the target. The ND280 detector is composed of several sub-detectors and will be described in section 2.4.2.

2.4.1 INGRID

As explained previously INGRID is the "on-axis" near detector. Its objective is to measure the direction of the neutrino beam [64]. In figure 2.9 a scheme the INGRID detector is

shown.

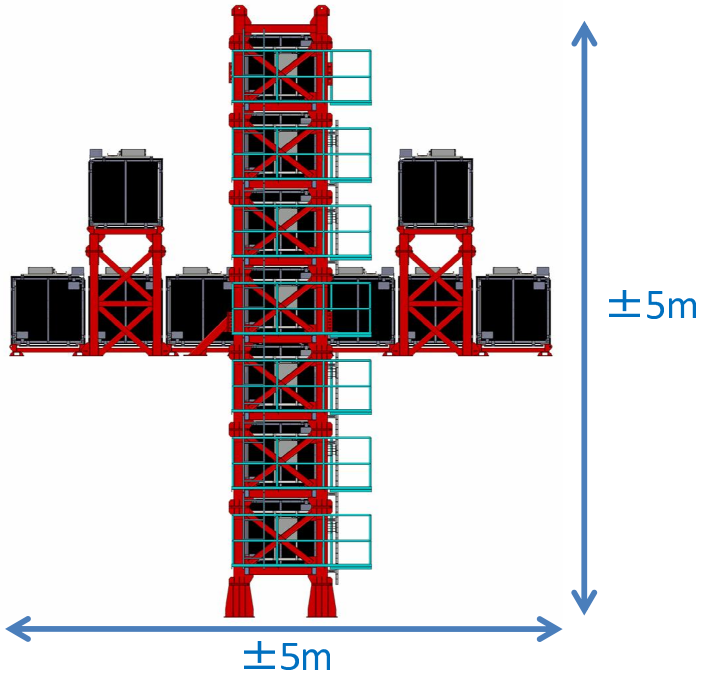

Figure 2.9: Schema of the INGRID detector. The horizontal and vertical bars are 10 meters long each (as shown in the schema they go from -5 meters to 5 meters). Figure extracted from [65].

Even though several control measurements are made during the propagation of the proton beam and on the μ produced by pions and kaons decays at the "muon monitor", these are only indirect measurements of the neutrino beam, and therefore it is not possible to guarantee that the neutrino beam is created as expected. This problem is solved by the measurement of the neutrino flux by INGRID which is able to study the neutrino beam direction and profile.

Given the small cross section of neutrino interaction it is not possible to use only INGRID for the beam monitoring, that is all the measurements made using the detectors in the accelerator and the muon monitor are used to adjust the beam parameters in real time, and the adjustment of the beam parameters and measure the "off-axis angle" of the beam center in relation to Super Kamiokande using INGRID will be confirmed once per day.

The INGRID detector is composed of 14 "standard modules" placed as a plus sign (with 7 modules aligned horizontally and 7 modules aligned vertically with the center of the plus sign being about the neutrino beam direction), 2 "standard modules" placed close to the diagonal of the horizontal and vertical bars (called "off-cross modules") and 1 "proton module" placed between the horizontal and vertical bars, as shown in figure 2.9. Eventually, the "proton module" can also be placed in front of the modules just to the right and left side of the central module of the horizontal bar for verifications of the normalization between INGRID modules.

The "standard modules" of the INGRID detector are composed of several layers of scintillators and iron put one after the other, as shown in figure 2.10. There are 9 iron layers with 6.5 cm thickness and 11 scintillator layers that are divided in 24 scintillators

placed side by side to measure the position in the horizontal direction perpendicular to the beam direction and other 24 scintillators placed side by side to measure the position in the vertical direction, therefore the position of each hit is measured at the same time in the horizontal and vertical axis separately. The neutrino interactions will mostly occur in the iron of the detector and the recoil protons are quickly absorbed by the iron not leaving a long enough track to be reconstructed usually, therefore in a CCQE interaction only the μ produced by ν_μ will leave tracks long enough to be detected with INGRID. The iron layers are placed between two consecutive scintillator layers, and there is no iron layer between the last two scintillator planes, as we consider that we need at least 3 tracking planes hit to reconstruct a track. In addition to the scintillator and iron layers, there are veto planes surrounding all INGRID modules at the top, bottom and sides of the module. Note however that when two "standard modules" are placed side by side there will be only one "veto plane" that will be used at the same time by both modules. We should also note that the first tracking plane of the "standard modules" is also considered as "veto plane" since there is no iron plane before it. Therefore the interactions observed by this plane will come from the outside of the modules. The "veto planes" are used to reject events where a track was reconstructed in the "standard modules" with direction of entering the INGRID module when we follow the beam direction in the sense of the neutrinos move, that is it is considered that CCQE reactions do not have any backward μ produced. The dimensions of INGRID "standard modules" are 124 cm×124 cm×110 cm.

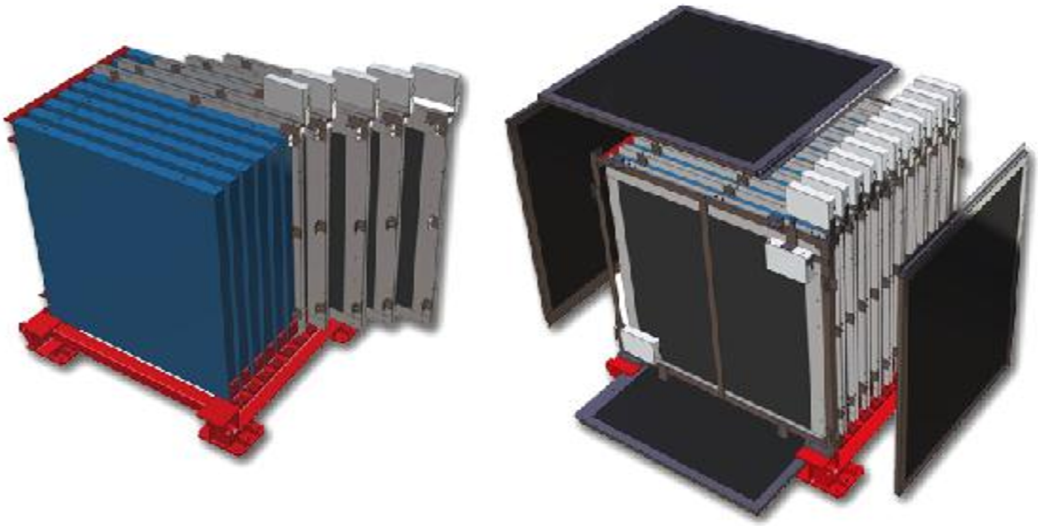

Figure 2.10: Schema of a "standard module" of the INGRID detector. In the left is shown only the interior of the module with the iron planes in blue and part of the scintillator planes in black and silver. In the right is shown the module composed of scintillator planes and iron planes with at the top, bottom and sides "veto planes" shown in black. In red are shown supporting structures of the INGRID modules. Figure extracted from [65].

The "proton module" is similar to the "standard modules", however without any iron planes. Its internal part is more finely grained with scintillators than the "standard modules". The purpose of this module is to be able to study the beam composition in more details, even though with less statistics, given that the iron planes are absent. It

will be possible to track the recoil protons and other particles produced by the neutrino interaction with the scintillators. Using the "proton module" we will be able to evaluate the current interaction models that are used to predict how much CCQE interactions are expected in the "standard modules" for the given neutrino energies in relation to other interactions. Furthermore, given the possibility to move the "proton module" to place it in front of 3 different "standard modules", it will also be used for systematic error studies of the normalisation between different "standard modules".

A typical event display from an INGRID "standard module" is shown in figure 2.11, where is is also possible to observe the described placement for the "standard module" INGRID scintillator and iron layers. For further information on the INGRID detector please refer to [65].

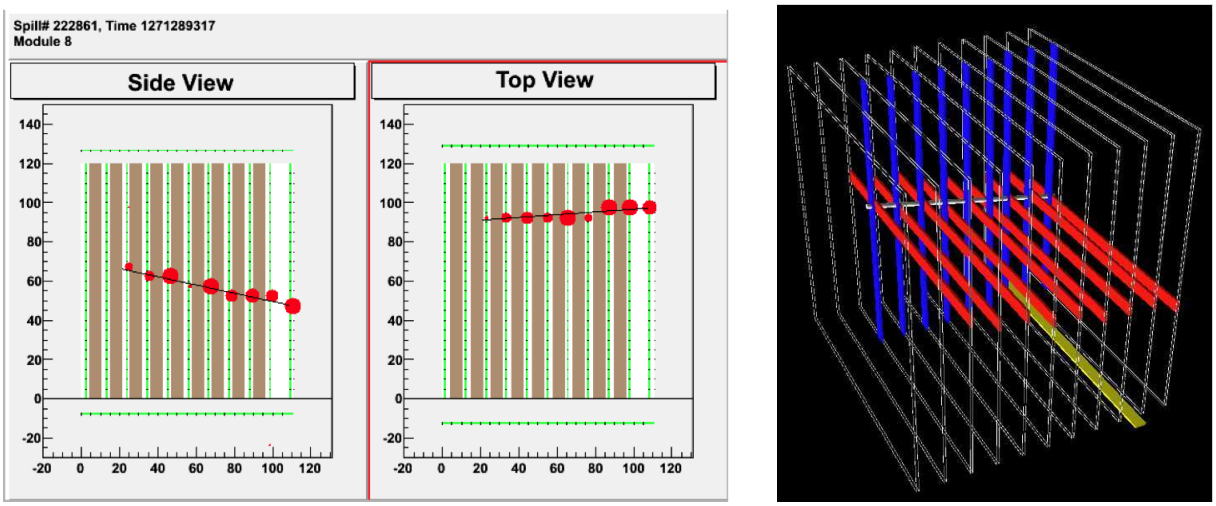

Figure 2.11: Typical event display from a neutrino event in the INGRID "standard module". In the left the event is shown in the vertical and horizontal projections separately, with the size of the red dots being the amount of charge deposited by the particle and the black line the reconstructed track. The axis show the position of the scintillators in centimeters from the bottom right corner of the module. In the right the same event is shown in 3D, where the horizontal scintillators are shown in red and the vertical scintillators are shown in blue and the reconstructed track is shown in white. In yellow is shown a "veto plane" that measured some charge.

2.4.2 ND280

As previously explained, ND280 detector is the "off-axis" near detector. It was designed to perform two different measurements. The first one is to measure the neutrino beam spectra and flavour composition at the "off-axis" direction. The second one is to measure of the cross-sections of different interaction types in relation to the CCQE cross-section.

The first objective is easy to understand in relation with the T2K objective, that is measure the neutrino oscillation between J-PARC and Super Kamiokande. It is essential in this kind of experiment to determine the composition of the beam emitted at J-PARC in order to compare with the composition of the beam measured at Super Kamiokande, estimating the oscillation parameters to fit the data. We should note that even though the ND280 and Super Kamiokande detectors are both "off-axis" and at the same direction,

the solid-angle of the neutrino beam observed by the near and far detectors are not the same. Therefore the extrapolation of the fluxes from ND280 to Super Kamiokande is not trivial and will rely on a beam simulation adjusted to the ND280 data.

The second objective, even though not directly related to the measure of the neutrino oscillation parameters, is as important as the first one to perform the measurement with the required precision. The determination of the neutrino cross-sections precisely for neutrinos with same energy as those neutrinos composing the T2K beam are essential in order to correctly estimate the fraction of interactions at the Super Kamiokande detector. Even though there are already measurements of these cross-sections they are not all known to the precision required by the T2K experiment. The NC $1\pi^0$ interaction at Super Kamiokande can, for example, produce a signal similar to the ν_e CCQE signature and it is currently one of the main backgrounds (about a third of the total background) for the T2K ν_e appearance search, as will be discussed in chapter 4. It is therefore essential to know well its cross-section.

The ND280 detector is composed of several sub-detectors to accomplish its two objectives. In addition to this segmentation it is also essential to know the sign of the charge of the particles to distinguish between the interaction types. A magnet is placed around several of the sub-detectors to create a magnetic field. These sub-detectors and the magnet are shown in figure 2.12.

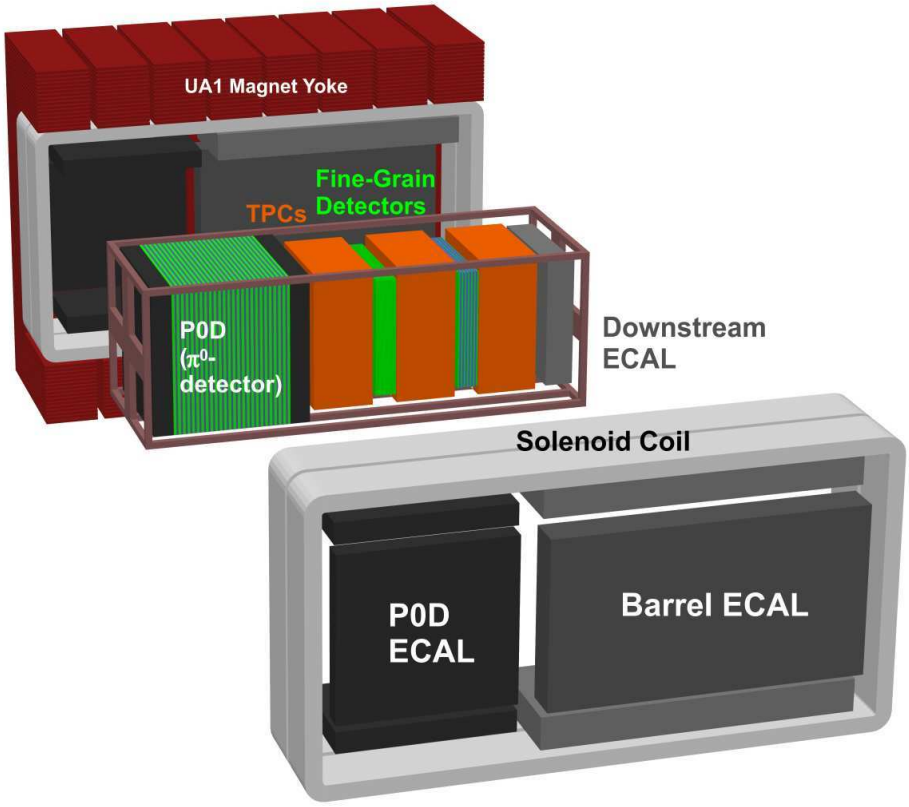

Figure 2.12: Schema of the ND280 detector. The sub-detectors are shown in an exploded view. Note that the "Side Muon Range Detector" is not shown and placed in the space between the plates of the "UA1 Magnet Yoke" structure.

The magnet of the ND280 detector is the one used in the UA1 experiment at CERN,

which was also used at the NOMAD experiment. The magnetized space in the interior of the magnet has the shape of a rectangular parallelepiped. The interior volume is about 88 m^3, and has an uniform, horizontal magnetic field that is also perpendicular to the beam direction. For T2K the magnet will be used with a 3 kA current, which corresponds to a 0.2 T field inside the magnet.

A neutrino of the T2K beam that passes through the center of the ND280 will first go through the "π^0-detector ("P0D"), after that it will go through the "Tracker" (that is composed of "Time Projection Chambers" ("TPC") and "Fine Grain Detectors" ("FGD")) and finally it will go through the electromagnetic calorimeter ("Downstream ECAL") before leaving the detector.

The "P0D" was designed to study specifically the π^0 production in water, which is one of the main backgrounds for the ν_e appearance oscillation analysis as mentioned previously. This detector is composed of three successive modules. The external modules are composed of scintillators and lead, while the central module is composed of scintillators, water (that is the main neutrino target of this detector with about 2850 kg) and brass (to reduce the energy of the particles produced by the neutrino interaction). The measure of the neutrino cross-section in the oxygen (from the water) will be performed by taking data with the "P0D" filled with water and empty. The π^0 production in each case will then be compared for the measurement of the cross-section.

The "Tracker" is the sub-detector which measures the flux and energy spectra of each neutrino flavour going through the ND280 detector. It will also be used to measure the cross-section of different types of interaction. The "Tracker" is composed of three "TPC" and two "FGD" placed between the "TPC". The "TPC" allows the reconstruction of particle tracks in three dimensions at the same time with a good spacial resolution. A precise reconstruction of the trajectory of the particles, and therefore of the moment and sign of the charge of each particle is obtained. The "FGD" detectors are made of scintillators placed either vertically or horizontally (as was done at the INGRID detector). In the first "FGD" there are only scintillators, however in the second "FGD" there are also water targets between the scintillator layers, and in this case there are less scintillator layers than in the first "FGD". The "FGD" will be the neutrino target of the "Tracker" given that most of its mass is at the "FGD" (each module weights about 1 ton). In figure 2.13 are shown examples of interactions in the ND280 Tracker.

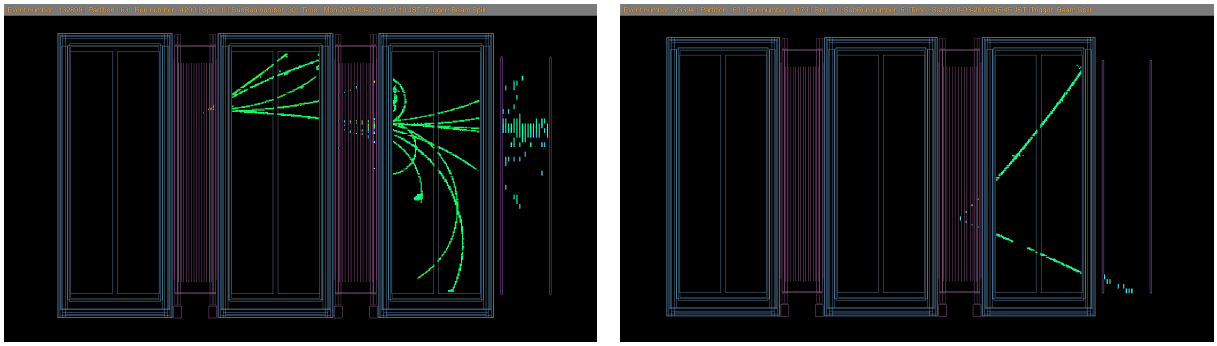

Figure 2.13: Typical event displays in the ND280 Tracker. In the left, an event display shows interaction produced at the first FGD that produces several particles and some of them will shower when passing through the second FGD. In the right, an event display shows a CC interaction produced in the second FGD with two tracks in the third TPC.

Downstream from the "Tracker" is placed the "Downstream ECAL". This electromagnetic calorimeter, together with the "P0D ECAL" and the "Barrel ECAL" (surrounding the "P0D" and "Tracker" respectively) form the "ECAL". This sub-detector is used to identify the particles that leave the "Tracker" and measure the energy of the particles such as the electron from the ν_e charged current interaction of the photons from the π^0 decays. These modules are composed of scintillator layers separated by lead layers. The "Downstream ECAL" was installed in the ND280 in October 2009, while the other ECAL modules were installed only between July and October 2010. Therefore only the "Downstream ECAL" was available from the beginning of the T2K data taking. The "Downstream ECAL" was present at the moment the event displays shown in figure 2.13 were made.

The remaining sub-detector that compose the ND280 is the "Side Muon Range Detector" or "SMRD". This detector is placed between plates of the "UA1 Magnet" structure and is composed of scintillators and because of that it is the only sub-detector from the ND280 that is not explicitly shown in figure 2.12. The "SMRD" is used to veto particles coming from outside the detector and to detect muons produced at the "Tracker" at large angles that will produce tracks that can not be correctly reconstructed by the "TPC".

For information on the ND280 detector please refer to [66] or to [67].

2.5 Super Kamiokande

The far detector of the T2K experiment is the Super Kamiokande detector (also called SK). This detector that is also used for other measurements than T2K, has been running since 1996, and is currently in its fourth phase. The Super Kamiokande detector is used to measure solar and atmospheric neutrino oscillations, from which are extracted the current best knowledge of some of the oscillation parameters. It also searches for proton decays and neutrinos from supernovae that occur in the Milky-Way, such as the 1987A supernova measured in 1987. The Super Kamiokande detector had been used as far detector for the K2K experience between 1999 and 2004.

The Super Kamiokande detector is located inside the Mount Ikenoyama in an old mine from the "Kamioka Mining and Smelting Co.". This mine is located near the Kamioka town, Gifu prefecture, Japan. The Super Kamiokande detector is at a depth of 1 km bellow the peak of the mount, with a horizontal entrance from the surface at the mount's base.

The different phases of the Super Kamiokande detector are :

- Phase I: between April 1996 and July 2001. This is the original detector configuration as described in [68] with 11146 Inner Detector (ID) PMTs.

- Phase II: between 2003 and fall 2005. During the refill of the Super Kamiokande detector after maintenance which lead to a chain effect that has destroyed about half the PMTs from the ID. The remaining PMT tubes were redistributed in the whole detector. The Super Kamiokande II has therefore a worse resolution and light collection than in the first phase.

- Phase III: between end of 2005 and summer 2008. This phase started after the reconstruction work made to reinstall almost all the PMTs that had been destroyed in the incident. To avoid an accident similar to the one that happened in 2001 acrylic covers were added in front of each of the PMTs, reducing the number of PMTs that could be put in the Super Kamiokande ID to 11129.

- Phase IV: since summer 2008. The main difference in relation to Super Kamiokande phase III is an upgrade on the electronics modules responsible for the data acquisition allowing higher trigger rate and more complex triggers. One of the reasons for this upgrade was to prepare Super Kamiokande for T2K data taking. Other benefit from this upgrade is the reduction of the "dead time" of the detector.

We should note that the T2K period starts during the fourth phase of data taking for Super Kamiokande and only this phase of data taking will be described.

The Super Kamiokande detector is a cylindrical pit, filled with ultra-pure water and inside of which are placed several photo-multiplier sensors (PMT), as shown in figure 2.14. The cylindrical pit has diameter of 39.3 m and height of 41.4 m. Inside the cylindrical pit are placed structures where the PMTs are mounted. These structure divides the detector in two parts : the outer detector (OD) and the inner detector (ID), where the ID is also a cylinder concentric to the pit with 33.8 m diameter and 36.2 m height.

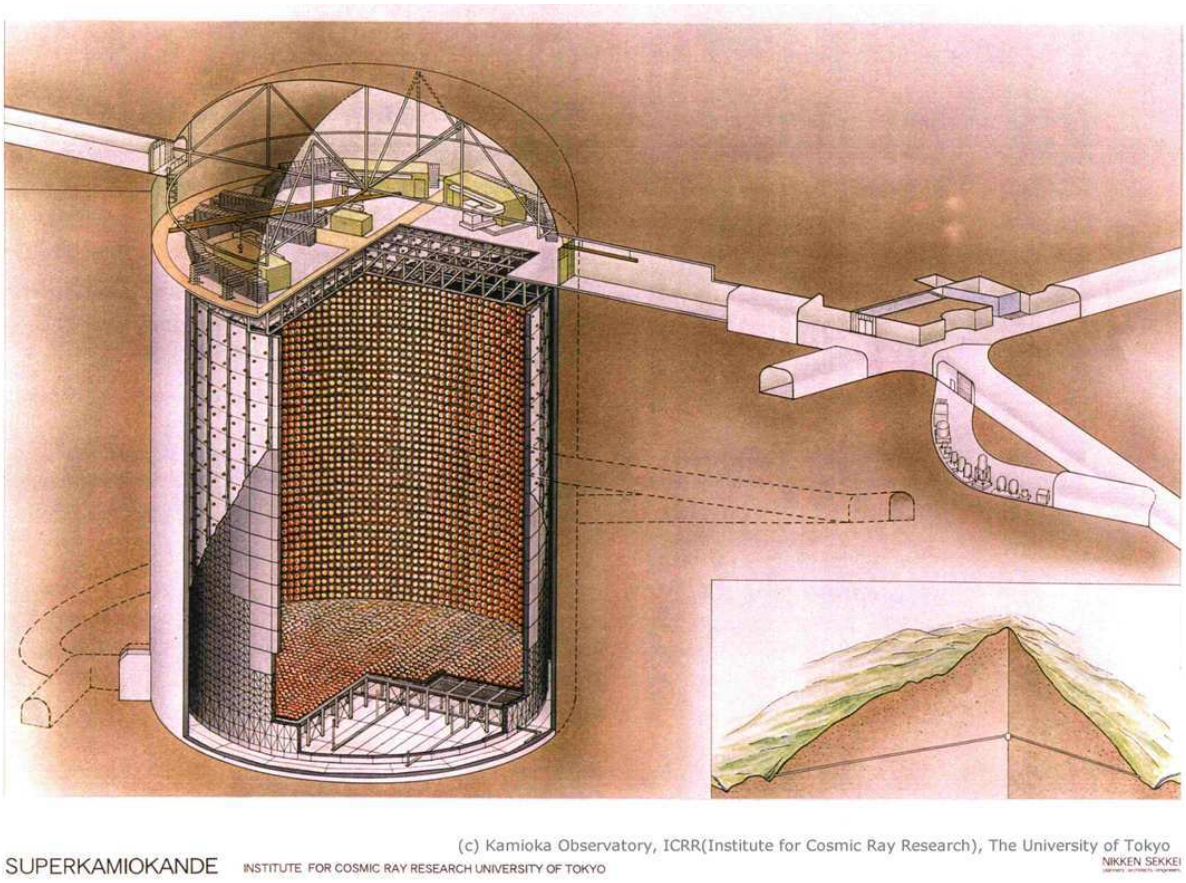

Figure 2.14: Scheme of the Super Kamiokande detector. The cilindrical pit is shown in a cut view where the interior of the detector is shown. Inside the detector are placed photo-multiplier sensors that are shown as yellow circles. In the bottom right side of the image is shown the location of the Super Kamiokande detector inside the Mount Kamioka.

On the inner wall of the OD facing towards the pit are placed 1885 8-inch PMTs of which 1275 are placed on the barrel of the cylinder, 302 on the top and the remaining 308 on the bottom of the cylinder. The distance between the OD PMTs and the tank wall is of about 2.6 m. The walls of the OD are covered with "Tyvek", a highly reflective material to increase the light collection of the OD, given the poor coverage of the PMTs on the

OD. The OD will be used mainly as veto for most of the Super Kamiokande analysis. It is essential that the OD collects as much light as possible even at the cost of good vertex resolution.

On the wall of the ID are placed 11129 20-inch PMTs facing towards the interior of the ID. Those PMTs are placed at interval of approximately 70 cm between neighbouring PMTs. The wall of the ID without PMT is covered by "black sheet", having the role to reduce as much as possible the light reflection in the wall of the ID. The PMT coverage of the ID is of about 40% and the volume of the inner detector corresponds to about 32.5 kton of water. Furthermore, for physics analysis, it is defined a region inside the ID where the reconstruction performance is considered good. This region is also a cylinder with constant distance to the ID wall of 2 m and is called the fiducial volume (FV). The fiducial volume corresponds to 22.5 kton of water and is used as the neutrino target of the Super Kamiokande detector.

The Super Kamiokande detector detects neutrinos through the detection of Cerenkov light emitted by charged particles moving faster than the light speed in the water. For the T2K case, these particles are created via the neutrino interaction with the water. The Cerenkov effect produces the emission of light in the shape of a cone, as explained in appendix C, as long as the particle is moving faster than the speed of light in the medium. The light produced by Cerenkov effect is then collected at the wall of the detector by the PMTs. Depending on the particle type the pattern the Cerenkov light will be a ring with either sharper or fuzzier edges. These characteristics correspond to muon or electron types of events, respectively, since the muons will tend to travel in a straight line in the detector because of their large mass, while the electrons will scatter more easily, therefore emitting Cerenkov light in several different directions. One muon-like and one electron-like event displays are shown in figure 2.15 where the characteristics described here are clearly shown.

In order for Super Kamiokande to have a good detection efficiency and energy resolution, as shown in figure 2.15, it is essential that the quality of the water used to fill the Super Kamiokande tank be pure, in order to reduce as much as possible the absorption and scattering of the light in the detector. Furthermore it is also essential that the radiation level of the water be kept as low as possible as decays inside the fiducial volume would produce a signal similar to the one produced by low energy neutrinos. To insure the high purity of Super Kamiokande water, a "water purification system" was constructed to filter and circulate the water in the Super Kamiokande tank. The water quality is monitored in real time using several different calibration sources.

For T2K data taking the Super Kamiokande detector uses a time based trigger which records data for each T2K beam spill. This new trigger relies on the upgrades made for the fourth phase of Super Kamiokande. The T2K specific trigger at Super Kamiokande is based on a trigger signal sent from J-PARC via a private network connection with the GPS time of the spill. The given GPS time is then corrected to take into account the time of flight of the neutrino between J-PARC and Super Kamiokande assuming the neutrino travels at the speed of light (which corresponds to about 984 μs for 295 km) and delays in the hardware used to set the time of the event. The data within $\pm$500 μs of the given time are saved, corresponding to 1 ms time window around the expected arrival time. The timing of the Super Kamiokande PMT hits is checked with a redundant clock system, which uses information from two independent GPS modules and a rubidium atomic clock. Events between -2 μs and 10 μs of the expected timing are considered on time events and are used in the T2K data analysis. The remaining events in the 1 ms time

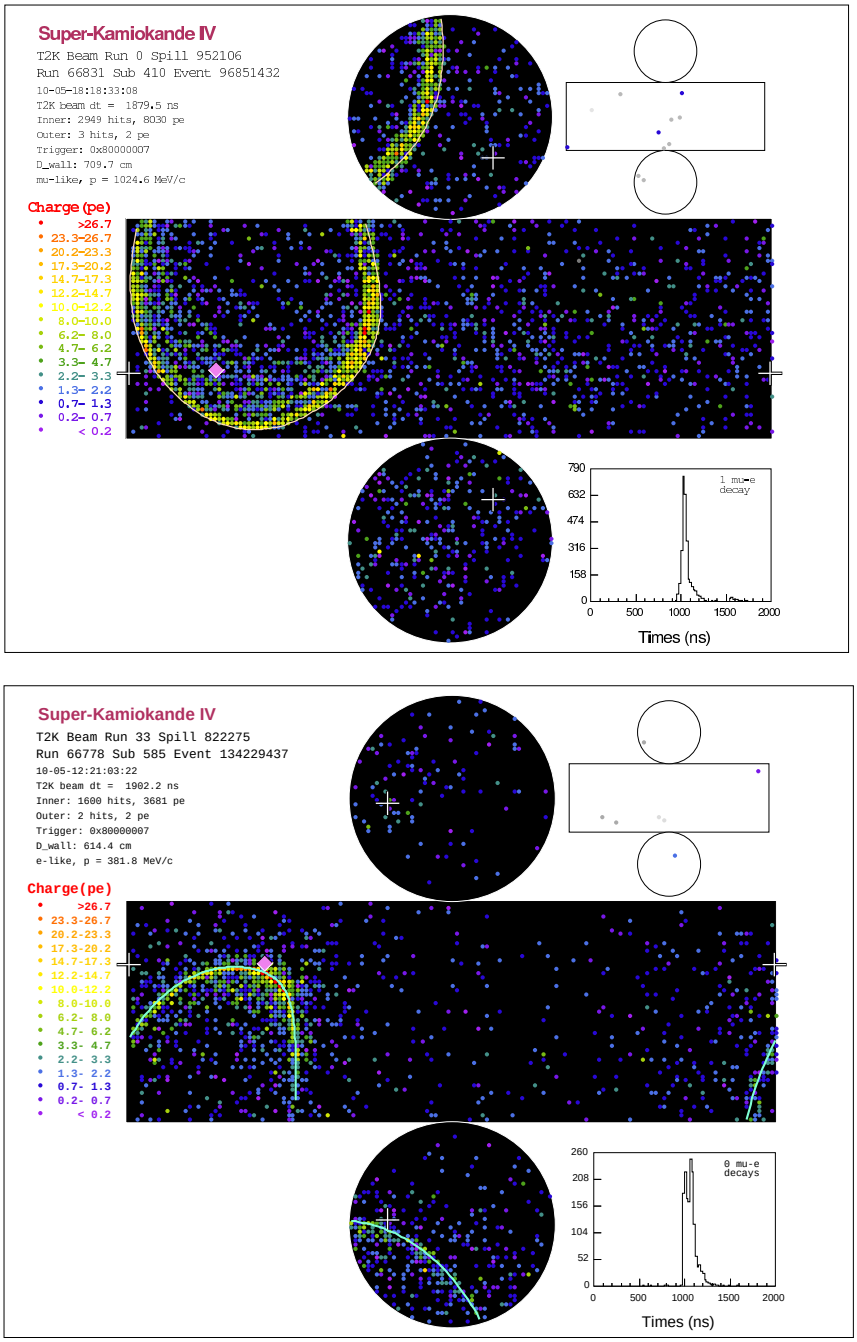

Figure 2.15: Event display of a muon like event (top) and an electron like event (bottom) that were observed in the expected T2K time window. In these event displays the Super Kamiokande detector is shown in an unrolled view with the rectangular band being the barrel and each circle the top and bottom of the ID in black and the OD is shown in the same way on the top right of each of the unrolled ID plots. Each dot in the event display correspond to a PMT where some charge was observed and its color indicates the amount of charge observed. In the top event display the ring has a sharp edge, which characterizes a muon-like ring. The reconstructed ring is shown in white, the rhombus represents the reconstructed particle direction from its vertex that is given by the crossing of the plane defined by the + signs in the barrel and the + signs at the top and bottom circles. In the bottom event display the ring has a fuzzy edge, which characterizes an electron-like ring. In both event there is almost no charge observed in the OD, which indicates these events were produced inside the ID.

window are used to evaluate the background and as backup in case of de-synchronization of the timing system.

2.5.1 Event selection and classification

The data taken during the T2K trigger needs to be classified before further usage. Even though this classification is somewhat similar to the usual Super Kamiokande classification for "atmospheric events" [53] it is not exactly the same. The event selection for T2K consists of :

1. Super Kamiokande DAQ is alive.

2. Reject sub-runs of data in case of problem, such as persistent "flasher", that is PMT malfunctions with emission of light. When a PMT enters in a "flasher" mode it is turned off as soon as possible and the events are rejected. A "flasher" is typically identified by charge pattern matching and correlation. This rejected about 0.5% of the spills in the T2K data period used for this dissertation.

3. Reject data if there is a problem in the DAQ (significantly less hits than what would be expected for the dark noise in the 1 ms time window) or in both GPS (that is if both GPS units report an error). This has not rejected any spill in the T2K data period used for this dissertation.

4. Reject data when during the on-timing region were done maintenance operations, such as "TDC reset block" which resets some counters on the TDC chips, or calibration tagged events, such as a "pedestal block" to take pedestal data from the ADCs. This rejected about 0.08% of the spills in the T2K data period used for this dissertation.

5. Reject data when there is an event at least 100 μs before the on-timing range in order to avoid contamination of the neutrino sample by particles decaying from these first events. This rejected about 0.3% of the spills in the T2K data period used for this dissertation.

Once the T2K data at Super Kamiokande passes through this first selection mentioned it is classified as follows, in the order (that is the first classification matching the data is used only) :

1. *Calibration* : events where the calibration flag was on. Obviously this data is not used in any regular analysis.

2. *Outer detector (OD)* : events with a hit cluster in the OD with more than 16 hits.

3. *Low energy (LE)* : events with less than 200 PE in the ID in a 300 ns time window or events where more than half of the total charge in the 300 ns time window are measured from a single PMT.

4. *Flasher* : this classification is similar to the categorization used for the event selection of "flasher" and is also verified via charge pattern matching using a "flasher database". The difference between this classification and the event selection mentioned previously is that in this case the selection is done on an event by event basis, while previously it was done in a sub-run by sub-run basis.

5. *Fully contained (FC)* : all events that are not in any of the previous classifications. That is events that are in the ID, with high energy, that are neither flashers nor calibration events. This is the sample that is mostly used for data analysis.

Given that for the neutrino oscillation analysis presented on this thesis only the fully contained sample was used, we will only describe the event selection of the fully contained sample. Note that there are other event reconstructions which are used to study the OD and LE samples.

2.5.2 Reconstruction for fully contained events

The reconstruction used for the fully contained events of the T2K data sample is the ATMPD (Atmospheric and Proton Decay group at Super Kamiokande) reconstruction that uses the "APfit" software [1]. This software performs several reconstruction steps to refine the quality of the reconstruction output. This reconstruction will perform in order :

1. vertex finding;
2. count number of rings;
3. particle type identification;
4. redetermine vertex for single ring events;
5. decay electron tagging;
6. momentum reconstruction;
7. correction of the number of observed rings from ring counting;
8. search of π^0 events that were mis-reconstructed.

Each of these steps will be described in more details in the following subsections. Some of these parts are merged into one subsection if they have the same function to give a more complete view of each algorithm.

In addition to the usual ATMPD reconstructions, we also calculate the neutrino reconstructed energy assuming the neutrino interacts through CCQE and that the interacting neutrino direction is the direction of the neutrino beam at Super Kamiokande.

Vertex finding

The vertex is reconstructed from the timing and charge observed in the SK tank. The first vertex is reconstructed assuming all the light is produced at a single point in SK. It is determined by the minimization of the spread of the timing distribution of hit PMTs corrected to take into account the time of flight of the light from the vertex to the PMT. A preliminary direction is then reconstructed by the direction of the charge barycenter of the PMTs.

After the preliminary direction reconstruction and the first vertex reconstruction, the direction and Cerenkov angle are fitted to the Cerenkov ring edge by analysing the charge distribution as a function of the opening angle for different directions. Once this new

[1] The description here is based on the code of "APfit" and on reference [69].

direction and the Cerenkov opening angle are obtained the vertex is re-fitted assuming the photons are emitted along the particle trajectory.

In the case of single ring events, we recalculate the vertex and direction by taking into account the expected charge produced by a particle of the reconstructed type in the detector taking into account detector effects. This recalculation of the vertex and direction performed just after the "particle type identification" allows a better vertex resolution than the usual reconstruction. It can only be used for single ring events.

The variables defined by this step used afterwards are :

- Interaction vertex
- Direction of the first ring
- Cerenkov angle of the first ring
- Distance between the interaction vertex and the detector wall ("distance from wall" or "`dwall`")
- Distance between the interaction vertex and the wall calculated following the T2K beam direction ("distance from wall parallel to beam")

Note that the fiducial volume condition described previously consists of requiring `dwall` $>$ 2 m and that the "distance from wall parallel to beam" is only defined for T2K events, given that a neutrino beam direction is not defined for atmospheric Super Kamiokande samples.

The interaction vertex is decomposed in the (r, z) plane, the "`dwall`" and the "distance from wall parallel to beam" are used as verification of the neutrino data distribution, given that we expect that neutrino interactions are randomly distributed in the detector.

Ring counting (RC)

The ring counting algorithm is separated in two parts. The first part, also called ring counting, tries to find the number of rings for each event using the Hough transformation [70] to select new ring candidates and a likelihood comparison to decide if such new ring found is reasonable given the charge distribution. The second part, also called "ring number correction", will further reduce the number of rings reconstructed by the first part of the algorithm using supplementary information that has been obtained between the first and second parts.

In the first part of the algorithm, new ring candidates are found by the position of peaks of direction in the Hough transformed distribution of the hits observed at the Super Kamiokande detector assuming the previously reconstructed vertex and that the new ring Cerenkov angle is 42°[2]. For each new ring candidate it is evaluated the likelihood of the charge pattern in SK for all previously found rings and the new ring, and if this likelihood is better than the likelihood of the charge pattern in SK for all previously found rings without the new ring then the new ring is considered found and this process is started again, up to five rings being found, in which case the ring search is stopped.

After the rings are found and separated, and the particle that produced each ring are identified, the total charge of each ring, given the charge distribution and ring type, is

[2] 42° is about the maximal Cerenkov that can be produced by particles moving in water, and therefore is typically the Cerenkov angle of an electron produced by a high energy neutrino through CCQE

calculated and corrected for detector effects and used to obtain the ring momentum via a table generated by simulation.

In the second part of the algorithm are rejected rings that had been found, but which have a low energy associated to them and at the same time are overlapping with other rings with higher energy. This procedure is useful to remove mis-reconstructed rings which could be generated by a showering of the first particle. Evidently, whenever a ring is rejected at this stage the rings are separated again and their momenta are reconstructed again.

The variables defined by this step used afterwards are :

- Ring counting likelihoods
- Number of rings ("`nring`")
- Direction of all rings but the first ring
- "Visible energy" ("`evis`")

Note that the likelihoods defined here are related to the first part of the ring counting algorithm and do not take into account the effect of the "ring number correction".

Note also that the "visible energy", despite what the name indicates, is not the total charge observed in the detector. In fact, it is defined as the sum of the momentum of all the reconstructed rings, where the momentum of each ring was calculated assuming the ring was produced by an electron.

Particle type identification (PID)

Once the first part of the "ring counting" algorithm is performed, we have a first number of rings for which we need to identify the particles that generated them. This is done ring by ring by calculating the likelihood that the ring corresponds to an electron (showering) or a muon (non-showering) ring. Examples are shown in figure 2.15. This likelihood will mainly depend whether the ring edge is fuzzy or sharp, which corresponds respectively to the electron and muon cases.

In the case of the single ring event the Cerenkov angle calculated at the vertex fitting step is used to calculate an "angle likelihood" that will be composed with to the "charge likelihood" described in the previous paragraph to compose the "PID likelihood". For the "angle likelihood" the particle type identification is performed by taking into account the probabilities that the measured Cerenkov angle could be produced by the given particle. Typically, the electron will have larger Cerenkov angle than a muon given that its mass is smaller and therefore its β will be larger, for the same momentum.

The particle type identification algorithm will only distinguish between electrons and muons, therefore it classifies events as "e-like" or "μ-like". In the case of other particles they will be classified as "e-like" or "μ-like" depending on their characteristics. Typically, a γ will be classified as "e-like" because it will pair-produce electrons while traveling in the water which will produce a showering ring. A charged pion will be classified as "μ-like" given that it has a large mass, compared to the electrons, and as the muon will roughly keep the same direction during all the propagation.

The variables defined by this step used afterwards are :

- Particle type likelihood for each ring
- Particle type identification for each ring

Decay electron tagging

In all other steps of the reconstruction we consider only hits from a narrow time window around the event. Typically this time window is defined between -50 ns and 250 ns around the peak of the time distribution of hit PMTs corrected by the light time of flight in water from the vertex to the PMT. For the decay electron search and tagging we will search for peaks in the number of hits during the 40 μs that follow the original event. When an increase in the number of hits is found, and is verified to be larger than what could be expected just from a statistical fluctuation of the background noise, a decay electron is considered to be found.

Decay electrons that have been identified as just described will be reconstructed only in some conditions using a low energy fitting algorithm called "Kai-fit". The required conditions to perform the fit is that in the 50 ns time window that maximizes the number of hit PMTs in the time of flight subtracted timing distribution there are more than 30 hit PMTs, and in this time window the total number of photo-electrons is smaller than 2000 PE. Furthermore it is also required that the decay electron was found at least 600 ns later than the original event to fit the decay electron found.

This procedure is effective to tag decay electrons at 95% of the μ^+ and 81% of the μ^- events, where inefficiencies are mainly caused by decays close to the parent event for both μ^+ and μ^- or by the capture of the μ^- by oxygen which will emit a low energy γ which has lower detection efficiency in the case of μ^-.

The variables defined by this step used afterwards are :

- Number of decay electrons ("`nmue`")
- Timing of each decay electron
- Position and direction of each the decay electron, if "kai-fit" is applied

π^0 search

After the main reconstruction procedure there could be several π^0 events not tagged as multi-ring events and are still in the single ring sample. This happens typically in the case where low momentum γ from the π^0 decay has momentum small enough that it will not be easily reconstructed by algorithms applied for the ring counting. In order to correct this mis-reconstruction, a special algorithm, called POLfit, was developed to tag π^0 events.

In this algorithm, it is assumed that the event observed is composed of two γ rings (π^0 decay in two γ with branching ratio of about 99%), and that the vertex and direction of the γ ring with higher momentum was correctly reconstructed previously. The algorithm will then search the direction and momentum of the second ring that will give the best likelihood for the two γ rings charge pattern corresponding to the observed charge pattern.

Once the second γ is found, the momentum of each ring is recalculated taking into account more detector details than POLfit does, by using the same algorithm previously used after particle type identification.

Finally, using the best fit for the second γ the invariant mass of the two γ is reconstructed (with the formula given in the appendix D.1.1). For events corresponding to π^0 events one would expect that the reconstructed mass would be around 135 MeV/c^2.

In the case where the observed event is produced by an electron and not a π^0 the likelihood of the best fit value will be small (no good fit for a second γ in the given event)

and the reconstructed mass will be small either because the second γ was reconstructed on top of the first γ or because the second γ momentum is very small.

The variable defined by this step used afterwards is :

- POLfit π^0 mass ("pi0mass")

Neutrino energy reconstruction

The neutrino energy for a CCQE event, that is for $\nu_l + n \rightarrow l^- + p$ interactions, can be calculated from the lepton momentum and direction assuming the original neutrino direction, even in the case where we cannot measure the recoil p because its momentum is below the Cerenkov threshold. As explained previously, the reconstruction of the neutrino energy is specific to the T2K data set because in atmospheric Super Kamiokande data there is not enough information to reconstruct the neutrino energy for CCQE interactions. For T2K however we know a priori the incident neutrino direction, that is the direction between J-PARC and Super Kamiokande, and therefore we can reconstruct the incident neutrino energy.

The expression for the reconstructed neutrino energy for CCQE events is shown in equation (2.1) where E_ν is the reconstructed neutrino energy, m_l, m_p and m_n are the masses of the lepton, proton and neutron, respectively, p_l is the lepton momentum, $E_l = \sqrt{p_l^2 + m_l^2}$ is the lepton energy, $\vartheta_{\nu l}$ is the angle between the lepton and the neutrino and V is the nuclear potential to take into account that the neutron is not a free neutron but bound. The value of V used is of 27 MeV. The demonstration of a simplified version of (2.1) is given in appendix D.2 in the case where we consider a free neutron.

$$E_\nu = \frac{2(m_n - V)E_l - m_l^2 - (m_n - V)^2 + m_p^2}{2(m_n - V - E_l + p_l \cos\vartheta_{\nu l})} \tag{2.1}$$

The reconstruction of other types of neutrino interaction at Super Kamiokande is not as accurate (or impossible) as for the CCQE interaction and therefore was not considered for the T2K analysis.

The variable defined by this step used afterwards is :

- Reconstructed neutrino energy ("E_ν^{rec}")

2.5.3 Event selection of ν_e CCQE sample used by T2K

The event reconstruction described previously is used to select the ν_e CCQE sample used for the search of ν_e appearance in the T2K beam. We should note here that the reconstructed neutrino energy criteria can only be used after the selection of CCQE events. The event selection applied, and which will be explained further on, is :

1. Event is fully contained with vertex in the fiducial volume (`dwall` > 2 m).
2. Event has visible energy (`evis`) greater than 100 MeV/c.
3. Event has only one reconstructed ring (`nring` $= 1$).
4. Reconstructed ring PID is "e-like".
5. No decay electrons were found (`nmue` $= 0$).

6. The reconstructed π^0 mass by POLfit (`pi0mass`) is smaller than 105 MeV/c^2.

7. The reconstructed neutrino energy (E_ν^{rec}) is smaller than 1250 MeV. We also require that the reconstructed neutrino energy be positive, given that a negative value indicates the given event came from a non CCQE interaction.

The first selection is a default Super Kamiokande event selection to choose events that are well understood, that is events that do not leave the detector (fully contained) and have not been generated close to the detector wall where the reconstruction is less accurate. They will deposit enough light in the detector to be correctly reconstructed.

The second selection is used to remove low energy events and noise events, such as eventual decay electrons from muons produced below the Cerenkov threshold, radioactive decays, while at the same time keeping most of the events produced by ν_e CCQE interesting for T2K ν_e search. The effect of the visible energy cut on the T2K Monte-Carlo sample is shown in figure 2.16.

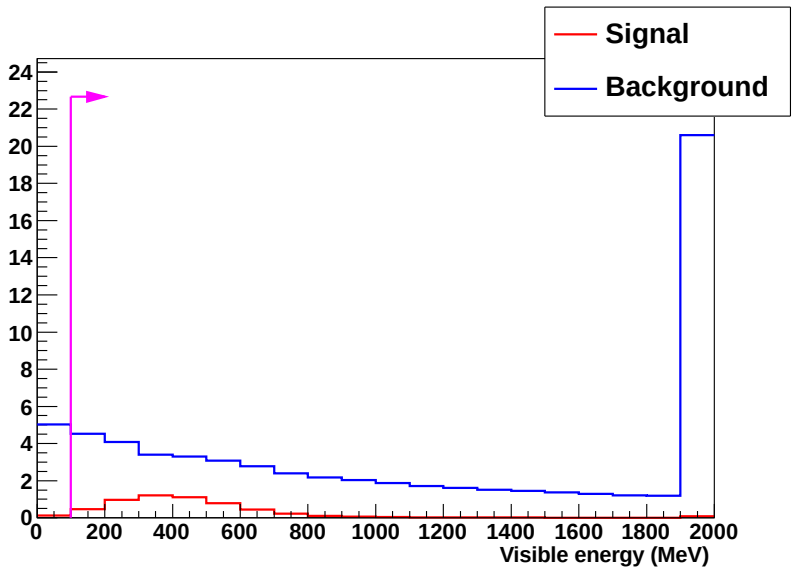

Figure 2.16: Expected signal (composed of ν_e CCQE events oscillated from ν_μ, in red) and background (composed of beam ν_e and non oscillated ν_μ events, in blue) distribution of visible energy for all events passing previous cuts, based on the T2K Monte-Carlo. The MC is normalized to T2K Run I+Run II POT three flavour oscillation is considered for the current best knowledge of the oscillation parameters as shown in table 1.3, assuming also that $\delta_{CP} = 0$ and normal hierarchy. The magenta arrow shows which events are selected. The right most bin of the plot contains the sum of all overflow values.

The third selection corresponds to selecting CCQE events, since in these events there is only one charged particle above Cerenkov threshold. The recoil proton or nucleus have rarely enough momentum to produce Cerenkov light. The effect of ring counting cut on the T2K Monte-Carlo sample is shown in figure 2.17.

The fourth and fifth selections selects interactions with one ν_e (assuming this is a CC event and not a NC event), since they require the usual characteristics of e events and refuse μ events, a ring with a fuzzy edge and withoug decay. The effect of the particle type identification cut and of the number of decay electron cuts on the T2K Monte-Carlo sample is shown in figure 2.18 and 2.19, respectively.

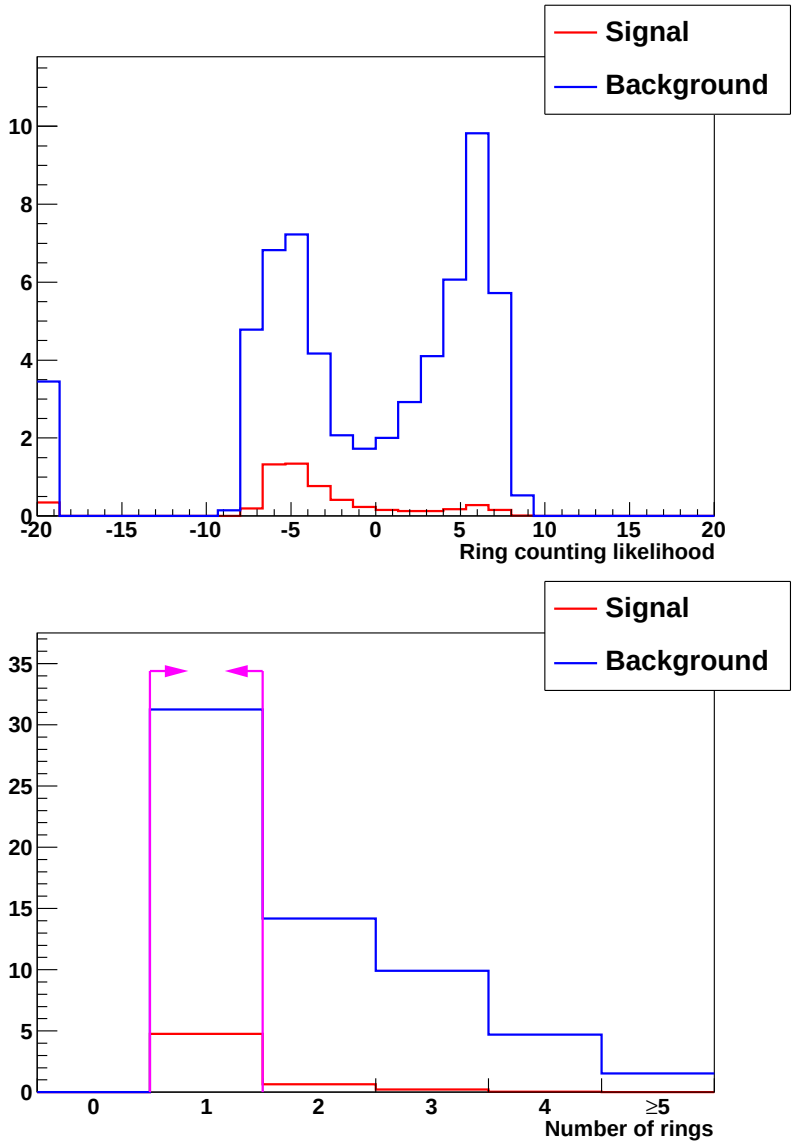

Figure 2.17: Expected signal (composed of ν_e CCQE events oscillated from ν_μ, in red) and background (composed of beam ν_e and non oscillated ν_μ events, in blue) distribution of ring counting likelihood (top) and number of rings (bottom) for all events passing previous cuts, based on the T2K Monte-Carlo. The MC is normalized to T2K Run I+Run II POT three flavour oscillation is considered for the current best knowledge of the oscillation parameters as shown in table 1.3, assuming also that $\delta_{CP} = 0$ and normal hierarchy. The magenta arrow shows which events are selected. In the top plot the events with ring counting likelihood negative are considered single-ring events and those with positive ring counting likelihood are multi-ring events by the first step of ring counting. A small fraction of the events with positive ring counting likelihood will be classified in the end as single-ring events after the "ring number correction" step of the "ring counting" algorithm. The left most and right most bin of the top plot contains the sum of all underflow and overflow values, respectively.

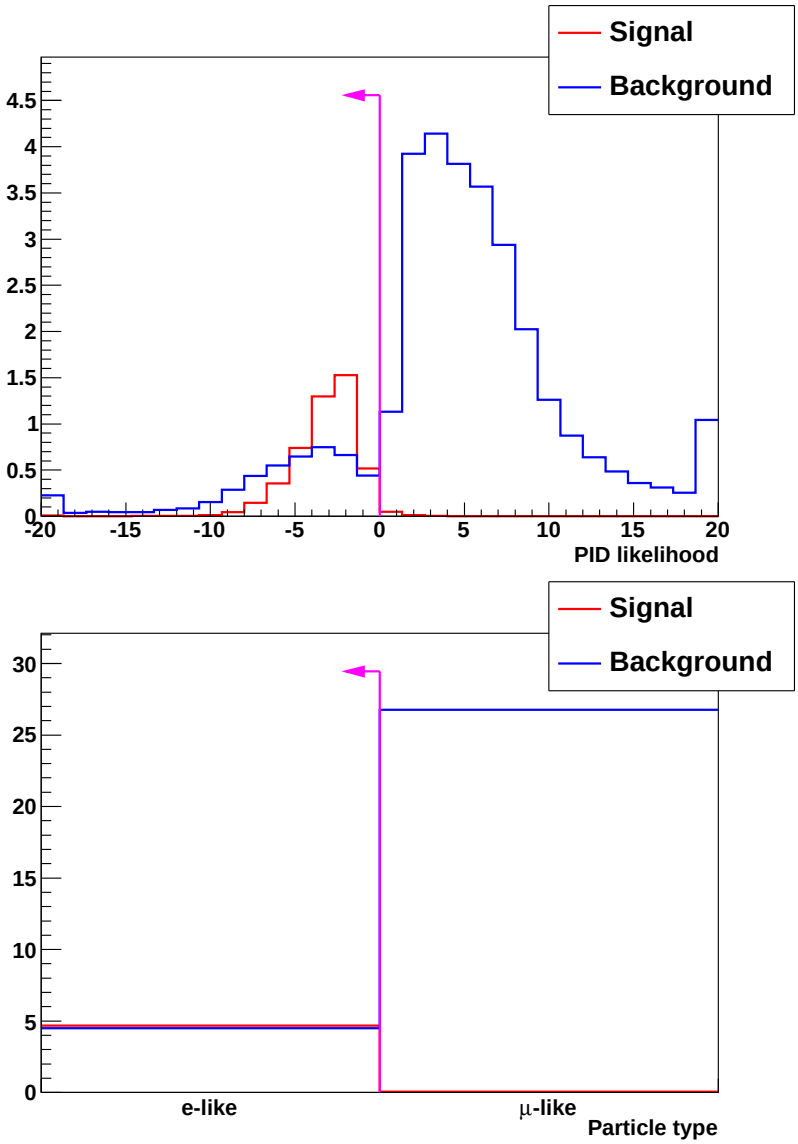

Figure 2.18: Expected signal (composed of ν_e CCQE events oscillated from ν_μ, in red) and background (composed of beam ν_e and non oscillated ν_μ events, in blue) distribution of the particle type likelihood (top) and particle type (bottom) for all events passing previous cuts, based on the T2K Monte-Carlo. The MC is normalized to T2K Run I+Run II POT three flavour oscillation is considered for the current best knowledge of the oscillation parameters as shown in table 1.3, assuming also that $\delta_{CP} = 0$ and normal hierarchy. The magenta arrow shows which events are selected. The leftmost and rightmost bin of the top plot contains the sum of all underflow and overflow values, respectively.

The sixth selection helps to remove remaining NC background similar to ν_e CCQE interaction by rejecting π^0 events. The effect of POLfit π^0 mass cut on the T2K Monte-Carlo sample is shown in figure 2.20.

The seventh selection will choose the energy range for which the ν_μ produced at J-PARC will oscillate to ν_e before arriving at Super Kamiokande. This event selection also reduces the effect of the beam ν_e contamination from kaons since the energy of neutrinos produced from kaon decay are typically higher than those produced from a pion decay. The effect of reconstructed neutrino energy cut on the T2K Monte-Carlo sample is shown in figure 2.21.

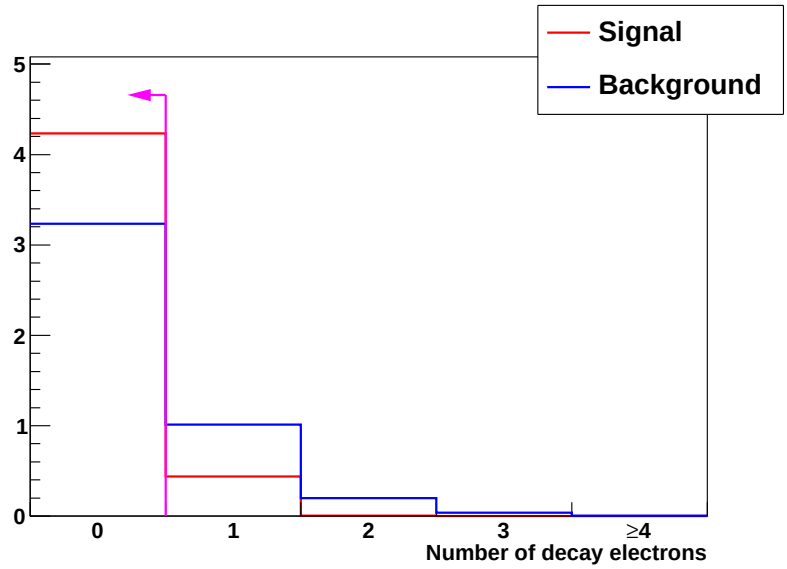

Figure 2.19: Expected signal (composed of ν_e CCQE events oscillated from ν_μ, in red) and background (composed of beam ν_e and non oscillated ν_μ events, in blue) distribution of the number of decay electrons for all events passing previous cuts, based on the T2K Monte-Carlo. The MC is normalized to T2K Run I+Run II POT three flavour oscillation is considered for the current best knowledge of the oscillation parameters as shown in table 1.3, assuming also that $\delta_{CP} = 0$ and normal hierarchy. The magenta arrow shows which events are selected.

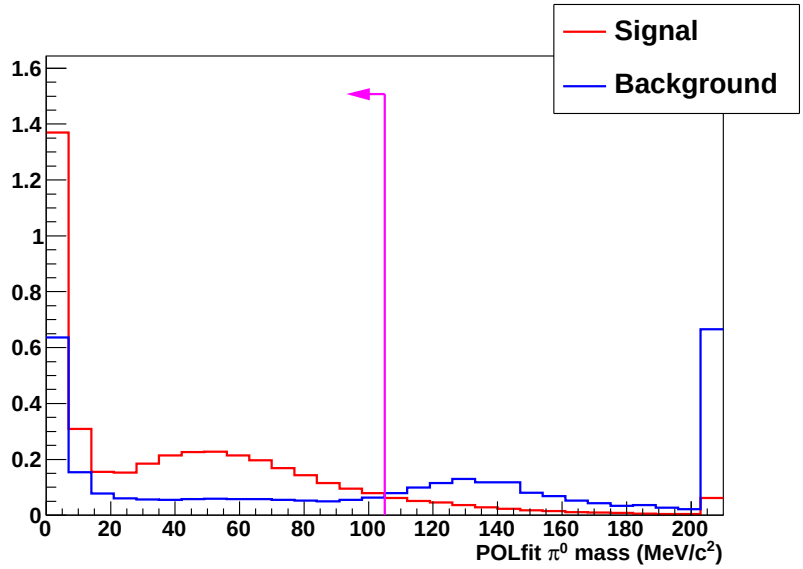

Figure 2.20: Expected signal (composed of ν_e CCQE events oscillated from ν_μ, in red) and background (composed of beam ν_e and non oscillated ν_μ events, in blue) distribution of POLfit π^0 mass for all events passing previous cuts, based on the T2K Monte-Carlo. The MC is normalized to T2K Run I+Run II POT three flavour oscillation is considered for the current best knowledge of the oscillation parameters as shown in table 1.3, assuming also that $\delta_{CP} = 0$ and normal hierarchy. The magenta arrow shows which events are selected. The rightmost bin of the plot contains the sum of all overflow values.

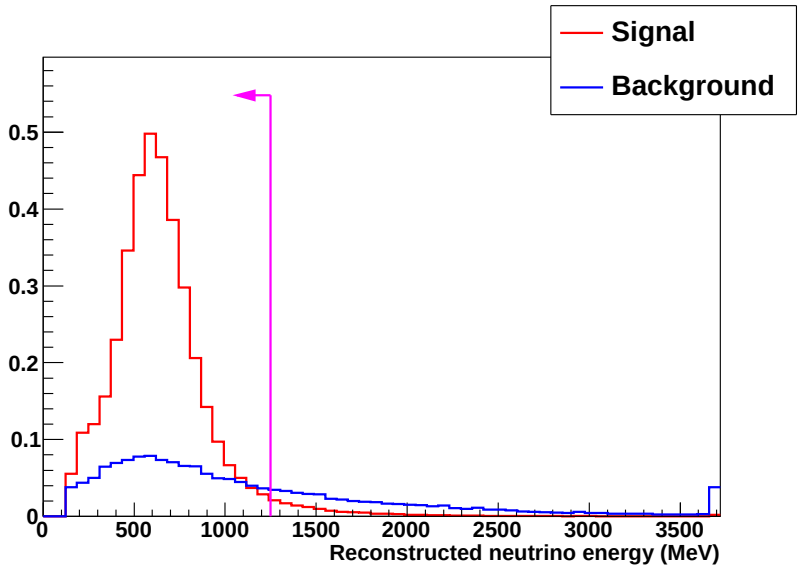

Figure 2.21: Expected signal (composed of ν_e CCQE events oscillated from ν_μ, in red) and background (composed of beam ν_e and non oscillated ν_μ events, in blue) distribution of the reconstructed neutrino energy for all events passing previous cuts, based on the T2K Monte-Carlo. The MC is normalized to T2K Run I+Run II POT three flavour oscillation is considered for the current best knowledge of the oscillation parameters as shown in table 1.3, assuming also that $\delta_{CP} = 0$ and normal hierarchy. The magenta arrow shows which events are selected. The rightmost bin of the plot contains the sum of all overflow values.

Chapter 3

Development of a multi-ring light source for calibration and systematic error studies of the Super Kamiokande detector

Contents

3.1 Motivation

The Super Kamiokande detector is currently calibrated using several different sources : the PMT's timing is calibrated via a diffuser ball placed at the center of the Super Kamiokande tank that flashes frequently; the PMT gain is calibrated using a Xe lamp and verified with Ni+Cf sources regularly; the water absorption and scattering are calibrated using laser injectors around the tank and through-going μ data; the energy scale of the detector is further calibrated using Multi-GeV and Sub-GeV stopping muons[1], decay electrons and π^0 events reconstructed in the detector, by comparing the results from these analysis with the expected values for these samples [68, 69]. Further calibrations for low energy events are also done using a LINAC installed on top of the Super Kamiokande tank and other radioactive sources.

The usual Super Kamiokande calibrations that use an external light source will either emit light in all directions at the same time, which is the case for the calibration sources placed in the center of the detector, or emit light in a given direction from the walls of the detector. In both cases the light pattern emitted by these sources is extremely different than the one produced by physics events and therefore these calibrations sources cannot be used for studies of detector response to different types of events. We should also note here that these calibration sources cannot monitor changes in the reflectivity of the black-sheet and of the PMT surface independently, even though appropriate measurements were made during one calibration of the detector and tuning of the detector simulation because these coefficients are not expected to vary in time.

The physics events used for calibrations, on the other hand, are also used for several detector performance studies, however, several of these samples suffer from low statistics, such as the π^0 events sample, and moreover these samples constitute the events "correctly reconstructed", therefore they are not adapted for studies where it is essential to understand how and when the reconstruction fails, such as the estimation of the contamination of NC π^0 events to the data sample passing all T2K ν_e CCQE event selections, which corresponds to about a third of the background for the T2K ν_e search. In the case of π^0 events, we know that typically they produce two γ rings inside the SK detector, and to mis-reconstruct a π^0 event the SK algorithms need to miss one of the rings, therefore the usage of a calibration source that can produce a known number of rings is an important control sample to study the efficiency of ring finding algorithms at SK.

We have taken over the development of a new multi-ring calibration source that is meant to address, at least in part, the issues that have just been raised : the Cone Generator (CG). The advantage of the Cone Generator, in relation to the usual calibration sources using external light, is that the light pattern produced by the Cone Generator is similar, though unfortunately not exactly the same, to the light pattern produced by physics events, that will be constituted of one or more rings, each ring corresponding to a different particle. Furthermore, since the Cone Generator is also an external light source, it is possible to have a large number of events produced during a small amount of time at the configurations we have decided beforehand.

In this chapter we will describe the development of the single CG itself, and the results obtained so far. Unfortunately the development of this new multi-ring calibration source has not been completed yet, and therefore it has not yet been used in any T2K related analysis.

[1]Here the Multi-GeV and Sub-GeV stopping muon samples are intentionally separated because different properties of these samples are used for calibration purposes.

A global scheme of how the CG is currently used is shown in figure 3.1, and we will follow this scheme in the presentation of this chapter. We first present the calibration source itself in section 3.2, and then we present the simulation to predict the emitted light pattern to obtain the "Single cone Monte-Carlo" (section 3.3). After that we present the data taking of the "Single cone data" and of which data it consists exactly (section 3.4). Finally we present the current status of the comparison between the current CG data and simulation (section 3.5), with which we were able to identify a bug in the Super Kamiokande detector simulation (the effect on physics events at SK is estimated in section 3.6). The perspectives for usage of this new calibration source are presented at the end of this chapter (section 3.7).

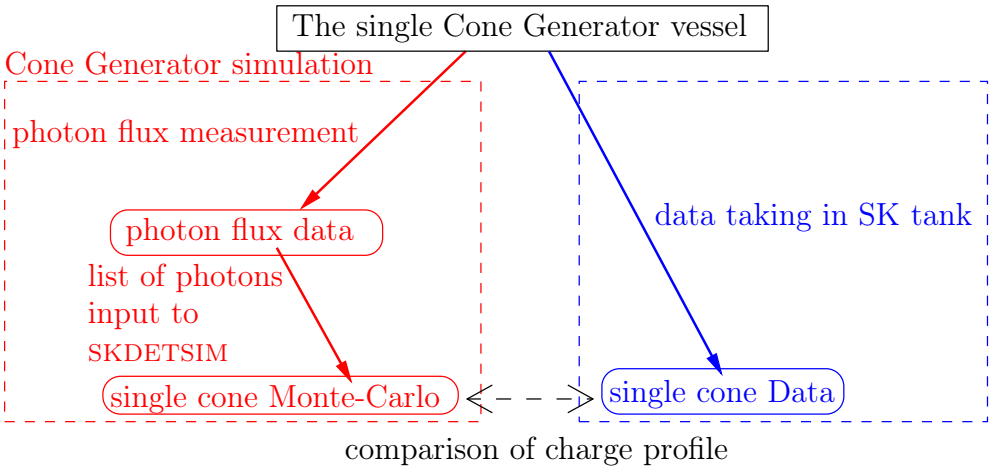

Figure 3.1: Global scheme of the Cone Generator usage. The CG simulation (red) consists of the "photon flux measurement" of the CG vessel that is used as input to the SK simulation (SKDETSIM) to obtain the CG "single cone" Monte-Carlo. The same CG vessel is also used at data taking in the SK tank (blue) to measure, in its turn, the "single cone" data.

3.2 The single Cone Generator vessel

The Cone Generator vessel is composed by a "delrin vessel", which is build using delrin plastic, inside of which is placed a "diffuser ball" connected to an optical fiber. At the edge of the optical fiber inside the "diffuser ball" is placed a 10000 ppm MgO tip to increase light diffusion in all the ball. The diffuser ball itself is doped with 1500 ppm of MgO. The other end of the optical fiber is connected to a laser. Before 2011 the laser source used was "dye laser" set to about 400 nm wavelength. Due to the poor "dye laser" intensity stability we have changed the laser source since 2011 to use a "laser diode" with wavelength of 405 nm. The Cone Generator vessel as described previously is shown on figure 3.2. A picture of the CG vessel is also shown in figure 3.3.

Due to the diffusion of the light from its production until it leaves the diffuser ball, the light should loose any polarization it could have had at its production point. Thus, in our studies the light emitted by the Cone Generator is considered unpolarized.

The "diffuser ball" was verified to be symmetric by rotation around the axis from which the fiber is inserted inside the ball to a precision of the percent level.

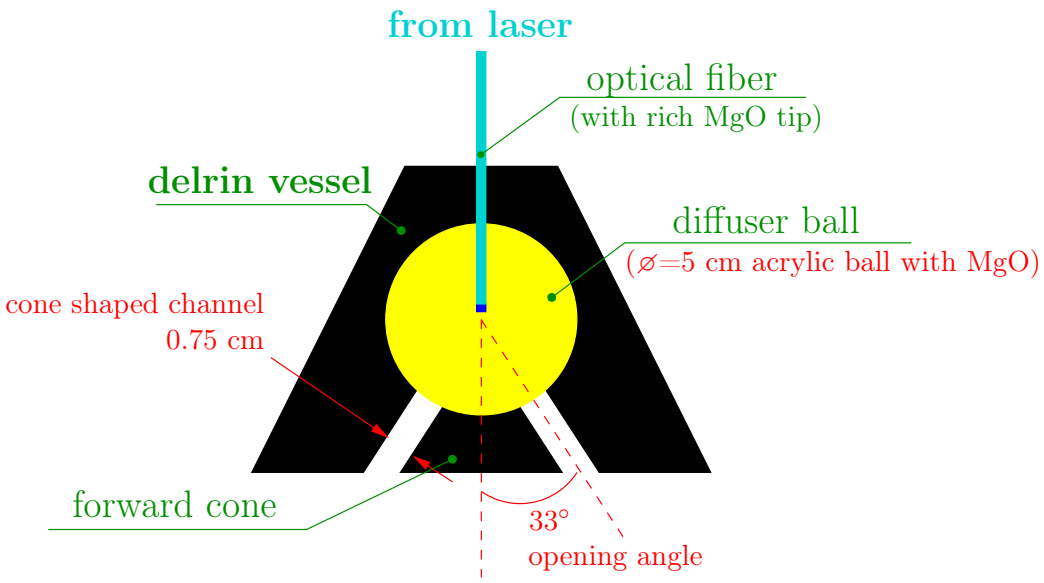

Figure 3.2: Scheme of the Cone Generator vessel.

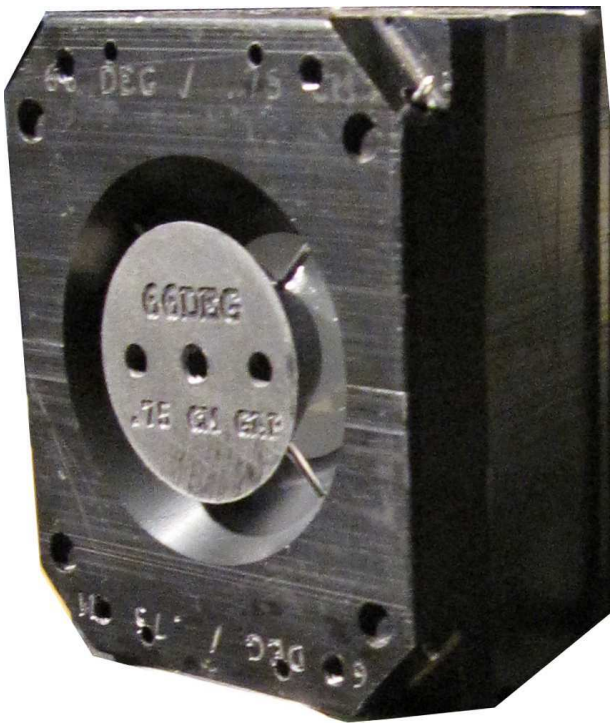

Figure 3.3: Picture of the CG vessel. In this picture are visible the "delrin vessel", the "diffuser ball" and the "forward cone" that is fixed to the "delrin vessel" with the metallic pins shown in the picture.

The "delrin vessel" is shaped to allow a cone of light to be emitted from the diffuser ball. To this cone the internal part is removed by adding another part to the delrin vessel called "forward cone". The light from this vessel thus produces a ring on a surface to which it is projected, as can be seen in the CG event display produced with only one CG inserted inside the SK tank shown in figure 3.4.

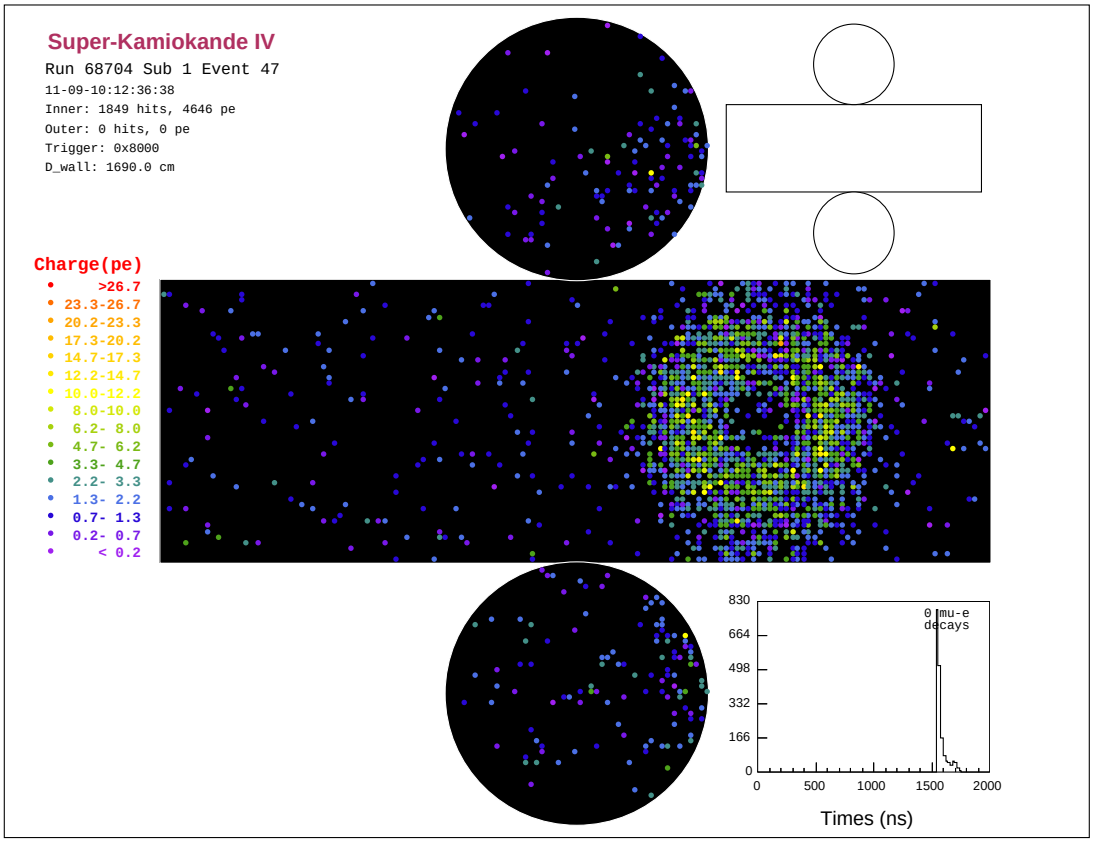

Figure 3.4: Event display of the single CG vessel inserted into SK.

The "opening angle" of the cone and width of the "cone shaped channel", which are shown in red in figure 3.2, are both determined by the dimensions of the "delrin vessel" and the "forward cone". Even though several "delrin vessel" and "forward cone" with different dimensions were available we chose to study one combination of "delrin vessel" and "forward cone" in more detail. The combination used have opening angle of 33° and width of the "cone shaped channel" of 0.75 cm as shown on figure 3.2. This combination was chosen because this is the vessel for which the cones defined at the "cone shaped channel" have the same angle for the "delrin vessel" and the "forward cone", among the already constructed vessels, and therefore a better symmetry in the charge profile could be expected from the parallelism of the walls of teh "cone shaped channel".

3.3 Simulation of the single Cone Generator vessel

In order to simulate the Cone Generator vessel it was decided that we would not simulate the light propagation and reflection through the optical fiber, diffuser ball and cone shaped channel, as simulations are usually done. This was decided given the complexity of the system that would need to have been simulated.

Instead of proceeding by the usual simulation method it was decided to use a data driven simulation, that is, we measure the photon flux emitted by the Cone Generator vessel using a dedicated experimental setup called "photon flux measurement setup" and then we use this measure to generate photons following the measured photon distribution. These photons are input to the SK detector simulation (skdetsim) that propagates each of them until they are either detected by the SK PMTs or absorbed. The Cone Generator simulation described here is shown inside the red box in figure 3.1.

3.3.1 The photon flux measurement setup

The goal of this setup is to measure the photon flux emitted by the Cone Generator, that is, to measure the distribution of direction and position of the photons emitted by the Cone Generator vessel at a given distance as shown in figure 3.5.

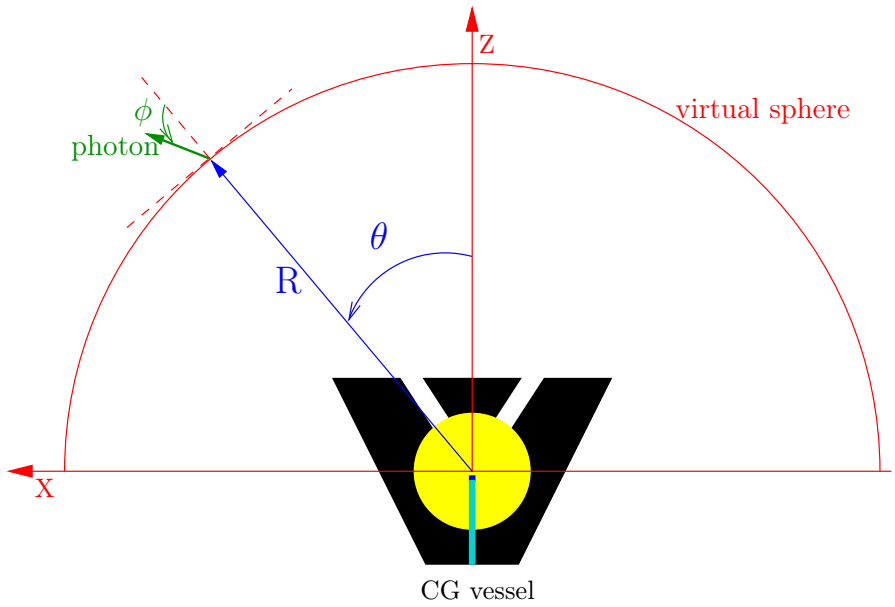

Figure 3.5: Scheme of the virtual sphere of radius R defined around the CG vessel (red). At each point of the virtual sphere (with position vector in blue) described by the angle θ we will measure the photon flux intensity at each photon direction (green) described by the angle ϕ. In the current "photon flux measurement setup" $R = 13$ cm, θ corresponds to the CGV angle and we assume the virtual sphere is symmetric by rotation around the Z axis, and ϕ corresponds to the (PMTV, PMTH) angles defined in the text.

The photon flux measurement setup was designed to measure the intensity of the photon flux at each position and direction from the Cone Generator vessel by placing a PMT mounted on a moving structure on top of the Cone Generator vessel and in between a collimator plate as is shown in the figure 3.6. The collimator hole in the plate placed on top of the Cone Generator vessel is used to define at which point of the virtual sphere we will measure the distribution of the photon direction. The position at which the photon flux is measured is changed by rotating the CG vessel while the direction at which the photons are measured is changed by rotating the PMT. The collimator hole was designed in a way that there is no reflection of light in its walls during the photon flux data taking. Dimensions of the photon flux measurement setup are given in figure 3.6.

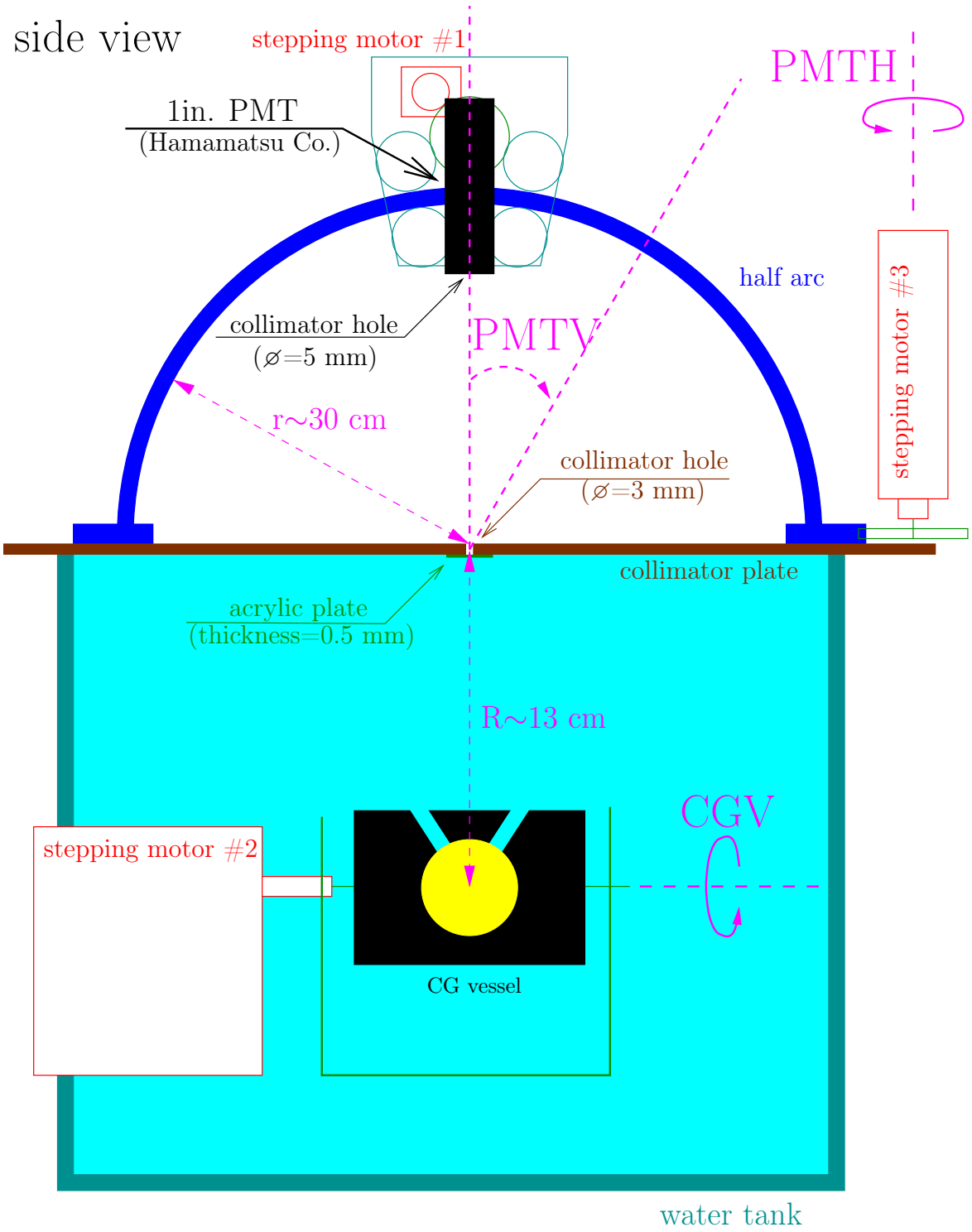

Figure 3.6: Side view of the "photon flux measurement setup". The CG vessel is inserted in a water tank, here shown filled with water. The CG vessel is connected to the stepping motor #2. The rotation of the CG vessel using this motor defines the "CGV" angle as shown. Above the CG vessel is a collimator plate with a collimator hole aligned between the CG vessel and the PMT at the top of the half arc, as shown. Via the rotation of the stepping motor #1 the PMT is moved along the half arc as shown by the "PMTV" angle. Finally, the half arc itself is rotated by using the stepping motor #3 around the vertical axis passing through the collimator hole in the collimator plane, as defined by the "PMTH" angle, here it is shown at the stepping motor axis.

The position in the virtual sphere at which data is taken is given by the angle "CGV", which corresponds to the θ angle in figure 3.5, where we suppose that the CG vessel and diffuser ball are symmetric by rotation around the Z axis. The direction at which data is taken is given by the angles "PMTV" and "PMTH", which correspond to the decomposition of the ϕ angle shown in figure 3.5 as the projection of the direction on the R vector ("PMTV") and the angle in respect to the plane perpendicular to the R vector direction ("PMTH").

3.3.2 Data taking with the photon flux setup

Each photon flux data taking consists of 2 different data sets that are measured at the same time. The so called "sequential data" is taken automatically by the DAQ changing the CGV angle within the given range using a fixed step size for each PMTV and PMTH, and then by changing automatically the PMTV angle within the given range and fixed step size. Each "sequential data" is taken at a fixed PMTH angle. Before and after each "sequential data" we measured the photon intensity at a given angle (CGV, PMTV, PMTH)=$(34°, 0°, 0°)$ to control the time variation of the measured laser intensity. This data set is called "stability data". The data set directly used to simulate the photon flux of the Cone Generator is the union of the "sequential data" for all PMTH in the given range and step.

The photon flux intensity is measured for each given angle (CGV, PMTV, PMTH) during "sequential data" taking by counting the number of ADC the PMT measured for 100 times the laser connected to the diffuser ball is turned on. The ADC distribution obtained is used to estimate the mean ADC value at the given angle which is proportional to the light intensity at the given angle once the ADC pedestal is subtracted. For example, the ADC distribution for (CGV, PMTV, PMTH)=$(34°, 0°, 0°)$ taken during "sequential data" taking is shown in figure 3.7. The same procedure is applied to measure the photon intensity of "stability data" however the ADC distribution is measured using 1000 pulses from the laser instead of 100 pulses as is the case for "sequential data".

Photon flux data were taken using the photon flux measurement setup at several different occasions listed in table 3.1 with the corresponding configuration used for the "sequential data" taking. The main advantages of each new data set in relation to the previous data set is a finer angle step for PMTV and PMTH to improve characterization of the photon flux for the August 2010 data set, a more stable light source for the January 2011 data set that greatly simplified the corrections needed to photon flux data from the time variation of the "stability data" and from the time variation of the pedestal value of the PMT used to measure the light intensity from the CG vessel. The change of the light source also simplified the setup needed for data taking because we no longer needed an optical table with a trigger PMT to measure when the laser emitted a light pulse at the reception of the signal from the clock[2], and because of this change the time required for taking data with the photon flux setup was reduced. Finally the main advantage of the May 2011 photon flux data taken in relation to previous data is the addition of the water tank to the photon flux measurement setup that allowed us to measure the photon flux of the Cone Generator when it is under water as it is the case when we insert the Cone Generator vessel in the Super Kamiokande tank. The water used to fill the water tank is the same water used to fill the SK tank. Note that the change in the range of the PMTV

[2]The "dye laser" did not always flash when there was a pulse from the clock, however the "laser diode" always flashes.

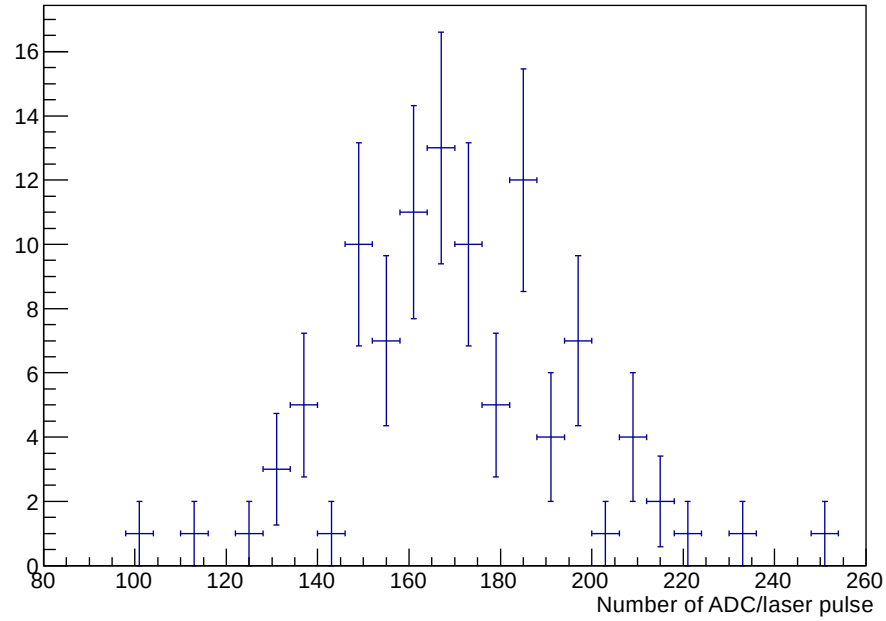

Figure 3.7: ADC distribution for angle (CGV, PMTV, PMTH)=(34°, 0°, 0°) taken during "sequential data" taking.

measurement for the May 2011 photon flux data is made in order to compensate the refraction of light at the surface of the water tank. If it is not explicitly stated otherwise the results presented here correspond to the last photon flux data we took in May 2011.

For the May 2011 photon flux data taking in addition to the usual "stability data" taken before and after each "sequential data" we also measured "stability data" in the day preceding our photon flux measurement and during the third day after we had finished taking "sequential data". This measurement was performed to evaluate the stability of the observed intensity of the laser in a longer period of time in order to be more sensitive to the degradation of the quality of the water stored in the "water tank" of the photon

Table 3.1: Summary of date and configuration at which we have taken "photon flux data". In the table are shown the range and step of the "CGV", "PMTV" and "PMTH" angles at which the data was taken following the format : minimum value → maximum value (step).

date	"sequential data" range (step) of			CG vessel in
	CGV	PMTV	PMTH	
09/2009*,†	0° → 70° (2°)	-27° → 27° (2.7°)	0° → 90° (30°)	air
07/2010*,†	0° → 66° (2°)	-27° → 27° (2.7°)	0° → 180° (30°)	air
08/2010†	0° → 66° (2°)	-18.9° → 18.9° (1.35°)	0° → 90° (10°)	air
01/2011	0° → 66° (2°)	-18.9° → 18.9° (1.35°)	0° → 90° (10°)	air
05/2011	0° → 66° (2°)	-24.3° → 24.3° (1.35°)	0° → 90° (10°)	water

* For these data sets, stability data was taken at CGV=30° and not CGV=34°.
† For these data sets, data was taken using an old laser source called "dye laser".

flux setup.

From geometrical considerations we do not expect to have any direct light from the cone generator vessel arriving at several (CGV, PMTV, PMTH) measured at the "sequential data". This is the case for example for CGV=66° and PMTV<0° for any PMTH, or for CGV=66° and PMTH≤60° for any PMTV. We have decided then to use data taken at these angles to evaluate the time fluctuation of the pedestal measurement during sequential data taking. The result from this measurement shown in figure 3.8 is that the pedestal value was constant during data taking with mean value of about 45.0 ADC counts.

Using the "stability data" it is evaluated the time dependence of the light intensity measured by the PMT during data taking. In this measurement it is taken into account both the time variation of the intensity emitted by the laser diode and the time variation of the water quality in the water tank. The result from this measurement shown in figure 3.9 is that the laser intensity was stable during all data taking and thus no time dependent laser intensity correction is needed.

The charge distribution measured from the photon flux data taking at PMTH 90° and 0° are shown in figures 3.10 and 3.11, respectively. These charge patterns are as expected from geometrical considerations :

- At the PMTH=90° configuration the CG and PMT move in the same plane, therefore a change in the PMT position is compensated by a change in the CG direction for the PMT to continue observing the same cone shaped channel from a different angle. From this argument it is expected a rather linear correlation between CGV and PMTV angles with charge changing by the difference in reflected and direct light flux intensities.

- Since the PMT rotates in the plane perpendicular to the CG movement when PMTH=0° and the CG vessel is symmetric in relation to the CG direction, we expect there is a PMTV symmetry in relation to PMTV=0°.

- Successive measures of the PMTV slices of PMTH=0° for at incresing CGV are expected to measure different cuts of the charge distribution relative to the CG direction, with the maximum light flux intensity when there is direct light from the CG arriving at the PMT, therefore creating a single spot centered around PMTV=0°. Above this region we do not expect any light to be observed given that the PMT would never be pointed towards the cone shaped channel of the Cone Generator vessel.

Even though the charge pattern shown on figure 3.11 is as expected it is observed that it is not symmetrical in relation to the PMTV=0°. This difference between the PMTV=0° and the center of symmetry of the charge distribution is due to a constant offset on the placement of the photomultiplier on the half-arc given by the sensor used to setting its position. It is thus necessary to correct the value of the PMTV angle by a constant offset by assuming that the charge distribution at PMTH=0° is symmetric and measuring its offset from data taken by changing PMTV while CGV and PMTH are constant. For this measurement we have used data taken with CGV=22° and PMTH=0° shown in figure 3.12 where the measured PMTV offset is given by $-0.9° \pm 0.1°$(syst) that is calculated by fitting a two Gaussian function given by (3.1) that is also shown in figure 3.12. The fitted parameters in (3.1) are a scaling constant (K), the width of the peaks (σ_{peak}) that is considered to be the same in both peaks, the position of the peak if

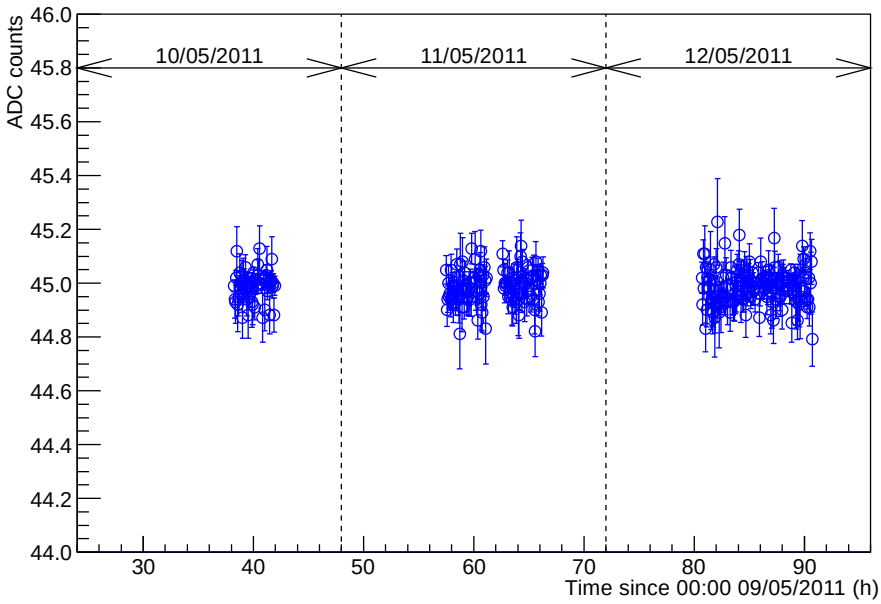

Figure 3.8: Time stability of the measurement of the PMT pedestal using "sequential data" for a (CGV, PMTV, PMTH) region where no direct light from the CG vessel is expected. The average pedestal value is about 45.0 ADC counts.

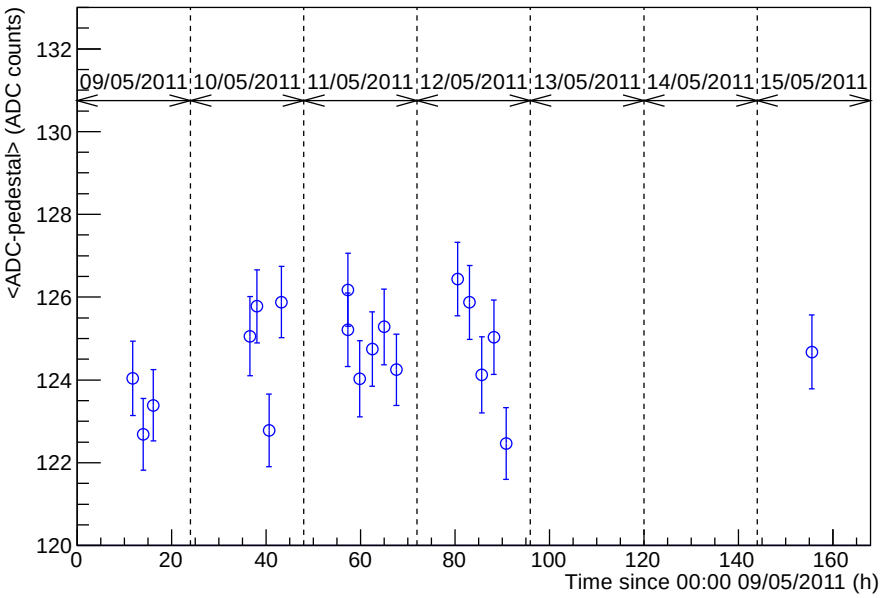

Figure 3.9: Number of ADC with constant pedestal subtracted for "stability data" in function of time. We only took "sequential data" on the 10, 11 and 12 May 2011, however we have left the laser diode turned on with water in the water tank for a longer time (one day before and three days after the "sequential measurements" were completed) in order to better estimate the time stability of the system. The average laser intensity for stability data is about 124.6 ADC counts.

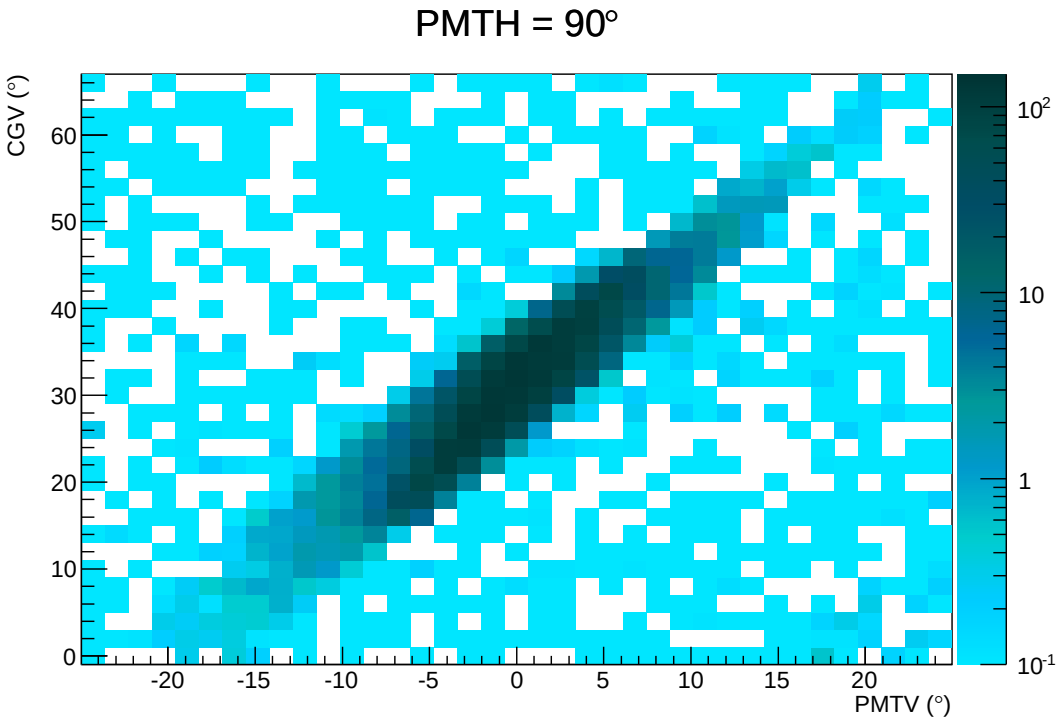

Figure 3.10: Number of ADC with pedestal subtracted measured in function of CGV and PMTV for PMTH=90°.

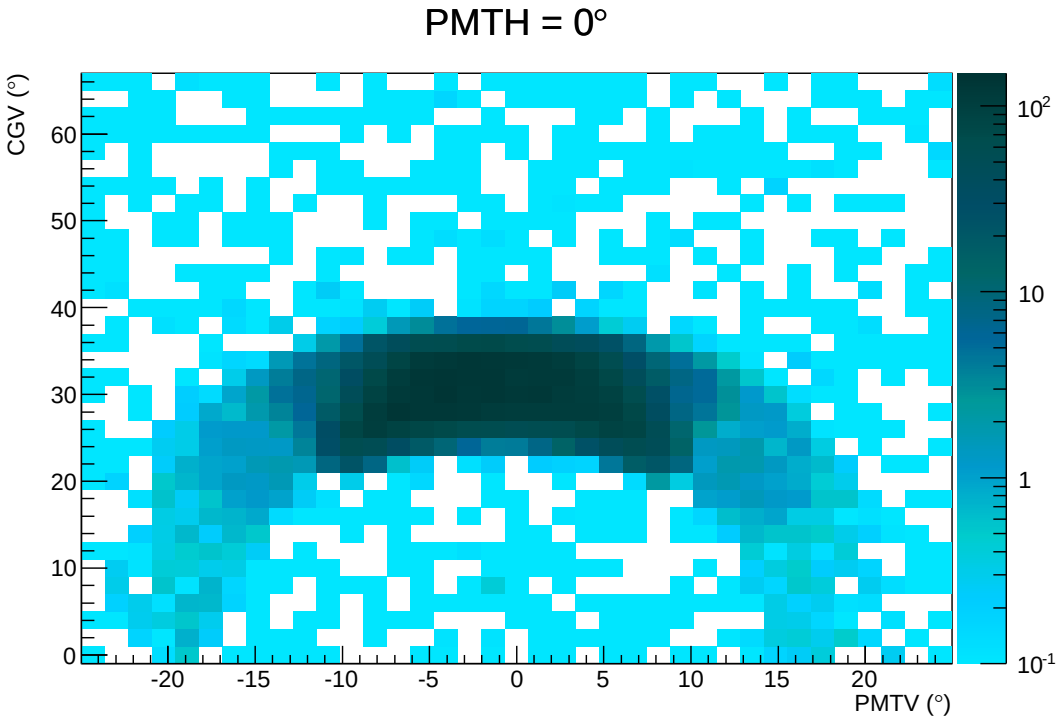

Figure 3.11: Number of ADC with pedestal subtracted measured in function of CGV and PMTV for PMTH=0°.

the peaks were symmetrical in relation to PMTV=0° (μ_{peak}) and the offset of this mean in relation to the PMTV=0° position (λ_{offset}).

$$K\left\{\exp\left[-\frac{1}{2}\left(\frac{PMTV-\mu_{\text{peak}}-\lambda_{\text{offset}}}{\sigma_{\text{peak}}}\right)^2\right]+\exp\left[-\frac{1}{2}\left(\frac{PMTV+\mu_{\text{peak}}-\lambda_{\text{offset}}}{\sigma_{\text{peak}}}\right)^2\right]\right\} \tag{3.1}$$

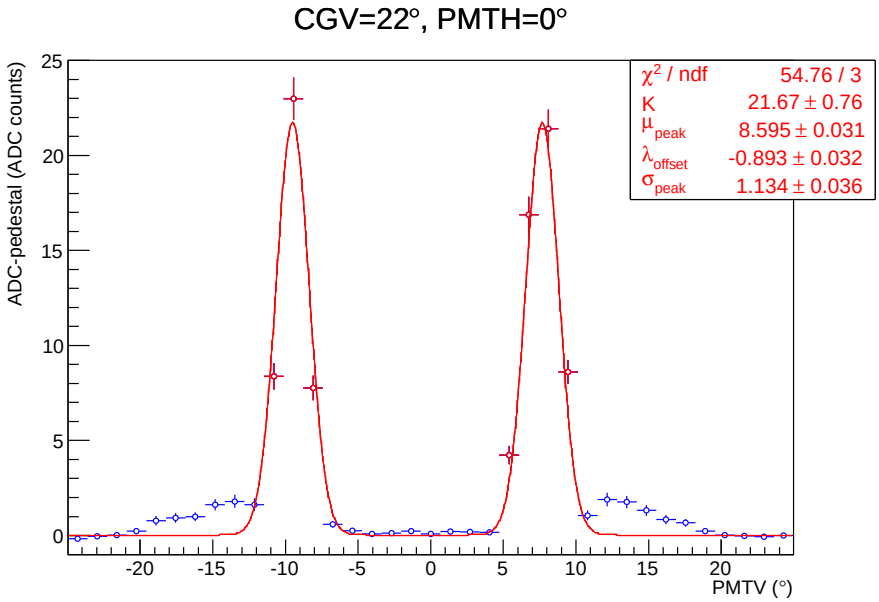

Figure 3.12: Number of ADC with pedestal subtracted measured in function of PMTV for PMTH=0° and CGV=22° (red and blue points). In red are shown the PMTV values for which we expect to measure mainly direct light from the CG vessel, while in blue are shown the remaining measured points. This distribution is used to calculate the PMTV offset by fitting equation (3.1) (red curve) using the points shown in red. The fitted parameters are shown on the top right of the figure with fit errors.

The systematic error on the PMTV offset was estimated using January 2011 photon flux data by applying the same procedure shown here for CGV=22° for other different CGV angle values and evaluating the standard deviation of these measurements from the average PMTV offset measured, which is shown in figure 3.13. It is not possible to reproduce this systematic error study done with January 2011 photon flux data using May 2011 photon flux data because there is not enough ADC counts at other values of CGV to reasonably fit (3.1) as the probability that light reflects at the wall of the cone shaped channel of the Cone Generator vessel is smaller when the Cone Generator vessel is under water than when it is in the air, which is due to the smaller difference between the refraction index of Delrin plastic and water than between Delrin plastic and air[3]. This estimation method is probably rather conservative, given that using direct light the number of ADC in the peak is much larger, therefore subject to less uncertainty, then at the angles where we fit the reflected light instead of the direct light. For the moment,

[3]This is explained by the Fresnel equations which will be described later on.

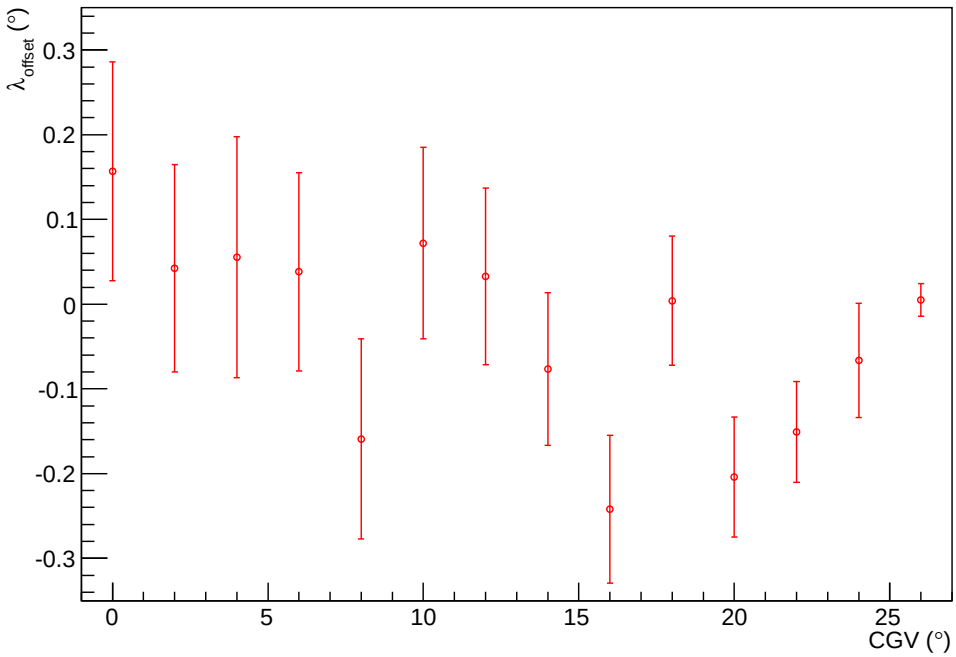

Figure 3.13: Value of λ_{offset} (see equation (3.1)) fitted using the PMTV distribution of ADC with pedestal subtracted for different values of CGV, with PMTH=0° always. Error bars show the fit uncertainty calculated by ROOT. These fits used photon flux data taken at January 2011, therefore the measured value of λ_{offset} is not required to be tha same between this data set and the May 2011 data set (usual data set used). The standard deviation of the fitted value of λ_{offset} of the above fits is of 0.113°±0.021°.

however we have not tried to further reduce this uncertainty given the need to improve the fitting function which is put in evidence by the poor reduced χ^2 value[4].

Furthermore, as the photon flux data is taken with water filled up to the collimator hole, where a thin acrylic layer is put to insure the water surface is flat, it is necessary to correct the measured photon intensity for each angle set to take into account the refraction of light between the water-acrylic and the acrylic-air surfaces.

The first effect that needs to be corrected is the difference between the angle the photon was emitted and measured, which changes due to the refraction in the interface between the air, the acrylic and water which is described by the Snell-Descartes law. This law links the incident angle of the photon ($PMTV_{\text{inc}}$) to the refraction index of the mediums and to the refracted angle ($PMTV_{\text{ref}}$) measured by the photon flux setup. The Snell-Descartes law used for this correction is given by the equation (3.2), where we note that the passage of the photon through the acrylic layer do not affect the relation between the angle of the photon in water in relation to the angle of the photon in the air.

$$PMTV_{\text{inc}} = \arcsin\left(\frac{n_{\text{water}}}{n_{\text{air}}}\sin PMTV_{\text{ref}}\right) \tag{3.2}$$

[4]If we try to increase the uncertainty of the ADC measurement to set the reduce χ^2 at 1, we automatically increase the fit uncertainty to 0.14°, which is also about 0.1°, showing the need to improve the fitted functions or fitting method.

The second effect that needs to be corrected is the difference in the refraction probability as a function of the angle at each surface. The refraction probability is described by the Fresnel equations, where the probability is described as a function of the photon polarization, incident angle and refraction coefficient of the mediums. For each angle we need to correct the observed photon flux intensity by how much light passed through the water-acrylic and acrylic-air interfaces. At each interface, for unpolarized light, the correction of the light intensity given by Fresnel equation is shown in equation (3.3), where I_b is the light intensity before the light reaches the surface, I_a is the light intensity after light goes through the surface, θ_i is the incident angle at the interface and θ_r is the refracted angle.

$$I_b = I_a \left(1 - \frac{1}{2}\left[\left(\frac{\sin(\theta_r - \theta_i)}{\sin(\theta_r + \theta_i)}\right)^2 + \left(\frac{\tan(\theta_r - \theta_i)}{\tan(\theta_r + \theta_i)}\right)^2\right]\right)^{-1} \tag{3.3}$$

At the acrylic-air interface, I_a is the light intensity measured by the PMT[5] and the θ_r angle is given by the measured PMTV (after PMTV offset correction). The θ_i is calculated from the θ_r and the refraction index of air and the acrylic via Snell-Descartes law. The intensity of light inside the acrylic, given by I_b, will be called I^{acr} and the incident angle θ_i will be called θ^{acr} for the next step of the corrections.

At the acrylic-water interface, I_a is the light intensity inside the acrylic layer given by I^{acr} previously calculated and the refracted angle θ_r is given by θ^{acr}. The incident angle θ_i is again calculated by the Snell-Descartes law. The light intensity inside the water I_b is what is considered to be the light intensity measured by the photon flux at a given angle after the all corrections.

After all the corrections described in this subsection are applied, the photon flux data is used to generate a photon distribution used as input for the SKDETSIM simulation that is described in the next subsection.

3.3.3 Using photon flux data to generate the photon distribution input for SKDETSIM

As explained previously, the photon flux data consists of the measurement of light intensity from the Cone Generator vessel at several different positions and directions given by (CGV, PMTV, PMTH). We should note that the photon flux data provides a relative measurement of the light intensity from the Cone Generator vessel, therefore the normalization in number of photons emitted by the CG per event needs to be done by tuning the total charge observed in the simulation the mean total charge of data taken at SK. This adjustment is performed to have better than 1% agreement between the mean total charge of data and Monte-Carlo.

The light intensity distribution from the Cone Generator as a function of the position and direction of the photon from the Cone Generator vessel is obtained by interpolating the photon flux data measured at several different positions and directions. The interpolated function is then normalized and transformed into a probability density function used as input for SKDETSIM.

From a technical point of view, in C++ libraries there are no routine that performs three-dimensional interpolations available, while one-dimensional and two-dimensional interpolations were available. Therefore we could not directly perform an interpolation

[5]The light intensity is given by the ADC - pedestal mean value.

in all photon flux data directly. We have decided to separately obtain a distribution of position of the photons and the distribution of the direction of the photons for each position. The distribution of the position of the photons was obtained by interpolating the photon flux data taken for different CGV, integrated for all PMTV and PMTH taking into account the solid angle each (PMTV, PMTH) set represent. The distribution of the direction of the photons for each position was obtained by interpolating the two-dimensional (PMTV, PMTH) distribution for the given position. We have also taken into account the difference in the solid angle represented by each (CGV, PMTV, PMTH) bin to correctly estimate the photon flux distribution.

3.3.4 Systematic errors on the Cone Generator simulations

Any uncertainty from the photon flux measurement or characteristic of the Cone Generator not implemented in SKDETSIM need to be taken into account as a systematic error on the Cone Generator simulation. For the moment we have taken into account as systematic error of the Cone Generator simulation the following errors :

1. Uncertainty on the mean pedestal value
2. Uncertainty on the constantness of the laser light intensity
3. Uncertainty in the measurement of the PMTV offset
4. Statistical uncertainty on the light intensity measurement
5. Difference between the total charge distribution at SK of data and Monte-Carlo

For the moment, we plan only to compare the shape of the charge distribution between single cone data and Monte-Carlo. More precisely, we will compare the charge distribution as function of the angle from CG direction, which allows a simple yet rather complete comparison between CG data and Monte-Carlo. This distribution is called "charge profile" for simplicity. Given that we perform currently only comparisons of the charge profile between data and Monte-Carlo we will need to estimate the effect of given systematic error directly at the charge profile. For the single cone Monte-Carlo charge profile these errors are usually taken into account by calculating how much the value of the charge in one bin changes in a simulation made assuming the parameter for which the systematic error is estimated changed by $\pm 1\sigma$. This method naturally produces asymmetric error bars related to the positive and negative fluctuations of the parameter.

1. Uncertainty on the mean pedestal value

The effect of the fluctuation of the pedestal on a measurement by measurement basis is taken into account when evaluating the uncertainty on the mean number of ADC counts for each (CGV, PMTV, PMTH) (see item 4), so we need in this item to take into account only the uncertainty on the mean pedestal value that is 44.997 ± 0.024 ADC counts. The effect of this fluctuation in the charge profile is shown in figure 3.14 and is within 2% in the peak region.

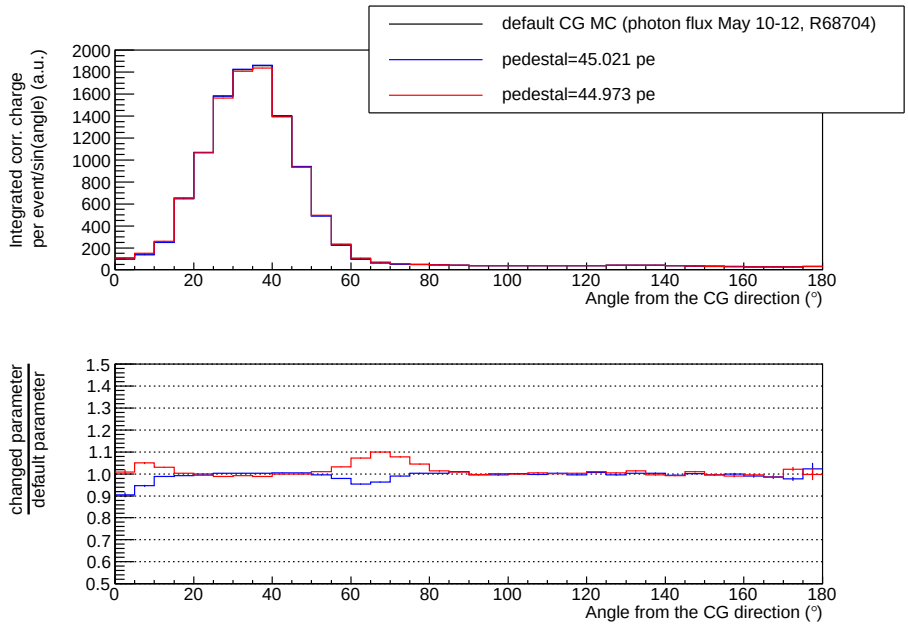

Figure 3.14: Effect of uncertainty of mean pedestal value of photon flux data for the single cone charge profile. In the top is shown the charge profile for the default single cone Monte-Carlo (black) as well as the $+1\sigma$ (blue) and -1σ (red) fluctuations of the pedestal. In the bottom is shown the ratio between the blue (or red) and black charge profiles to better estimate the uncertainty on the charge profile shape.

2. Uncertainty on the constantness of the laser light intensity

As discussed, the observed laser intensity was assumed to be constant during the data taking. In order to evaluate the effect of this hypothesis in the charge profile we have compared with the case of a linear time dependency of the observed light intensity fitted to the charge variation of the "stability data" shown in figure 3.9. The effect of the fluctuation in the charge profile is shown in figure 3.15 and is well within 1% at the peak region.

3. Uncertainty in the measurement of the PMTV offset

As discussed, there is an uncertainty on the measurement of the PMTV offset angle. The effect of this uncertainty in the charge profile is shown in figure 3.16 and is within 5% at the peak region.

4. Statistical uncertainty on the light intensity measurement

Differently from taking into account the fluctuation of the total charge from an uncertainty that changed the measured photon flux at each angle setting at the same time, we want here to evaluate the uncertainty on the charge profile due to statistical fluctuations of the measured mean ADC count used to measure the light intensity. We have generated several different samples of photon flux data by changing randomly the mean ADC value measured within it's uncertainty, assuming Gaussian errors. For the current study, 40 different random fluctuations of the photon flux data were used.

The effect of the fluctuations in the charge profile is shown in figure 3.17 for the first

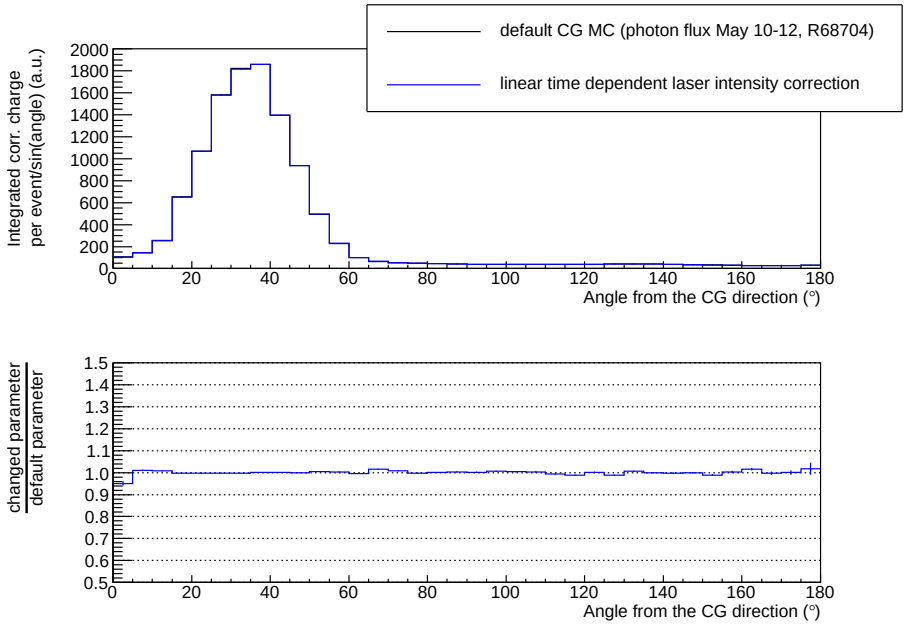

Figure 3.15: Effect of difference between applying no time dependent correction (black) and a linear time dependent correction (blue) using stability data on photon flux data at for the single cone charge profile. In the top is shown the charge profile and in the bottom is shown the ratio between the blue and black charge profiles to better estimate the uncertainty on the charge profile shape.

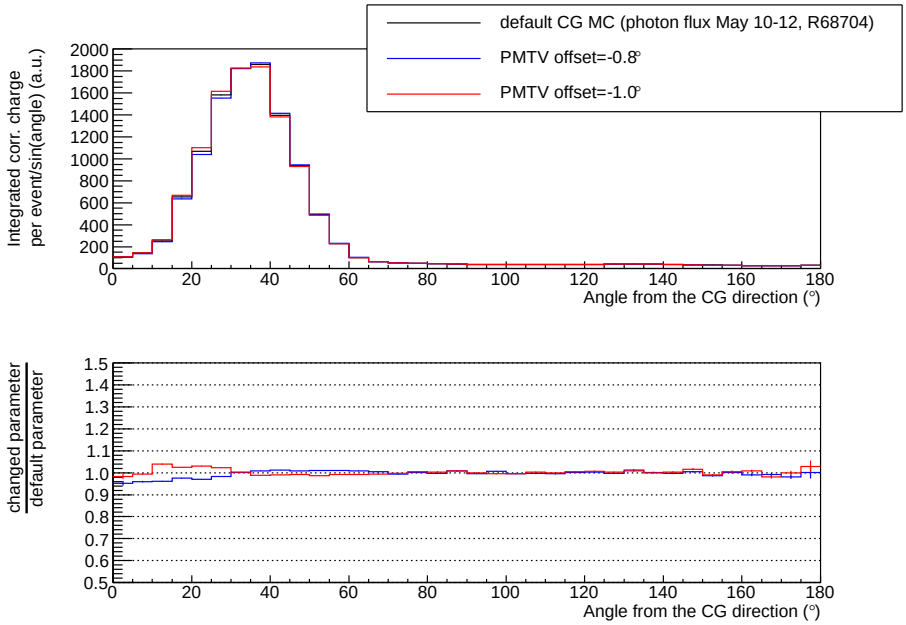

Figure 3.16: Effect of uncertainty of the PMTV offset of the photon flux data at for the single cone charge profile. In the top is shown the charge profile for the default single cone Monte-Carlo (black) as well as the $+1\sigma$ (blue) and -1σ (red) fluctuations of the PMTV offset. In the bottom is shown the ratio between the blue (or red) and black charge profiles to better estimate the uncertainty on the charge profile shape.

two different random fluctuations. The bin by bin higher and lower edges of the charge profile from this uncertainty is shown in figure 3.18. It is within 2% in the peak region and is below 5% between 5° and 150°.

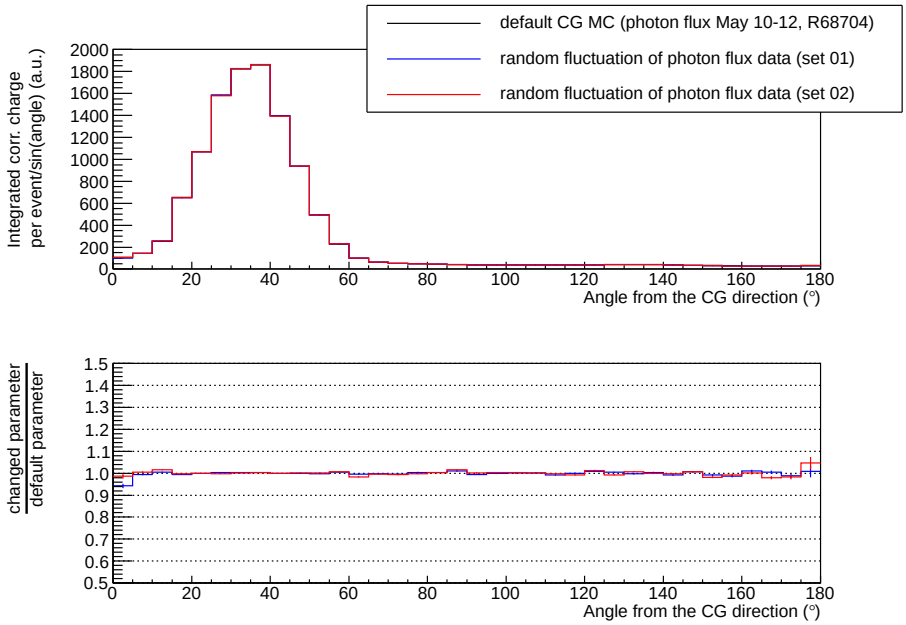

Figure 3.17: Effect of uncertainty of photon flux data in the single cone charge profile shown for two random variations of the photon flux data within the measurement errors. In the top is shown the charge profile for the default single cone Monte-Carlo (black) as well as two random fluctuations in blue and red. In the bottom is shown the ratio between the blue (or red) and black charge profiles to better estimate the uncertainty on the charge profile shape.

5. Difference between the total charge distribution at SK of data and Monte-Carlo

Note the uncertainty described here is not related to the photon flux itself, but rather to how the Cone Generator was implemented in SKDETSIM.

To perform the CG simulation in SKDETSIM we simulate a fixed number of photons per event, however in real data taking the number of photons emitted by the laser reaching the diffuser ball can fluctuate on an event by event basis. The pulse by pulse fluctuation of the emitted light intensity is also the cause of the uncertainty in the constantness of the laser light intensity (item 2, previously mentioned). However the uncertainty mentioned on item 2 has effect of changing the relative shape of the photon flux data, while the uncertainty taken into account in this item is related to the effect of the total charge global fluctuation in the charge profile.

When using the dye laser, these fluctuations were large and thus it was imperative to evaluate the effect on the charge profile by comparing the usual charge profile with charge profiles simulated with the mean total charge at the edges of the mean total charge distribution. However since we have now changed the light source to a laser diode which has a stable emitted light intensity the difference between the total charge distribution of Monte-Carlo and data is small, as shown in figure 3.19, and we no longer take this

error source into account. We have decided to neglect such effect when using laser diode because the effect of such uncertainty in the charge profile was already small when we took data using dye laser.

For reference the effect of the difference of mean total charge in an event in the charge profile to take into account the fluctuation of the total charge of the dye laser (see figure 3.20 for the total charge fluctuation of data and at which total charges Monte-Carlo were generated) is shown in figure 3.21 and is within a few percent at the peak region and of about 10% at the tail region.

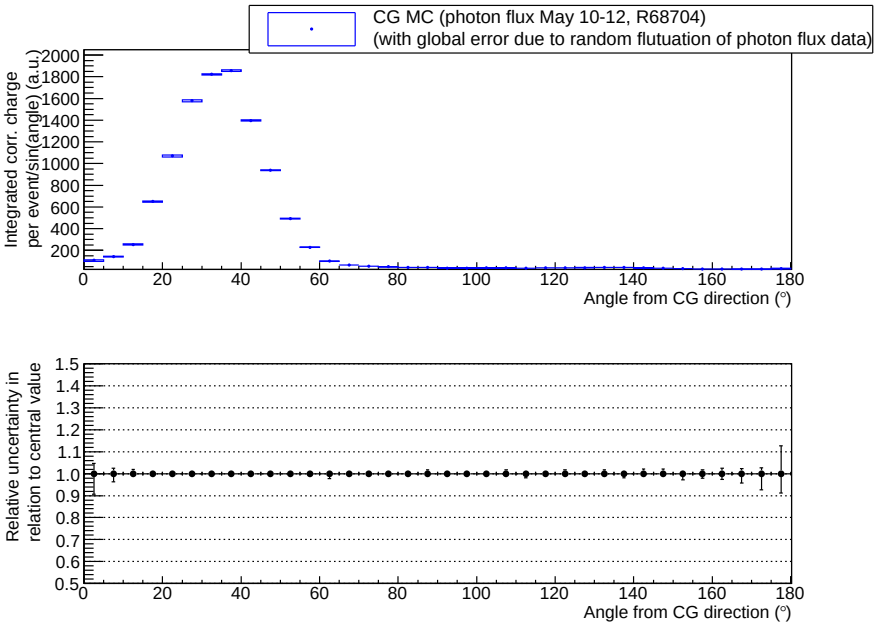

Figure 3.18: Effect of uncertainty of photon flux data in the single cone charge profile. The envelope shown takes into account 40 different sets of random variations of the photon flux data within the measurement errors. In the top is shown estimated uncertainties on the charge profile for the single cone Monte-Carlo by blue boxes. In the bottom is shown the ratio between the estimated uncertainties shown by the boxes in relation to the default single cone Monte-Carlo.

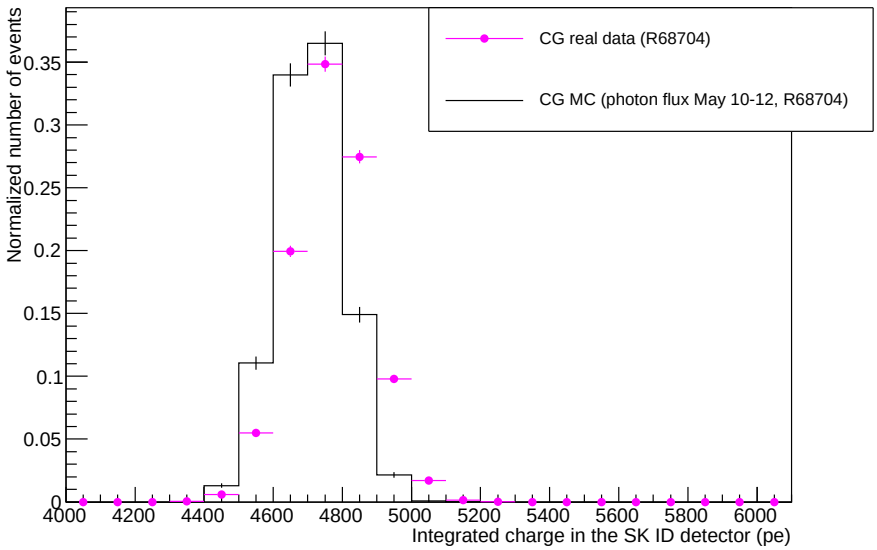

Figure 3.19: Distribution of the total charge measured in the SK detector per event for single cone data (magenta) and MC (black). The MC has been tuned to have mean total charge within 1% of the data mean total charge.

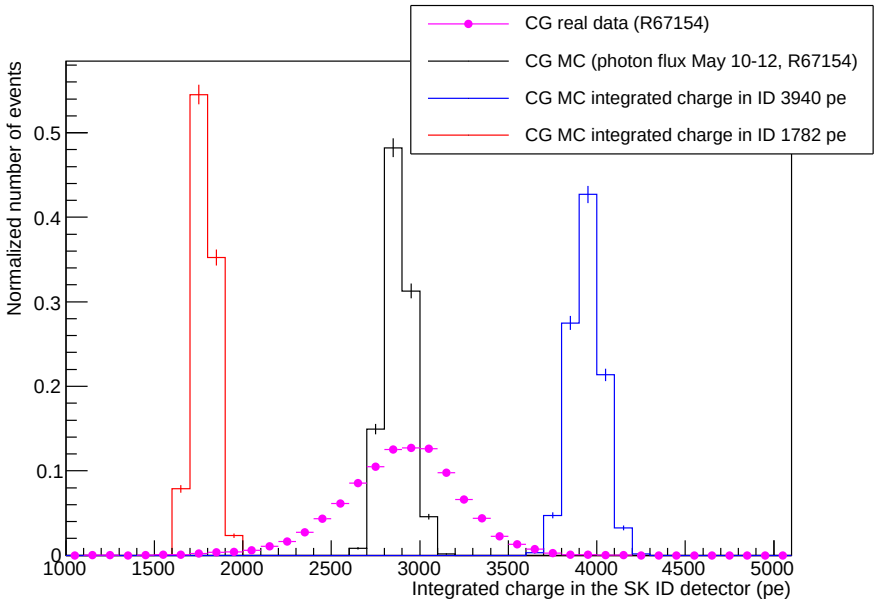

Figure 3.20: Distribution of the total charge measured in the SK detector per event for single cone data from 2010 using dye laser (magenta) and default MC for that data set (black). The default MC has been tuned to have mean total charge within 1% of the data mean total charge. Furthermore are shown two other single cone MC which have been tuned to be at the high and low tail of the data distribution to evaluate the effect of a fluctuation in the total charge in the charge profile.

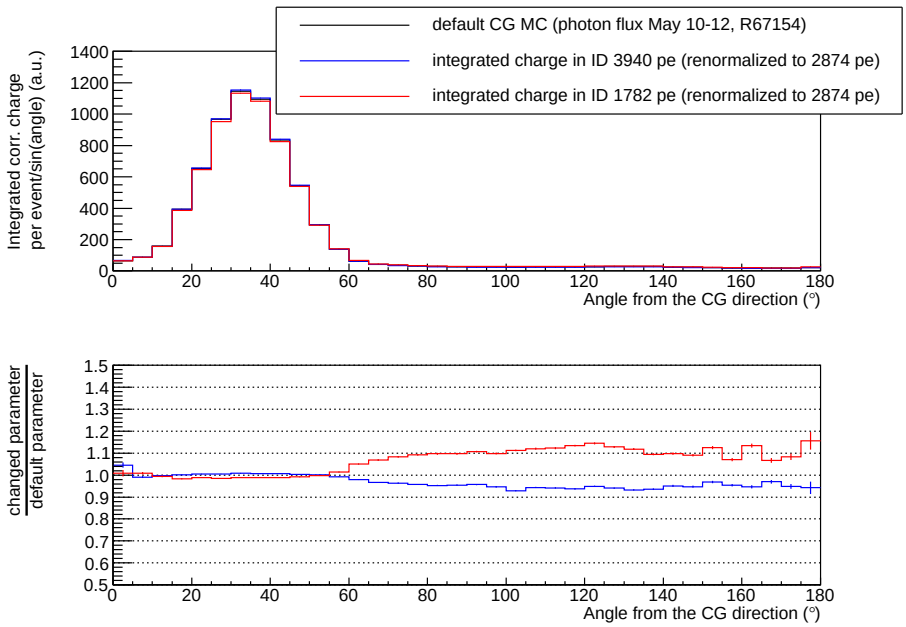

Figure 3.21: Effect of change of the mean total charge observed in the detector tuned for the single cone Monte-Carlo for 2010 data (black) and both lower (red) and upper (blue) fluctuations of the total observed charge as shown in figure 3.20. In the top is shown the charge profile for the default single cone and in the bottom is shown the ratio between the blue (or red) and black charge profiles to better estimate the uncertainty on the charge profile shape.

3.4 Data taking in the Super Kamiokande detector

In order to take data in Super Kamiokande using the single Cone Generator vessel, a pole system is used to place the Cone Generator vessel at the desired position and direction inside the Super Kamiokande detector. The pole system is composed by 10 separate poles of 2 meters each which allow the placement of the Cone Generator vessel to set 10 different Z positions inside the detector separated by 2 meters from one another. The lowest position we can place the Cone Generator vessel is near the center of the detector in the vertical direction (that is Z=0 m in SK coordinates). At the end of the pole system, the Cone Generator vessel is screwed to a horizontal plate. It is also possible to screw a second Cone Generator vessel to the bottom of this horizontal plate even though no data was taken using this configuration. Below this plate in a U-shaped structure is placed the "Locator vessel" below the pole system. In figure 3.22 is shown the end of the pole system with the Cone Generator vessel and the "Locator vessel" installed. In figure 3.23 is shown the scheme of the electronics and trigger used during "single cone data taking" and "Locator data taking".

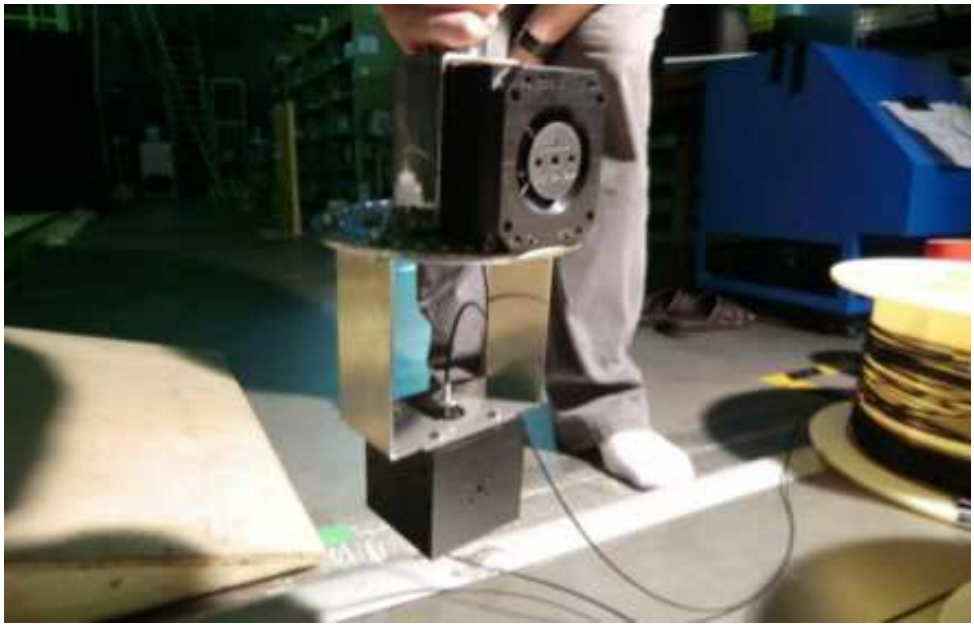

Figure 3.22: Picture of the equipment used to lower the CG vessel and Locator vessel into SK. The poles from the pole system are connected on top of the "U" shaped metal plate covering the CG vessel sides. This "U" shaped metal plate is screwed to the disk, which itself is screwed both to the CG vessel and to the lower part of the disk, lower "U" shaped metal plate, to which the Locator is screwed. This picture was taken before inserting the CG for the 2011 data taking at SK.

The "Locator vessel" used for "Locator data taking" is a delrin vessel similar to the Cone Generator vessel, however instead of having a cone shaped opening for the light from the diffuser ball it has five cylindrical holes at the four horizontal walls of the vessel and at the bottom of the vessel. Data taken using this vessel is used to measure the position and direction of the Cone Generator vessel inside the Super Kamiokande detector.

3.4.1 Summary of single Cone Generator data taking

In table 3.2 is shown a summary of the single cone data taking from June 2011 that will be used here. Even though more single cone data was taken in June 2011, its analysis has not been completed yet. The data presented here consists of the single cone data taken for verification of the stability of the measurement, which was performed by taking twice or thrice data at the same condition (with the cone pointing towards the $+y$ direction in the SK detector coordinates). In addition to the verification runs we also list a run at $Z = 0$ m towards $-y$ direction (which is close to the T2K beam direction) which will be used to compare to single cone Monte-Carlo.

Table 3.2: Summary table of the 2011 SK single cone data taking that are used in the current analysis. The vertex and directions are given in SK detector coordinates (where Z is the vertical direction). During the CG data taking we have only rotated the pole system without removing and reinserting it from the "first" and "fifth" CG data taken for all vertexes.

Run of single cone data	Run of Locator data	vertex Z (m)	expected direction	
68674	68676	8	$+Y$	first CG data taken at this vertex
68690	68692	8	$+Y$	fifth CG data taken at this vertex
68739	68741	8	$+Y$	extra CG data taken at this vertex after removing and reinserting CG vessel
68696	68698	0	$+Y$	first CG data taken at this vertex
68712	68714	0	$+Y$	fifth CG data taken at this vertex
68704	68706	0	$-Y$	for use in comparison with CG MC
68718	68720	16	$+Y$	first CG data taken at this vertex
68734	68736	16	$+Y$	fifth CG data taken at this vertex

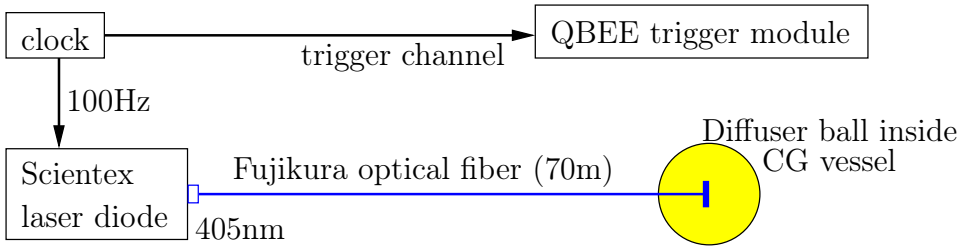

Figure 3.23: Scheme of the data taking setup used to flash the laser for the CG or Locator vessels (here is only shown the diffuser ball) and the SK trigger module (QBEE trigger module). Once the laser is flashed the light emitted by the diffuser ball will be collected at the SK PMTs which have already been triggered by the QBEE trigger module.

3.4.2 Measurement of the Cone Generator vessel position and direction in SK

The pole system was designed to be able to precisely place the vessel inside the SK detector. However, it is necessary to measure the position and direction of the Cone Generator in the SK tank. We have performed such measurement using "Locator data" that was taken using an independent device, called Locator, from the Cone Generator vessel.

The Locator is constructed similarly to the Cone Generator, being composed of a "Locator vessel" inside of which is placed a diffuser ball connected to the laser via an optical fiber. The "Locator vessel" is a cubic delrin vessel with holes at the center of each face, the optical fiber leaving the "Locator vessel" by the hole situated in the top face of the cube. Therefore, in SK the Locator generates 4 laser spots in the barrel of the tank and one spot at the bottom of the tank as shown in figure 3.24. By measuring the center of each spot in the barrel and assuming that the two lines drawn from the center of opposite spots cross at the position of the "Locator vessel", as shown on figure 3.25, we can determine the position of the Locator and then of the Cone Generator given that the relative position between the CG vessel and the Locator vessel is known.

For the moment we do not use the information of the timing distribution to measure the position and direction of the "Locator vessel" because we consider the current method gives sufficient precision.

Furthermore the Z coordinate of the "Locator vessel" position is well determined by the pole system itself : if there is a $\sim$ 1 m shift of the "Locator vessel" in the XY plane the corresponding shift in the Z position[6] would be $\sim$ 3 cm, on the other hand we expect and have measured the shift in the XY plane from the expected position to be less than 15 cm. Due to this we will not use "Locator data" to determine the Z position of the "Locator vessel" and consequently of the "Cone Generator vessel".

We have calculated the center of each spot in the "Locator data" taken in run 68676 and the distribution of each Locator spot is shown on figure 3.26 where we have fitted a Gaussian to the peak of each distribution to obtain the parameters shown on table 3.3.

Using the measured mean for each spot we have calculated the position of the Locator by the crossing point of the line $\overline{L_{+x}L_{-x}}$ and $\overline{L_{+y}L_{-y}}$. In order to estimate the systematic error caused from the estimation of the position of the Locator we have generated several samples of "Locator simulation" from different positions and directions and compared the difference between the calculated and inputed position and direction. The so called "Locator simulation" consists of simulating four Gaussian spots in the barrel and one Gaussian spot in the bottom of the SK detector where the light emitted to generate all spots has the same vertex and 90° between one spot and it's neighbour spot.

The "Locator simulation" used to estimate systematic error of the reconstruction method is set to have the same vertex as the expected Locator position near the center of the tank just below the calibration hole used to insert the CG vessel, that is at $(35, -70, 0)$ cm in the SK coordinate system, and with the L_{+x} direction the same as the $+X$ direction. Each parameter of the simulation is then modified separately to perform this study which defines four different samples :

- the X position of the Locator was changed from -1 cm to 59 cm with 3 cm step;

[6]This shift was calculated assuming the connection between poles of the pole system is rigid, which even though is not exactly true is a reasonable approximation of the pole system used.

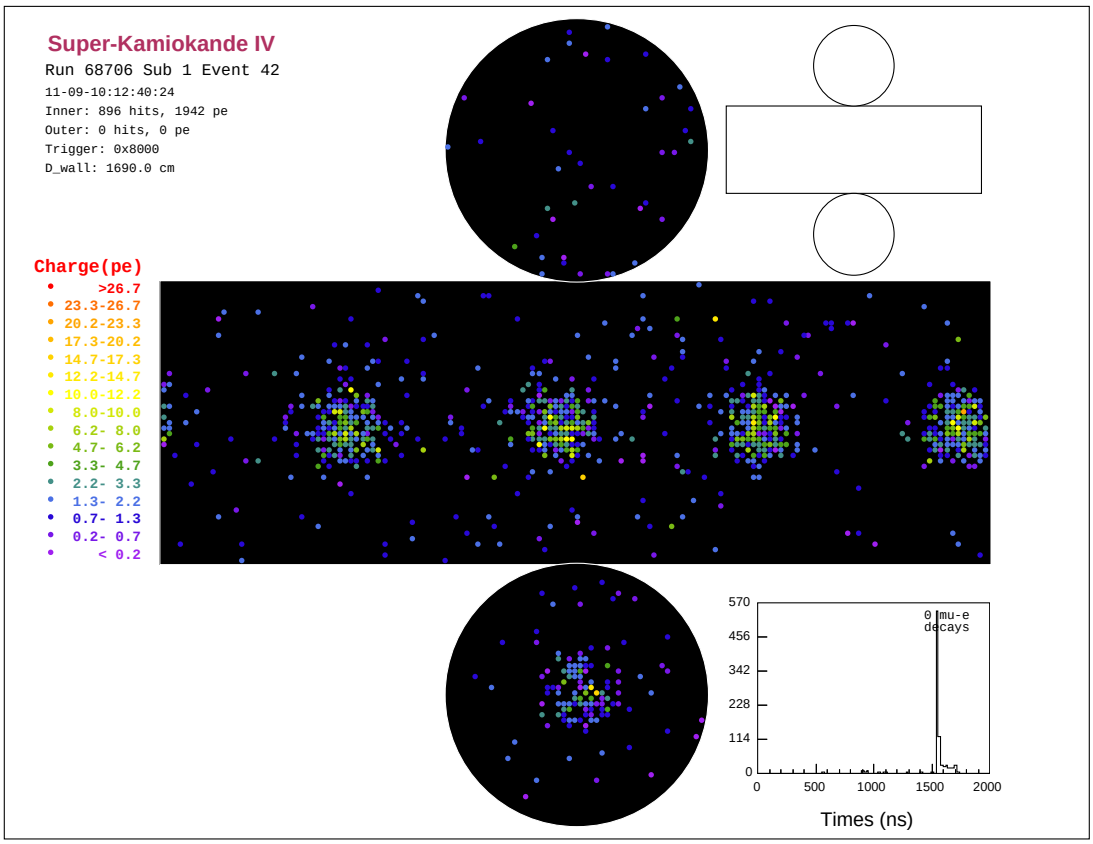

Figure 3.24: Event display of a Locator event.

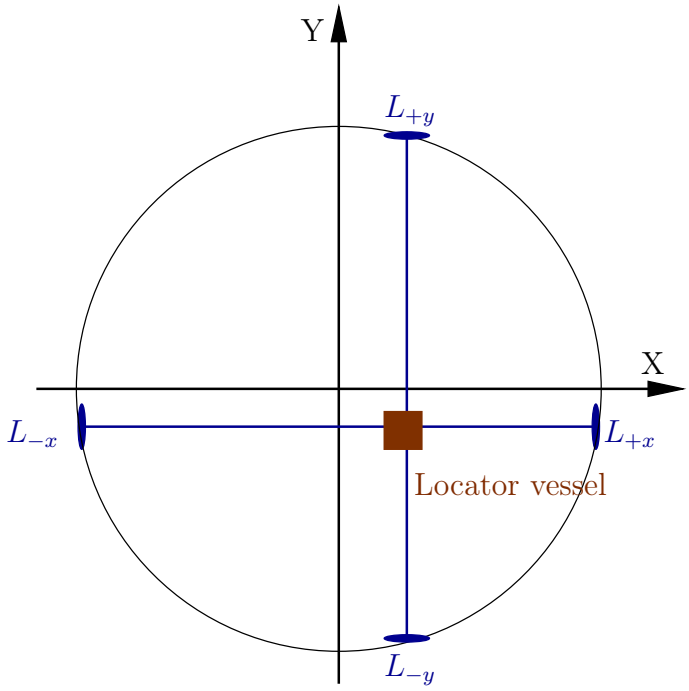

Figure 3.25: Schema of the Locator vessel data taking with the four spots produced in the side of the SK tank represented and identified. Note that this schema is not in scale.

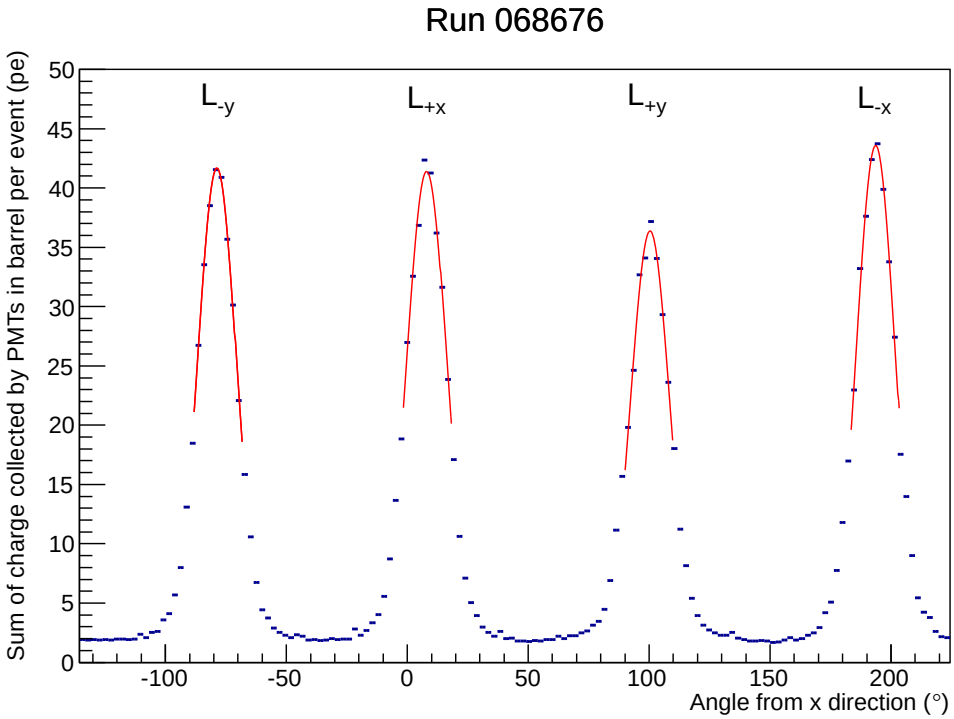

Figure 3.26: Distribution of the integrated charge on a column of PMTs on the SK barrel in function of the angle of the PMTs from the x direction measured from the center of the SK tank for run 68676. Each spot shown in the figure 3.25 is identified here. In red are shown the fit made to the peak of each spot to measure their center. We fitted a Gaussian to each spot peak to avoid having to take into account the effects of scattering in the water of the SK tank, reflection at the SK tank wall and dark noise of SK PMTs.

Table 3.3: Fit results used to obtain the center of each Locator spot that is shown in figure 3.26. The uncertainties quoted are given by the fitting procedure and therefore could be underestimated given the quality of the fits shown in figure 3.26.

Name	Constant (pe)	Mean (°)	Sigma (°)
L_{+x}	38.052±0.031	-1.865±0.009	8.638±0.015
L_{+y}	30.838±0.028	89.667±0.010	9.023±0.018
L_{-x}	35.729±0.029	183.247±0.008	8.933±0.013
L_{-y}	35.849±0.031	-88.305±0.008	8.011±0.013

- the Y position of the Locator was changed from -114 cm to 54 cm with 3 cm step;
- the Z position of the Locator was changed between 0 cm, ±3 cm, 8 cm, 16 cm, 8 m, 16 m;
- the angle between the Locator direction of the L_{+x} spot and the X direction was changed between -20° and 20° with 1° step and at ±25° and ±30°.

The comparison between expected and calculated X and Y position from the Locator and the direction of the Locator obtained using these different parameters of "Locator simulation" are shown on figures 3.27, 3.28 and 3.29, respectively. From these estimations, we have taken the systematic error from Locator data analysis near the position where the "Locator vessel" was placed. It is 6 cm in the X position, 8 cm in the Y position and 0.16° in the measured angle from the X direction. The values quoted are probably slightly overestimated, however since we generated "Locator simulation" by changing at each simulation only one of the parameters from the default value we could have not taken into account effects coming from the correlation of the errors in the vertex and direction of the Locator. The same logic could explain the bias observed in all distributions, and further studies would be needed to precisely determine if this reconstruction bias is due to geometrical considerations that would correlate all these parameters, or if the bias is due to other effects.

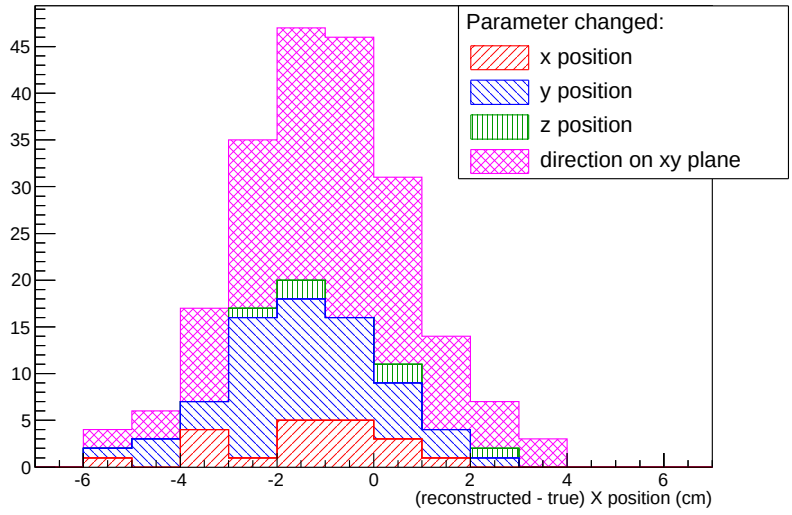

Figure 3.27: Systematic error calculated for the measured X position of the Locator with the Locator simulation. The different stacked histograms show different sets of Locator simulation where either the X position (red), Y position (blue) or Z position (green) or the angle between the Locator and the X direction (magenta) was changed. These histograms are added on top of each other to better show the global shape and limits of all data sets at the same time. The systematic error on the X position is ±6 cm.

The result from the measurement of the position and direction of the Locator taking into account the estimated systematic errors for runs presented in table 3.2 is shown in table 3.4.

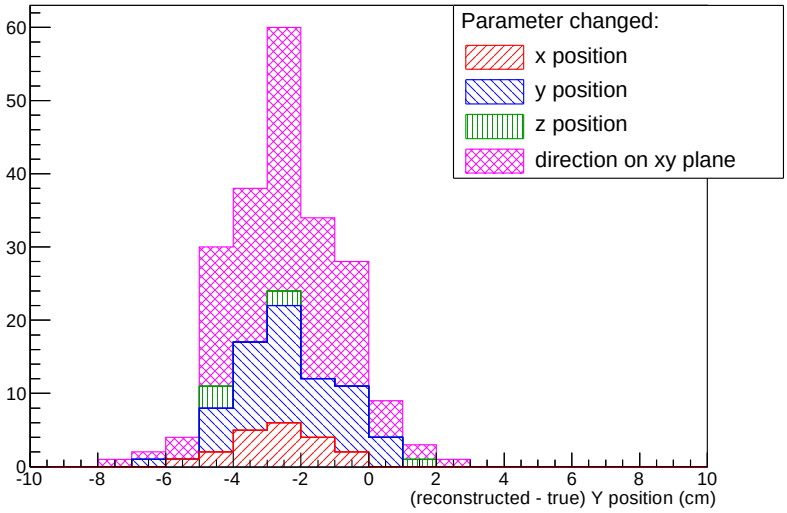

Figure 3.28: Systematic error calculated for the measured Y position of the Locator with the Locator simulation. The different stacked histograms show different sets of Locator simulation where either the X position (red), Y position (blue) or Z position (green) or the angle between the Locator and the X direction (magenta) was changed. These histograms are added on top of each other to better show the global shape and limits of all data sets at the same time. The systematic error on the Y position is ±8 cm.

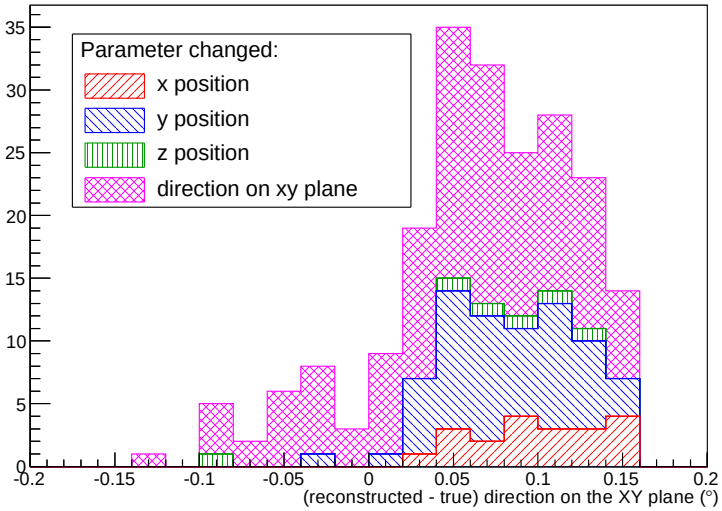

Figure 3.29: Systematic error calculated for the measured XY direction of the Locator with the Locator simulation. The different stacked histograms show different sets of Locator simulation where either the X position (red), Y position (blue) or Z position (green) or the angle between the Locator and the X direction (magenta) was changed. These histograms are added on top of each other to better show the global shape and limits of all data sets at the same time. The systematic error on the direction measurement is ±0.16°.

Table 3.4: Measured position and direction of the Locator vessel using the Locator data corresponding to the studied single cone data runs. The position and direction of the CG are obtained from the position and direction of the Locator through measurements of the experimental apparatus geometry made before inserting it inside the SK tank.

Run of single cone data	Run of Locator data	(X,Y) vertex measured with Locator data (cm)	angle between the Locator spots expected and measured position (°)
68674	68676	(31±6,-75±8)	0.77±0.16
68690	68692	(28±6,-76±8)	1.43±0.16
68639	68741	(31±6,-76±8)	0.85±0.16
68696	68698	(26±6,-70±8)	10.71±0.16
68712	68714	(24±6,-67±8)	11.70±0.16
68704	68706	(29±6,-79±8)	10.86±0.16
68718	68720	(33±6,-68±8)	-3.82±0.16
68734	68736	(31±6,-68±8)	-3.19±0.16

From "Locator data" analysis we can already notice that for data that were taken at the same conditions, supposedly, we obtain consistent measures for their positions. For the runs that have been taken at the same nominal direction the angle from the +X direction is within 1° from each other, which is the precision of the tool used to set the direction of the pole system at the top of the calibration hole. Note that even though the angle measured with different runs with same nominal angle was compatible within 1° with each other, this does not imply that the measured angle is within 1° of the expected direction.

3.5 Comparison of single cone data and Monte-Carlo

We use the charge profile at SK to compare single cone data and Monte-Carlo simulation. The charge profile is expected to be peaked at about 33° which is the opening angle from the Cone Generator vessel. The distribution of the light in the SK detector depends on several different effects depending on the angle from the Cone Generator direction : near the peak of light and in the forward region most of the light comes directly from the Cone Generator vessel, while for angles larger than 90° the signal is due to either reflected or scattered light.

Because we do not know the absolute number of photons in the SK tank from our experimental setup we need to adjust the total number of photons generated per event in the simulation so that the mean value of the total detected charge is the same for data and Monte-Carlo, as it is shown in figure 3.19 for run 68704.

3.5.1 First comparison between single cone data and Monte-Carlo

The first charge profile comparison between data and Monte-Carlo is shown in figure 3.30 done by September 2011. From this comparison we obtain that for angle below 60° the agreement between single cone data and Monte-Carlo was within systematical error (of about 5% in the peak region). However, at the backward region the disagreement between

data and Monte-Carlo was of about 50%.

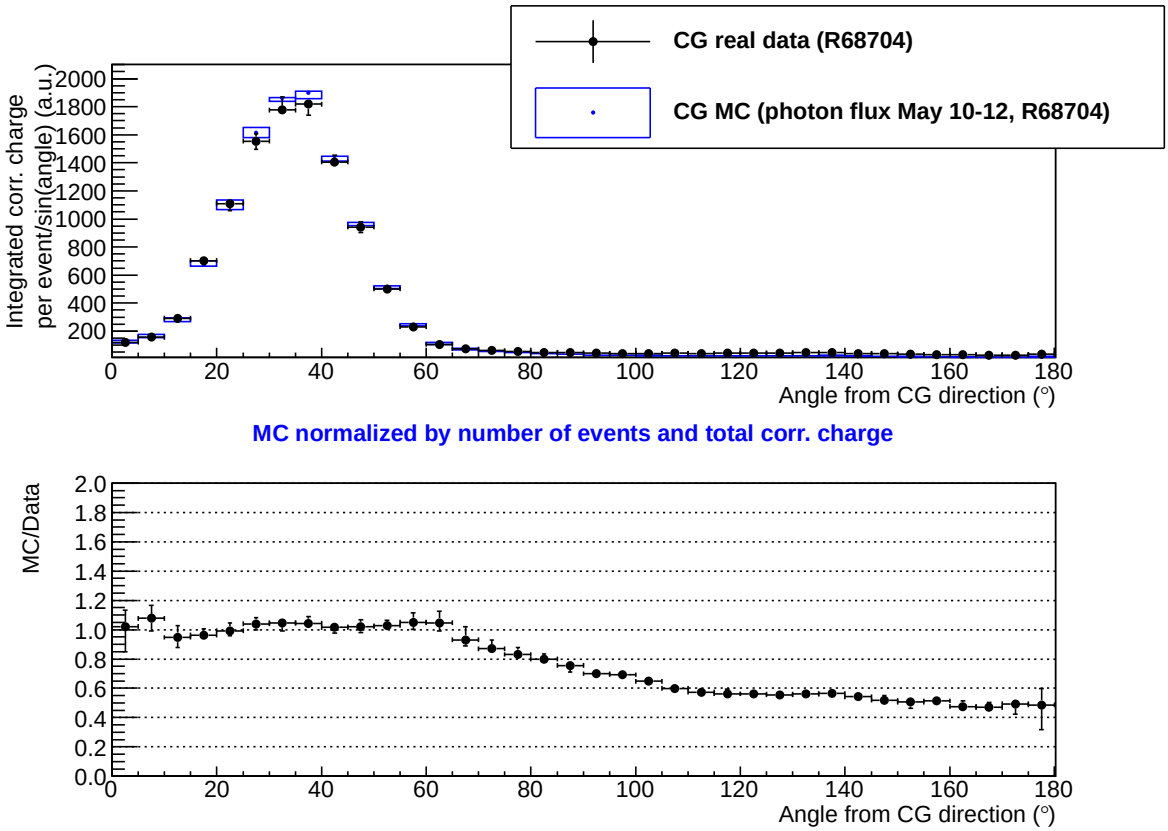

Figure 3.30: First comparison between data (black) and Monte-Carlo (blue) single cone charge profile, taking into account the estimated systematic errors. The single cone Monte-Carlo total charge per event is tuned to the total charge per event of the CG real data. In the top is shown the charge profile and in the bottom is shown the ratio between the Monte-Carlo charge profile to the data charge profile for better comparison of the relative shapes.

In order to understand the reason of the difference observed in the backward region, we have compared the hit timing distribution for data and Monte-Carlo of hits at the backward region from the direction of the Cone Generator as shown in figure 3.31. In the data we observe light originated from scattering and from reflection, however in Monte-Carlo, at the backward region, the intensity of scattered light is roughly null.

From this comparison we conclude there is a problem in the simulation of the scattering in SKDETSIM. In order to evaluate whether the Monte-Carlo calculation of the angular distribution of the Rayleigh scattering (Rayleigh scattering is the main component of scattering at Super Kamiokande, and in addition, is also the component of scattering that should produce charge in the backward region) was correct we have decided that we would draw the distribution of the Rayleigh-scattered photon angle with respect to the original photon direction. This is shown in figure 3.32. As it is shown there is no scattered light generated with opening angle larger than 90° from the Cone Generator direction, which is incorrect as the angular dependency of Rayleigh scattering is proportional to $(1 + cos^2\theta)$ for unpolarized light. This angular dependency is symmetric between the backward and forward region. Based on this observation we have found a bug in the

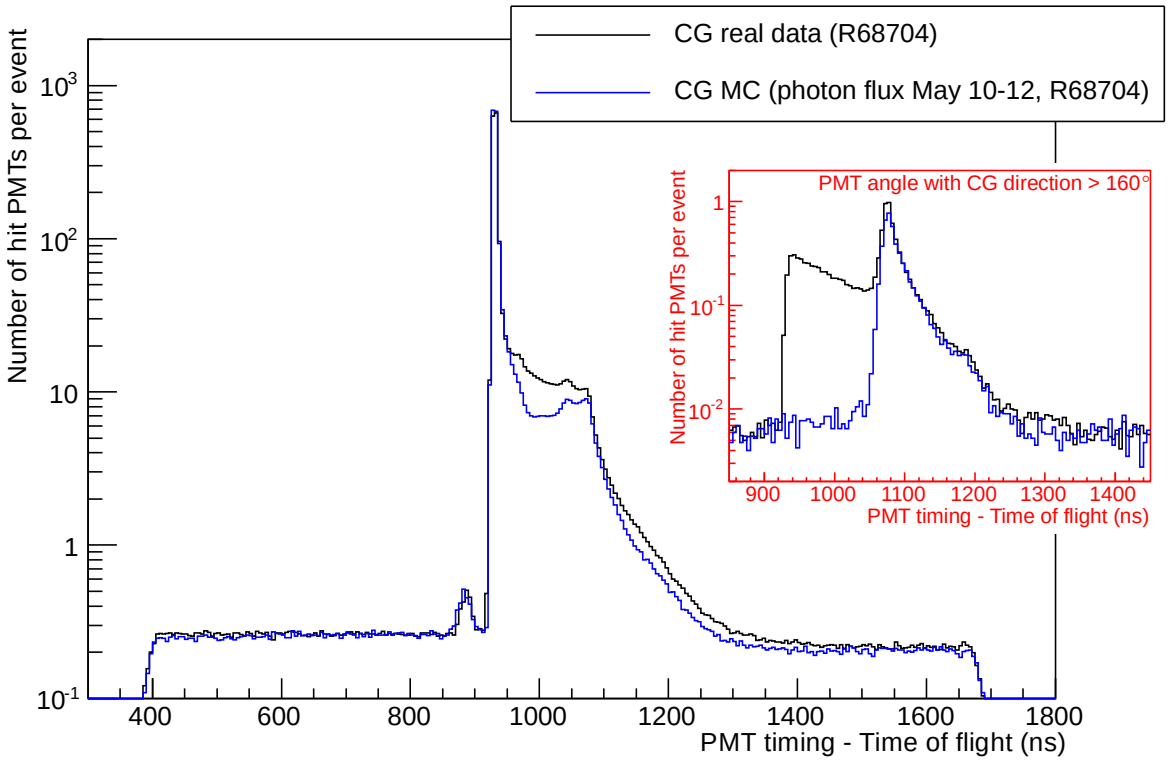

Figure 3.31: Distribution of the hit time recorded for each hit PMT subtracted by the time of flight corresponding to direct light for single cone data (black) and Monte Carlo (blue). The single cone Monte-Carlo and data used here are the same as used for figure 3.30 for all possible angles from the CG direction in the main plot, or for angles from CG direction larger than 160° in the red chart. The peak around 950 ns corresponds to the direct light peak for barrel PMTs, and as is shown in the red chart in the single cone Monte-Carlo there is no increase in the number of hits observed near the direct light peak, which would be associated with the scattering that typically follows after the direct light region. Such increase is however seen on data and expected from Rayleigh scattering. On the other hand a peak associated with reflected light (around 1080 ns) is still present and compatible between single cone data and Monte-Carlo even in the backward region.

calculation of the scattered angle in SKDETSIM. After correcting this bug the distribution of the Rayleigh-scattered photon angle with respect to the original photon direction is now symmetric, as shown in figure 3.33. It is important to notice though that the bug that was found affects only the unpolarized light scattering and that for polarized light the Rayleigh scattering angular dependency was already correctly calculated as shown in figure 3.34. The effect of this bug on physics results from SK will be discussed at section 3.6.

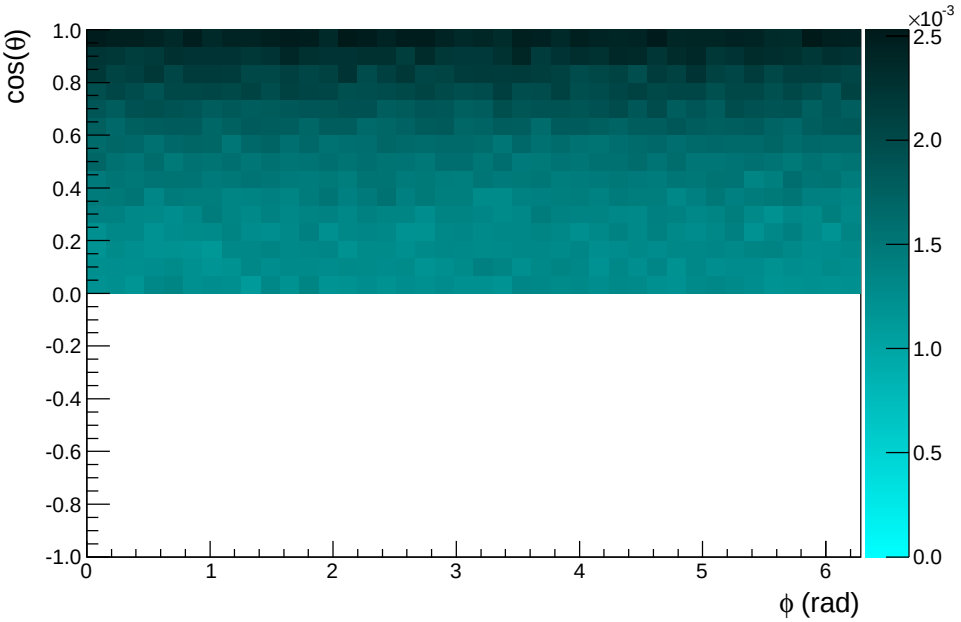

Figure 3.32: Distribution of the direction of Rayleigh-scattered photons from the original photon direction as calculated by SKDETSIM for unpolarized photons. This distribution was obtain using the same SKDETSIM version used to generate the single cone Monte-Carlo shown in figure 3.30, and as is shown there is no photons generated in the backward region from Rayleigh scattering, which should happen as often as photons generated in the forward region.

3.5.2 Comparison between single cone data and Monte-Carlo after Rayleigh scattering angular distribution bug fix

After the bug in Rayleigh scattering calculation was fixed we have performed again the charge profile comparison as previously. This is shown in figure 3.35. There is still a difference of about 10% for angles above 70°.

As shown on the timing distributions in figure 3.36 the Monte-Carlo and data distributions at this moment have the same shape in the backward region, therefore the correction of the bug found in SKDETSIM is sufficient to create as much scattered light in the backward region as the observed difference between data and MC shown in figure 3.31. Currently there is a small difference between the size of the reflected light peak between single cone data and Monte-Carlo, as shown in figure 3.36 at about 1080 ns which could help explain the 10% difference of the observed charge in the backward region shown

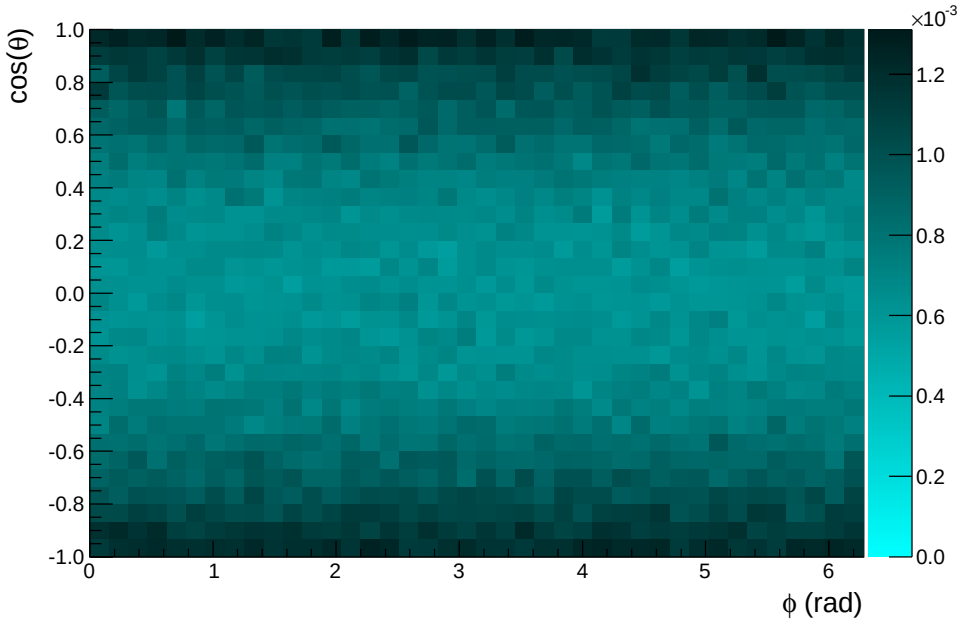

Figure 3.33: Distribution of the direction of Rayleigh-scattered photons from the original photon direction as calculated by SKDETSIM for unpolarized photons. This distribution was obtain using the same SKDETSIM version used to generate the single cone Monte-Carlo shown in figure 3.35, that is with the observed bug in Rayleigh scattering corrected.

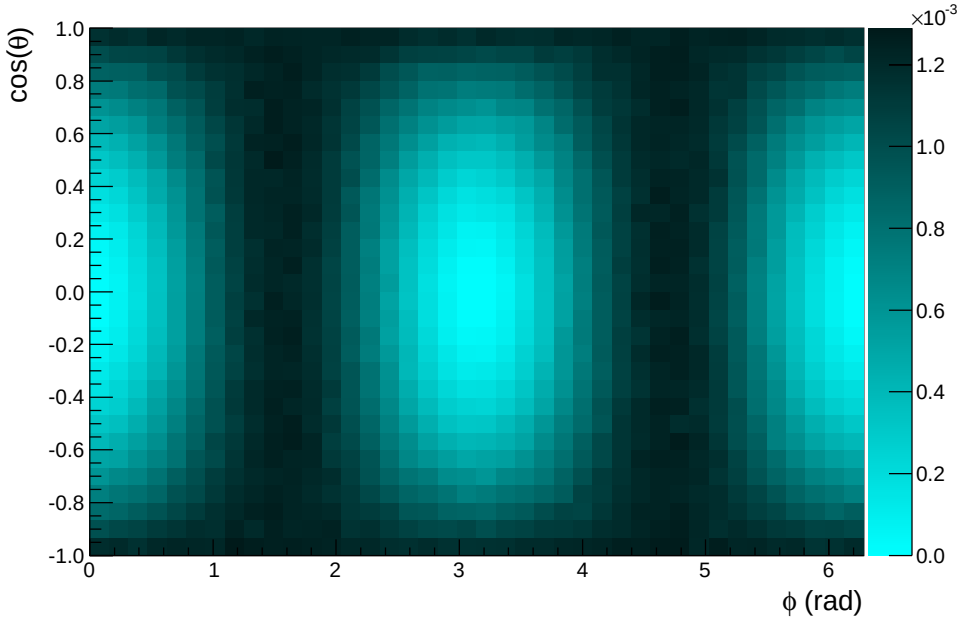

Figure 3.34: Distribution of the direction of Rayleigh-scattered photons from the original photon direction as calculated by SKDETSIM for polarized photons. This part of SKDETSIM is not affected by the bug or its correction, and its distribution is as expected.

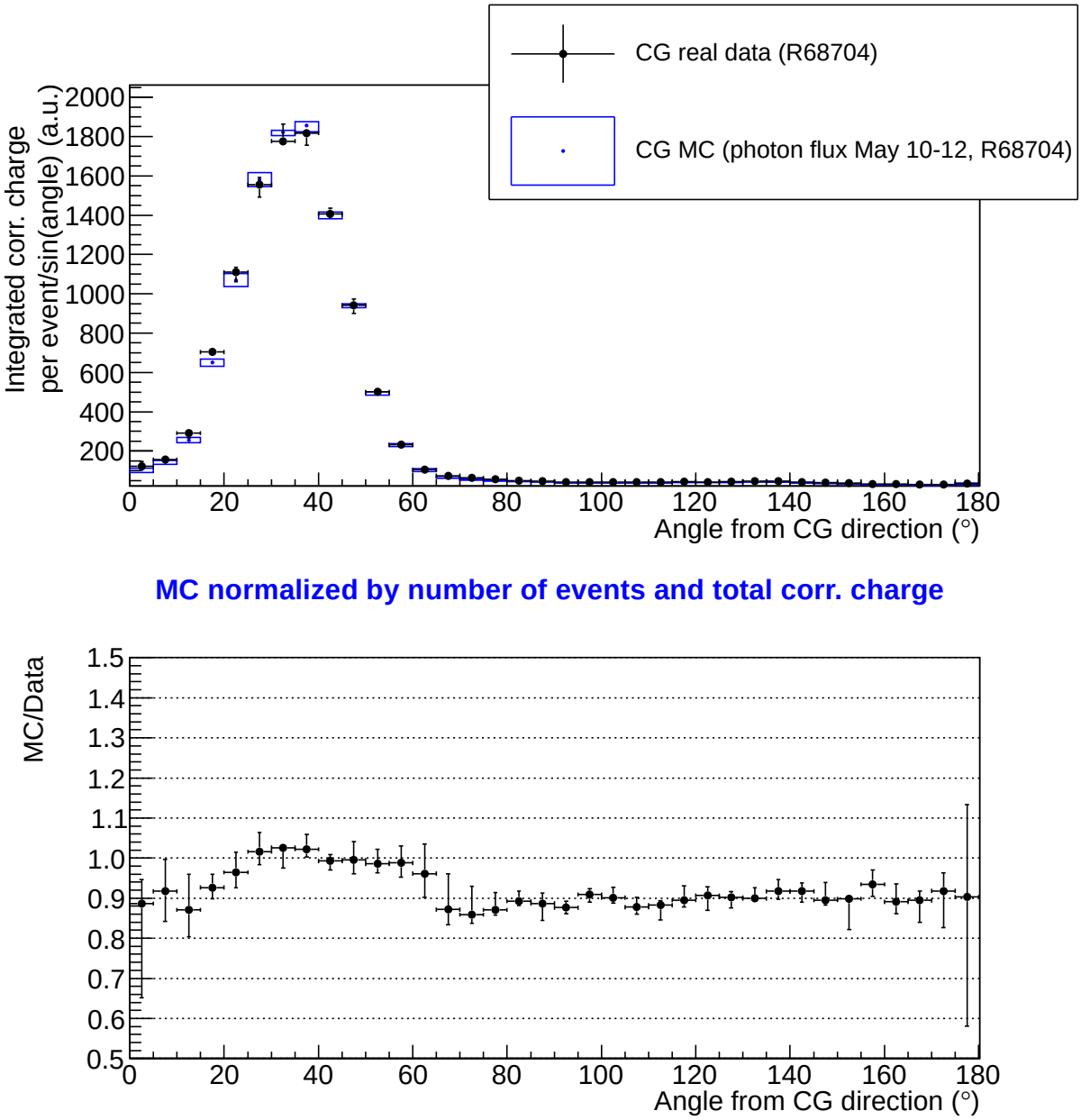

Figure 3.35: Comparison between data (black) and Monte-Carlo (blue) single cone charge profile, taking into account the estimated systematic errors and the correction to the scattering bug in SKDETSIM. The single cone Monte-Carlo total charge per event is tuned to the total charge per event of the CG real data. In the top is shown the charge profile and in the bottom is shown the ratio between the Monte-Carlo charge profile to the data charge profile for better comparison of the relative shapes.

in figure 3.35, however no studies have been done at the moment to understand these differences.

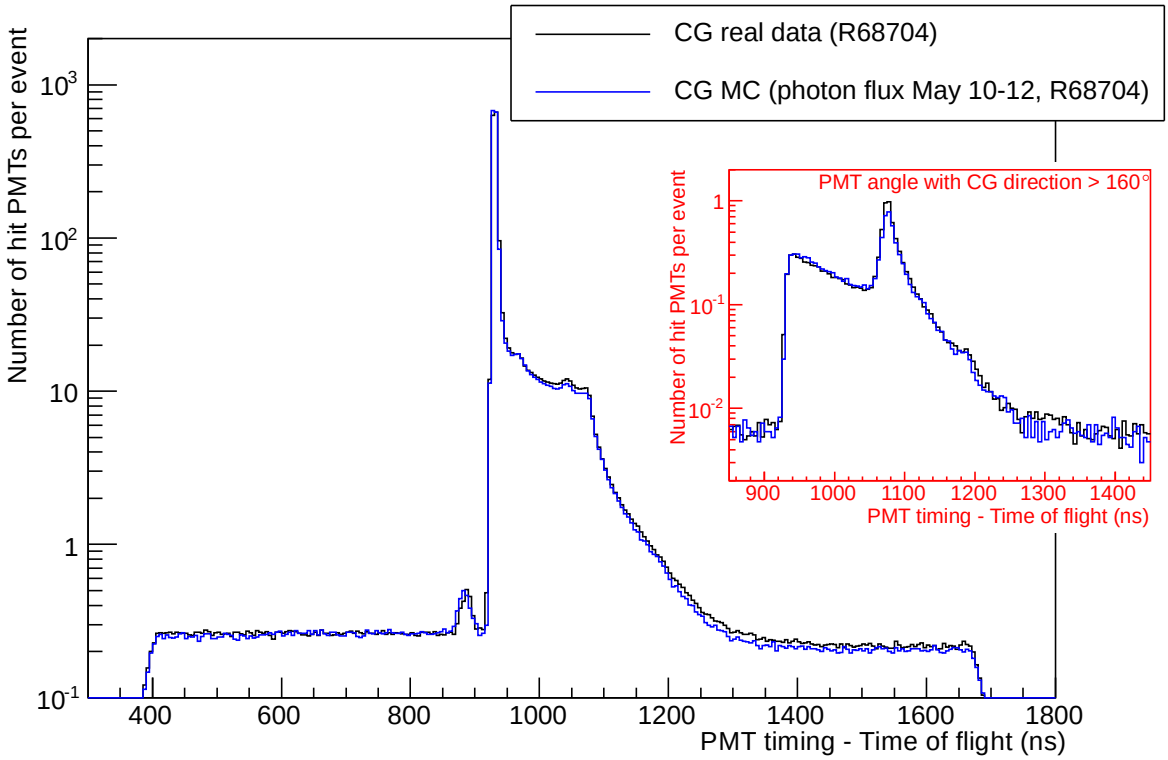

Figure 3.36: Distribution of the hit time recorded for each hit PMT subtracted by the time of flight corresponding to direct light for single cone data (black) and Monte Carlo (blue). The single cone Monte-Carlo and data used here are the same as used for figure 3.35 for all possible angles from the CG direction in the main plot, or for angles from CG direction larger than 160° in the red chart. The peak around 950 ns corresponds to the direct light peak for barrel PMTs and the peak around 1080 ns corresponds to the reflected light. The difference in the number of hit PMTs between data and Monte-Carlo shown either for any CG direction or for the backward region do not shown any large differences between single cone data and Monte-Carlo.

The difference in the reflection peak is to be expected because there has not yet been a retuning of the reflectivity of the black sheet and PMT, and because these tunings were made to a Monte-Carlo with the reported bug on the Rayleigh scattering angular distribution, they are slightly incorrect. From this retuning we expect that the reflection coefficient at the PMT and black sheet will increase which is in the same sense as the observed difference between single cone data and Monte-Carlo. Preliminary studies show that an increase of 10% in the reflection coefficients of the Monte-Carlo increase the observed charge in the backward region by 5%, without any significant change in the peak region.

Furthermore, one extra verification was made by changing how we deal with polarization of photons in the CG Monte-Carlo to produce photons that are individually polarized, but whose global polarization is not existent. This condition is certainly closer to the physical reality, though statistically both treatments should yield the same result.

The verifications performed have shown a perfect compatibility between both methods after the bug on the polarization calculation was corrected.

3.5.3 Reproducibility check of single cone data taking

During the 2011 single cone data taking we have decided to take single cone data with direction $+Y$ twice at each Z position and one extra measurement at the end of the data taking with the same Z position used for the first data taking (Z=8 m). The purpose of taking this data was to verify the reproducibility of our experimental setup and data analysis, for example by comparing the single cone charge profile of different data we can verify if the systematic error assigned on the single cone charge profile shape due to the uncertainty of Locator data analysis is enough to explain the difference between the two data sets or if there is still some other source of error that was not taken into account at the single cone data taking.

The comparison between data at the same position and direction show agreement of the charge profiles within systematic error from the measure of the position and direction as shown in figures 3.37, 3.38 and 3.39, for the positions Z=0 m, 8 m and 16 m respectively. The large differences, specially in the tail region, between different data sets are mainly due to PMTs that migrated to other bins in the charge profile from the slight difference in position and direction measured with Locator data for each data set.

At Z=8 m we have taken data also at the end of all data taking which is shown in figure 3.40. This last measurement was done to validate that the process of removing and inserting the pole system did not change the charge profile. Because we have decided to disconnect the optical fiber every time we changed the Z position of the Cone Generator vessel to simplify the procedure to insert and remove the CG from the SK tank we cannot directly compare the total charge from the first and last runs. It could be expected a slight change on the shape of the charge profile due to the difference in the total charge, however from Monte-Carlo study previously presented the change in the charge distribution due to the change in the total charge is expected to be small.

3.6 Effect of bug in scattering in results from SK

The effect of the bug found in SKDETSIM on the usual analysis at SK has also been checked to evaluate how it would change the current physics results from the experiment using the Super Kamiokande detector.

Before evaluating the effect of the Rayleigh scattering angular dependency bug in physics results it is useful to understand what it affects. As we have previously described the bug in the Rayleigh scattering angular distribution only affected unpolarized light, however as Cerenkov light is polarized perpendicularly to the Cerenkov cone direction it is not affected by this bug. In the same manner when light scatters the SK detector simulation calculates the new polarization of the scattered light and this light is not affected also by this bug. However, when light reflects at either the PMT or the black-sheet, because the reflection is not modeled simply as a specular reflection but as a mixture of specular and diffuse reflection the reflected light do not carry any polarization information and thus its scattering is affected by the bug.

In summary the effect of this bug fix in the distribution of the charge in the Super Kamiokande detector should be small as it only affects light that would be scattered after being reflected at the detector wall.

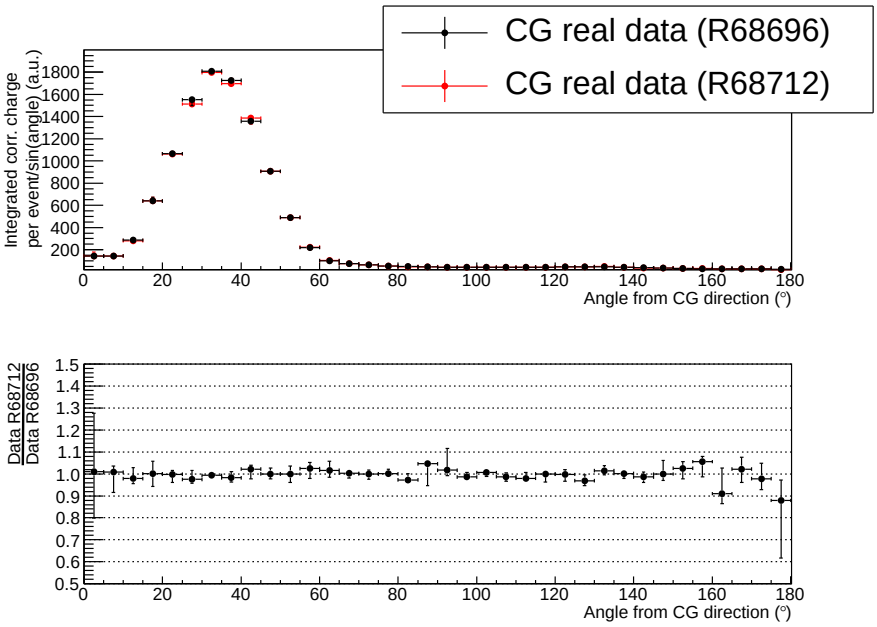

Figure 3.37: Comparison of single cone data taken at approximately same vertex (at $Z \approx 0$ m from the center of SK) and direction (towards $+y$) for runs 68696 (black) and 68712 (red) with systematic error uncertainty. Between these runs the CG was only rotated inside the SK tank.

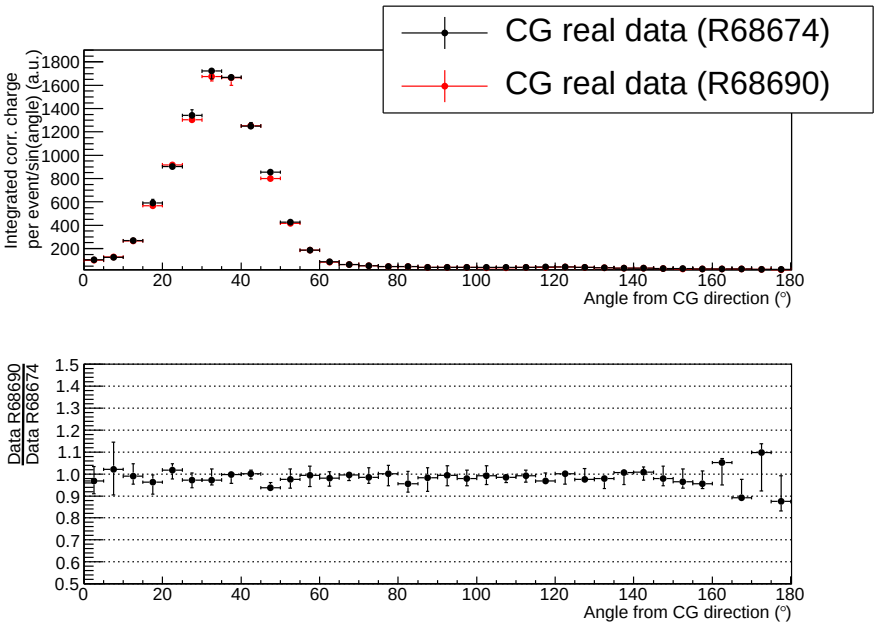

Figure 3.38: Comparison of single cone data taken at approximately same vertex (at $Z \approx 8$ m from the center of SK) and direction (towards $+y$) for runs 68674 (black) and 68690 (red) with systematic error uncertainty. Between these runs the CG was only rotated inside the SK tank.

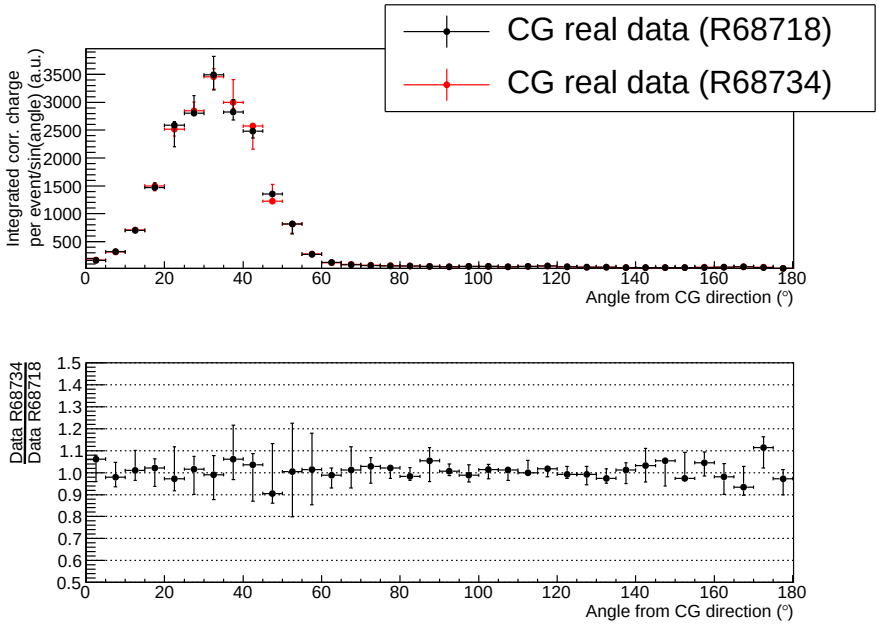

Figure 3.39: Comparison of single cone data taken at approximately same vertex (at $Z \approx 16$ m from the center of SK) and direction (towards $+y$) for runs 68718 (black) and 68734 (red) with systematic error uncertainty. Between these runs the CG was only rotated inside the SK tank.

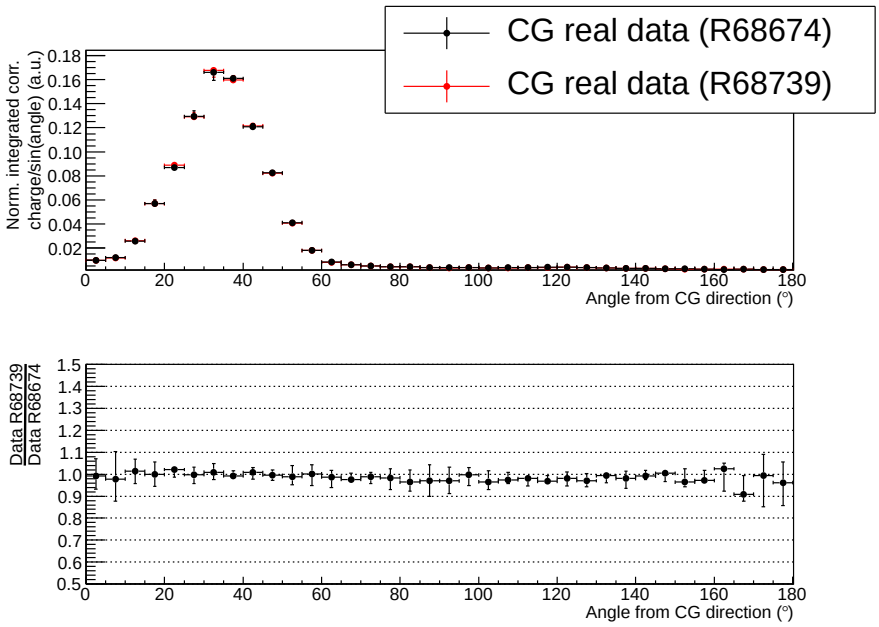

Figure 3.40: Comparison of single cone data taken at approximately same vertex (at $Z \approx 8$ m from the center of SK) and direction (towards $+y$) for runs 68674 (black) and 68739 (red) with systematic error uncertainty. Between these runs the CG was removed and reinserted in the SK tank and the laser diode and the optical fiber between the CG and the laser was disconnected and reconnected, therefore the total charge of the events is not expected to be the same and therefore the charge profiles are normalized.

The first sample that was verified after bug fix was the though going muon sample. In this sample the difference between the charge profile of Monte-Carlo before and after bug fix is of 1% level.

It was further investigated the effect of the correction of the Rayleigh scattering angular distribution by comparing the efficiency of usual SK event selections before and after bug fix. The samples used for this evaluation were a 500 MeV/c electron, a 500 MeV/c muon and a 500 MeV/c π^0 and the results following the event selections are shown in tables 3.5, 3.6 and 3.7, respectively. In summary the difference between the Monte-Carlo before and after bug-fix was within statistical error of the samples and below 1%. The difference between measured momentum using the Monte-Carlo before and after bug fix for electrons and muons are also within 1% (after/before bug fix is 1.0004±0.0002 for electron MC and 1.0006±0.0001 for muon MC). The difference of the measured π^0 mass is also within 1% (after/before bug fix is 1.000±0.001).

Table 3.5: Difference in the efficiency of reconstruction of electron events generated by the version of SKDETSIM with the Rayleigh scattering bug and after this bug was fixed.

event selection	ratio of efficiency after and before bug fix
fully contained in fiducial volume	0.9997±0.0045
and single ring	0.9999±0.0046
and electron like by PID	0.9992±0.0046
and no decay electrons	0.9992±0.0046

Table 3.6: Difference in the efficiency of reconstruction of muon events generated by the version of SKDETSIM with the Rayleigh scattering bug and after this bug was fixed.

event selection	ratio of efficiency after and before bug fix
fully contained in fiducial volume	1.0006±0.0045
and single ring	1.0004±0.0045
and muon like by PID	1.0004±0.0046
and one decay electron	1.0005±0.0046

Table 3.7: Difference in the efficiency of reconstruction of π^0 events generated by the version of SKDETSIM with the Rayleigh scattering bug and after this bug was fixed.

event selection	ratio of efficiency after and before bug fix
fully contained in fiducial volume	1.002±0.006
and two rings	0.997±0.008
and two rings are electron like by PID	0.998±0.008
and no decay electrons	0.998±0.008

In addition to having evaluated the effect of the bug fix along the event selection for usual samples it is essential to evaluate the effect of the bug fix on the tuning of the detector. As it was mentioned the bug affects unpolarized light that is usually produced after reflection, thus we can expect that the reflection tuning will need to be updated, which

is being done by the Duke University T2K/SK group. The other detector calibrations should not be affected directly by this bug.

3.7 Perspectives

We have successfully created an external device that emits single ring-shaped light inside the Super Kamiokande detector and measured its properties in an external setup. The single cone simulation based on this measurement and the single cone data taken at SK agree well at the ring region, even though at the backwards region there is still a slight difference between data and Monte-Carlo even after the correction of a bug found in SKDETSIM.

The next step for the Cone Generator project will be to either calibrate the Super Kamiokande detector or to improve the understanding of Super Kamiokande reconstruction. There are currently three different groups that are using the Cone Generator data for different purposes :

- The TRIUMF T2K/SK group are using the CG data to test a new reconstruction algorithm they are developing for Super Kamiokande. In this algorithm the shape and timing informations of all PMTs are used to perform the reconstruction and the CG is therefore an useful control sample where verifications can be made.
- The Imperial College T2K group are using the CG data taken at about $Z = 16$ m to evaluate the vertex reconstruction at the fiducial volume boundary with the intention of increasing the fiducial volume.
- The LLR T2K group will continue the development of the CG Monte-Carlo and plan to measure the Z dependency of the scattering of light in water using the different CG measurements. Furthermore we plan to take two cone data at SK at different configurations reproducing the π^0 kinematics, specially when the SK reconstruction fails to measure two rings, and use the understanding of the SK detector reconstruction imparted by such measurements to improve its reconstruction and further reduce the π^0 background at SK, given that the control sample currently used to estimate such error, which is presented in the next chapter, is limited by its statistics.

Chapter 4

Systematic error estimation for the reconstruction efficiency of π^0 events in Super Kamiokande

Contents

4.1 Introduction

In order to compare the T2K neutrino data with what would be expected from the T2K beam it is essential to understand to which precision we know the Super Kamiokande reconstruction algorithms for each type of particle. The dominant background sources at Super Kamiokande for T2K are the ν_e CCQE beam contamination (∼49%) and mis-reconstructed π^0 events[1] generated by neutral current (∼34%). Table 4.1 shows the breakdown by "final state" of expected signal and background for the T2K Run I+Run II.

Table 4.1: Expected number of events in SK after the ν_e CCQE selection (see section 2.5.3) and in parenthesis the fraction of ν_e selected events categorized by final state for signal and background samples. The number of events correspond to the Run I+Run II ($1.431 \cdot 10^{20}$ POT) expected statistics using the `10d v3.1` beam flux, near detector normalization of 1.036. In order to estimate number of events we assume $\sin^2 2\theta_{13} = 0.1$, $\delta_{CP} = 0°$ and normal mass hierarchy. The samples for which we estimate systematic error in this chapter are highlighted.

Final state	Signal	Background
ν_e CC 1e	3.986 (97.0%)	0.659 (49.1%)
other ν_e CC	0.122 (3.0%)	0.042 (3.1%)
ν_μ CC without π^0	0.000 (0.0%)	0.024 (1.8%)
ν_μ CC with π^0	0.000 (0.0%)	0.005 (0.4%)
NC $1\pi^0$	0.000 (0.0%)	0.457 (34.1%)
other NC with π^0	0.000 (0.0%)	0.049 (3.7%)
NC 1γ	0.000 (0.0%)	0.036 (2.7%)
NC $1\pi^\pm$	0.000 (0.0%)	0.039 (2.9%)
other NC	0.000 (0.0%)	0.031 (2.3%)

At Super Kamiokande there is no pure π^0 control sample available independent of the event selection therefore in order to understand the Super Kamiokande reconstruction for π^0 events it was necessary to create a control sample.

The hybrid-π^0 method was originally developed to estimate the uncertainty of the rejection efficiency of NC $1\pi^0$ events using the T2K selection cuts. Afterwards the use of the hybrid-π^0 sample was extended to estimate the uncertainty of the "other NC with π^0" sample and the "ν_μ CC with π^0" sample. In this chapter we will discuss in more details the hybrid-π^0 technique and the estimated systematic uncertainty of the reconstruction efficiency of events with a π^0 in the final state at Super Kamiokande.

The hybrid-π^0 method consists of the following steps which will be explained further :

1. construct the hybrid-π^0 samples following the π^0 kinematics of the T2K Monte-Carlo;

2. apply the usual Super Kamiokande reconstruction for the hybrid-π^0 samples events;

3. estimate systematic errors of the reconstruction efficiency by comparing the reconstruction efficiency of hybrid-π^0 data and Monte-Carlo samples.

[1]Mis-reconstructed π^0 events in this case are the π^0 events that passes all ν_e CCQE event selections, that is, events where only one ring was reconstructed.

4.2 The hybrid-π^0 sample

4.2.1 Overview

The hybrid-π^0 data sample is constructed by superposing an electron ring from Super Kamiokande data and a Monte-Carlo γ ring following the π^0 kinematics obtained using the T2K Monte-Carlo. The hybrid-π^0 Monte-Carlo sample is constructed similarly to the aforementioned sample using an electron ring from the Super Kamiokande Monte-Carlo instead of an electron ring from Super Kamiokande data. This construction process for the hybrid-π^0 sample is shown in figure 4.1.

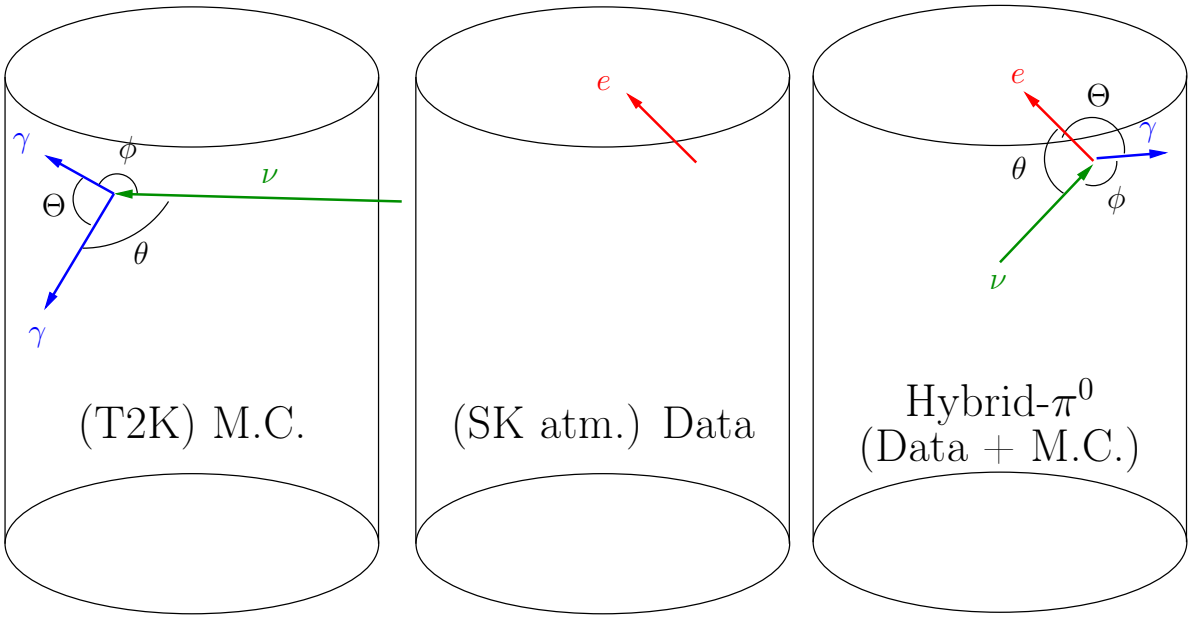

Figure 4.1: Scheme of construction of the hybrid-π^0 samples. The left part of the plot shows a ν (green) that interacts inside the Super Kamiokande tank (cylinder) to generate a π^0 decaying in two γ (blue). In the center part one electron (red) in Super Kamiokande with momentum similar to one of the γ shown in the left is shown. The right part shows the hybrid-π^0 event generated by combining the electron in the middle with a γ Monte-Carlo following the π^0 decay kinematics given on the left. Note that the angle between the ν and each γ shown in the left figure (namely, θ, Θ and ϕ) are the same as the corresponding angle between the ν, the e and the γ shown in the right figure, only the direction of the neutrino and γ have changed.

Since there is no pure π^0 control sample available, we could create a π^0 control sample by superposing two γ events following the π^0 decay kinematics ($\pi^0 \rightarrow 2\gamma$ at 98.8% of the decays, the remaining fraction (1.2%) is composed by the Dalitz decay $\pi^0 \rightarrow \gamma + e^+ + e^-$ [14]). However it does not solve the original problem as there is also no γ control sample available at Super Kamiokande either. Since the charge pattern from a γ and an electron ring are similar to a 1% level (see section 2.5.2 and [71]) and there is a electron control sample from usual Super Kamiokande analysis available we have decided to replace one of the γ of the π^0 decay by an electron.

Since the $\pi^0 \rightarrow 2\gamma$ produces two γ rings, we will replace any on those rings by an electron ring. We do not know beforehand which of the γ rings is the dominant part

of the systematic error. We need therefore to evaluate the systematic error related with each ring separately. Each part of the systematic error will be estimated using a different hybrid-π^0 sample. These samples are :

Primary hybrid-π^0 : constructed by replacing the most energetic γ from the π^0 decay by an electron. To construct this sample, only electrons from the atmospheric ν_e sample are used. The momentum distribution of the replaced γ is shown in figure 4.2.

Secondary hybrid-π^0 : constructed by replacing the least energetic γ from the π^0 decay by an electron. To construct this sample, electrons from the atmospheric ν_e or μ decay samples are used depending whether the momentum of the least energetic γ is above or below 60 MeV/c, respectively. The momentum distribution of the replaced γ is shown in figure 4.3.

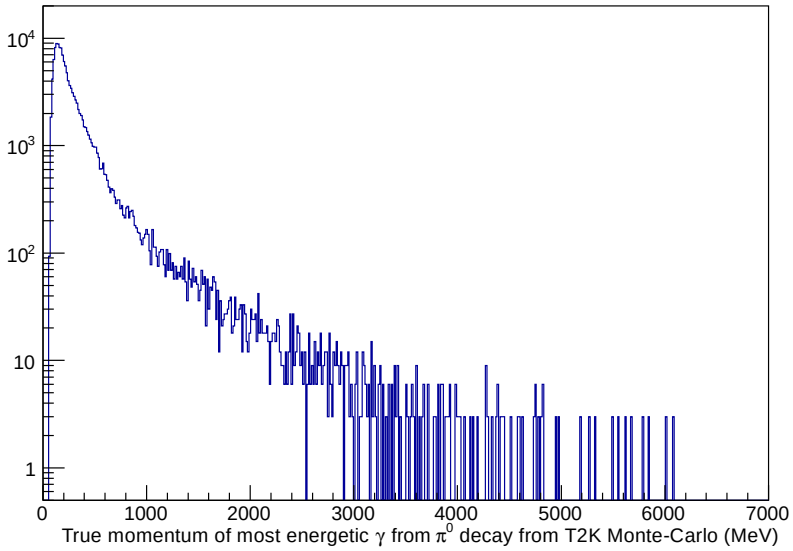

Figure 4.2: Distribution of the momentum of the most energetic γ produced from a π^0 decay in the T2K Monte-Carlo. Note that when this γ is replaced by an electron to create a hybrid-π^0 sample the new sample is called "primary hybrid-π^0" sample.

The usual electron ring samples available from Super Kamiokande data are composed of electrons from the atmospheric ν_e CCQE interaction and from the decay of muons. These samples will be referred respectively as "electron from atmospheric ν_e" and "decay electron" and will be described in detail at subsection 4.2.2 and 4.2.3. Because these samples are created through different processes the momentum distributions are different as shown in figures 4.4 and 4.5 respectively.

Electrons from decay electron sample have a small momentum, typically well below 70 MeV/c as shown in figure 4.5. Therefore we cannot use decay electrons to construct the "primary hybrid-π^0" sample, because the γ with lowest momentum that would need to be replaced would have momentum of $\sim$ 67 MeV/c (see appendix D.1.2). Given this limitation the "primary" hybrid-π^0 sample will be composed by replacing the most energetic γ from the π^0 decay by an electron ring from atmospheric ν_e sample.

In the "secondary" hybrid-π^0 sample on the other hand, the replaced γ can have momentum in the same range as the decay electrons momentum shown in figure 4.5 as well as momentum well above this momentum range. Therefore the replaced γ in the "secondary" hybrid-π^0 sample will be replaced by an electron from either the atmospheric ν_e sample (if replaced γ momentum above 60 MeV/c) or the decay electron sample (if replaced γ momentum below 60 MeV/c).

To construct the hybrid-π^0 sample, we compare the reconstructed information of both data and Monte-Carlo sample to the true Monte-Carlo information of the replaced γ from the T2K Monte-Carlo. We do not have two different procedures for data and Monte-Carlo to avoid introducing a bias in the difference between these hybrid-π^0 samples.

4.2.2 Construction of the electron from the atmospheric ν_e sample

The data control sample with electron rings from atmospheric ν_e was generated by applying the usual Super Kamiokande event reconstruction for events that are fully contained, with visible energy greater than 50 MeV where only one e-like ring was reconstructed and with no decay electron. We also require that the POLfit π^0 mass of these events be smaller than 100 MeV/c^2 to select a cleaner electron sample. This sample was created using all Super Kamiokande 4 data from October 2008 (beginning of Super Kamiokande 4) until February 2011 and contains 2056 events of which 1542 events are in the fiducial volume.

After generating the hybrid-π^0 sample, we noticed that some events were more prone to migrate between e-like and μ-like because the reconstruction of these events did not perform well (for more information about this problem please see example given in section 4.2.5). In order to avoid this problem, we have afterwards removed from the hybrid-π^0 sample events where the original electron reconstruction presented goodness of fit below 0.6 as shown in figure 4.6. The remaining electron rings from atmospheric ν_e data sample contains 2041 events of which 1541 events are in the fiducial volume.

The Monte-Carlo sample for electrons from atmospheric ν_e data sample is constructed using the same procedure described previously. We used the official Super Kamiokande 4 default atmospheric ν_e Monte-Carlo instead of atmospheric ν_e data from Super Kamiokande 4.

The full Super Kamiokande 4 default atmospheric ν_e Monte-Carlo has much more electron events than those obtained from the Super Kamiokande 4 atmospheric ν_e data sample. To construct non biased hybrid-π^0 samples we have selected the first 2056 events from the Super Kamiokande 4 atmospheric ν_e Monte-Carlo which correspond to the same number of events observed in the Super Kamiokande 4 atmospheric ν_e data sample. Among these Monte-Carlo events, 1595 are in the fiducial volume and 2051 have goodness of fit greater than 0.6, of which 1592 are in the fiducial volume.

4.2.3 Construction of the decay-electron sample

The decay-electron data sample was created by selecting the decay of muons that stop inside the Super Kamiokande detector. For this analysis, we use the so called MIDRD stopping muons, that is muons that have total charge in the inner detector between 250 PE and 10000 PE with maximum charge in one PMT below 225 PE and which present more than 300 PE total charge in a 300 ns window. We further require only one cluster seen in the outer detector, only one decay electron found with a timing larger than 1.2 μs, and a goodness of fit of the decay electron above 0.5. The requirement for the timing to be larger larger than 1.2 μs guarantees that the decay electrons are separated from the

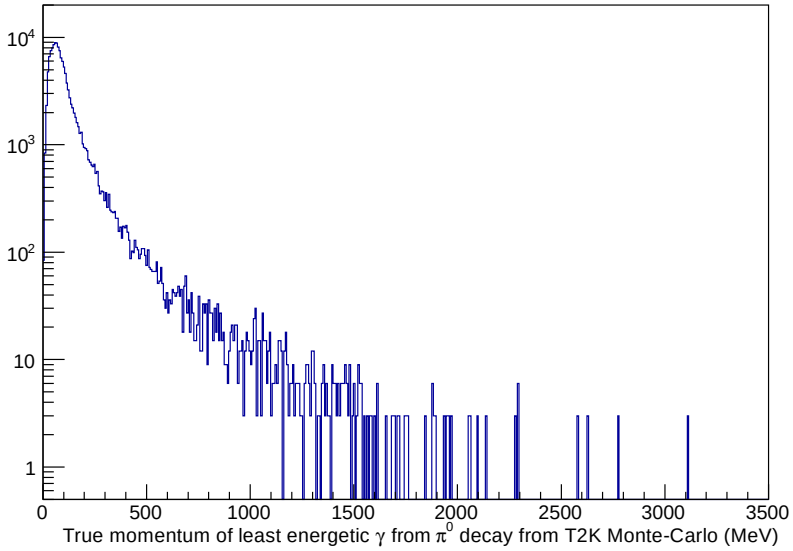

Figure 4.3: Distribution of the momentum of the least energetic γ produced from a π^0 decay in the T2K Monte-Carlo. Note that when this γ is replaced by an electron to create a hybrid-π^0 sample the new sample is called "secondary hybrid-π^0" sample.

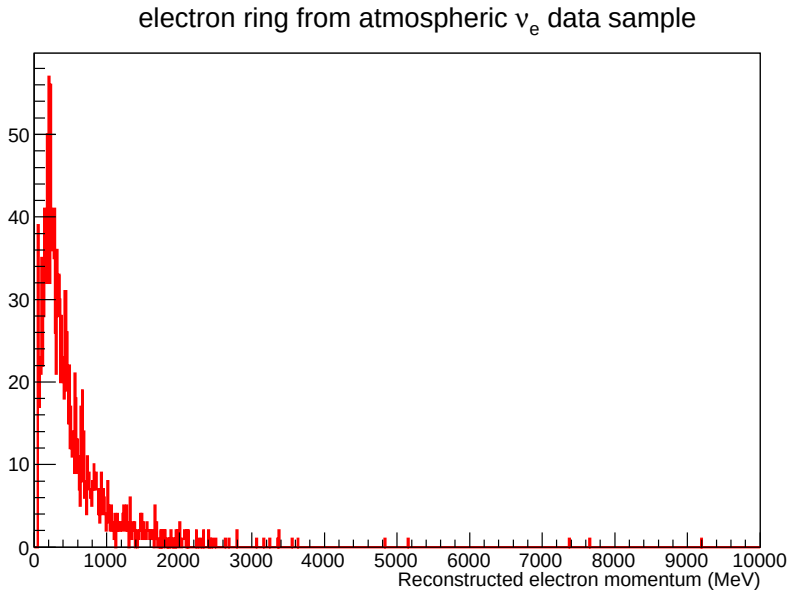

Figure 4.4: Distribution of the reconstructed momentum of the electron by APFIT (default SK reconstruction for high-energy events) at the atmospheric ν_e data sample. These electrons will be used to replace one γ to create the hybrid-π^0 samples. Note that electrons from this sample will be used to generate the "primary hybrid-π^0" sample and part of the "secondary hybrid-π^0" sample.

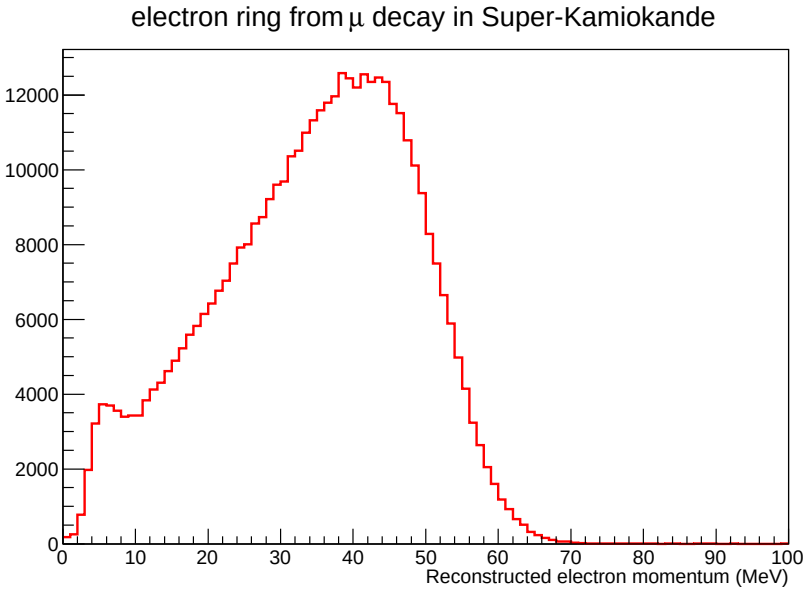

Figure 4.5: Distribution of the reconstructed momentum of the electron by KaiFit (default SK reconstruction for "decay electrons") from a μ decay. These electrons will be used to replace one γ to create the hybrid-π^0 samples. Note that electrons from this sample will be used to generate only part of the "secondary hybrid-π^0" sample.

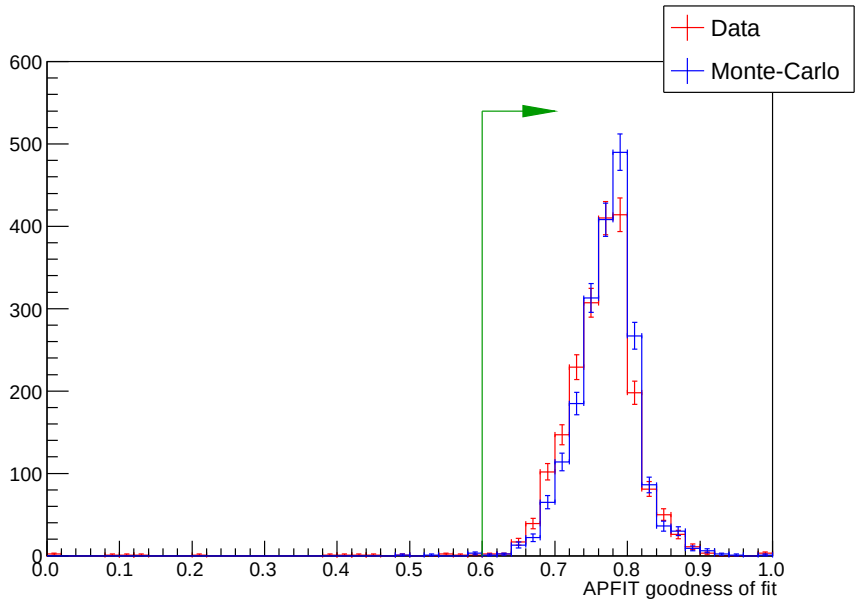

Figure 4.6: Goodness of fit distribution calculated by APFIT for the atmospheric ν_e data (red) and Monte-Carlo (blue) samples which were selected as candidates to construct hybrid-π^0 events. The atmospheric ν_e sample requires events to be fully contained, with visible energy larger than 50 MeV, with one e-like ring, without any decay electron and POLfit π^0 mass smaller than 100 MeV/c^2 and is defined using all available Super Kamiokande 4 data until February 2011 or the same number of events from the atmospheric Monte-Carlo sample. Electron events with goodness of fit below 0.6 are removed from the sample as shown by the green arrow.

parent muon events.

We note that the software used to fit the vertex and direction of decay electrons is not the same used for fitting the atmospheric data. In the current study, the KaiFit algorithm is used to reconstruct decay electrons as used by the Super Kamiokande ATMPD group[2].

We are currently using decay electron from muon decay data that was taken during T2K Run I (from January until June 2010) and Run II (from November 2010 until March 2011). In this case we do not use all Super Kamiokande 4 data because there is already enough data in the T2K time period to generate hybrid-π^0 events. The "decay-electron" data sample contains 431917 events of which 322116 events are in the fiducial volume.

The Monte-Carlo sample is generated by simulating electrons at Super Kamiokande with the same vertex, direction and momentum than those from the "decay-electron" data sample. These Monte-Carlo events are then reconstructed using KaiFit with the same smearing effects on the position and direction as those present in the data sample. For simplicity, even though the Monte-Carlo sample corresponding to the "decay-electron data sample" is not generated from the decay of muons, we call this sample the "decay-electron Monte-Carlo sample" since it has the same kinematics as the "decay-electron data sample". The number of events in this Monte-Carlo sample is by construction the same as the number of events in the "decay-electron data sample".

To improve the construction the Monte-Carlo sample, we have decided to take into account the effect of the mis-reconstruction by KaiFit (which will always output one electron) of the muon decay mode $\mu^- \to e^- \overline{\nu_e} \nu_\mu \gamma$ with branching ratio of $(1.4 \pm 0.4)\%$[14]. Since this decay mode is present in the "decay-electron data sample", it is essential for it to be present also in the Monte-Carlo sample to avoid a bias between these samples. To take into account this decay mode we have generated with Geant4 a list of the electron and γ momenta for this decay mode which is used as input for skdetsim. This new sample is reconstructed using KaiFit. Finally, we replaced 1.4% of the original "decay-electron Monte-Carlo sample" events with events generated with an electron and a γ with the same final reconstructed momentum, and after such replacement the final "decay-electron Monte-Carlo sample" has the same final state composition as the "decay-electron data sample" at statistical level.

4.2.4 Construction of the hybrid-π^0 sample

As it was explained previously, the hybrid-π^0 samples are constructed by overlapping a electron ring from either data or Monte-Carlo and a Monte-Carlo γ ring following the T2K π^0 decay kinematics. In this subsection it is explained how the electron ring event is chosen to construct the hybrid-π^0 event and how the kinematics of the Monte-Carlo γ is defined.

Given that the hybrid-π^0 samples need to have the same kinematics as the T2K π^0 sample, it was decided to construct the same number of events in the hybrid-π^0 as of NC $1\pi^0$ events in the T2K Monte-Carlo. This way, the hybrid-π^0 sample has the same decay kinematics as the T2K Monte-Carlo on an event by event basis.

For each NC $1\pi^0$ event in the T2K Monte-Carlo, we select an electron ring from the "atmospheric ν_e sample" with momentum closest to the momentum of the γ from the π^0 with higher momentum to create the "hybrid-π^0 primary samples". Since there are

[2]The low energy group uses currently the BONSAI algorithm to fit electrons with similar momentum to decay electron momentum and the ATMPD group plans to change the reconstruction of decay electrons from KaiFit to BONSAI in the future

only about 2000 electron rings available in the "atmospheric ν_e sample" while there are 136056 π^0 events it is necessary to reuse several times the same electron event. Because of that, we will need later on to apply a more advanced statistical error calculation for the hybrid-π^0 sample statistical uncertainty.

In the case of the "hybrid-π^0 secondary samples" we will apply the same procedure described for the "hybrid-π^0 primary samples" replacing by an electron the γ with lower momentum instead of the γ with higher momentum produced by the π^0 in a given NC $1\pi^0$ event in the T2K Monte-Carlo. To construct this sample we can benefit from the high statistics of the "decay-electron samples" to create part of this hybrid-π^0 sample using "decay electrons" instead of electrons from atmospheric ν_e interaction. This is the case when the momentum of the lowest γ in the π^0 decay is below 60 MeV/c, and since there are enough events in the "decay-electron" sample we do not have to reuse any electron events to create "hybrid-π^0" events where a decay electron is used.

Once we have selected an electron ring, we need to define the direction of the γ Monte-Carlo ring to be superposed to the electron ring. The γ Monte-Carlo ring vertex is the same as the electron ring, its momentum is the same as from the T2K Monte-Carlo. Its direction is defined by requiring that three angles shown in figure 4.1 be the same between the T2K Monte-Carlo and the hybrid-π^0 sample. Note that such requirement defines a new beam direction called "fake beam direction". In order to have the same properties of the π^0 decay from T2K in the SK tank, and assuming the SK tank is symmetric by rotation around the vertical axis, we require that the projection of the "fake beam direction" in the vertical axis be the same as the projection of the T2K beam direction. This constraint means the "fake beam direction" is the T2K beam direction plus a rotation around the vertical axis and the assumption the SK tank is symmetric by rotation around the vertical axis is reasonable given that the SK tank is a cylinder and that we do expect the water quality at SK to depend only on the vertical position in the detector. This constraint imply that there are zero to two possible directions for the γ and the "fake beam", as shown in figure 4.7. If there is no direction that satisfies all the constraints we reject this electron event for the construction of the given hybrid-π^0 event and we try again to construct it using the next best electron event, using the same algorithm already described to select the electron event. If on the other hand there are two possible solutions we randomly select one of them, as they have the same kinematics.

Even though we have defined the hybrid-π^0 kinematics to be as similar as possible to the NC $1\pi^0$ from T2K Monte-Carlo kinematics, it should be noted that this does not imply that the other parameters in relation to the Super Kamiokande detector are the same between these samples. For example, the vertex of one hybrid-π^0 event and of the corresponding NC $1\pi^0$ event are not correlated since the vertex of the hybrid-π^0 event depends on the vertex of the electron event used and not on the vertex of the NC $1\pi^0$ event. These differences will be discussed more in detail in section 4.3.

4.2.5 Effect of reuse of electrons from atmospheric ν_e sample

As explained previously, we need to reuse electron rings from the atmospheric ν_e sample in order to be able to construct the hybrid-π^0 sample following the T2K kinematics. However, when we create two hybrid-π^0 events using the same electron ring, they are not independent from one another even though the γ ring superposed to each of these events is not the same.

When we compare hybrid-π^0 data and Monte-Carlo we are in reality comparing the ef-

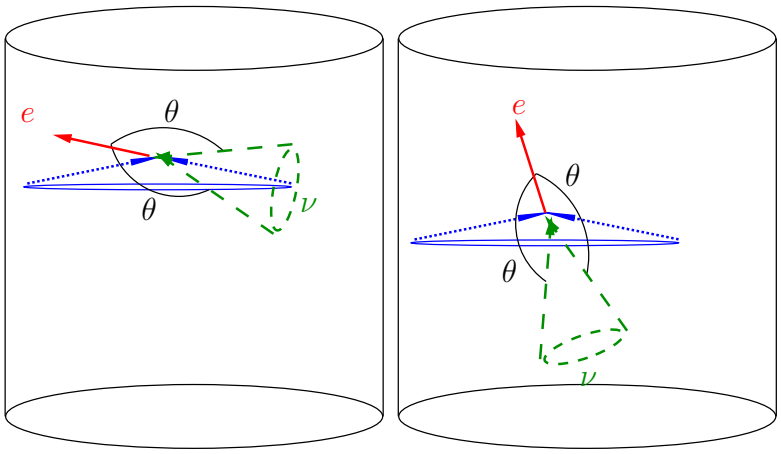

Figure 4.7: Electron events (red) candidates to construct a given hybrid-π^0 event with angle θ between the ν and the replaced γ. In green is shown the cone whose generatrixes are all directions of the ν given the angle θ In blue is shown the cone of whose generatrixes are all possible "fake beam direction" created by rotating the T2K beam around the vertical axis. The intersection between the two cones are the "fake beam direction" that satisfy both constraints. In the left there are two possible "fake beam directions", while in the right there are none. Note the other γ produced by the π^0 decay and used to construct the hybrid-π^0 sample is not shown here for simplicity.

fect to the π^0 event reconstruction between the electron ring data and Monte-Carlo (which is also the reason we estimate error on the primary and secondary samples separately). The fact that two hybrid-π^0 events were generated using the same original electron ring means that on both events the base charge pattern use to generate these events will be the same and the part that is different, namely the γ that is not replaced, is simulated using the same software in both cases. Therefore we will assume that there is a complete correlation[3] between hybrid-π^0 events generated using the same electron event from the atmospheric sample. Therefore we need to know how many times each atmospheric event was reused and which events it generated.

To clarify the need to make the appropriate calculation of the uncertainty due to the reuse of electrons from the atmospheric ν_e, it is useful to compare the size of the statistical error from the number of events only and the one calculated by taking the reuse into account in a situation where we had found a problem and which exemplifies the need to take the reuse into account. This is the case of the PID likelihood distribution of the primary hybrid-π^0 sample generated without removing electron events from the atmospheric ν_e sample with goodness of fit below 0.6, which is shown in figure 4.8. For this analysis the goodness of fit requirement to construct the hybrid-π^0 sample was removed to create the situation where events that were not well reconstructed (thus with lower goodness of fit) are used to generate hybrid-π^0 events. In these events the probability to the event changes its classification from a slight change in the charge distribution is higher. This is the reason for which there is a peak at the PID likelihood distribution shown in figure 4.8 at the value of 1.5. Furthermore, it is clear that the $\sqrt{N}$ statistical

[3]A complete correlation between N events means that the uncertainty on the number of events is N and not $\sqrt{N}$ as would be the case if they were independent. For example, lets suppose we have constructed 3 events and to construct 2 of them we have used the same original event, therefore the uncertainty on the 3 events is not $\sqrt{3}$ but $\sqrt{2^2+1^2}=\sqrt{5}$.

error only is not enough to explain the difference between the primary hybrid-π^0 data and Monte-Carlo for this value of PID likelihood. The reuse error shows that such difference is due to the usage of the same event many times and not due to some significant difference between the data and Monte-Carlo.

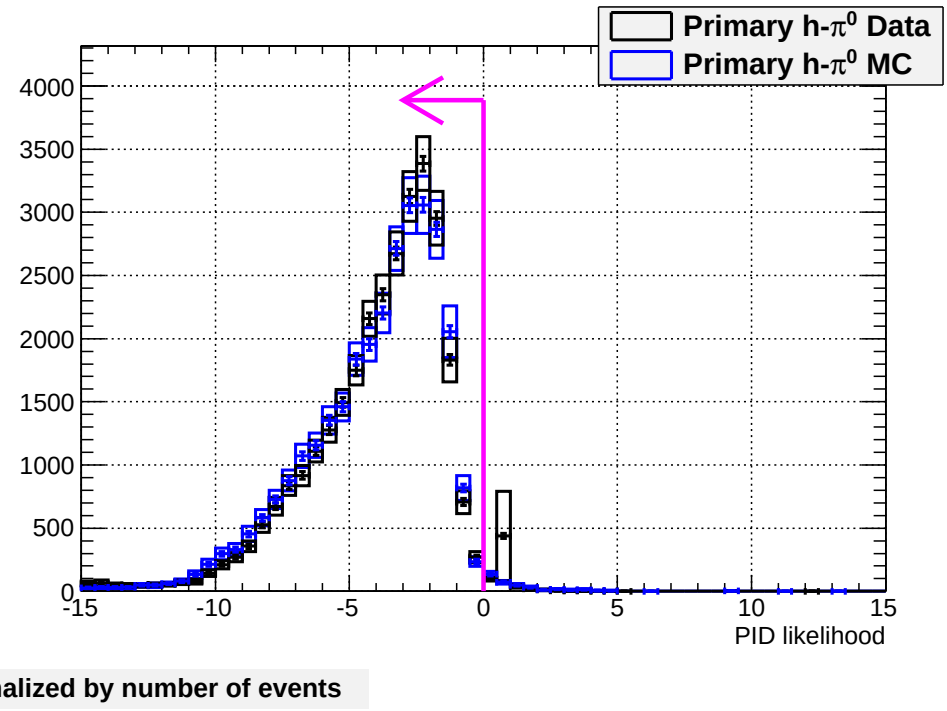

Figure 4.8: Distribution of the PID likelihood of the primary hybrid-π^0 sample constructed without requiring the goodness of fit of the electrons from the atmospheric ν_e sample to be greater than 0.6, which was done merely to illustrate the need that the uncertainty be calculated taking into account the reuse, and not only from the expected uncertainty from the number of events. Primary hybrid-π^0 data (black) and Monte-Carlo (blue) are shown here both with statistical error only (crosses) and by taking into account also the reuse of events (boxes). The arrow in magenta shows which events are identified as e-like events. For this example special attention should be given to the bin with PID likelihood of 1.5 where the statistical error only do not explain the difference in this bin between the primary hybrid-π^0 data and Monte-Carlo, however, as shown by the uncertainty calculated taking the reuse into account this is due mainly to one electron event that was reused several times and to which by adding a γ Monte-Carlo ring typically was classified as μ-like.

4.2.6 Extension of the hybrid-π^0 sample to study non single π^0 final states

It was explained how we generated the hybrid-π^0 sample used to obtain estimation of systematic error on the efficiency of the T2K event selections for NC $1\pi^0$ events. The systematic error of the efficiency of the T2K event selection for other final states shown in table 4.1 could also be estimated.

We certainly could apply the same principles from the hybrid-π^0 technique to create other hybrid samples with multiple particles, however this would require to have typically $\pi^\pm$ and proton control samples which are not available currently.

A π^0 decay in Super Kamiokande always produce at least one γ event with momentum high enough that it will be seen by the detector. Therefore, for an event where the final state contains a π^0 and another charged particle and that passes the T2K ν_e event selection the reconstructed electron will be from the γ from the π^0 decay with higher momentum. The remaining γ and other particles will either have small momentum or a momentum close to the Cerenkov momentum threshold, therefore these particles will only slightly alter the reconstruction result from the hypothetical case where only the γ from the π^0 decay with higher momentum would be present.

We can expect that by estimating the error on the efficiency of the T2K event selection related to the π^0 part, for example a $\pi^0 + \pi^\pm$ final state, we would also be estimating the systematic error on the efficiency of the T2K event selection of the whole event. We have thus created several hybrid-π^0+other particle samples that are constructed in the same way the hybrid-π^0 sample was constructed but where other particles are superposed to the electron event on top of the γ Monte-Carlo ring. This is shown in figure 4.9 for an example of construction of the "hybrid-π^0+$\pi^\pm$" sample where a π^+ was added to the existing hybrid-π^0 event.

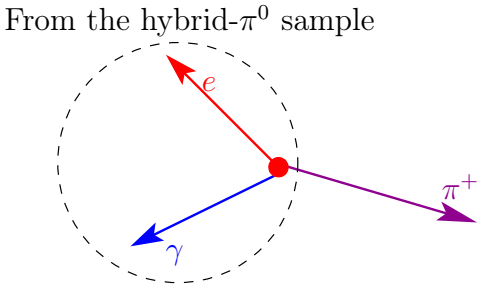

Figure 4.9: Scheme of the construction of an event "hybrid-π^0+$\pi^\pm$" from the hybrid-π^0 sample. The original hybrid-π^0 event is inside the dotted circle and is composed of an electron (red) from the atmospheric ν_e or μ decay sample and a γ (blue). To the hybrid-π^0 event, a π^+ (magenta) following the kinematics of one of the NC $\pi^0 + \pi^\pm$ events from the T2K Monte-Carlo is added.

The samples that were generated using this method are "hybrid-π^0+$\pi^\pm$", "hybrid-π^0+p", "hybrid-π^0+p + $\pi^\pm$", "hybrid-π^0+μ" and "hybrid-π^0+μ + $\pi^\pm$" that correspond to the final states of NC π^0+$\pi^\pm$, NC π^0+p, NC π^0+p+$\pi^\pm$, ν_μ CC π^0+μ and ν_μ CC π^0+μ+$\pi^\pm$, respectively. These final states consist of parts of the "other NC with π^0" and "ν_μ CC with π^0" samples.

4.3 Difference between hybrid-π^0 samples and π^0 decays from the T2K Monte-Carlo

There are several differences between the hybrid-π^0 samples and the T2K π^0 Monte-Carlo that were generated by the processes used for the construction of the hybrid-π^0 sample. The differences between the samples and the Monte-Carlo are :

1. The vertex distribution of π^0;

2. The direction of each γ produced by the π^0 decay;

3. The difference of the momentum of the replaced γ and electron;

4. In the hybrid-π^0 sample, one of the rings is an electron ring and not a γ ring;

5. In the hybrid-π^0 sample, the reconstructed information from the electron samples are used to construct the hybrid-π^0 samples as if it was the true information for the replaced γ, and therefore a reconstruction bias could have been introduced.

At this moment, we have not yet completely studied the effect of each of these differences in the event reconstruction, thus we do not compare the efficiency from a hybrid-π^0 sample with the efficiency of a π^0 Monte-Carlo sample. We can nevertheless evaluate systematic error of event reconstruction by comparing hybrid-π^0 samples that present the same construction characteristics listed above. It is essential to evaluate how close the difference between the π^0 and hybrid-π^0 samples are, keeping in mind that we could try to improve the construction method of the hybrid-π^0 sample, however for the current analysis, the performed estimation is precise enough.

4.3.1 The difference of the vertex distribution between NC $1\pi^0$ and hybrid-π^0 samples

The hybrid-π^0 sample is constructed based on the vertex distribution of electron rings from data or Monte-Carlo.

The vertex of "electron data from atmospheric ν_e sample" are randomly distributed in the Super Kamiokande detector, therefore the probability density function of the these events is the same as for the NC $1\pi^0$ events from the T2K Monte-Carlo. From this consideration follows that the difference on the vertex distribution of the "primary hybrid-π^0 samples" and of the T2K π^0 sample is due to the reuse of the same electron event (thus with the same vertex) for several different hybrid-π^0 events. This effect is however taken into account in the calculation of the statistical error of the hybrid-π^0 sample. As shown in figures 4.10, 4.11 and 4.12, the distributions of the vertex on "primary hybrid-π^0 samples" and the T2K π^0 Monte-Carlo samples are consistent with each other.

The vertex of "decay-electron sample", on the other hand, are more concentrated at the top of the Super Kamiokande detector as is shown in figure 4.13. The higher rate of decay-electrons at the top of the Super Kamiokande detector is due to a higher rate of muons entering from the top of the detector than from the bottom of the detector due to $\nu_\mu \rightarrow \nu_\tau$ oscillation of atmospheric neutrinos. The effect of this asymmetry at the constructed hybrid-π^0 secondary samples shown in figures 4.14, 4.15 and 4.16 is small given that a large fraction of these hybrid-π^0 samples comes from "reused" electrons from the atmospheric ν_e.

From the precedent considerations, we have observed that the vertex distribution for all hybrid-π^0 samples is consistent with the vertex distribution of NC $1\pi^0$ events from the T2K Monte-Carlo.

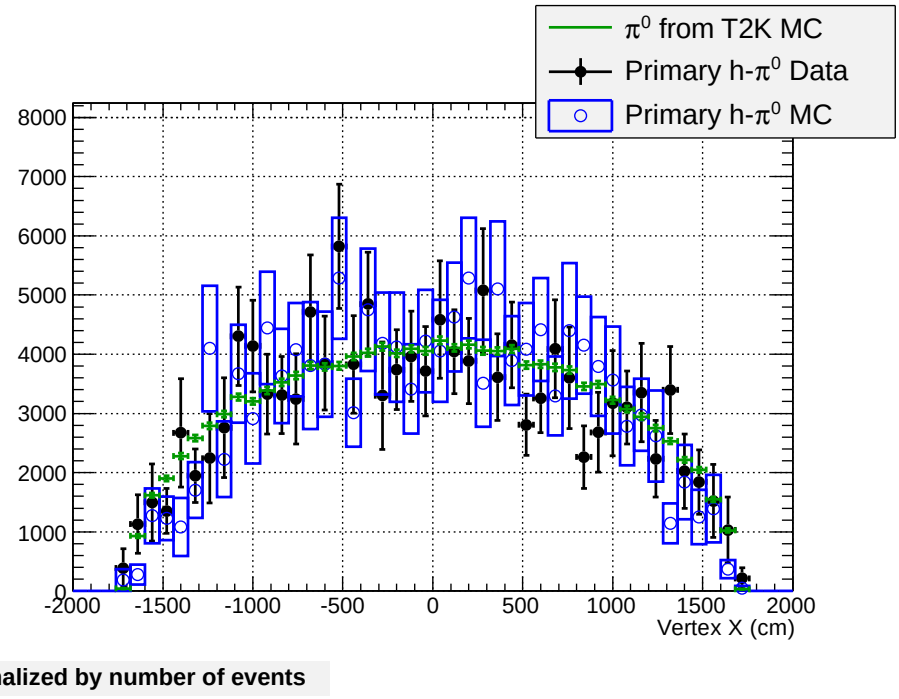

Figure 4.10: Distribution of the vertex in the X axis of π^0 events from NC $1\pi^0$ from the T2K Monte-Carlo sample (green), the primary hybrid-π^0 data (black) and Monte-Carlo (blue) samples. For the hybrid-π^0 samples the error shown was calculated taking the reuse into account.

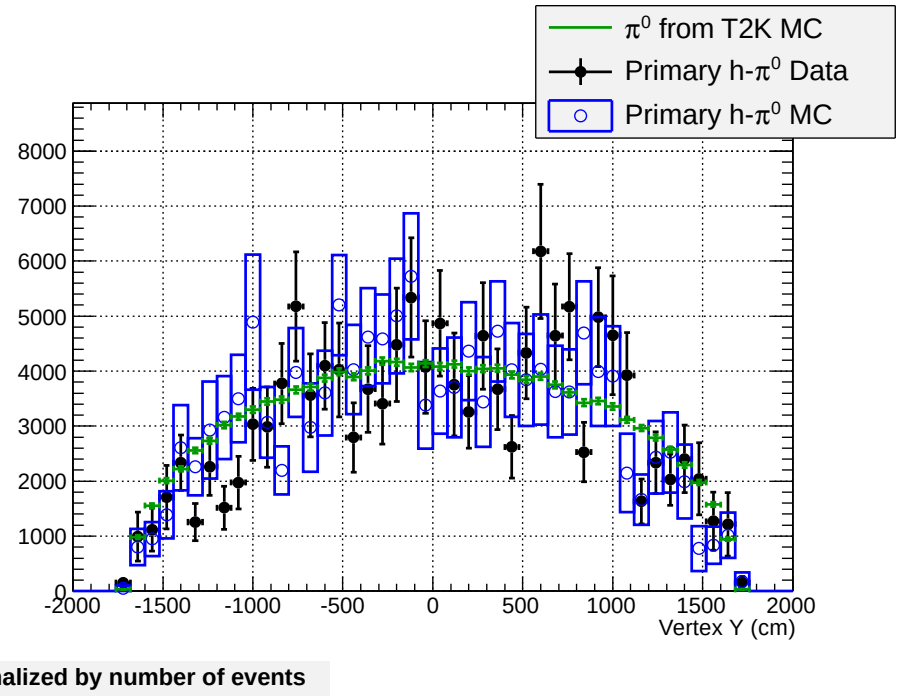

Figure 4.11: Distribution of the vertex in the Y axis of π^0 events from NC $1\pi^0$ from the T2K Monte-Carlo sample (green), the primary hybrid-π^0 data (black) and Monte-Carlo (blue) samples. For the hybrid-π^0 samples the error shown was calculated taking the reuse into account.

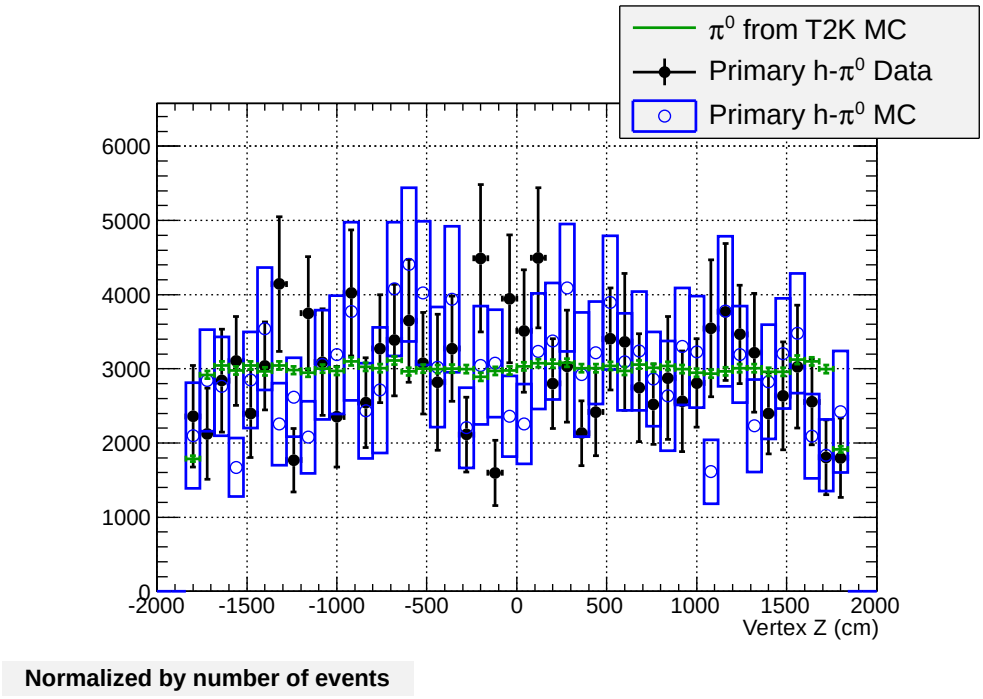

Figure 4.12: Distribution of the vertex in the vertical axis of π^0 events from NC $1\pi^0$ from the T2K Monte-Carlo sample (green), the primary hybrid-π^0 data (black) and Monte-Carlo (blue) samples. For the hybrid-π^0 samples the error shown was calculated taking the reuse into account.

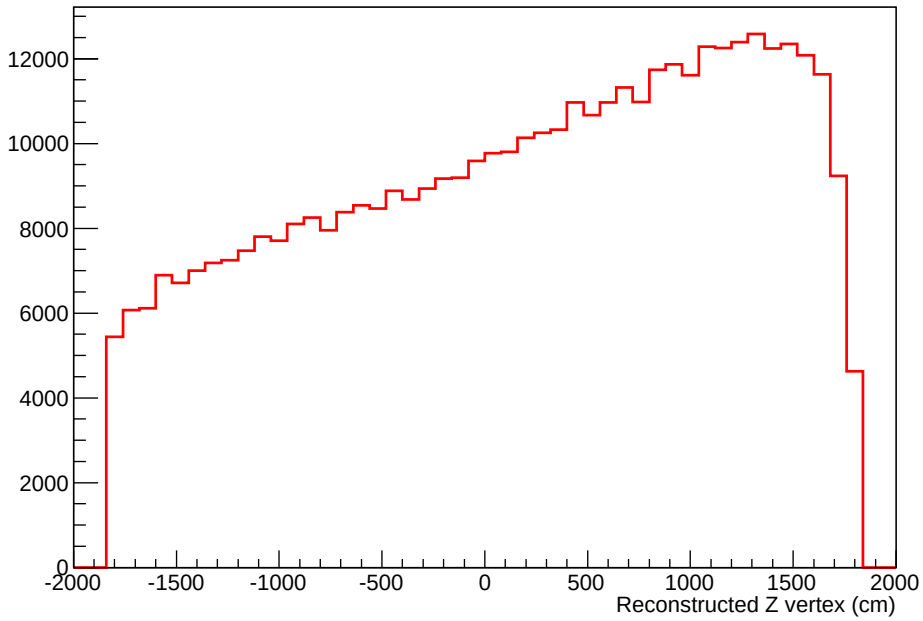

Figure 4.13: Distribution of the reconstructed vertical vertex of the electrons from μ decay sample.

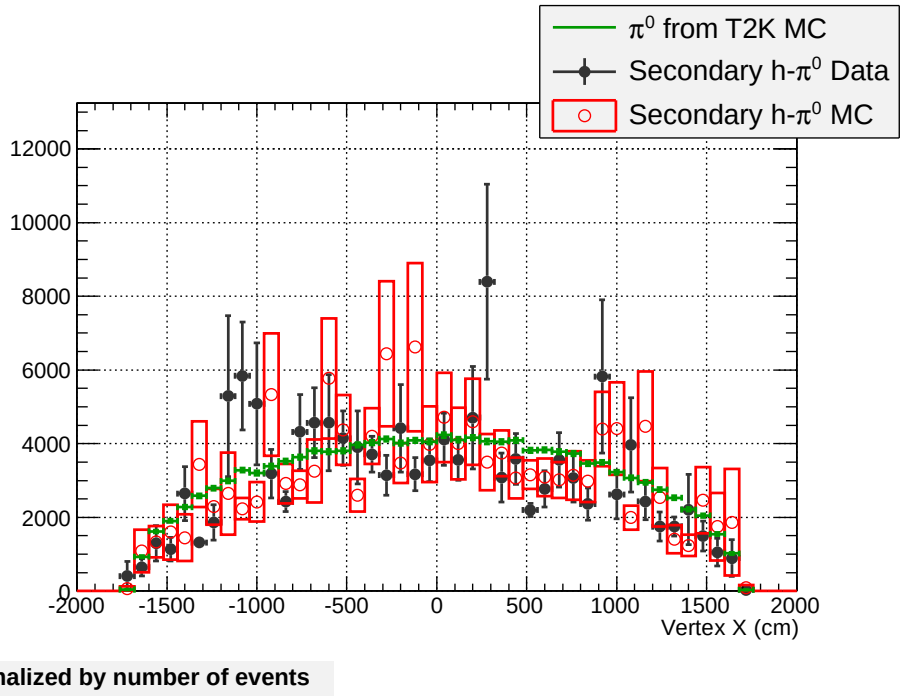

Figure 4.14: Distribution of the vertex in the X axis of π^0 events from NC $1\pi^0$ from the T2K Monte-Carlo sample (green), the secondary hybrid-π^0 data (grey) and Monte-Carlo (red) samples. For the hybrid-π^0 samples the error shown was calculated taking the reuse into account.

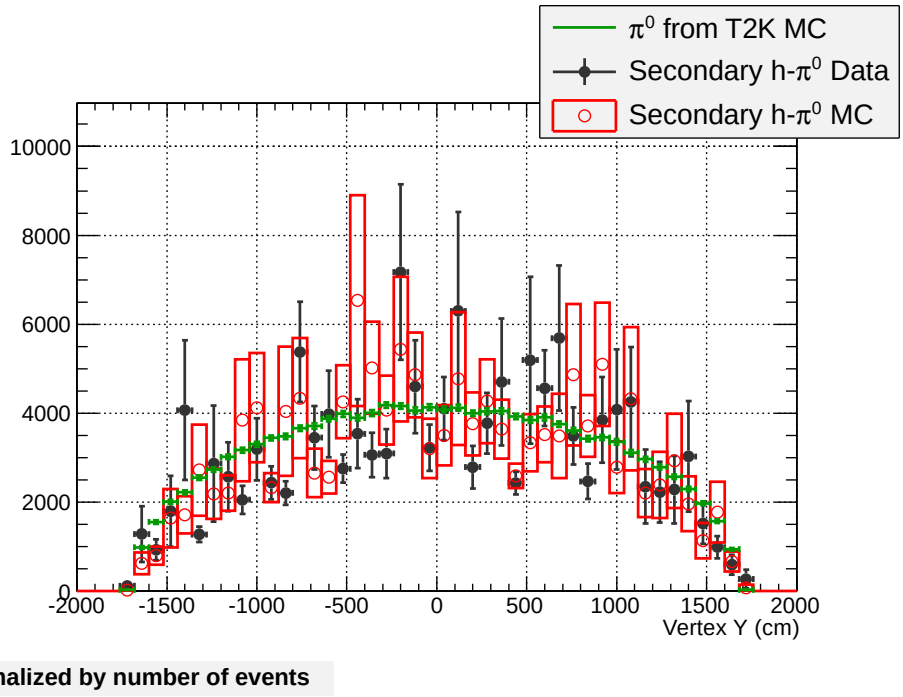

Figure 4.15: Distribution of the vertex in the Y axis of π^0 events from NC $1\pi^0$ from the T2K Monte-Carlo sample (green), the secondary hybrid-π^0 data (grey) and Monte-Carlo (red) samples. For the hybrid-π^0 samples the error shown was calculated taking the reuse into account.

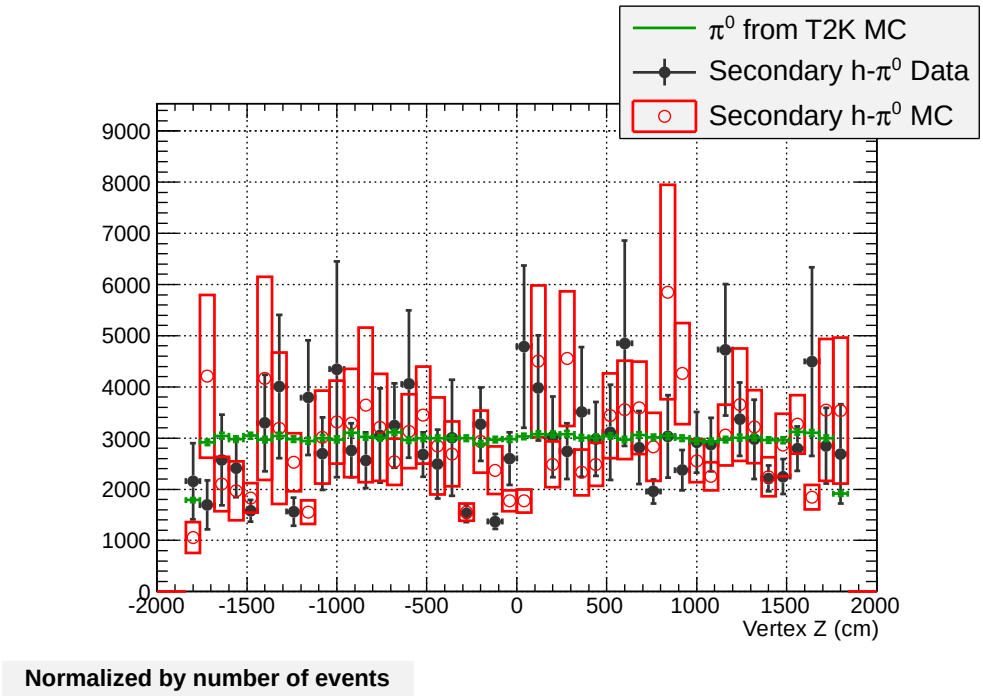

Figure 4.16: Distribution of the vertex in the vertical axis of π^0 events from NC $1\pi^0$ from the T2K Monte-Carlo sample (green), the secondary hybrid-π^0 data (grey) and Monte-Carlo (red) samples. For the hybrid-π^0 samples the error shown was calculated taking the reuse into account.

4.3.2 The difference in the directions between γ from π^0 decay of the NC $1\pi^0$ sample and γ or e from the hybrid-π^0 sample

From the construction of the hybrid-π^0 sample, mainly two differences due to the π^0 kinematics are created. The first difference is because the beam direction can only rotate around the Z axis, the γ and electron rings directions are randomly distributed in the XY plane, while for the T2K π^0 events it is concentrated at the beam direction. These effects are shown on figures 4.17 and 4.18 for the distribution of the direction of the electron ring of the primary sample in the X and Y axis respectively. This difference between γ and electron directions is not really an issue since the Super Kamiokande detector is symmetric by rotation around the Z axis.

The second difference in the direction of the electron ring is because the events where the electron ring direction has same projection in the vertical axis tend to be used more frequently than events where the electron ring direction is vertical. This effect can be understood from the constraints we impose at the construction of the hybrid-π^0 sample that are shown in figure 4.7 : an electron ring whose direction is vertical will frequently not have any possible solution given the constraints and therefore is seldom used. The difference between the Z projection of the direction is shown in figure 4.19. However we should note that since this constraint applies directly only for the electron ring of the hybrid-π^0, we can expect that the γ ring direction do not present this same tendency, as shown in figure 4.20.

For the moment, even though there is a difference between the π^0 and hybrid-π^0 distribution of directions in the Z axis, we assume the difference between the reconstruction

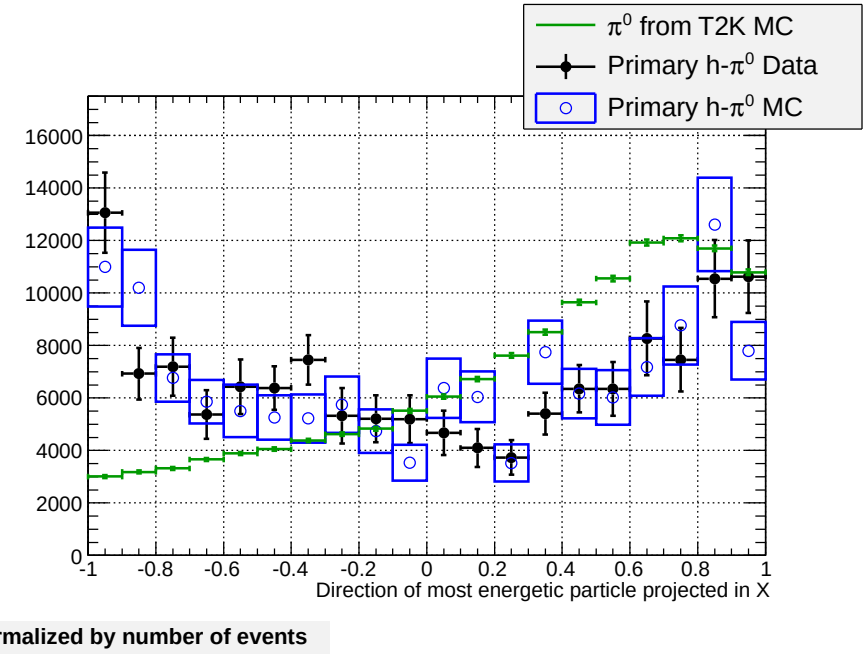

Figure 4.17: Distribution of the projection of the direction vector in the X axis of the γ from the π^0 decay from NC $1\pi^0$ from the T2K Monte-Carlo sample with higher momentum (green) or of the e of the primary hybrid-π^0 data (black) or Monte-Carlo (blue) samples. For the hybrid-π^0 samples the error shown was calculated taking the reuse into account. The peak in the green distribution at ∼0.7 corresponds to the T2K beam direction.

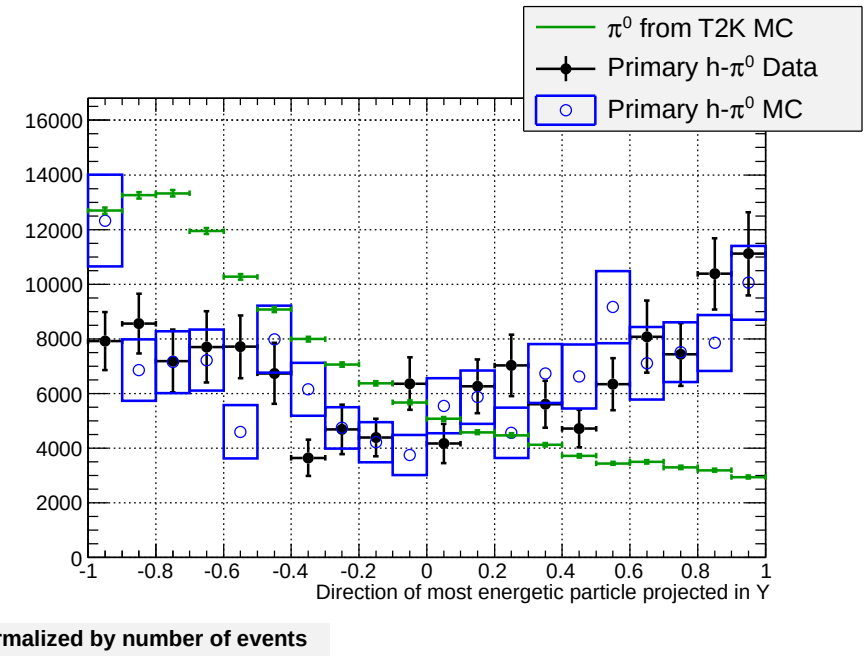

Figure 4.18: Distribution of the projection of the direction vector in the Y axis of the γ from the π^0 decay from NC $1\pi^0$ from the T2K Monte-Carlo sample with higher momentum (green) or of the e of the primary hybrid-π^0 data (black) or Monte-Carlo (blue) samples. For the hybrid-π^0 samples the error shown was calculated taking the reuse into account. The peak in the green distribution at ∼-0.8 corresponds to the T2K beam direction.

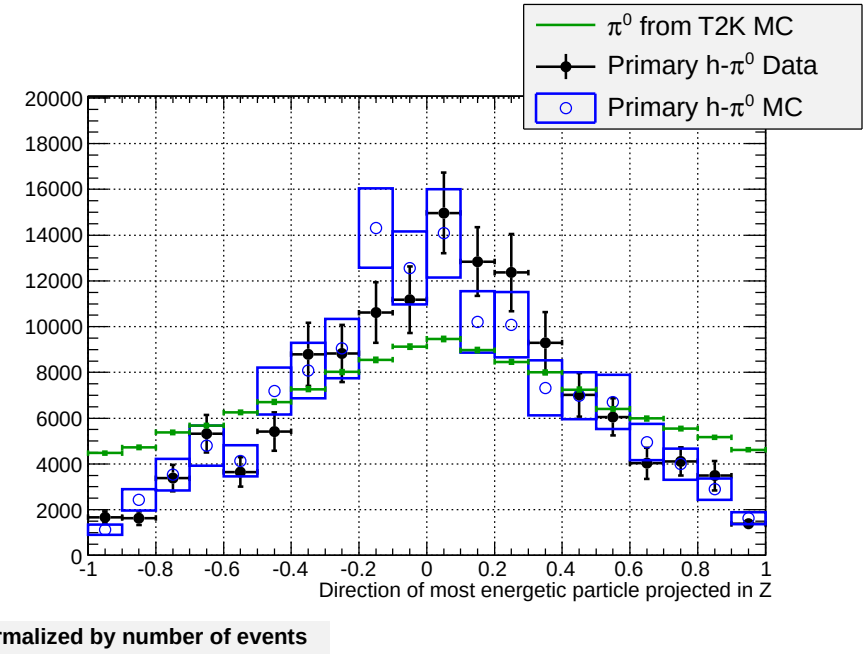

Figure 4.19: Distribution of the projection of the direction vector in the Z axis of the γ from the π^0 decay from NC $1\pi^0$ from the T2K Monte-Carlo sample with higher momentum (green) or of the e of the primary hybrid-π^0 data (black) or Monte-Carlo (blue) samples. For the hybrid-π^0 samples the error shown was calculated taking the reuse into account. The difference in the distribution in green in relation to the distributions in black or blue is due to the procedure to construct the hybrid-π^0 sample.

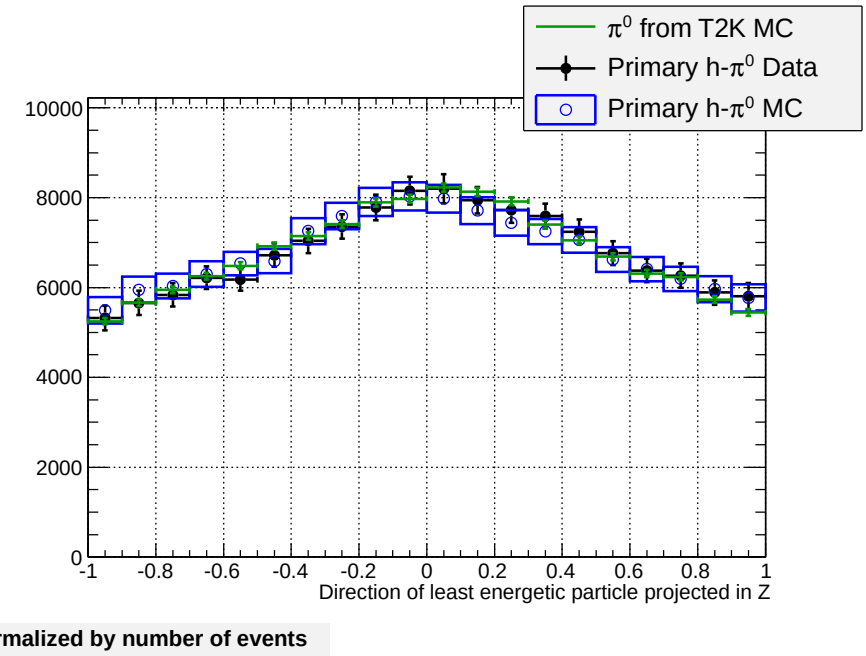

Figure 4.20: Distribution of the projection of the direction vector in the Z axis of the γ from the π^0 decay from NC $1\pi^0$ from the T2K Monte-Carlo sample with lower momentum (green) or of the γ of the primary hybrid-π^0 data (black) or Monte-Carlo (blue) samples. For the hybrid-π^0 samples the error shown was calculated taking the reuse into account.

performance of data and of Monte-Carlo do not strongly depends on the direction of the events in relation to the Super Kamiokande detector. Therefore by comparing hybrid-π^0 data and Monte-Carlo sample, for which the direction distributions are compatible, we can estimate the systematic error of the efficiency of the event reconstruction for T2K using the hybrid-π^0 sample.

4.3.3 Difference between the γ momentum from the NC $1\pi^0$ sample and the momentum of the electron from the hybrid-π^0 sample

Through the matching process of the momentum of electron rings and γ rings there can be differences between the electron with momentum closest to the γ momentum and the γ momentum itself. For a larger electron sample we expect that in average these differences will be reduced, it is essential that the electron data and Monte-Carlo samples have the same size. In the current hybrid-π^0 sample, this difference is usually less than a few MeV as shown in figures 4.21 and 4.22 for the primary and secondary hybrid-π^0 samples respectively. The error on the momentum matching done currently is most often within the detector momentum resolution, thus we consider this difference small enough therefore not affecting our current results, specially since both the hybrid-π^0 data and hybrid-π^0 Monte-Carlo samples were created with the same characteristic regarding distribution of differences of the reconstructed momentum of the matched of the electron and of the true momentum of the original γ.

4.3.4 Difference between γ and e in the Super Kamiokande detector

As explained previously, we do not have any γ control sample available. Because the charge pattern from a γ and an electron is similar, we can use electron rings to replace one of the γ rings from π^0 decays.

Furthermore the difference between a γ and electron events was also studied along the T2K event selection, via comparison between electron and γ Monte-Carlo. This study was performed to estimate the systematic error for the NC 1γ final state and has shown that the difference of efficiency of the T2K event selection was always within 1% between γ and electron rings [71]. Thus this difference is not taken into account until any systematic error calculated using the hybrid-π^0 sample is of this order of magnitude.

4.3.5 Motivation to use the reconstructed information for e instead of its Monte-Carlo information

In order to construct the hybrid-π^0 sample based on a data control sample, we use the reconstructed momentum of the data control sample and compare it with the true momentum of the π^0 Monte-Carlo sample. It is certain that the true momentum of each of the electrons in the data control sample is different than the reconstructed momentum. However, we have no access to the true information of our data and we know from other studies that the error and the bias of the Super Kamiokande event reconstruction are expected to be small.

In order to avoid bias between hybrid-π^0 data and Monte-Carlo sample, we use the reconstructed information of the Monte-Carlo samples to construct the hybrid-π^0 samples.

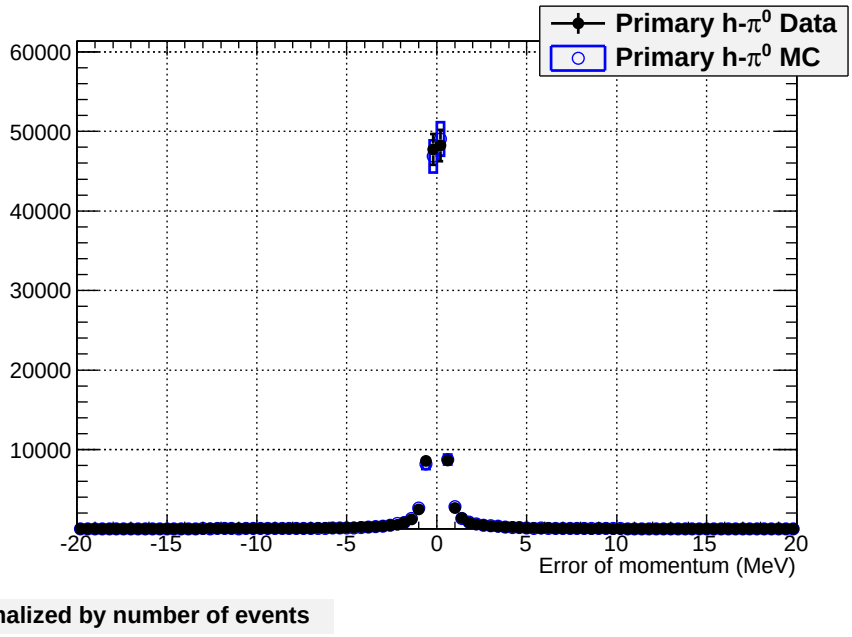

Figure 4.21: Distribution of the difference of the momentum between the γ from the π^0 decay from NC $1\pi^0$ from the T2K Monte-Carlo sample with highest momentum and the e of the primary hybrid-π^0 data (black) or Monte-Carlo (blue) samples. For the hybrid-π^0 samples the error shown was calculated taking the reuse into account.

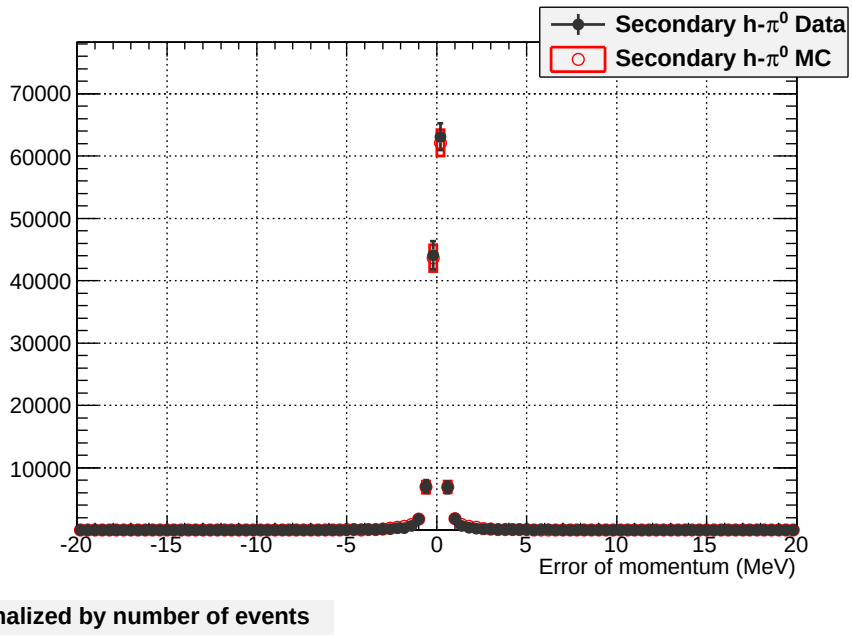

Figure 4.22: Distribution of the difference of the momentum between the γ from the π^0 decay from NC $1\pi^0$ from the T2K Monte-Carlo sample with lowest momentum and the e of the secondary hybrid-π^0 data (gray) or Monte-Carlo (red) samples. For the hybrid-π^0 samples the error shown was calculated taking the reuse into account.

Even though there might be a bias on the difference between the hybrid-π^0 samples and π^0 from T2K samples, nothing can be done to improve this situation.

4.4 Results

In this section we will explain in detail the results of the hybrid-π^0 samples comparison used to estimate systematic error of the NC $1\pi^0$ background. The method used is similar for all systematic error estimations that were made. Then the differences of the technique used for the estimation of the other systematic errors in relation to the estimation of the NC $1\pi^0$ sample will be presented.

4.4.1 NC $1\pi^0$ background

After having constructed all hybrid-π^0 samples we apply usual Super Kamiokande event reconstruction to these samples and compare the distributions used along the event selection between the data hybrid-π^0 sample and the corresponding Monte-Carlo sample. This allows to evaluate whether data and Monte-Carlo distributions are compatible and if their shape is similar to the expected shape for π^0 events, which, for example, will typically present two rings classified as e-like. Differences between the shape of the hybrid-π^0 data and Monte-Carlo samples indicate cases where it would be possible to improve either the reconstruction or the simulation to obtain better agreement between data and Monte-Carlo. This could result in the reduction of the estimated systematic errors or even of the contamination of the signal by the background.

In this section we will be presenting only the comparison of data and Monte-Carlo along event selection of the "primary hybrid-π^0 sample". The corresponding plots from the "secondary hybrid-π^0 sample" do not present different characteristics than those shown here and can be found at the end of this subsection.

Following the event selection, we compare the visible energy distribution of the hybrid-π^0 samples shown in figure 4.23.

The next event selection is the number of rings. Figure 4.24 shows the ring counting likelihood of the hybrid-π^0 samples. Even though there is statistical agreement between data and Monte-Carlo for every value of the ring counting there are some regions where there is a similar difference between hybrid-π^0 data and Monte-Carlo, for example near ring-counting likelihood of -4. For the moment it is not possible to know if this disagreement is purely statistical or if there is a real reason for it. We can expect to decide in either way by improving the statistical significance of the hybrid-π^0 sample in the future by using more electrons from atmospheric ν_e data when available.

The following event selection is the particle type. Figure 4.25 shows the PID likelihood of the hybrid-π^0 samples. Even though there are some differences between hybrid-π^0 data and Monte-Carlo, they are currently within the statistical error. We should also note that the probability that the first ring is identified as a μ ring in the hybrid-π^0 sample is small (of about 2%) which means that any slight difference between hybrid-π^0 data and Monte-Carlo will not strongly affect the efficiency of the event selection as most of the events are identified as electron rings.

The following event selection is the requirement that no decay electrons are observed. Figure 4.26 shows the number of decay electrons of the hybrid-π^0 samples. By construction we expect that there are no decay-electrons observed in these samples, which is exactly what is observed.

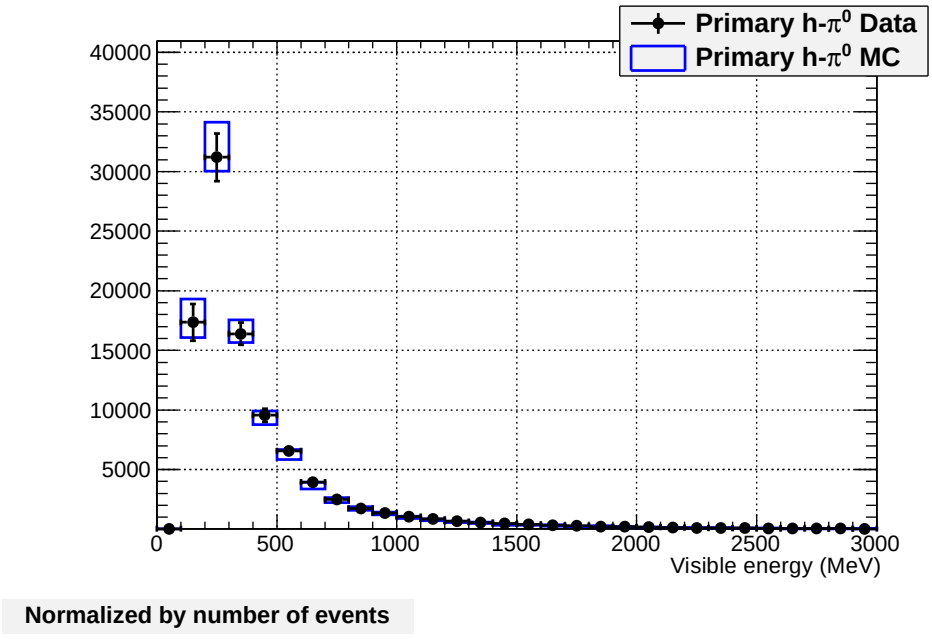

Figure 4.23: Visible energy distribution of the primary hybrid-π^0 data (black) and Monte-Carlo (blue) samples. The events selected by the T2K ν_e event selection have visible energy greater than 100 MeV. The error bars are calculated by taking the reuse into account.

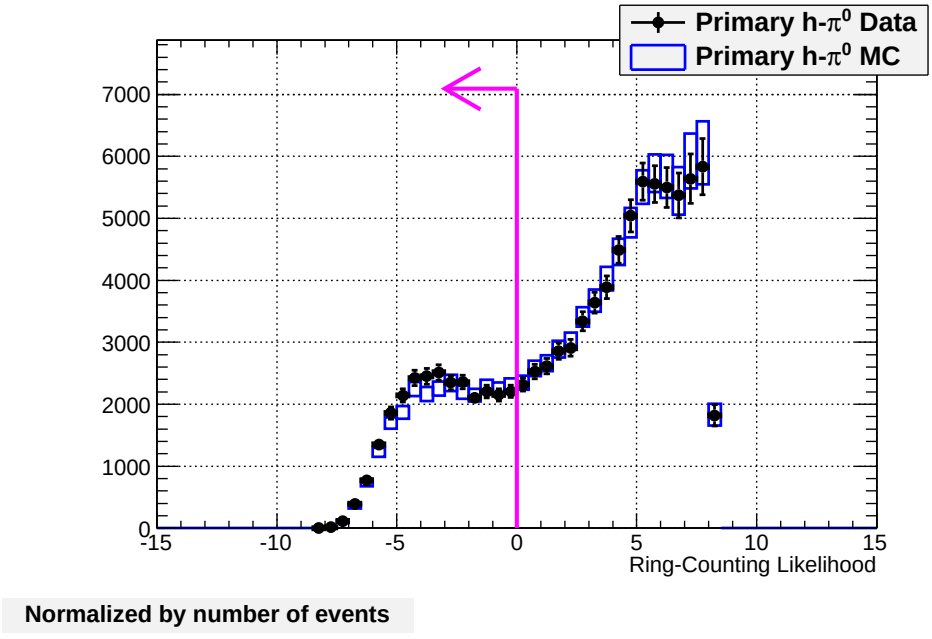

Figure 4.24: Ring counting likelihood distribution of the primary hybrid-π^0 data (black) and Monte-Carlo (blue) sample. The events selected by the T2K ν_e event selection have ring counting likelihood lower than 0 (one ring sample) and are indicated by the magenta arrow. The error bars are calculated by taking the reuse into account.

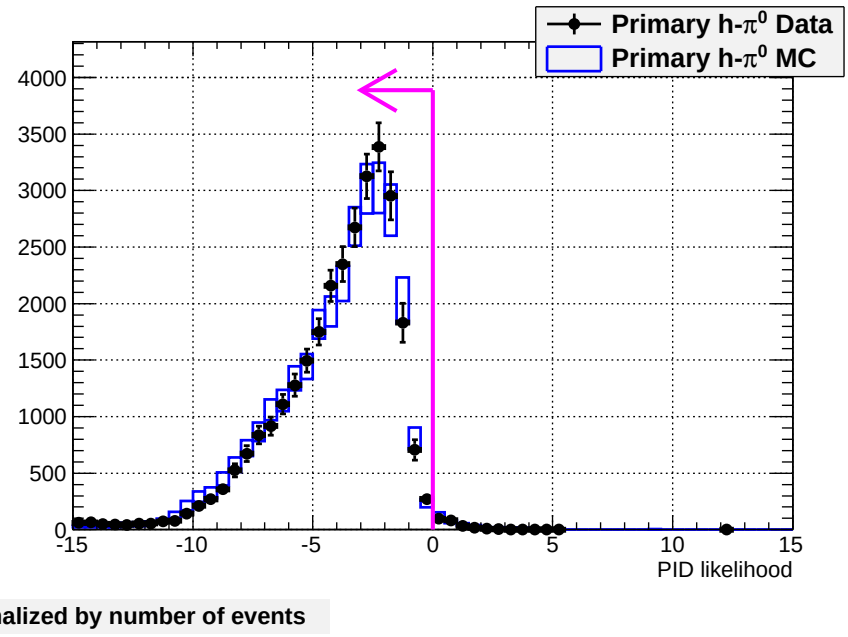

Figure 4.25: PID likelihood distribution of the primary hybrid-π^0 data (black) and Monte-Carlo (blue) sample. The events selected by the T2K ν_e event selection have PID likelihood lower than 0 (e-like sample) and are indicated by the magenta arrow. The error bars are calculated by taking the reuse into account.

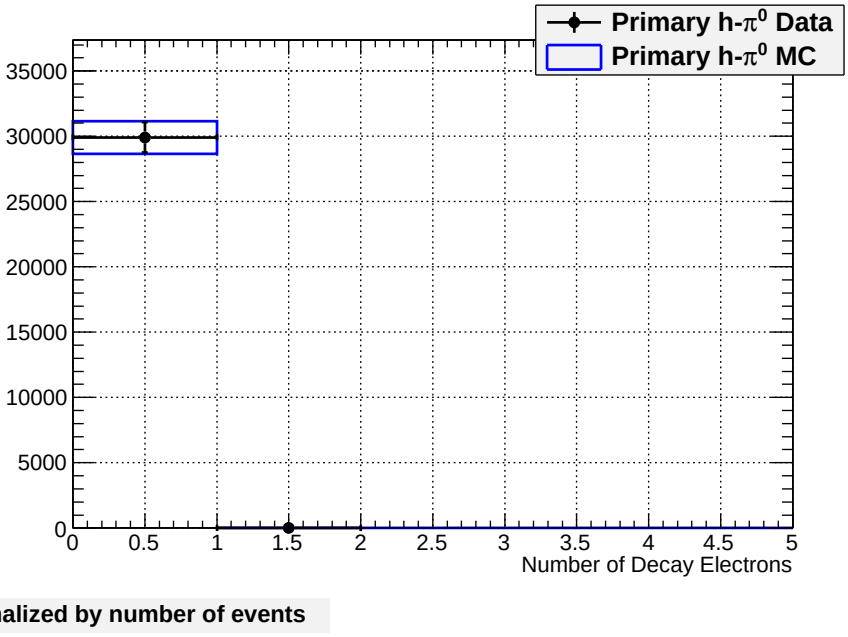

Figure 4.26: Number of decay electrons distribution of the primary hybrid-π^0 data (black) and Monte-Carlo (blue) sample. The events selected by the T2K ν_e event selection have 0 decay electrons. The error bars are calculated by taking the reuse into account.

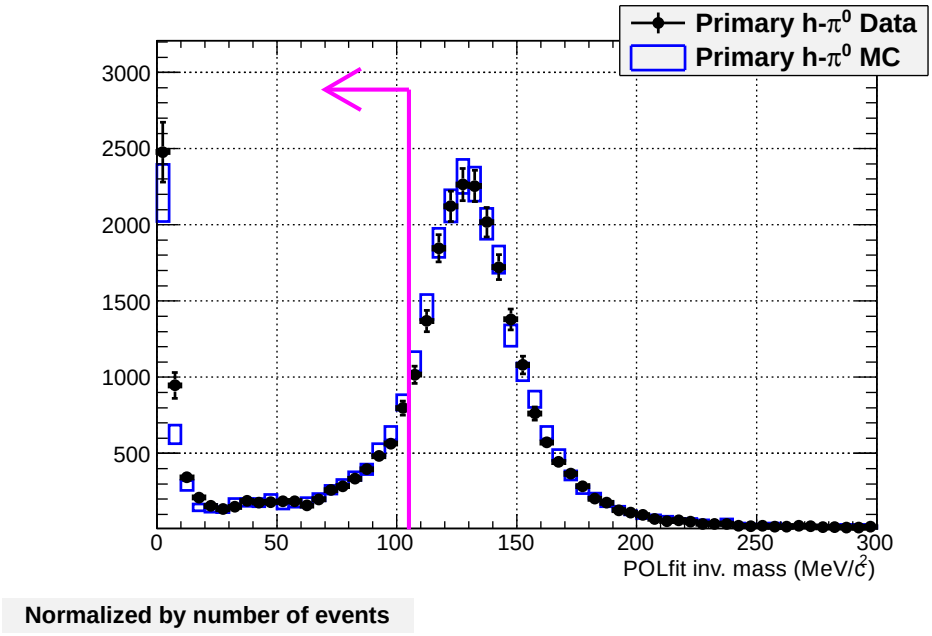

Figure 4.27: POLfit reconstructed π^0 mass distribution of the primary hybrid-π^0 data (black) and Monte-Carlo (blue) sample. The events selected by the T2K ν_e event selection have POLfit reconstructed π^0 mass lower than 105 MeV/c^2 and are indicated by the magenta arrow. The error bars are calculated by taking the reuse into account.

The following event selection is the requirement that the reconstructed POLfit mass is smaller than 105 MeV/c^2. Figure 4.27 shows the POLfit mass distribution of the hybrid-π^0 samples. The POLfit mass distribution has a peak at the value of the π^0 mass, which is to be expected from the cases where the POLfit algorithm correctly finds the lowest momentum γ ring. There is also a peak at small POLfit mass which is due to POLfit identifying in some cases the lowest momentum γ ring to be on top of the highest momentum γ ring, that is the POLfit algorithm could not find the lowest γ ring. On this plot it is also shown that there is visibly some slight difference between the behaviour of hybrid-π^0 data and Monte-Carlo, but for further studies it is essential that we have a better statistical significance of the hybrid-π^0 samples as most differences shown could just be statistical fluctuations. Furthermore, currently the π^0 reconstruction is being improved by two independent groups : the LLR (France) and TRIUMF (Canada) groups. The LLR group works in the improvement of POLfit, while the TRIUMF group is recreating a π^0 fitter. Both groups intend to improve the π^0 reconstruction and e/π^0 separation.

Finally, the last event selection is based on the reconstructed neutrino energy. Figure 4.28 shows the reconstructed neutrino energy of the hybrid-π^0 samples. There are some differences between hybrid-π^0 data and Monte-Carlo, however they are concentrated at small reconstructed energy, thus do not affect the current value of the cut.

In order to understand better which event selections are responsible for the removal of π^0 events the plot 4.29 summarizes the efficiency as function of the cut number for the primary hybrid-π^0 samples. The efficiency of the event selection is defined by the ratio of the number of events remaining after a given cut and the original number of fully contained events that were generated in the fiducial volume. As expected from previous

plots, the two cuts that are more effective to reduce the number of π^0 events on the final sample are the ring counting and POLfit mass cuts. This is also to be expected from the topology of the π^0 events, given that the topological difference between a π^0 event and an electron event is the number of rings which is studied first by ring counting and then by POLfit under the assumption that the two rings are supposed to reconstruct a π^0. It also means that for these two cuts that we expect to have a larger disagreement between hybrid-π^0 data and Monte-Carlo samples, as is shown in the figure 4.30 and 4.31 for the primary and secondary samples respectively.

In order to estimate the systematic error on the efficiency of the T2K event selection of π^0 events we calculate the relative difference between hybrid-π^0 data and Monte-Carlo efficiencies for both primary and secondary samples. Then we assume that these samples are independent from each other as we are using each sample to study a different part of the π^0 decay kinematics and then combine these relatives differences in quadrature. Since we cannot compute simply the total error, given that the statistical error of the efficiency difference is not much smaller than the central value of the efficiency difference measured, we have propagated the errors using a toy Monte-Carlo where we add two Gaussian distributions with given values and errors. We have furthermore added in quadrature the central value of the measured difference between data and Monte-Carlo in order to obtain 11.8% systematic error of the efficiency of the T2K ν_e event selection for events with a π^0 in the final state. The value of the efficiencies of the hybrid-π^0 samples used to obtain the given systematic error are shown in table 4.2.

Table 4.2: Efficiency of T2K ν_e event selection for all hybrid-π^0 samples. The systematic error of the reconstruction efficiency of the NC $1\pi^0$ sample is defined by the quadratic sum of the relative difference between hybrid-π^0 data and Monte-Carlo samples (shown in the rightmost column) and of their uncertainties. The uncertainties are calculated by taking the reuse into account. The combination of these uncertainties gives a 11.8% final uncertainty.

Sample	Efficiency (%)	(data-MC)/data (%)
Primary hybrid-π^0 data	6.27±0.31	**7.8±6.7**
Primary hybrid-π^0 Monte-Carlo	5.78±0.31	
Secondary hybrid-π^0 data	6.42±0.17	**4.3±3.3**
Secondary hybrid-π^0 Monte-Carlo	6.14±0.14	

4.4.2 other NC events with π^0 background

For the study of the systematic error on the selection efficiency of the "other NC with π^0" background sample we needs to alter slightly the hybrid-π^0 sample by adding other particles to the π^0 to have the same visible final state as the studied sample. In fact, since there is not only one particle that composes the "other NC with π^0" background sample, we have constructed a hybrid-π^0 sample for each "final state" present on this sample for which we could construct a statistics significant sample, while we assume an ad-hoc 100% error for the remaining "final states". In table 4.3 is shown the breakdown in "final state" of this sample where we have neglected γ and electrons with low momentum and decay-electrons as they are not visible in the events that pass the SK CCQE ν_e event selection.

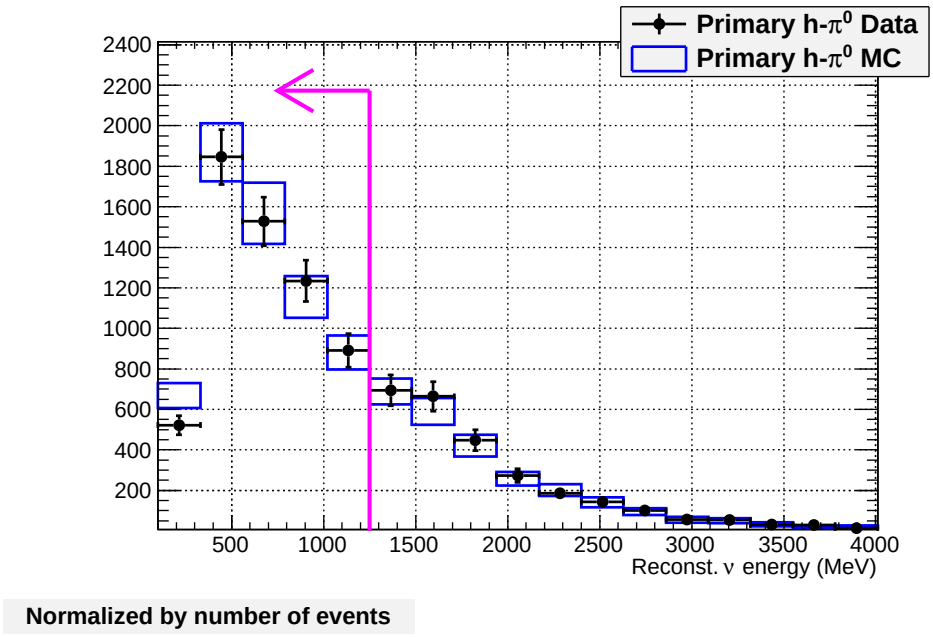

Figure 4.28: Reconstructed ν_e energy distribution of the primary hybrid-π^0 data (black) and Monte-Carlo (blue) sample. The events selected by the T2K ν_e event selection have reconstructed ν_e energy lower than 1250 MeV and are indicated by the magenta arrow. The error bars are calculated by taking the reuse into account.

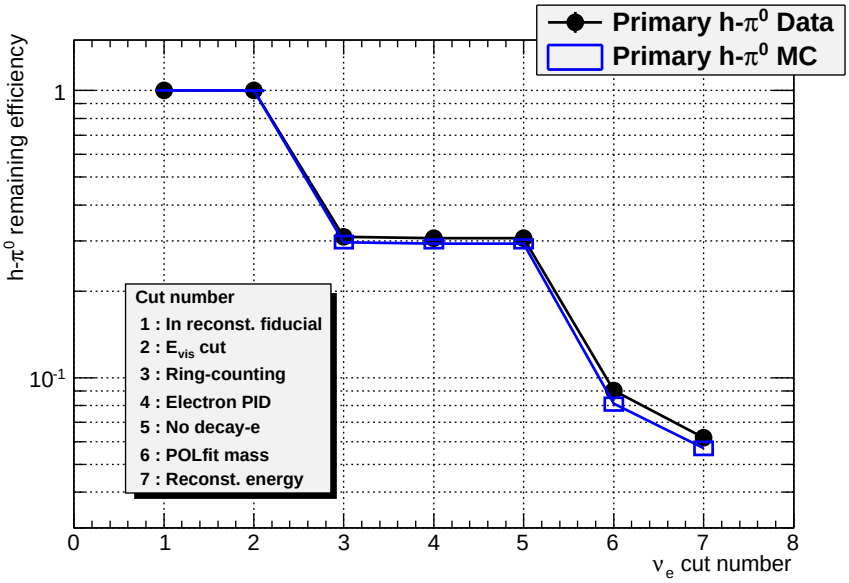

Figure 4.29: Efficiency of the T2K ν_e event selection for the primary hybrid-π^0 data (black) and Monte-Carlo (blue) sample in function of the cut number. The error bars are calculated by taking the reuse into account.

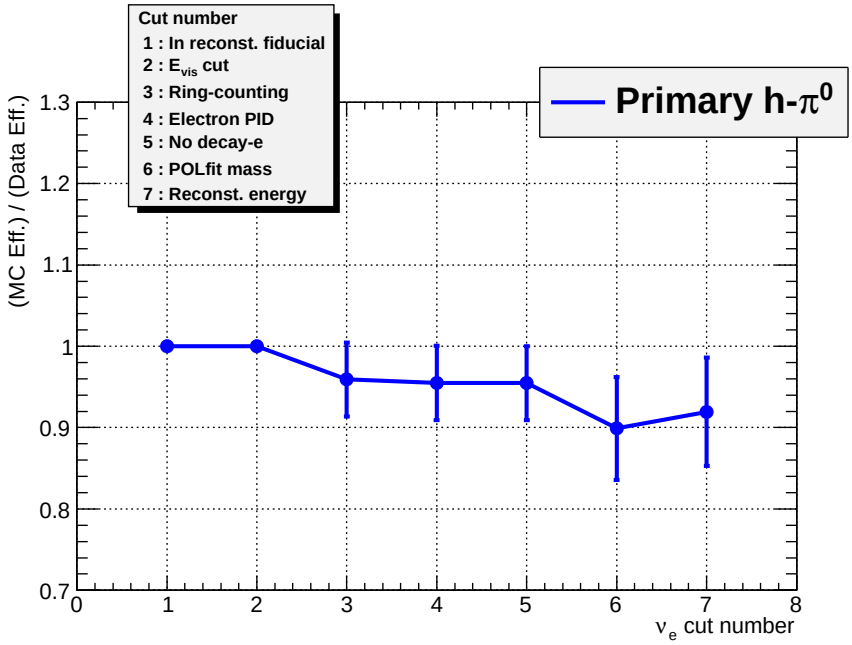

Figure 4.30: Ratio between remaining efficiency after T2K ν_e event selection of the primary hybrid-π^0 data and Monte-Carlo sample. The error bars are calculated by taking the reuse into account.

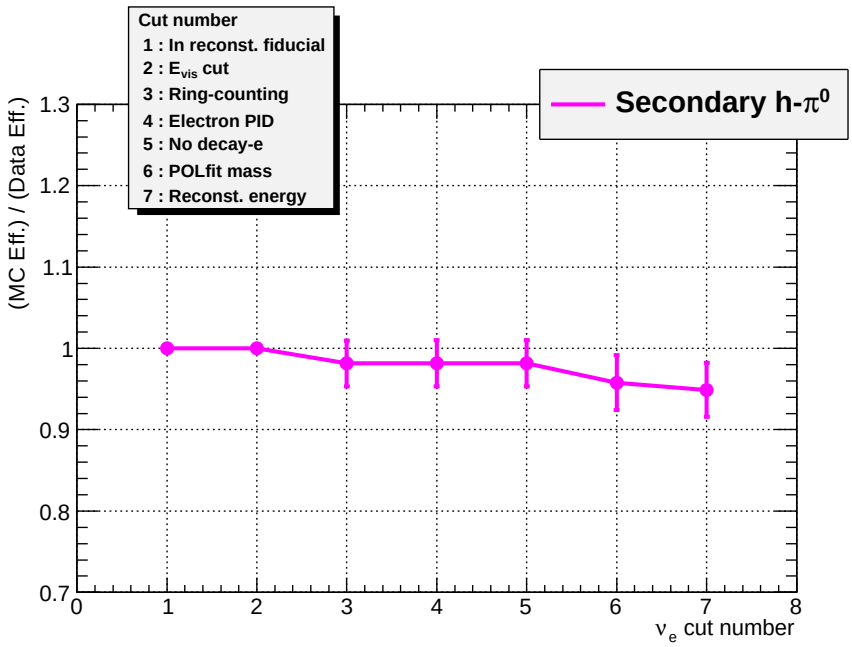

Figure 4.31: Ratio between remaining efficiency after T2K ν_e event selection of the secondary hybrid-π^0 data and Monte-Carlo sample. The error bars are calculated by taking the reuse into account.

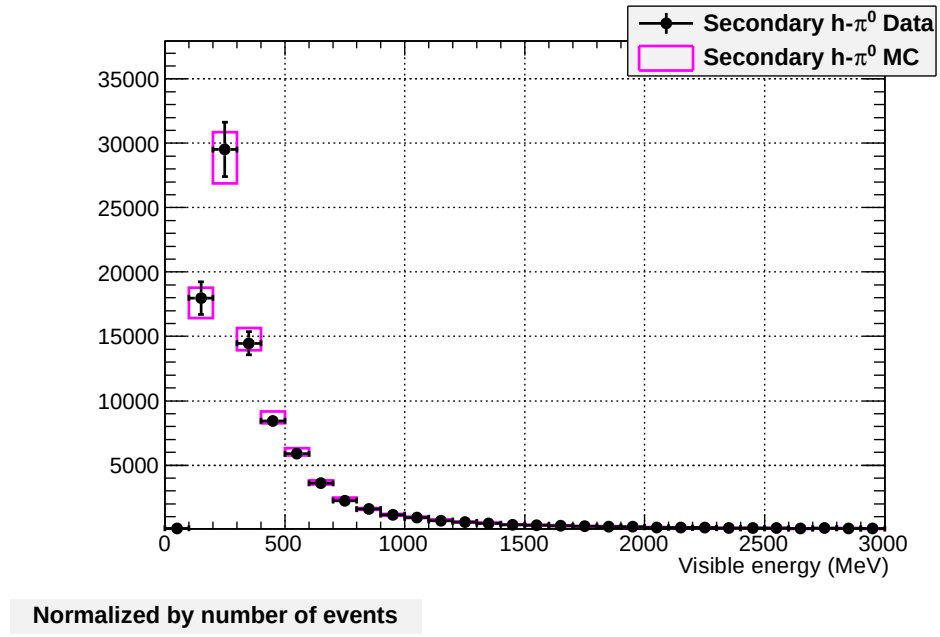

Figure 4.32: Visible energy distribution of the secondary hybrid-π^0 data (black) and Monte-Carlo (magenta) samples. The events selected by the T2K event selection have visible energy greater than 100 MeV. The error bars are calculated by taking the reuse into account.

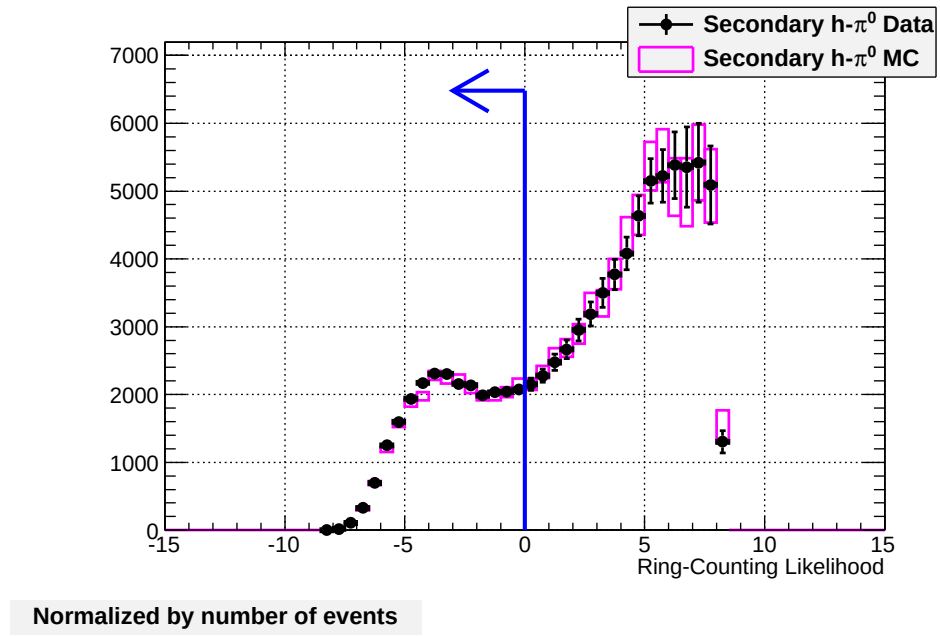

Figure 4.33: Ring counting likelihood distribution of the secondary hybrid-π^0 data (black) and Monte-Carlo (magenta) sample. The events selected by the T2K ν_e event selection have ring counting likelihood lower than 0 (one ring sample) and are indicated by the blue arrow. The error bars are calculated by taking the reuse into account.

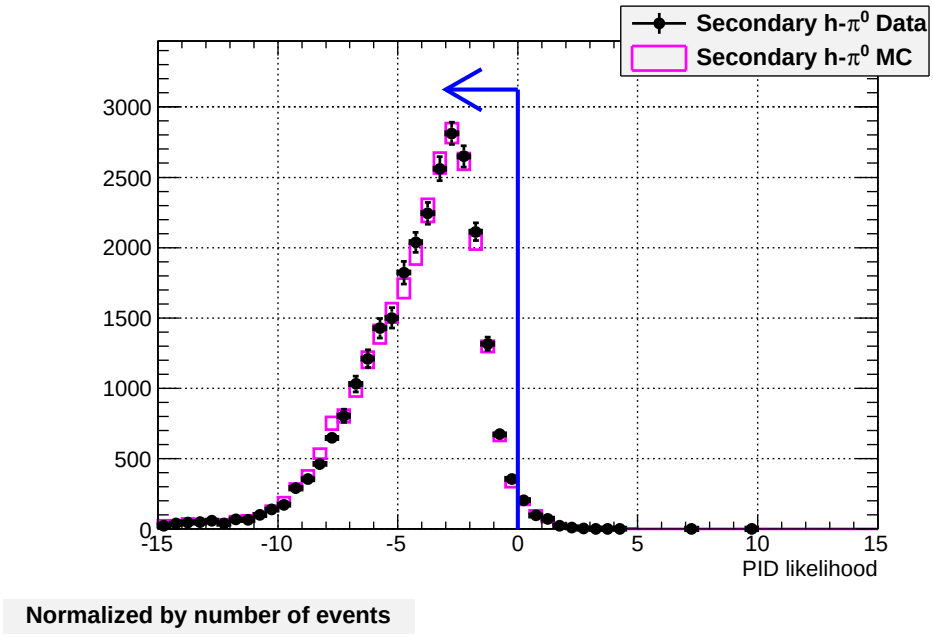

Figure 4.34: PID likelihood distribution of the secondary hybrid-π^0 data (black) and Monte-Carlo (magenta) sample. The events selected by the T2K ν_e event selection have PID likelihood lower than 0 (e-like sample) and are indicated by the blue arrow. The error bars are calculated by taking the reuse into account.

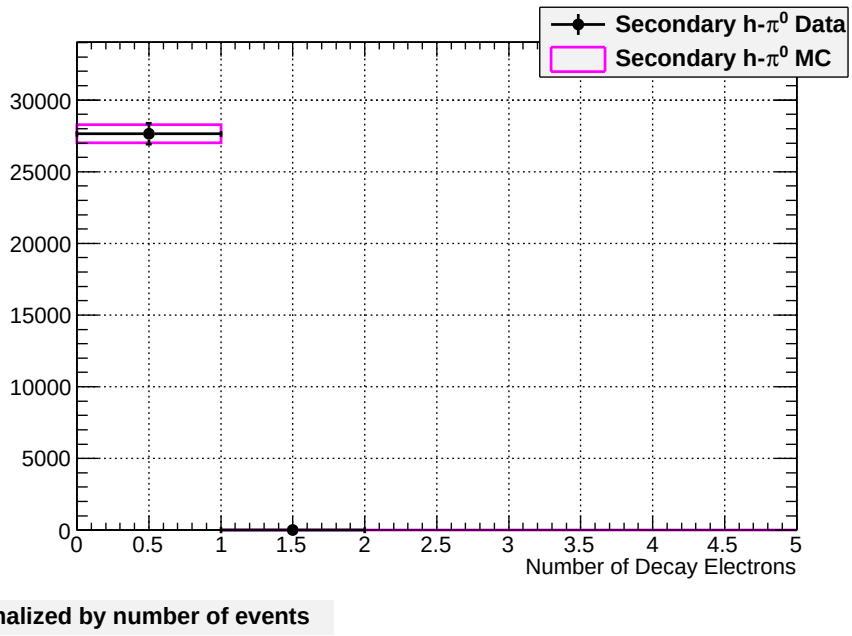

Figure 4.35: Number of decay electrons distribution of the secondary hybrid-π^0 data (black) and Monte-Carlo (magenta) sample. The events selected by the T2K ν_e event selection have 0 decay electrons. The error bars are calculated by taking the reuse into account.

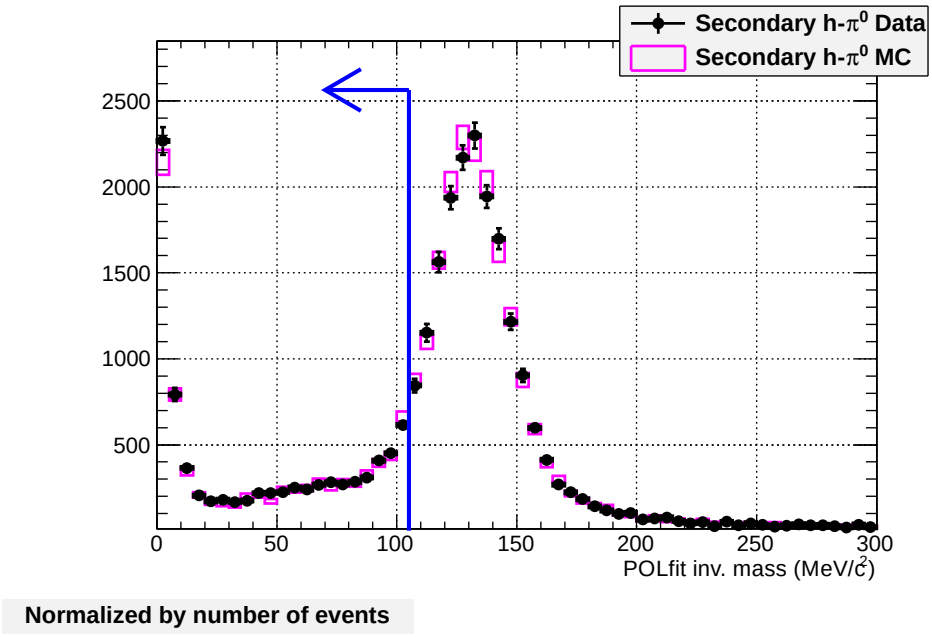

Figure 4.36: POLfit reconstructed π^0 mass distribution of the secondary hybrid-π^0 data (black) and Monte-Carlo (magenta) sample. The events selected by the T2K ν_e event selection have POLfit reconstructed π^0 mass lower than 105 MeV/c^2 and are indicated by the blue arrow. The error bars are calculated by taking the reuse into account.

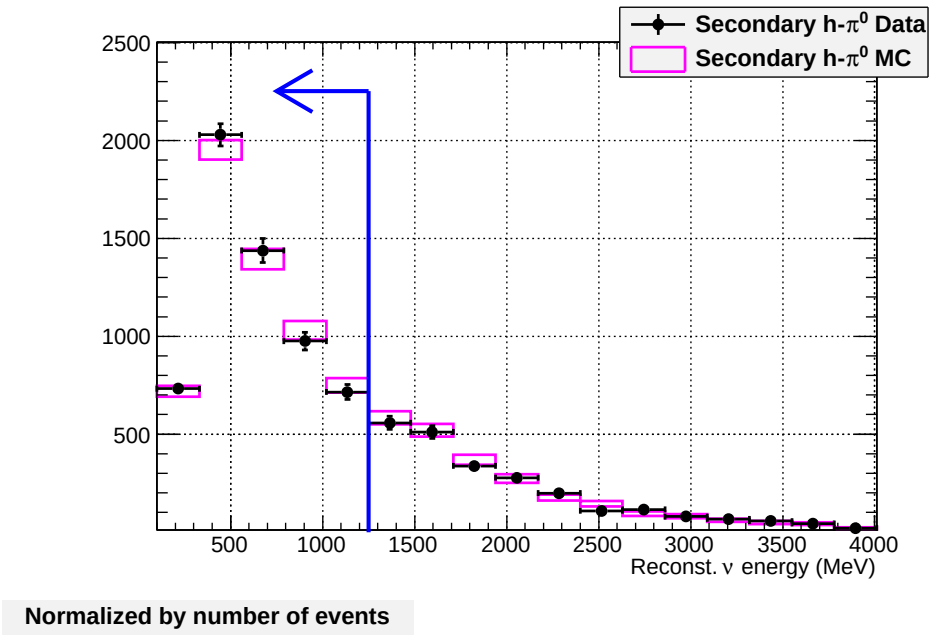

Figure 4.37: Reconstructed ν_e energy distribution of the secondary hybrid-π^0 data (black) and Monte-Carlo (magenta) sample. The events selected by the T2K ν_e event selection have reconstructed ν_e energy lower than 1250 MeV and are indicated by the blue arrow. The error bars are calculated by taking the reuse into account.

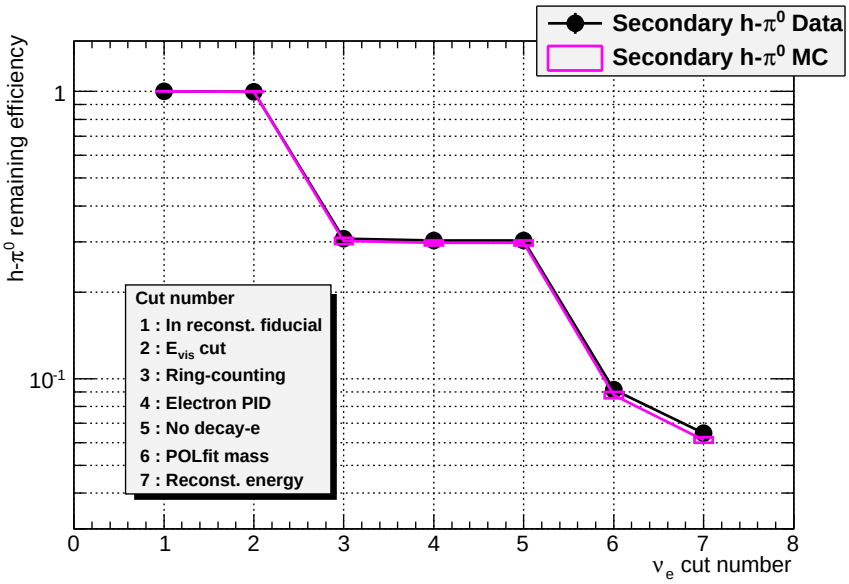

Figure 4.38: Efficiency of the T2K ν_e event selection for the secondary hybrid-π^0 data (black) and Monte-Carlo (magenta) sample in function of the cut number. The error bars are calculated by taking the reuse into account.

Table 4.3: Breakdown of events in the "other NC with π^0" sample with particles in the Monte-Carlo above Cerenkov threshold. For each final state, there is defined the number of events expected in run I+run II (and its fraction in the "other NC with π^0" sample). In the last column it is indicated how the error is estimated, which can be either by constructing a hybrid-π^0 sample (in which case the name of the sample is given) either by assuming some ad-hoc 100% error.

Final state	expected number of events in T2K run I+run II	systematic error
NC π^0+$\pi^\pm$	0.0235 ($\sim$ 48%)	use "hybrid-$\pi^0 + \pi^\pm$" sample
NC $\pi^0 + p$	0.0171 ($\sim$ 35%)	use "hybrid-$\pi^0 + p$" sample
NC $\pi^0 + p + \pi^\pm$	0.0029 ($\sim$ 6%)	use "hybrid-$\pi^0 + p + \pi^\pm$" sample
NC $\pi^0 + 2\pi^\pm$	0.0039 ($\sim$ 8%)	assume 100% error
NC $\pi^0 + \pi^0$	0.0005 ($\sim$ 1%)	assume 100% error
NC $\pi^0 + \pi^0 + p$	0.0005 ($\sim$ 1%)	assume 100% error
NC $\pi^0 + 3\pi^\pm$	0.0005 ($\sim$ 1%)	assume 100% error

For each of the sub-samples we have applied the same verifications applied to the usual hybrid-π^0 samples discussed previously, that is we have compared the shape of data and Monte-Carlo distributions along the event selection. These comparisons show compatible shapes for data and Monte-Carlo, as it was the case for the hybrid-π^0 samples, though with poorer statistics. Furthermore, we have calculated the systematic error related to each of these sub-samples with the same method described previously and the results are shown in table 4.4. In this table is also shown the result (σ) from combining these estimated systematic errors (σ_i) for each sub-sample with their weight from the fraction (f_i) of the sample (i) using the equation (4.1), leading to the overall estimated systematic error for the "other NC with π^0" background sample.

$$\sigma = \sqrt{\sum_i f_i^2 \sigma_i^2} \tag{4.1}$$

Table 4.4: Systematic error on the efficiency of the T2K ν_e event selection for each final state defined on table 4.3. For the constructed hybrid sample, this error was estimated with the hybrid sample, while for the final states with no hybrid sample, the systematic error was assumed 100% and merged in only one line. Finally in the last line is shown the final value of the systematic error estimated for the "other NC with π^0" sample.

Final state	fraction	systematic error
NC $\pi^0 + \pi^\pm$	48%	31.8%
NC $\pi^0 + p$	35%	30.7%
NC $\pi^0 + p + \pi^\pm$	6%	64.1%
remaining final states	11%	ad-hoc 100%
other NC with π^0	100%	**22.0%**

4.4.3 ν_μ CC with π^0 background

For the same reasons the "other NC with π^0" background sample needed to be divided so did the "ν_μ CC with π^0" background sample. The "final state" decomposition of this sample is shown in table 4.5 and the results from estimating the systematic error from adapting the hybrid-π^0 sample is shown in table 4.6. This error estimation is done in the same way as it was explained for the "other NC events with π^0" background.

We should note that one of the possible final states in the "ν_μ CC with π^0" sample shown in table 4.5 is the ν_μ CC π^0, for which we had not created a specific hybrid sample. The ν_μ CC π^0 sample is composed from events where the ν_μ CC interaction produced a μ and a π^0 and for which the μ momentum was below the Cerenkov threshold and therefore did not emit light and was not added to the final state. For this final state only one π^0 is produced as is the case for the "NC $1\pi^0$" sample, albeit with different π^0 momentum distribution. In order to reproduce the ν_μ CC π^0 final state and estimate the related systematic error, we have used the hybrid-π^0 sample created for study of NC $1\pi^0$ and re-weighted its π^0 momentum distribution to be that of the ν_μ CC π^0 final state.

Furthermore, all verifications that were performed to the other hybrid-π^0 samples were also performed for the samples composing the "ν_μ CC with π^0" final state samples. As for the other NC events with π^0 background samples we do not show here the data and

Table 4.5: Breakdown of events in the "ν_μ CC with π^0" sample with particles in the Monte-Carlo above Cerenkov threshold. For each final state, there is defined the number of events expected in run I+run II (and its fraction in the "ν_μ CC with π^0" sample). In the last column it is indicated how the error is estimated, which can be either by constructing a hybrid-π^0 sample (in which case the name of the sample is given) either by assuming some ad-hoc 100% error.

Final state	expected number of events in T2K run I+run II	systematic error
ν_μ CC $\pi^0 + \mu$	0.00250 ($\sim$ 50%)	use "hybrid-$\pi^0 + \mu$" sample
ν_μ CC π^0	0.00108 ($\sim$ 22%)	use existing "hybrid-π^0"
ν_μ CC $\pi^0 + \mu + \pi^\pm$	0.00075 ($\sim$ 15%)	use "hybrid-$\pi^0 + \mu + \pi^\pm$" sample
ν_μ CC $\pi^0 + \mu + p$	0.00055 ($\sim$ 11%)	assume 100% error
ν_μ CC $\pi^0 + \mu + 2\pi^\pm$	0.00005 ($\sim$ 2%)	assume 100% error

Table 4.6: Systematic error on the efficiency of the T2K ν_e event selection for each final state defined on table 4.5. For the constructed hybrid sample, this error was estimated with the hybrid sample, while for the final states with no hybrid sample, the systematic error was assumed 100% and merged in only one line. Finally in the last line is shown the final value of the systematic error estimated for the "ν_μ CC with π^0" sample.

Final state	fraction	systematic error
ν_μ CC $\pi^0 + \mu$	50%	89.2%
ν_μ CC π^0	22%	12.3%
ν_μ CC $\pi^0 + \mu + \pi^\pm$	15%	109.9%
remaining final states	13%	ad-hoc 100%
ν_μ CC with π^0	100%	**49.4%**

Monte-Carlo comparison along event selection of the hybrid samples and whose shapes are compatible between data and Monte-Carlo samples, though with poorer statistics that in the hybrid-π^0 sample.

4.4.4 Summary

Using the hybrid samples we have estimated the systematic error for the background samples highlighted in table 4.1. The result of these systematic error estimations is shown in table 4.7 that summarises the results that have been presented previously.

Table 4.7: Systematic error on the efficiency of the T2K ν_e event selection for each final state listed in table 4.1 using the hybrid samples.

Final state	systematic error
ν_μ CC with π^0	**49.4%**
NC $1\pi^0$	**11.8%**
other NC with π^0	**22.0%**

4.5 Impact of these results and perspectives

The estimation of the systematic error for the reconstruction efficiency of π^0 events in Super Kamiokande for the T2K ν_e appearance analysis with the hybrid samples provides the official value for such systematic error, which composes about a third of the total background events expected at SK. The estimated systematic error using the hybrid-π^0 samples has been used in the 2011 oscillation analysis and publication [13].

Recently, the T2K oscillation analysis group requested that the systematic errors at SK be quoted as a function of the reconstructed ring momentum and direction. Therefore the hybrid-π^0 analysis presented here was extended to take into account such request, in which case we estimate the systematic error using the same method presented here, but for the different momentum and direction ranges. This new results, which are not presented here, are the current official systematic error of detection efficiency of π^0 events at SK, and therefore used for the 2012 oscillation analysis.

Even though the hybrid samples have successfully estimated the systematic error on the reconstruction efficiency of π^0 events at SK we would still like to further reduce such error given that it is still among the dominant uncertainties for the SK detection efficiency.

Given that currently the statistical uncertainty of hybrid samples is still rather large we can expect a reduction of the systematic error, and possibly a better understanding of possible differences between data and Monte-Carlo, by increasing the number of events from the SK atmospheric ν_e sample. Currently the hybrid samples were created using all SK 4 data until February 2011 as it was the data available when we had performed the analysis, which correspond to 29 months of data, however at the moment there are more than 15 months of SK 4 atmospheric ν_e data that could be added to the construction of the hybrid samples. This improvement would reduce the statistical error of each hybrid sample by about 30% now, and could even further reduce the statistical error in the future, though the reduction will be rather slow as the data set increases.

Another possibility to reduce the statistical uncertainty of the hybrid sample would be to generate additional hybrid Monte-Carlo samples using different sets of SK 4 atmospheric ν_e Monte-Carlo. By combining the results from these different hybrid Monte-Carlo generations it would be possible to reduce the uncertainty on the detector efficiency of the hybrid Monte-Carlo sample to be negligible in relation to the statistical uncertainty of the hybrid data sample. Note this method can be combined with the increase of the number of SK 4 atmospheric events used to generate the hybrid samples aforementioned.

Even though there are possible means to reduce the currently estimated systematic error of the reconstruction efficiency of π^0 events in Super Kamiokande, as it was just mentioned, the proposed methods are limited by how much we could reduce the systematic errors. One possible method to further reduce these errors would be to combine the analysis presented here with other analysis that could study separately parts of the reconstruction algorithm independently, for example by using the Cone Generator presented in chapter 3 to study the ring counting or POLfit algorithm. In this case it is essential to perform further studies on how to combine both results and which results from the Cone Generator, in the given example, are needed. We expect that studies using the Cone Generator to control part of the π^0 systematic error related to ring finding algorithms should reduce the systematics, specially taking into account that the Cone Generator samples are not limited by statistics as is the hybrid-π^0 sample.

Finally, the TRIUMF T2K/SK group has been developing a new reconstruction with the intent of better tagging events at SK. This new reconstruction should reduce the contamination of π^0 events in the T2K ν_e search background. For the π^0 related background the main difference of the fitter would be to replace POLfit by a new π^0 fitter being developed by the TRIUMF group. The new reconstruction uses the timing information of the event in addition to the charge information which is used by POLfit. Furthermore the new reconstruction also takes into account the conversion length of the γ which are fitted to improve the performance of the algorithm, which is not currently done by POLfit. When this new reconstruction algorithm will be accepted and ready for use in publications it will be essential to reevaluate the systematic errors estimated in this chapter, and such estimation can be done by reprocessing the hybrid samples using the new algorithm. The same analysis method can still be used in this case.

Chapter 5

First study of the CP violation phase using T2K ν_e appearance data

Contents

5.1 Introduction

Using the data taken until the 2011 earthquake, the T2K collaboration has published its result for the ν_e appearance with a ν_μ beam [13]. In this analysis, the T2K data was used to estimate the value of $\sin^2 2\theta_{13}$ between 0.03 (0.04) and 0.28 (0.34) for $\delta_{CP} = 0$ and normal (inverted) hierarchy at 90% confidence level. At the time this analysis was performed the value of such angle had not yet been measured by reactor experiments, as explained in section 1.2.4, therefore it was not possible in such analysis to separate the effect for $\sin^2 2\theta_{13}$ and δ_{CP} phase. The results were presented in two-dimensional correlation plots of $(\sin^2 2\theta_{13}, \delta_{CP})$ for each possible hierarchy, as shown in figure 5.1.

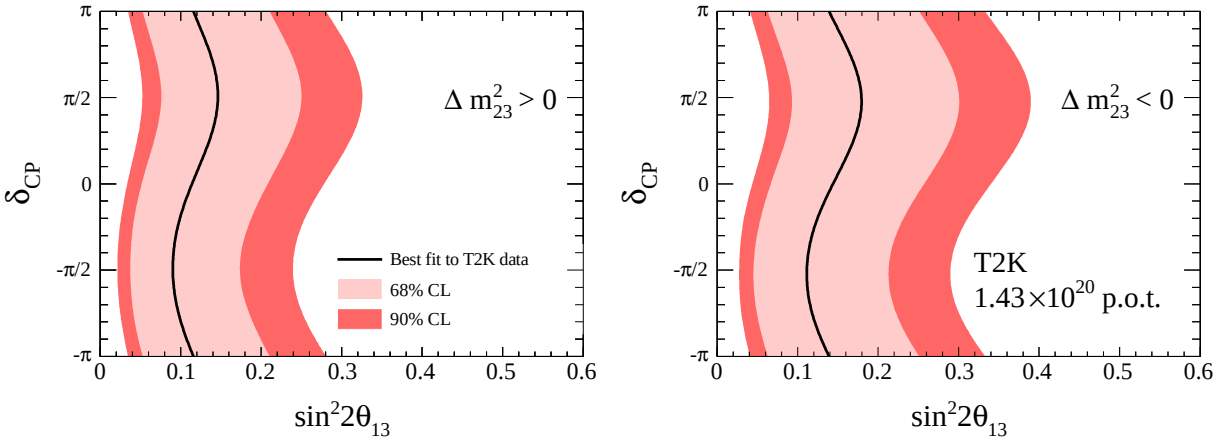

Figure 5.1: Best-fit and allowed region at 68% and 90% C.L. for normal hierarchy (left) and inverted hierarchy (right) given by the official 2011 ν_e appearance search [13]. The shaded region is allowed for each hierarchy case. This plot shows 1-dimensional allowed region of $\sin^2 2\theta_{13}$ for each δ_{CP} value, and uses a raster scan for constructing the Feldman-Cousins likelihood ratio.

With the current knowledge, however, it is possible to combine the $\sin^2 2\theta_{13}$ measurement from the reactor experiments[1] with the data taken by T2K to do a first estimative of the δ_{CP} phase value. This analysis will be described and its results, using the same data set as used in [13], will be quoted in this chapter.

We should also note that using the current T2K data we cannot directly measure δ_{CP} because the oscillation probability terms where the CP violation phase appears are always dependent on the other mixing parameters. Given such dependency, we will take into account the uncertainties on all the measured parameters for a correct estimation of the δ_{CP} phase. The uncertainties on the oscillation parameters were defined previously and summarized in table 1.3, which for simplicity is also shown in table 5.1.

5.2 Definition of relevant quantities for this oscillation analysis

In order to be able to take into account the uncertainty of the oscillation parameters given in table 1.3 we have decided that the best approach would be using the Bayes theorem [14]

[1] For this analysis we will take into account only the Daya-Bay result [58], as explained in section 1.2.4.

to calculate the probability of a set of oscillation parameters (called O_i, the i-th set of possible oscillation parameters) to be consistent with the measurement performed by T2K (called M). This probability is written using the usual conditional probability notation as $\mathcal{P}(O_i|M)$.

From Bayes theorem we can write the equation (5.1)

$$\mathcal{P}(O_i|M) = \frac{\mathcal{P}(M|O_i)\mathcal{P}(O_i)}{\mathcal{P}(M)} \tag{5.1}$$

where $\mathcal{P}(O_i|M)$ is written as function of :

- The prior $\mathcal{P}(O_i)$, that is the probability of a given set of oscillation parameters given the current knowledge coming from independent measurements.
- The $\mathcal{P}(M|O_i)$, that is the probability to obtain the results from T2K (M) given the oscillation parameters (O_i). Note that $\mathcal{P}(M|O_i)$ and $\mathcal{P}(O_i|M)$ differ in the sense that both represents the same probability function where in one case we study the probability of M assuming O_i, while in the other case we assume the probability of O_i assuming M, that is in each case we study the projection of this probability in a different axis.
- The $\mathcal{P}(M)$, that is a normalization factor related to the probability of the measurement T2K made which is the same for any oscillation parameters.

The $\mathcal{P}(O_i|M)$ defines a probability density function of O_i, which by definition has integral over all O_i to be 1. For the oscillation analysis, however, we need always to compare the relative probability between the different parameter sets O_i and O_j for $i \neq j$, that is $\frac{\mathcal{P}(O_i|M)}{\mathcal{P}(O_j|M)}$, to verify if one parameter is more likely than another one. To better reflect such need we will redefine the probability density functions to have maximum probability to be 1, and to distinguish these definitions of probability we use P to note the probabilities which have maximum of 1 and $\mathcal{P}$ to note the probabilities that are correctly normalized, the difference between P and $\mathcal{P}$ is therefore only a normalization factor.

This new definition has the advantage that it corresponds by construction to the relative probability, which simplifies its usage in the oscillation analysis, while being only different by a normalization factor. Furthermore this redefinition of the probability density function simplifies the formulas of some of the probabilities we need to define because it is no longer needed to define a normalization factor obtained from the functions integral. Using this definition of the probability density function we have $P(M) = 1$ given that this probability does not depend on O_i.

Table 5.1: Summary of current best knowledge of the neutrino oscillation parameters. This is same table as 1.3.

$\sin^2(2\theta_{12})$	$= 0.861^{+0.026}_{-0.022}$
$\sin^2(2\theta_{23})$	$= 1.000^{+0.000}_{-0.045}$
$\sin^2(2\theta_{13})$	$= 0.092 \pm 0.017$
Δm^2_{21}	$= (7.59 \pm 0.21)10^{-5}$ eV^2/c^4
$\lvert\Delta m^2_{32}\rvert$	$= (2.43 \pm 0.13)10^{-3}$ eV^2/c^4

The prior $P(O_i)$ is defined for a given $O_i = (\theta_{12}, \theta_{23}, \theta_{13}, \Delta m^2_{21}, \Delta m^2_{32}, \delta_{CP})_i$ by combining the probability for the realisation of each of these components of O_i independently from the prior of each of these oscillation parameters, as shown in equation (5.2). The prior for each component of O_i is given in equations (5.3) to (5.8) for $(\Delta m^2_{21})_i$, $(\Delta m^2_{32})_i$, $(\theta_{12})_i$, $(\theta_{23})_i$, $(\theta_{13})_i$ and $(\delta_{CP})_i$ respectively, where the prior are assumed to be either Gaussian distribution if such parameter is already measured or constant distribution if that is not the case. More precisely, in the case the parameter is already measured, we assume Gaussian distributions if the error is symmetric and asymmetric Gaussian distributions if the error is asymmetric. In these equations the mean values from table 1.3 are written as $\langle \text{parameter} \rangle$, their uncertainty are written as $\sigma_{\text{parameter}}$ when they are symmetric, or as $\sigma^{+}_{\text{parameter}}$ and $\sigma^{-}_{\text{parameter}}$ for their upper and lower bounds, respectively, when they are asymmetric.

Assuming the independence hypothesis explained in section 1.2.4 :

$$P(O_i) = P\Big((\Delta m^2_{21})_i\Big) \cdot P\Big((\Delta m^2_{32})_i\Big) \cdot P\Big((\theta_{12})_i\Big) \cdot P\Big((\theta_{23})_i\Big) \cdot P\Big((\theta_{13})_i\Big) \cdot P\Big((\delta_{CP})_i\Big) \tag{5.2}$$

with :

$$P\Big((\Delta m^2_{21})_i\Big) = \exp\left[-0.5\left(\frac{(\Delta m^2_{21})_i - \langle \Delta m^2_{21} \rangle}{\sigma_{\Delta m^2_{21}}}\right)^2\right] \tag{5.3}$$

$$P\Big((\Delta m^2_{32})_i\Big) = \exp\left[-0.5\left(\frac{(\Delta m^2_{32})_i - \langle \Delta m^2_{32} \rangle}{\sigma_{\Delta m^2_{32}}}\right)^2\right] \tag{5.4}$$

$$P\Big((\theta_{12})_i\Big) = \begin{cases} \exp\left[-0.5\left(\frac{(\sin^2 2\theta_{12})_i - \langle \sin^2 2\theta_{12} \rangle}{\sigma^{+}_{\sin^2 2\theta_{12}}}\right)^2\right] & , (\sin^2 2\theta_{12})_i \geq \langle \sin^2 2\theta_{12} \rangle \\ \exp\left[-0.5\left(\frac{(\sin^2 2\theta_{12})_i - \langle \sin^2 2\theta_{12} \rangle}{\sigma^{-}_{\sin^2 2\theta_{12}}}\right)^2\right] & , (\sin^2 2\theta_{12})_i < \langle \sin^2 2\theta_{12} \rangle \end{cases} \tag{5.5}$$

$$P\Big((\theta_{23})_i\Big) = \begin{cases} 0 & , (\sin^2 2\theta_{23})_i > \langle \sin^2 2\theta_{23} \rangle (= 1) \\ \exp\left[-0.5\left(\frac{(\sin^2 2\theta_{23})_i - \langle \sin^2 2\theta_{23} \rangle}{\sigma^{-}_{\sin^2 2\theta_{23}}}\right)^2\right] & , (\sin^2 2\theta_{23})_i \leq \langle \sin^2 2\theta_{23} \rangle \end{cases} \tag{5.6}$$

$$P\Big((\theta_{13})_i\Big) = \exp\left[-0.5\left(\frac{(\sin^2 2\theta_{13})_i - \langle \sin^2 2\theta_{13} \rangle}{\sigma_{\sin^2 2\theta_{13}}}\right)^2\right] \tag{5.7}$$

$$P\Big((\delta_{CP})_i\Big) = \begin{cases} 1 & , (\delta_{CP})_i \in [0, 2\pi[\\ 0 & , (\delta_{CP})_i \notin [0, 2\pi[\end{cases} \tag{5.8}$$

The probability of the T2K measurement given the oscillation parameter $P(M|O_i)$ depends on the data we use. In this analysis we will perform a rate only analysis to measure the ν_e appearance in the T2K beam, that is, we will compare the number of observed events at SK (n_{obs}) with the number of expected events at SK ($(n_{exp})_i$, for a given O_i) as was performed in [13]. In section 5.3 the T2K data sample used for this analysis, and its event section will be described. For a given O_i we expect that n_{obs}

follows a Poisson distribution[2] with mean $(n_{exp})_i$, because this distribution expresses the probability of a given number of events to happen in a fixed interval given an average rate of events and assuming one event does not depend on the previous events or the total number of observed events [14]. Therefore the value of $P(M|O_i)$ is given by equation (5.9), where by construction the probability has a maximum of 1.

$$P(M|O_i) = \frac{\text{Poisson}(n_{obs}; (n_{exp})_i)}{\text{Poisson}(n_{obs}; n_{obs})} = \left(\frac{(n_{exp})_i}{n_{obs}}\right)^{n_{obs}} e^{n_{obs}-(n_{exp})_i} \tag{5.9}$$

In the expression (5.1) we have not taken into account the systematic errors ε from the T2K measurement itself. These systematic errors obviously need to be taken into account for a correct oscillation analysis. The probability of a given O_i taking into account the systematic errors ε is written as in equation (5.10), where the probability is the maximum probability that can be obtained from a given experiment of ε. ε_j denotes a particular realisation of ε.

$$P(O_i|M, \varepsilon) = \max_j \Big(P(O_i|M, \varepsilon_j) \Big) \tag{5.10}$$

The probability of O_i given the measurement M and a systematic error set ε_j can be calculated again via the Bayes theorem as shown in (5.11).

$$\mathcal{P}(O_i|M, \varepsilon_j) = \frac{\mathcal{P}(M|O_i, \varepsilon_j)\mathcal{P}(O_i, \varepsilon_j)}{\mathcal{P}(M)} = \frac{\mathcal{P}(M|O_i, \varepsilon_j)\mathcal{P}(\varepsilon_j|O_i)\mathcal{P}(O_i)}{\mathcal{P}(M)} \tag{5.11}$$

The probabilities defined in (5.11) are mostly defined as previously. More precisely, the $P(M)$ and $P(O_i)$ are defined exactly as previously, and the $P(M|O_i, \varepsilon_j)$ has the same formula as $P(M|O_i)$, where now the number of expected events at SK depends also on the specific realisation of systematic errors used for the probability estimation. Finally $P(\varepsilon_j|O_i)$[3] is the probability that we have a given realisation of systematic errors given the oscillation parameters and is written similarly as the $P(O_i)$ expression. The detail of the each component of ε taken into account in the this analysis will be described in section 5.4 along with the expression of the $P(\varepsilon_j|O_i)$.

In table 5.2 are summarized the main quantities defined in this section along with the formula for the defined probabilities.

5.2.1 Calculation of oscillation probability with a Gaussian systematic error on the number of expected events

Even though we have performed a full systematic error estimation to perform the oscillation analysis it is also useful to have a simpler estimative by supposing that the composition of all systematic errors can be summarized as a systematic error on the number of expected events, independent of the oscillation parameters. This systematic error treatment is specially useful to evaluate the expected sensitivity of the oscillation analysis assuming improvements in the understanding of the detectors and their responses. For this estimation, the systematic error is assumed Gaussian around the number of expected events with given width (σ_{SE}). In the published T2K ν_e analysis [13] $\sigma_{SE} = 18\%$.

[2] We note here the Poisson probability of k events in a distribution with parameter λ as $\text{Poisson}(k; \lambda)$. Therefore the Poisson probability is written as $\text{Poisson}(k; \lambda) = \frac{\lambda^k e^{-\lambda}}{k!}$.

[3] In the case where the systematic errors do not depend on the oscillation parameters this can also be written simply as $P(\varepsilon_j)$.

Table 5.2: Summary of relevant quantities for this oscillation analysis.

O_i	:	Set of oscillation parameters	
M	:	Measurement by T2K used for this analysis	
ε	:	Systematic errors on the T2K experiment	
ε_j	:	A particular experience of systematic errors	
$P(O_i\|M)$	:	Probability of the O_i parameter set given the T2K measurement	(5.1)
$P(O_i\|M,\varepsilon)$	:	Probability of the O_i parameter set given the measurement and systematic errors	(5.10)
$P(M\|O_i)$	:	Probability to measure M given an oscillation parameter set O_i	(5.9)
$P(M\|O_i,\varepsilon_j)$	:	Probability to measure M given an oscillation parameter set O_i and assuming that the systematic errors true value is ε_j	(5.9)
$P(O_i)$	:	Probability of the O_i parameter set from our current knowledge	(5.2)
$P(\varepsilon_j\|O_i)$	:	Probability to have a set of systematic errors ε_j given the oscillation parameters O_i	(5.15)

In this case we know the expression $P(\varepsilon_j|O_i)$ to be (5.12), where ε_j is fractional shift from the number of expected events in SK. Likewise the $P(M|O_i,\varepsilon_j)$ is written as in expression (5.13).

$$P(\varepsilon_j|O_i) = P(\varepsilon_j) = \exp\left[-0.5\left(\frac{\varepsilon_j}{\sigma_{SE}}\right)^2\right] \tag{5.12}$$

$$P(M|O_i,\varepsilon_j) = \left(\frac{(n_{exp})_i(1+\varepsilon_j)}{n_{obs}}\right)^{n_{obs}} e^{n_{obs}-(n_{exp})_i(1+\varepsilon_j)} \tag{5.13}$$

In this case we can explicitly calculate for which ε_j the probability $P(O_i|M,\varepsilon_j)$ is maximal and therefore calculate $P(O_i|M,\varepsilon)$ explicitly. This maxima calculation is performed in appendix E and was calculated to be for ε_j given by equation (5.14), which for small systematic error depends roughly only on the difference between the observed and expected number of events and on the systematic error.

$$\begin{aligned}\varepsilon_j &= \frac{-1-(n_{exp})_i\sigma_{SE}^2+\sqrt{(1-(n_{exp})_i\sigma_{SE}^2)^2+4n_{obs}\sigma_{SE}^2}}{2} \\ &\approx (n_{obs}-(n_{exp})_i)\,\sigma_{SE}^2 \quad \text{for } \sigma_{SE}^2 \ll 1\end{aligned} \tag{5.14}$$

5.3 T2K data sample used in this analysis

The T2K data sample used for the current oscillation analysis consists of the first two physics runs of T2K : Run I (January to June 2010) and Run II (November 2010 to March 2011), that is all data taken until the 2011 earthquake. This data corresponds to $1.43 \cdot 10^{20}$ POT after detector quality cuts as shown in figure 5.2.

For this oscillation analysis, as was mentioned previously, we have decided to take into account only the number of ν_e events measured at SK and compare with the expected number of ν_e events. More precisely, the ν_e events which will be measured at SK are defined by the event selection described in section 2.5.3 for the ν_e CCQE sample. After the ν_e CCQE event selections the remaining number of ν_e candidate events at SK (n_{obs})

was 6 events, as shown in figure 5.3 where the number of observed events is shown as function of the POT.

5.4 Systematic errors on the number of expected events at SK

The number of expected events at SK is estimated using the T2K Monte-Carlo, therefore any uncertainty on the neutrinos flux at SK, their interaction cross-section or the detection efficiency needs to be taken into account to compute total systematic error. The estimation of such systematic errors has been performed by several different working groups represents a large amount of work that is described in different T2K internal technical notes not explained here in detail. In this section we will only present a brief description of what has been taken into account to compute the systematic error.

These uncertainties define the $P(\varepsilon_j|O_i)$ as given by equation (5.15) where $\varepsilon_j = (\varepsilon_j^{\mathrm{F}}, \varepsilon_j^{\mathrm{I}}, \varepsilon_j^{\mathrm{D}})$ is the decomposition of the global systematic error set ε_j into components related to the neutrino flux at SK (F), interaction (I) and detection efficiency (D) uncertainties, which will be discussed in sections 5.4.1, 5.4.2 and 5.4.3, respectively.

$$P(\varepsilon_j|O_i) = P(\varepsilon_j^{\mathrm{F}}|O_i)P(\varepsilon_j^{\mathrm{I}}|O_i)P(\varepsilon_j^{\mathrm{D}}|O_i) \tag{5.15}$$

5.4.1 Neutrino flux uncertainties at the far detector (F)

The neutrino flux at the far detector is estimated by the measured neutrino flux at the near detector (ND280) which is then extrapolated to the far detector (SK) position. From this description it is clear that the error on the neutrino flux has two components : the uncertainty in the measurement of the neutrino flux at the ND280 detector and the uncertainty of the extrapolation of the flux from the near to the far detector. Each of these uncertainties is estimated by a different group, namely the T2K ND280 group and the T2K Beam group, respectively.

The uncertainty coming from the measurement at ND280 is divided in statistical uncertainty and detector systematics. The statistical uncertainty is considered to be a Poisson error on the number of ND280 events ($N_{\mathrm{data}}^{\mathrm{ND280}}$). The fractional fluctuation on the number of events is noted $\varepsilon_j^{F_1}$ and the fluctuation of the number of events is about 2.7%. The detector systematic uncertainties are estimated to be $\sigma^{F_2} = 4.2\%$[4] Gaussian error on the number of ND280 events, with value $\varepsilon_j^{F_2}$ for a given realisation of the systematic errors. This uncertainties are described in more details in [72].

The uncertainty in the extrapolation of the measurement from the near detector to the far detector is calculated on the ratio of the number of selected events in the far and near detectors. For this uncertainty calculation it is essential to take into account the partial cancellation of the systematic errors between the near and far detectors. The cancellation, and consequently the uncertainty, depends on the neutrino energy spectrum at both detectors which depends on the oscillation parameter. The estimation of the uncertainty on the extrapolation of the number of measured events between the near and far detectors is rather complicated and depends also on the knowledge of the beam composition (measured by NA61 [63] and monitors on the proton beam line) and the

[4] In fact in reference [72] the estimated ND280 detector systematic uncertainty is (-3.6,+4.2)% and for simplicity we use only the upper bound as symmetric Gaussian error.

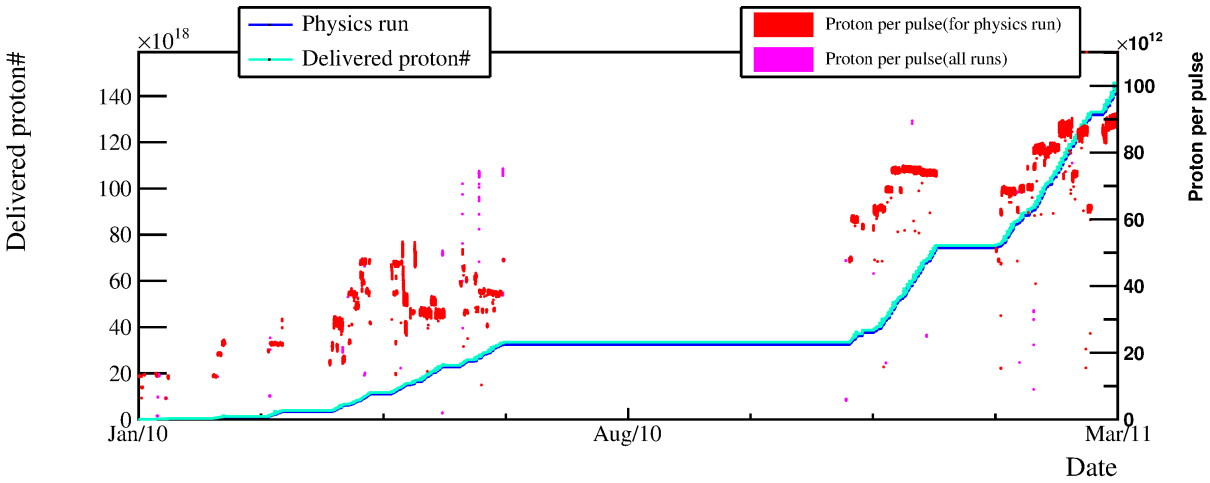

Figure 5.2: Accumulated number of protons on target from T2K Run I and Run II as function of date. Run I was between January and June 2010 (6 months) and Run II was between November 2010 and March 2011 (5 months).

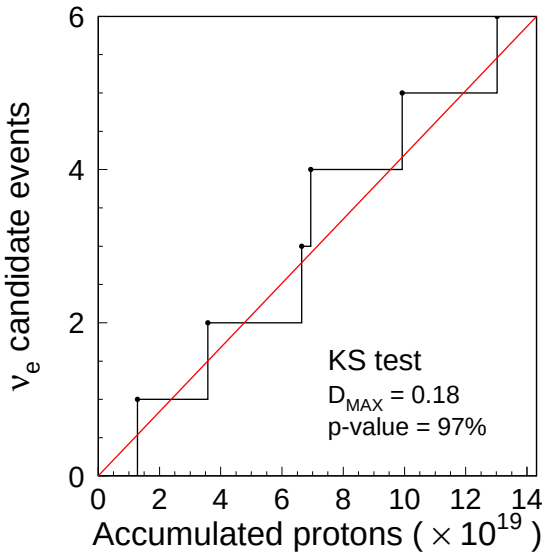

Figure 5.3: Number of candidate ν_e events as function of accumulated number of protons on target. In red is also shown the hypothesis which is verified with the Kolmogorov–Smirnov (KS) test showing good agreement with data. The KS test compares a probability distribution with a sample to quantify the maximal distance between such distributions and the probability they are the same given the maximal distance between them.

beam direction (measured by the muon monitor and INGRID). We will use the software provided by the T2K Beam group that takes as input the energy spectrum expected for signal and background at the ND280 and SK to calculate the uncertainty on the number of expected events at SK $\sigma^{F_3}(O_i)$. This uncertainty estimation is described in more details in [73]. The calculated systematic error follows a Gaussian distribution applied to the number of events at SK calculated for each oscillation parameter set O_i. Typically the value of $\sigma^{F_3}(O_i)$ is between 7.5% and 10%.

As described the systematic error due to uncertainties on the neutrino flux at the far detector is parametrized as 3 different independent errors, therefore one set of systematic errors is described by $\varepsilon_j^{\mathrm{F}} = (\varepsilon_j^{\mathrm{F}_1}, \varepsilon_j^{\mathrm{F}_2}, \varepsilon_j^{\mathrm{F}_3})$. The $\varepsilon_j^{\mathrm{F}_1}$ term corresponds to the statistical uncertainty on the number of events measured at ND280 and its probability density function described by a Poisson distribution. The $\varepsilon_j^{\mathrm{F}_2}$ term corresponds to the ND280 detector systematic uncertainty and is considered to be Gaussian. Finally the $\varepsilon_j^{\mathrm{F}_3}$ term corresponds to the flux extrapolation uncertainty from the near to the far detector. This last term is also considered to be Gaussian with width depending on the value of the set O_i of oscillation parameters. We obtain :

$$P(\varepsilon_j^{\mathrm{F}}|O_i) = \left(1+\varepsilon_j^{\mathrm{F}_1}\right)^{N_{\mathrm{data}}^{\mathrm{ND280}}} e^{-\varepsilon_j^{\mathrm{F}_1} N_{\mathrm{data}}^{\mathrm{ND280}}} \exp\left[-0.5\left(\frac{\varepsilon_j^{\mathrm{F}_2}}{\sigma^{\mathrm{F}_2}}\right)^2\right] \exp\left[-0.5\left(\frac{\varepsilon_j^{\mathrm{F}_3}}{\sigma^{\mathrm{F}_3}(O_i)}\right)^2\right] \tag{5.16}$$

5.4.2 Uncertainties on neutrino interaction (I)

The uncertainties on the neutrino interaction absolute and relative cross-sections are computed by the T2K Neutrino Interaction Working Group (NIWG) and are summarized in [74]. This group used first external data and recently started using the ND280 cross-section data to estimate global and relative cross-sections to determine the composition of final states to be observed in SK shown in table 4.1 for example. The uncertainties provided by the NIWG are different weightings to be used at the T2K MC to take into account uncertainties of the neutrinos relative cross-sections both at the near detector and the far detector.

Table 5.3 shows the cross section uncertainties for charged and neutral current interactions in relation to the CCQE cross-section. These uncertainties are considered totally correlated between the two energy bins and not correlated between types of interactions. In addition to these errors listed on table 5.3 it is also added an additional 6% uncertainty to the ν_e CC interactions from the uncertainty between the cross-section ν_e CC and ν_μ CC cross-sections.

The uncertainty of the CCQE interaction properties[6] between the near and far detector is calculated as a function of the true neutrino energy by comparing the prediction from different models implemented in different interaction libraries. This error is larger for small neutrino energies due to the differences between the different methods in which it is more pronounced at this energy region, as shown in figure 5.4. This shape error is

[5]The coherent π production differ from the single π production in the sense that the single π production happen in interactions between the ν and a nucleon and on the other hand the coherent π production happen with the interaction of the ν coherently with the whole nucleus.

[6]The difference between interaction properties between near and far detectors arise from the difference in the detector materials and acceptance between the detectors.

applied to the SK number of events directly to take into account differences between the normalization from ND280 and SK due to the uncertainty of neutrino interactions with matter.

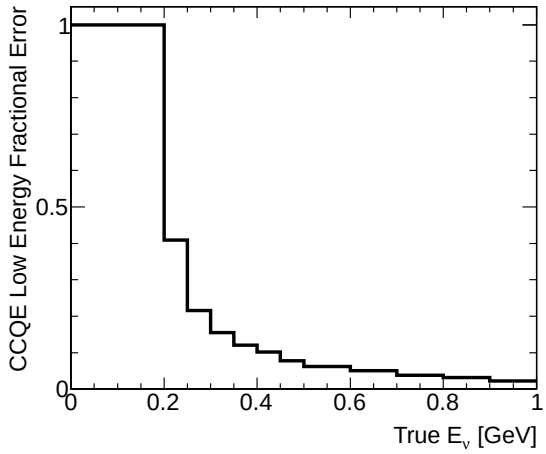

Figure 5.4: Fractional systematic uncertainty on CCQE events as function of true neutrino energy. This error takes into account the differences between the CCQE interaction properties in the near and far detectors due to differences in the target material and acceptance between these detectors.

Finally the last uncertainty taken into account linked to the neutrino interactions is the uncertainty on the fraction for each "Final State Interaction" (FSI) that is calculated for both SK and ND280. At SK this uncertainty is parametrized as a function of reconstructed neutrino energy and were computed for signal and background separately and is shown in figure 5.5. At the ND280 this uncertainty was estimated by changing the ND280 Monte-Carlo parameters for nucleon ejections, pion interaction and interaction kinematics which yielded an uncertainty of 3.7% applied to the number of events observed at the ND280. The FSI uncertainty at the ND280 and SK are assumed to be not correlated given the huge differences between the detectors and detection techniques.

As described, the systematic error due to uncertainties in the neutrino interaction are

Table 5.3: Fractional systematic uncertainty on neutrino NC and CC interactions cross-section for single π production, coherent π production[5] and other production types (such as multiple π production and deep inelastic scattering) classified as "others". The fractional systematic uncertainty is relative to the cross-section of CCQE events.

Mode	$<$2 GeV	$>$2 GeV
CC 1π	30%	20%
CC coherent π	100%	100%
CC other	30%	25%
NC $1\pi^0$	30%	20%
NC coherent	30%	30%
NC other	30%	30%

parametrized by 10 different independent errors[7], therefore one set of systematic errors is described by $\varepsilon_j^{\mathrm{I}} = (\varepsilon_j^{\mathrm{I}_1}, \ldots, \varepsilon_j^{\mathrm{I}_{10}})$ that represent how much each parameter changes from the model central value, with Gaussian shapes, with uncertainties given by $\sigma^{\mathrm{I}_k}(O_i)$ for $\varepsilon_j^{\mathrm{I}_k}$, which take the values presented in this chapter. Finally, the $P(\varepsilon_j^{\mathrm{I}}|O_i)$ as the product of the probability given for each $\varepsilon_j^{\mathrm{I}_k}$ as given by the expression (5.17).

$$P(\varepsilon_j^{\mathrm{I}}|O_i) = \prod_{k=1}^{10} \exp\left[-0.5\left(\frac{\varepsilon_j^{\mathrm{I}_k}}{\sigma^{\mathrm{I}_k}(O_i)}\right)^2\right] \tag{5.17}$$

5.4.3 Detection uncertainty in Super Kamiokande (D)

The final systematic error that needs to be taken into account for this oscillation analysis is the uncertainty on the detection and selection of each type of event in SK. The different event types are shown in table 4.1.

We have already described in detail in chapter 4 the estimation of the detection efficiency of events with a π^0 "final state interaction" for the T2K ν_e event selection. Such FSI compose about 38% of the background to the oscillation analysis. Other analysis have been performed by the T2K-SK group to estimate the detector uncertainty of other final states present on table 4.1 and are summarized in [71].

After having estimated detector efficiency uncertainty for several different final states (and assuming an ad-hoc error of 100% for each algorithm where systematic error was not estimated) the T2K-SK group performed a Monte-Carlo calculation to summarize systematic errors on the number of signal and background events. The error on the number of signal and background events are considered completely correlated because the error sources are similar given that they are defined by SKDETSIM and the reconstruction algorithms that are the same for both type of events. Furthermore about 50% of the background is composed by ν_e CCQE interaction (coming from the intrinsic ν_e composition of the T2K beam) which is also roughly all the signal and therefore indicates a large correlation between the samples. Given this correlation both errors are determined by one Gaussian with width $\sigma^{\mathrm{D}}(O_i)$ that is used for the signal error and accordingly scaled for the background error defining $P(\varepsilon_j^{\mathrm{D}}|O_i)$ to be given by the expression (5.18), with the values of $\sigma^{\mathrm{D}}(O_i)$ given by table 5.4 for signal and background.

Note that, as mentioned in the end of chapter 4, the uncertainties are not exactly the same used for the Monte-Carlo estimation performed by the T2K-SK group, though the method to calculate them is the same. This was done to keep compatibility of the systematic error between different oscillation analysis.

$$P(\varepsilon_j^{\mathrm{D}}|O_i) = \exp\left[-0.5\left(\frac{\varepsilon_j^{\mathrm{D}}}{\sigma^{\mathrm{D}}(O_i)}\right)^2\right] \tag{5.18}$$

We should furthermore note that because of recent improvements which were performed on the systematic errors related to detector efficiency described in this thesis (chapter 4) we have decided to use the systematic error on detector efficiency estimated for the 2012a analysis which are presented in table 5.4 from [71]. On the other hand,

[7] The 10 systematic errors mentioned here are the 6 systematic errors shown in table 5.3, the ν_e CCQE interaction cross-section uncertainty in relation to ν_μ CCQE, the CCQE uncertainty as function of true neutrino energy and the FSI uncertainty for ND280 and SK.

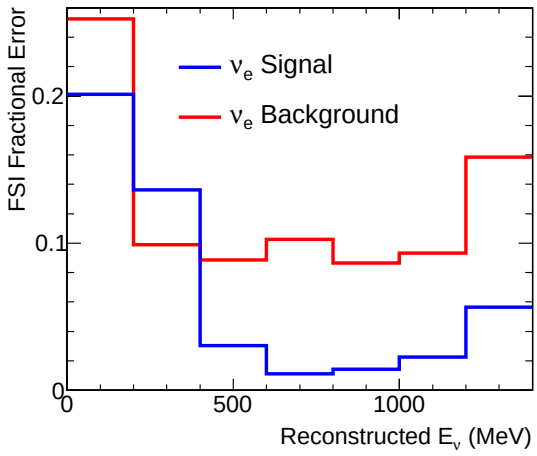

Figure 5.5: Uncertainty of the "final state interaction" (FSI) at SK as function of the reconstructed neutrino energy for signal and background. Note that the signal is divided in less different final states than the background as shown in table 4.1 and that the background is composed of several hadronization. Therefore the signal FSI uncertainty is smaller than the background FSI uncertainty at SK.

Table 5.4: Breakdown of the systematic error due to the T2K ν_e event selection for signal and background events for the different final states described in table 4.1. $\delta n/n$ is the fractional error estimated for the given final state while $\delta n/\Sigma n$ is the fractional error in relation to the total sample. Note that when $\delta n/\Sigma n$ more than one algorithm has not been studied for a given sample its error is larger than 100%.

Event type	Fraction (%)	$\delta n/n$ (%)	$\delta n/\Sigma n$ (%)	
ν_e CC 1e	97.0	2.6	2.5	Signal
other ν_e CC	3.0	29.5	0.9	
Total signal	100.0		2.2	
ν_e CC 1e	49.1	2.5	1.2	Background
other ν_e CC	3.1	29.5	0.9	
ν_μ CC without π^0	1.8	126	2.2	
ν_μ CC with π^0	0.4	22.0	0.1	
NC $1\pi^0$	34.1	15.7	5.4	
other NC with π^0	3.6	39.0	1.4	
NC $1\pi^\pm$	2.9	174	5.1	
NC 1γ	2.7	2.7	0.07	
other NC	2.3	173	4.1	
Total beam background	100.0		9.2	

for the systematic errors coming from calculation of the expected neutrino flux at SK or from the neutrino interactions we have used exactly the same systematic errors as from the 2011a analysis presented in [13], which also corresponds to the T2K data set we have taken into account for this analysis.

5.5 Procedure for calculation of the oscillation probability

As described in section 5.2 we need to compute the $P(O_i|M,\varepsilon)$ for each oscillation parameter set (O_i), to determine the new neutrino oscillation parameters taking into account the T2K data.

The first step of the oscillation analysis is to define at which O_i we want to estimate $P(O_i|M,\varepsilon)$. Given the dimension of the O_i vector we have decided to have a density of different O_i increasing with the value of $P(O_i)$, that is we will have a higher density of O_i near the maximum of the $P(O_i)$ function at the best fit oscillation points. This was implemented as a random walk starting from the peak position where each step is evaluated using the Metropolis-Hastings algorithm [14] to decide if the step is validated or if another step needs to be tried. Using this method we have selected $5 \cdot 10^5$ set of parameters O_i at which we will calculate the probability density function. Even though the number of parameters selected seems small we have a good coverage close to the maximum of $P(O_i)$ thanks to the Metropolis-Hastings algorithm. Finally in order to improve the precision of the calculation of the low probability contours, more specifically the contour with probability of 1%, we have decided to only randomly pick O_i following the distributions of each of the components of O_i independently for $5 \cdot 10^5$ O_i, in addition to the previously chosen values of O_i.

The second step of the oscillation analysis is to calculate the $P(O_i|M)$ for each O_i and choose at which values we will perform a full estimation of the probability of O_i taking into account the systematic errors. This step is required mainly because the calculation of the probability taking into account systematic error for all O_i points would require too much CPU time. The values of O_i for which will be performed a full estimation of $P(O_i|M,\varepsilon)$ are chosen to be the sets parameters O_i for which a maximum in the $P(O_i|M)$ is found within a fixed grid of oscillation parameters. The current definition of these grids are the 2D histograms whose axes are picked two by two from table 5.5.

Table 5.5: Definition of the axis of the 2D grid used to select at which of O_i would be performed the computation of the probability $P(O_i|M,\varepsilon)$. The ranges given for each parameter correspond to about $\pm 4\sigma$ regions for these parameters given by table 1.3.

Parameter	minimum value	maximum value	number of bins
Δm^2_{21}	$6.75 \cdot 10^{-5}$ eV^2/c^4	$8.43 \cdot 10^{-5}$ eV^2/c^4	100
$\lvert\Delta m^2_{32}\rvert$	$1.91 \cdot 10^{-3}$ eV^2/c^4	$2.95 \cdot 10^{-3}$ eV^2/c^4	100
$\sin^2 2\theta_{12}$	0.757	0.965	100
$\sin^2 2\theta_{23}$	0.82	1	100
$\sin^2 2\theta_{13}$	0.024	0.16	100
δ_{CP}	0	2π	100

The third and final step of the oscillation analysis is to calculate $P(O_i|M,\varepsilon)$ at the

O_i selected at the second step. For this calculation we use MIGRAD minimization algorithm [75] to maximize the $P(O_i|M,\varepsilon_j)$ with respect to ε_j, which is composed of a total of 14 different parameters : $(\varepsilon^{\mathrm{F}_1}, \varepsilon^{\mathrm{F}_2}, \varepsilon^{\mathrm{F}_3}, \varepsilon^{\mathrm{I}_1}, \ldots, \varepsilon^{\mathrm{I}_{10}}, \varepsilon^{\mathrm{D}})$.

5.6 Results

Using the described oscillation analysis we have determined the value of δ_{CP} with highest probability to be about $\delta_{CP} = 4.7$ rad for both normal and inverted hierarchy, which are also referred to as NH and IH respectively, as shown in figures 5.6 and 5.7.

This measurement of δ_{CP} to be about $\frac{3\pi}{2}$ rad in both normal and inverted hierarchy is due to the fact that the number of ν_e events observed by T2K is slightly larger than the number of ν_e events that would be expected given the value of $\sin^2 2\theta_{13}$ measured by the reactor experiments[8]. Such effect is also observed further on at the probability density function obtained for $\sin^2 2\theta_{13}$ using T2K data which tends to be slightly larger than the prior distribution as shown in figures 5.8 and 5.9 for normal and inverted hierarchies, respectively.

For the purpose of comparing the sensitivity of each result we define ΔP to be the ratio between the minimum and maximum $P(O_i|M,\varepsilon)$ shown on the presented figures of the probability as function of δ_{CP} with all other oscillation parameters taken to maximize $P(O_i|M,\varepsilon)$. This quantity defines how well the value of δ_{CP} is measured since it is the probability that the least possible δ_{CP} is reasonable considering the data, therefore the discrimination is better for smaller values of ΔP. For the current T2K data the inverted hierarchy presents the highest discrimination with $\Delta P = 0.48$, which is lower than the value of discrimination obtained for the normal hierarchy of $\Delta P = 0.60$. This difference can be understood by the change in the oscillation maximum of the oscillation probability for $\nu_\mu \to \nu_e$ which depends on the sign of Δm^2_{32} as shown in the oscillation formula.

In addition to the presented study on the sensitivity and measurement of δ_{CP}, the oscillation analysis we have performed allows us to evaluate the effect of the used T2K data on the other oscillation parameters, either in the sense of constraining them, or in the sense of correlating them. The only notable effects the T2K data considered in this oscillation analysis had on other oscillations parameters was to prefer a slightly higher distribution for both $\sin^2 2\theta_{23}$ and $\sin^2 2\theta_{13}$, the later one which had already been previously mentioned, for both hierarchies, as it is shown in the $\sin^2 2\theta_{23}$ and $\sin^2 2\theta_{13}$ correlation plots 5.10 and 5.11 for normal and inverted hierarchy, respectively.

5.7 Perspectives for future analysis

The current oscillation analysis cannot determine the value of δ_{CP} at more than about 1σ level, given that it would correspond to a ΔP of about 0.16 or lower. We can expect that with more data we could obtain a better separation and estimate the sensitivity of this analysis to δ_{CP} with a larger statistical sample.

For such purpose we have estimated how the sensitivity ΔP changes as function of the exposure. For this estimation we scaled the number of events measured as function of the exposure supposing different systematic error size hypothesis of $\sigma_{SE} = 18\%$ and $\sigma_{SE} = 5\%$ on the number of events, as described in subsection 5.2.1. The 18% error

[8] For $\sin^2 2\theta_{13} = 0.092$ given by Daya-Bay and the mean value of the other parameters, we expect 5.6 (4.9) events at most for the normal (inverted) hierarchy.

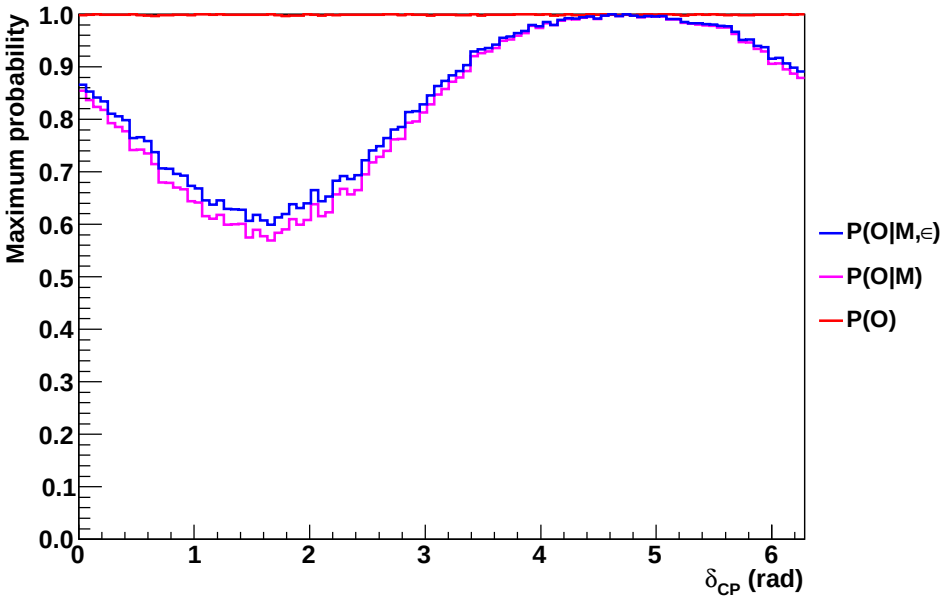

Figure 5.6: Non normalized probability density function as function of δ_{CP} maximized for all other parameters assuming normal hierarchy. In red is shown the prior $P(O_i)$ knowledge of such parameter which is about 1 as expected, in magenta is shown the probability density function calculated without systematic errors $P(O_i|M)$ and in blue is shown the probability density function with systematic errors $P(O_i|M,\varepsilon)$.

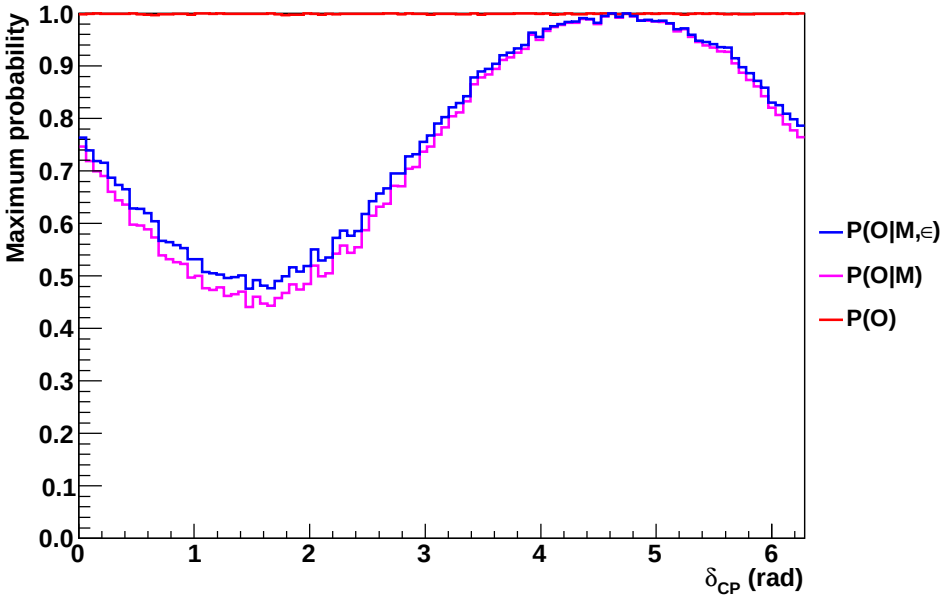

Figure 5.7: Non normalized probability density function as function of δ_{CP} maximized for all other parameters assuming inverted hierarchy. In red is shown the prior $P(O_i)$ knowledge of such parameter which is about 1 as expected, in magenta is shown the probability density function calculated without systematic errors $P(O_i|M)$ and in blue is shown the probability density function with systematic errors $P(O_i|M,\varepsilon)$.

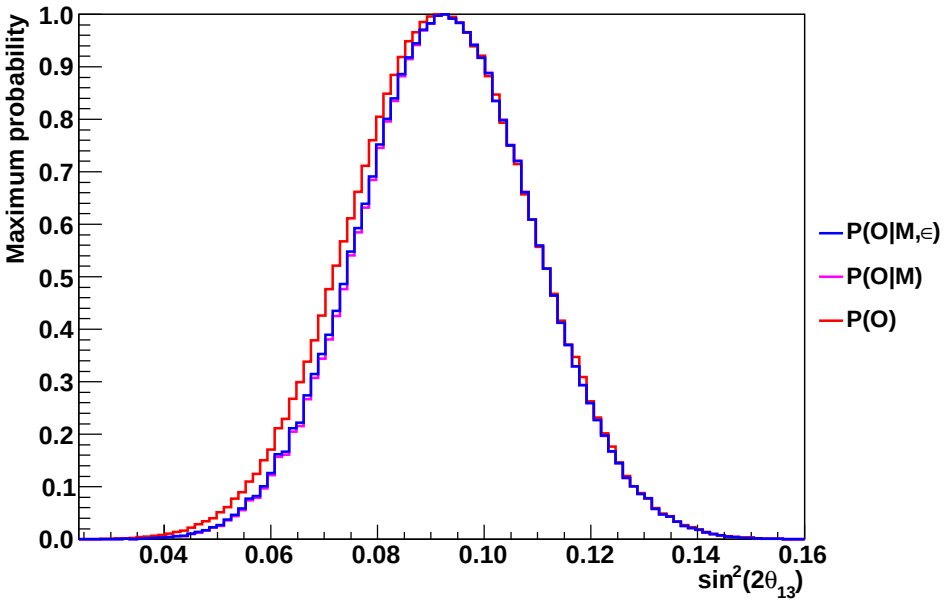

Figure 5.8: Non normalized probability density function as function of $\sin^2 2\theta_{13}$ maximized for all other parameters assuming normal hierarchy. In red is shown the prior $P(O_i)$ knowledge of such parameter, in magenta is shown the probability density function calculated without systematic errors $P(O_i|M)$ and in blue is shown the probability density function with systematic errors $P(O_i|M,\varepsilon)$.

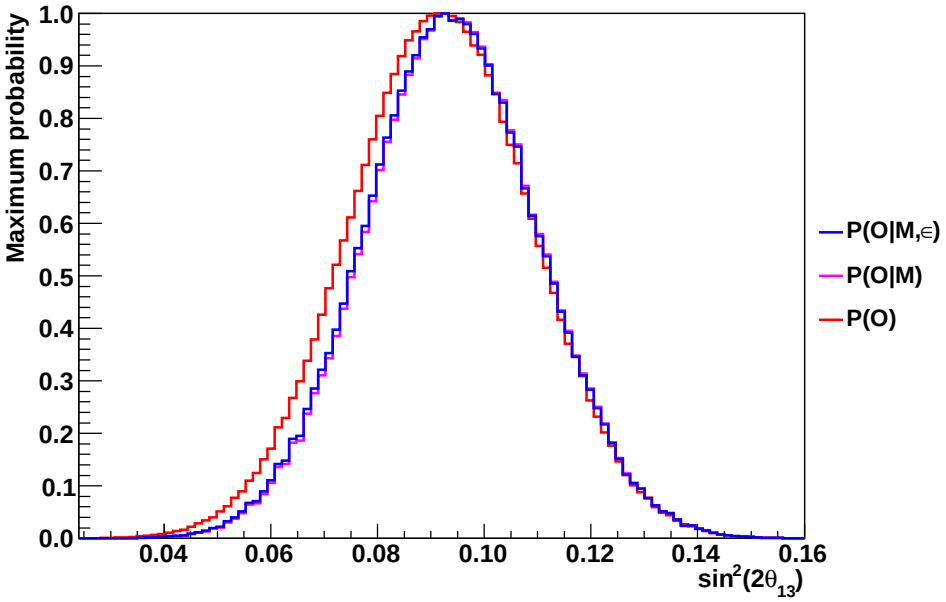

Figure 5.9: Non normalized probability density function as function of $\sin^2 2\theta_{13}$ maximized for all other parameters assuming inverted hierarchy. In red is shown the prior $P(O_i)$ knowledge of such parameter, in magenta is shown the probability density function calculated without systematic errors $P(O_i|M)$ and in blue is shown the probability density function with systematic errors $P(O_i|M,\varepsilon)$.

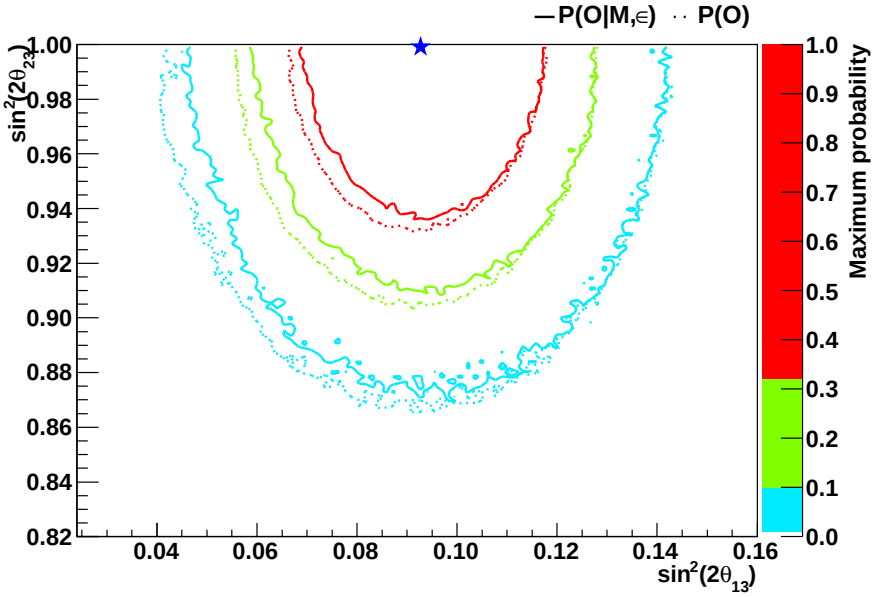

Figure 5.10: Non normalized probability density function as function of $\sin^2 2\theta_{13}$ and $\sin^2 2\theta_{23}$ maximized for all other parameters assuming normal hierarchy. In dotted line is shown the prior $P(O_i)$ knowledge of such parameters, and in solid line is shown the probability density function with systematic errors $P(O_i|M,\varepsilon)$. The contours are shown correspond to the value of the probability being 68% (red), 90% (green) and 99% (cyan) lower than the maximum probability, shown by a blue star (same for $P(O_i)$ and $P(O_i|M,\varepsilon)$).

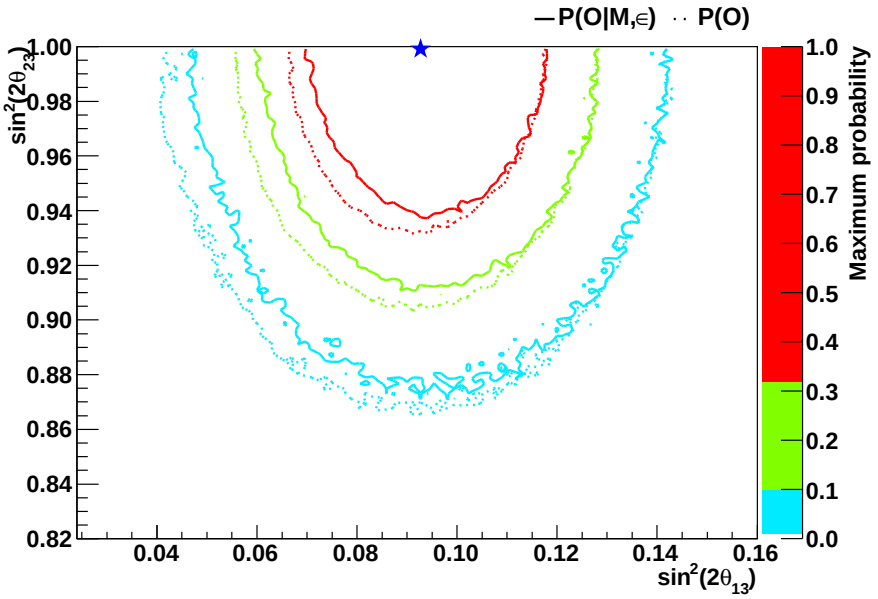

Figure 5.11: Non normalized probability density function as function of $\sin^2 2\theta_{13}$ and $\sin^2 2\theta_{23}$ maximized for all other parameters assuming inverted hierarchy. In dotted line is shown the prior $P(O_i)$ knowledge of such parameters, and in solid line is shown the probability density function with systematic errors $P(O_i|M,\varepsilon)$. The contours are shown correspond to the value of the probability being 68% (red), 90% (green) and 99% (cyan) lower than the maximum probability, shown by a blue star (same for $P(O_i)$ and $P(O_i|M,\varepsilon)$).

hypothesis describes approximately the current size of the systematic errors, while the 5% error hypothesis is, albeit optimistic given the current knowledge, assumed to be a possible value for the T2K systematic uncertainty by the end of the experiment. This comparison is shown in figure 5.12. Even though for current analysis the value of the systematic error used has a small effect on the result obtained it would be essential to reduce as much as possible the systematic error to improve the significance of the measurement of δ_{CP} in future analysis. Even with 5 times larger statistics, the effects of having 18% systematic error are already reducing strongly the sensitivity of the δ_{CP} measurement.

Furthermore, in the example we have just shown, where we have scaled the current number of events, we have not necessarily taken into account all the required information for a correct estimative of the resolution of T2K to δ_{CP} using this analysis. What remains to be taken into account is whether the current data set could have contained a positive fluctuation of the number of measured events[9], in which case the we would overestimate the resolution of T2K in the future by using an unrealistically large number of events. To take into account such possibility, we have calculated the sensitivity ΔP for four different values of δ_{CP} of 0, $\pi/2$, π and $3\pi/2$ radians as function of the exposition for both inverted and normal hierarchy assuming 5% systematic error and that the number of measured events for each value of exposition would be exactly the number of expected events for the given exposition and δ_{CP} using the other oscillation parameters as the most probable values for them. As explained previously, given that the number of measured events was somewhat larger than the number of expected events the sensitivity of the analysis is somewhat reduced when assuming the number of events is the same as the number of expected events for a given δ_{CP} as is shown in figures 5.13 and 5.14 for the normal and inverted hierarchies respectively.

Even though results obtained by scaling the number of events measured using T2K Run I+II data would tend to show a discrimination of about 3 σ or more with a 35 larger statistics than from T2K Run I+II, it is probably more realistic to expect that the discrimination that can be achieved only by increasing the statistics and improving the systematic errors would be at 2 σ level at most, which corresponds to the best expected discrimination assuming the extrapolated number of events to be the same as a value of δ_{CP}, as shown in figures 5.13 and 5.14.

It is nevertheless essential to recall that the current oscillation analysis takes into account the current T2K measurements in a rather simple (only the number of events is compared) and incomplete (we only use ν_e CCQE measurements at SK) way and therefore we can expect improvements on the analysis to increase its sensitivity once more data is available to justify using more information or taking into account other samples. These improvements to the oscillation analysis are currently being implemented and will be used in future T2K analysis.

Furthermore, the current analysis relies strongly on the current knowledge of the other neutrino oscillation parameters. A better knowledge of the oscillation parameters would further constrain the range these parameters may vary and therefore would also improve the precision of the δ_{CP} measurement for the parameters that are in the same terms as δ_{CP} in the oscillation probability equation. Even though it is hard to estimate how much the reducing the uncertainty of these others parameters will increase the sensitivity of the δ_{CP} measurement, we can expect an increase in sensitivity to δ_{CP} by reducing the uncertainty of the other oscillation parameters, specially for θ_{13} and θ_{23} to which the

[9]In fact, the most recent T2K data that was not included in this analysis shows a reduction of the event rate per POT, which goes in the same sense as mentioned here.

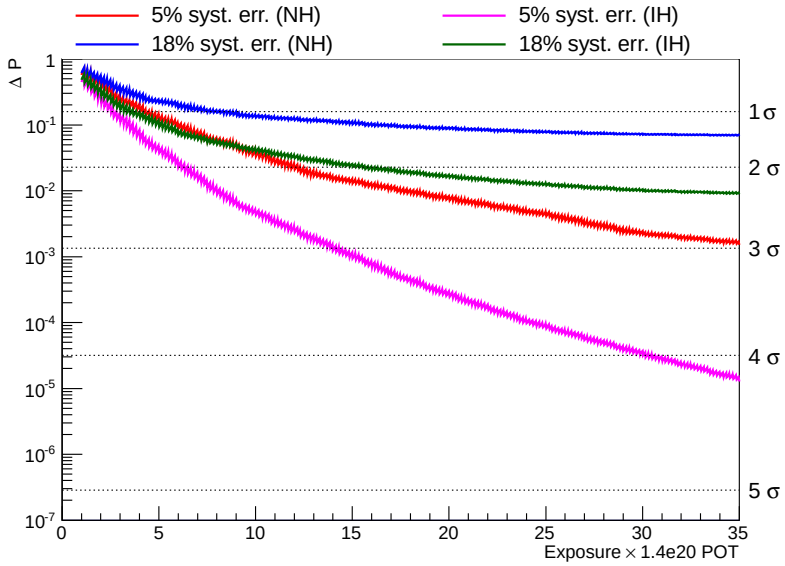

Figure 5.12: Sensitivity plot as function of exposure up to 35 times the T2K Run I+II exposure, which corresponds to the number of POT expected for T2K after 5 years running given at the T2K LOI [61], for different values of the assumed global systematic error and shown for both normal (NH) and inverted (IH) hierarchy. The number of "measured events" used to perform the calculations was scaled from the number of measured ν_e CCQE events during T2K Run I+II. Dotted lines corresponding to a significance, as defined by [14], of 1 to 5 σ are also shown.

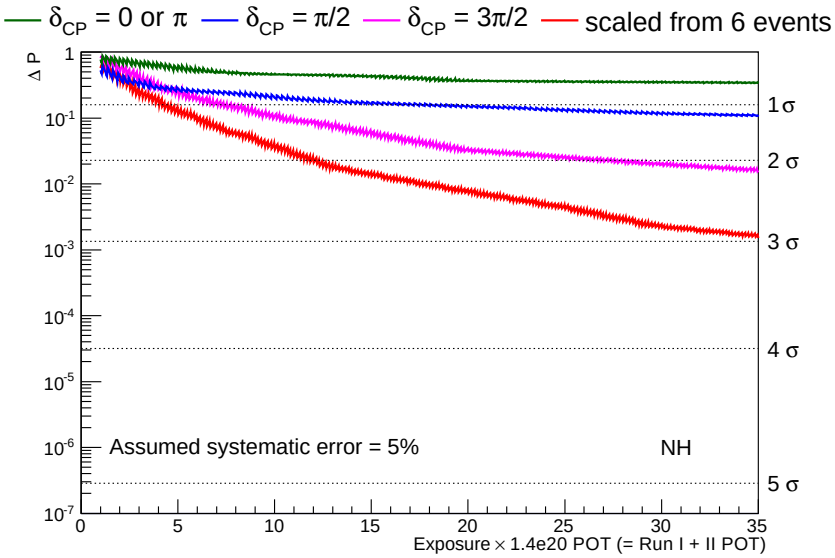

Figure 5.13: Sensitivity plot as function of exposure up to 35 times the T2K Run I+II exposure, which corresponds to the number of POT expected for T2K after 5 years running given at the T2K LOI [61], for different values of δ_{CP} assuming 5% global systematic error and normal hierarchy. The values of δ_{CP} used to estimated the number of expected events were 0 (or π with approximately the same number of events) in green, $\pi/2$ in blue and $3\pi/2$ in magenta. The sensitivity expected only by scaling the 6 already observed events is also shown in red. Dotted lines correspond to the significance, as defined by [14].

presented oscillation analysis was already sensitive.

Finally, in the current analysis we have not taken into account the possibility to run T2K with $\overline{\nu}$ beam, instead of the currently used ν beam. The switch between ν and $\overline{\nu}$ beam allows us to decouple the estimation of δ_{CP} and $\sin^2 2\theta_{13}$ because the change from ν to $\overline{\nu}$ will invert the sign of δ_{CP} in the terms of the oscillation probability expression, therefore we could calculate $P(\nu_\mu \to \nu_e) - P(\overline{\nu_\mu} \to \overline{\nu_e})$, that is proportional to $\sin\delta_{CP}$, and $P(\nu_\mu \to \nu_e) + P(\overline{\nu_\mu} \to \overline{\nu_e})$ to partially separate the contribution from δ_{CP} and $\sin^2 2\theta_{13}$, which in this case leads to a separation between the effect of these two parameters as shown in figure 5.15. We could imagine given the complementarity of these measurements that there would be an improvement of the sensitivity of the δ_{CP} measurement also by changing to $\overline{\nu}$ beam, however given the current efforts from the reactor experiments to measure the value of $\sin^2 2\theta_{13}$ precisely it is probable that the improvement from switching between a ν to a $\overline{\nu}$ run will not drastically increase the discrimination of δ_{CP}. Changing the T2K beam from ν to $\overline{\nu}$ will nevertheless serve as a verification that for the neutrino oscillation model.

Eventually such studies could also be used to determine the sign of Δm^2_{32} given that ν and $\overline{\nu}$ present different matter effects. This study however is not simple given the correlation between δ_{CP} and matter effects and the rather short baseline in relation to what would be required for efficient studies of the sign of Δm^2_{32}.

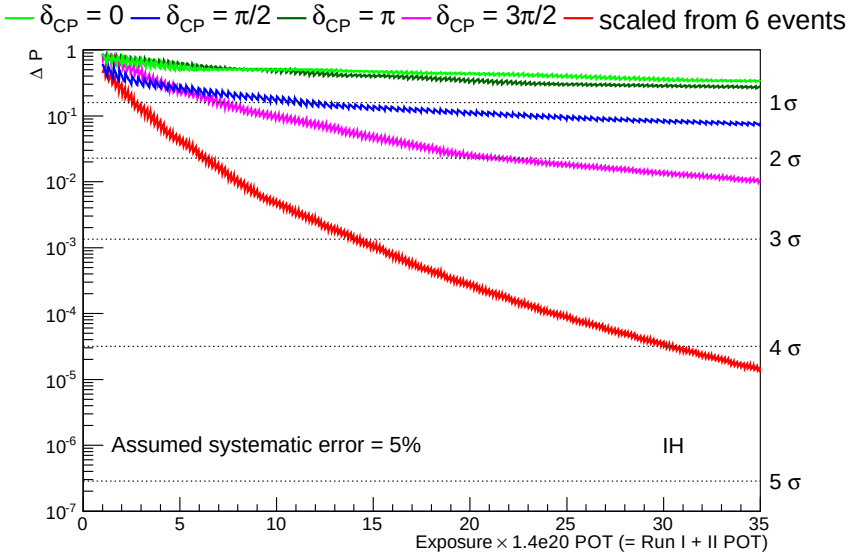

Figure 5.14: Sensitivity plot as function of exposure up to 35 times the T2K Run I+II exposure, which corresponds to the number of POT expected for T2K after 5 years running given at the T2K LOI [61], for different values of δ_{CP} assuming 5% global systematic error and inverted hierarchy. The values of δ_{CP} used to estimated the number of expected events were 0 in light green, $\pi/2$ in blue, π in dark green and $3\pi/2$ in magenta. The sensitivity expected only by scaling the 6 already observed events is also shown in red. Dotted lines correspond to the significance, as defined by [14].

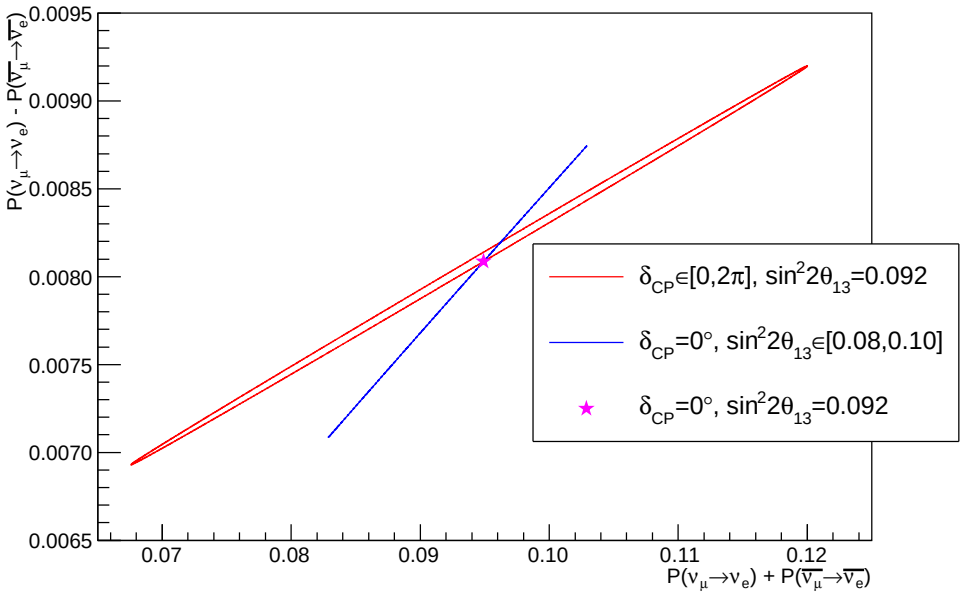

Figure 5.15: $P(\nu_\mu \to \nu_e) - P(\overline{\nu_\mu} \to \overline{\nu_e})$ as function of $P(\nu_\mu \to \nu_e) + P(\overline{\nu_\mu} \to \overline{\nu_e})$ for different values of δ_{CP} (red) and $\sin^2 2\theta_{13}$ (blue) assuming normal hierarchy. A star is shown at $\delta_{CP} = 0°$ and $\sin^2 2\theta_{13} = 0.092$.

Conclusion

Through recent years, many progress have been made in the understanding of fundamental particles, in particular neutrinos. In the very end of the 20^{th} and beginning of the 21^{st} century, we have experimentally demonstrated that neutrinos oscillate, and started measuring precisely each of their oscillation parameters such as mixing angles and mass squared differences. Few years ago, only an upper bound on the value of the θ_{13} mixing angle obtained by the CHOOZ experiment was established. There is, at the present time, still no constraint on the sign of the Δm^2_{32} mass squared difference nor on the value of leptonic CP violation phase δ_{CP}. The latter only exists if all mixing angles are not null. The measurement of the value of these parameters has fundamental consequences in our understanding not only of neutrino flavour oscillations but more generally on high energy physics. In fact the leptonic CP violation could open the way for a possible explanation of the observed matter-antimatter asymmetry in the universe. The progress achieved in the last two years has allowed the measurement of θ_{13}, at first in 2011 by T2K which observed it to be non zero at 2.5 σ confidence level through the observation of ν_e appearance in a ν_μ beam. This measurement was followed by measurements performed by reactor experiments, namely Double-Chooz, Daya-Bay and RENO, which observed $\overline{\nu_e}$ disappearance to measure θ_{13}. Daya-Bay has published the first "5 σ" measurement for the value of θ_{13} in April 2012.

Part of the main objectives of the T2K experiment are the measurement of θ_{13} and the improvement of the current value for other neutrino mixing parameters, θ_{23} and $|\Delta m^2_{32}|$, through ν_μ disappearance. T2K could also start the first study of δ_{CP}, through ν_e appearance. Even though the value of θ_{13} has already been measured by reactor experiments, it is an important verification of our current understanding of neutrino oscillation to measure it through a different oscillation channel. Such measurement can only be achieved by T2K, among the currently running neutrino experiments. Furthermore, it is through the combination of the measurements of T2K and reactor experiments that first studies on the value of δ_{CP} will be done, since reactor experiments are not sensitive to δ_{CP}, showing the complementarity of both reactor and accelerator approaches.

To perform such precise measurements in T2K, it is essential to understand the neutrino beam production at J-PARC, the neutrino interaction cross-section, and the detectors response. In this thesis, we have studied improvements of the understanding of the Super Kamiokande detector (SK), far detector of T2K, and provided to the collaboration the systematic error on the π^0 reconstruction efficiency which has been used in official results.

At the SK detector, the main backgrounds for the T2K ν_e appearance search are the intrinsic ν_e contamination of the T2K ν_μ beam and the π^0 produced through neutral current. The latter corresponds to π^0 events mis-reconstructed as ν_e CCQE events, which happens when one of the rings produced by a γ from the π^0 decay is not found by the SK reconstruction algorithms. On one hand, the intrinsic ν_e contamination, about half

of total ν_e CCQE background, is studied using the atmospheric ν_e sample from SK. On the other hand, there was no control sample available to study the mis-reconstructed π^0 background, about a third of total ν_e CCQE background, and therefore it was essential to create π^0 like samples to perform the necessary background studies.

At first we have developed a new multi-ring light source, the Cone Generator, that can be used for SK detector calibration and systematic error studies. Even if we still have not fully used the possibilities of the Cone Generator, the development of this tool and its Monte-Carlo has allowed to identify and fix a bug in the SK detector simulation. The Cone Generator is currently being used in different studies by different groups, namely to test a new reconstruction algorithm that is being developed for SK (TRIUMF), to study the vertex reconstruction near the fiducial volume boundaries (Imperial College), and to measure the vertical dependence of the light scattering in water (LLR). We plan to use it to perform systematic error studies on the ring finding algorithms at SK, which would help to better estimate part of the π^0 reconstruction efficiency and associated systematic error.

In parallel to the development of the Cone Generator, we have constructed a hybrid sample mixing data and Monte-Carlo to study the systematic error on the π^0 reconstruction efficiency. Because mis-reconstructed π^0 events are one of the dominant background for the ν_e search, it is essential to understand the selection efficiency of π^0 events as well as possible to measure θ_{13}. Using this sample we have estimated the systematic error on the dominant π^0 production channels gathered into three different composite final states : the "NC $1\pi^0$", the "other NC with π^0" and the "ν_μ CC with π^0" which correspond to about 34%, 4% and 0.4% of the background. The relative systematic errors estimated for each final state are of 11.8%, 22.0% and 49.4%, respectively. The resulting systematic errors using these hybrid samples have been used in the first T2K ν_e appearance result. The hybrid samples are also being used for new analyses taking into account the information on the shape of the signal.

Finally, by combining the first T2K results and the value of θ_{13} measured by reactor experiments, we have performed a first estimation of δ_{CP}, with a best fit value of 4.7 rad, though with small significance. The value of δ_{CP} with lowest probability has a 48% (normal hierarchy) or 60% (inverted hierarchy) lower probability to be compatible with T2K data than with the best fit value. We expect to increase in the future the significance of the δ_{CP} measurement by taking more data, by improving the estimation of systematic error, and by performing more complete analysis of T2K data. The improvement in the determination of θ_{13} and θ_{23} would also lead to a more precise measurement of δ_{CP} using the current analysis.

The T2K experiment has restarted data taking in the beginning of this year (2012) after the recovery work from the 2011 Tōhoku earthquake. Since the beginning of the new data taking, the experiment has been able to collect high quality data. Using this new data set, an improved analysis and reduced systematic errors, T2K will improve its measurement of the value of θ_{13} and other neutrino oscillation parameters.

Bibliography

[1] A. H. Becquerel, *On the rays emitted by phosphorescence*, Compt.Rend.Math. **122**, 420 (1896).

[2] J. Chadwick, *The intensity distribution in the magnetic spectrum of beta particles from radium (B + C)*, Verh.Phys.Gesell. **16**, 383 (1914).

[3] W. Pauli, *Dear radioactive ladies and gentlemen*, Phys.Today **31N9**, 27 (1978).

[4] E. Fermi, *An attempt of a theory of beta radiation*, Z.Phys. **88**, 161 (1934).

[5] J. Chadwick, *Possible existence of a neutron*, Nature **129**, 312 (1932).

[6] C. Cowan et al., *Detection of the free neutrino: A Confirmation*, Science **124**, 103 (1956).

[7] G. Danby et al., *Observation of High-Energy Neutrino Reactions and the Existence of Two Kinds of Neutrinos*, Phys.Rev.Lett. **9**, 36 (1962).

[8] K. Kodama et al. (DONUT Collaboration), *Observation of tau neutrino interactions*, Phys.Lett. **B504**, 218 (2001), `arXiv:hep-ex/0012035`.

[9] J. Abdallah et al. (The ALEPH, DELPHI, L3 OPAL, SLD Collaborations, the LEP Electroweak Working Group, the SLD Electroweak and Heavy Flavour Groups), *Precision electroweak measurements on the Z resonance*, Physics Reports **427**, 257 (2006), `arXiv:hep-ex/0509008`.

[10] J. Davis, Raymond et al., *Search for neutrinos from the sun*, Phys.Rev.Lett. **20**, 1205 (1968).

[11] Y. Fukuda et al. (Super-Kamiokande Collaboration), *Evidence for oscillation of atmospheric neutrinos*, Phys.Rev.Lett. **81**, 1562 (1998), `arXiv:hep-ex/9807003`.

[12] Q. R. Ahmad et al. (SNO Collaboration), *Measurement of the Rate of* $\nu_e + d \rightarrow p + p + e^-$ *Interactions Produced by* ^8B *Solar Neutrinos at the Sudbury Neutrino Observatory*, Phys.Rev.Lett. **87**, 071301 (2001), `arXiv:nucl-ex/0106015`.

[13] K. Abe et al. (T2K Collaboration), *Indication of Electron Neutrino Appearance from an Accelerator-Produced Off-Axis Muon Neutrino Beam*, Phys. Rev. Lett. **107**, 041801 (2011), `arXiv:1106.2822`.

[14] K. Nakamura et al. (Particle Data Group), *Particle listing*, Journal of Physics **G37**, 075021 (2010), and 2011 partial update for the 2012 edition.

[15] G. Aad et al. (ATLAS Collaboration), *Observation of a new particle in the search for the Standard Model Higgs boson with the ATLAS detector at the LHC*, Phys.Lett.B (2012), arXiv:1207.7214.

[16] S. Chatrchyan et al. (CMS Collaboration), *Observation of a new boson at a mass of 125 GeV with the CMS experiment at the LHC*, Phys.Lett.B (2012), arXiv:1207.7235.

[17] M. Goldhaber et al., *Helicity of Neutrinos*, Phys. Rev. **109**, 1015 (1958).

[18] *Occam's razor*, URL http://en.wikipedia.org/wiki/Occam's_razor.

[19] Z. Maki et al., *Remarks on the unified model of elementary particles*, Prog.Theor.Phys. **28**, 870 (1962).

[20] E. Majorana, *Theory of the Symmetry of Electrons and Positrons*, Nuovo Cim. **14**, 171 (1937).

[21] V. Lobashev et al., *Direct search for mass of neutrino and anomaly in the tritium beta spectrum*, Phys.Lett. **B460**, 227 (1999).

[22] C. Kraus et al., *Final results from phase II of the Mainz neutrino mass search in tritium beta decay*, Eur.Phys.J. **C40**, 447 (2005), arXiv:hep-ex/0412056.

[23] A. Osipowicz et al. (KATRIN Collaboration), *KATRIN: A Next generation tritium beta decay experiment with sub-eV sensitivity for the electron neutrino mass. Letter of intent* (2001), with improvements described in http://www.katrin.kit.edu/128.php., arXiv:hep-ex/0109033.

[24] T. J. Loredo et al., *Bayesian analysis of neutrinos observed from supernova SN-1987A*, Phys.Rev. **D65**, 063002 (2002), arXiv:astro-ph/0107260.

[25] G. Pagliaroli et al., *Neutrino mass bound in the standard scenario for supernova electronic antineutrino emission*, Astropart.Phys. **33**, 287 (2010), arXiv:1002.3349.

[26] S. Hannestad et al., *Neutrino and axion hot dark matter bounds after WMAP-7*, JCAP **1008**, 001 (2010), arXiv:1004.0695.

[27] U. Seljak et al., *Cosmological parameters from combining the Lyman-alpha forest with CMB, galaxy clustering and SN constraints*, JCAP **0610**, 014 (2006), arXiv:astro-ph/0604335.

[28] *Results from KamLAND-Zen*, Neutrino 2012 (Kyoto, Japan, 2012), URL http://kds.kek.jp/contributionDisplay.py?contribId=33&confId=9151.

[29] C. Aalseth et al. (IGEX Collaboration), *The IGEX Ge-76 neutrinoless double beta decay experiment: Prospects for next generation experiments*, Phys.Rev. **D65**, 092007 (2002), arXiv:hep-ex/0202026.

[30] R. Arnold et al. (NEMO-3 Collaboration), *First results of the search of neutrinoless double beta decay with the NEMO 3 detector*, Phys.Rev.Lett. **95**, 182302 (2005), arXiv:hep-ex/0507083.

[31] J. Argyriades et al. (NEMO-3 Collaboration), *Measurement of the two neutrino double beta decay half-life of Zr-96 with the NEMO-3 detector*, Nucl.Phys. **A847**, 168 (2010), arXiv:0906.2694.

[32] J. Argyriades et al. (NEMO-3 Collaboration), *Measurement of the Double Beta Decay Half-life of Nd-150 and Search for Neutrinoless Decay Modes with the NEMO-3 Detector*, Phys.Rev. **C80**, 032501 (2009), arXiv:0810.0248.

[33] C. Arnaboldi et al. (CUORICINO Collaboration), *Results from a search for the 0 neutrino beta beta-decay of Te-130*, Phys.Rev. **C78**, 035502 (2008), arXiv:0802.3439.

[34] S. Umehara et al., *Neutrino-less double-beta decay of Ca-48 studied by CaF(2)(Eu) scintillators*, Phys.Rev. **C78**, 058501 (2008), arXiv:0810.4746.

[35] F. A. Danevich et al., *Search for 2 beta decay of cadmium and tungsten isotopes: Final results of the solotvina experiment*, Phys.Rev. **C68**, 035501 (2003).

[36] T. Bernatowicz et al., *Neutrino mass limits for a precise determination of beta-beta decay rates of Te-128 and Te-130*, Phys.Rev.Lett. **69**, 2341 (1992).

[37] H. V. Klapdor-Kleingrothaus et al., *The evidence for the observation of 0nu beta beta decay : The identification of 0nu beta beta events from the full spectra*, Mod. Phys. Lett. **A21**, 1547 (2006).

[38] B. Pontecorvo, *Mesonium and anti-mesonium*, Sov.Phys.JETP **6**, 429 (1957).

[39] G. Danby et al., *Observation of High-Energy Neutrino Reactions and the Existence of Two Kinds of Neutrinos*, Phys.Rev.Lett. **9**, 36 (1962).

[40] R. Wendell et al. (Super-Kamiokande Collaboration), *Prob3++ release 2009.08.31*, URL http://www.phy.duke.edu/~raw22/public/Prob3++/.

[41] K. N. Abazajian et al., *Light Sterile Neutrinos: A White Paper* (2012), arXiv:1204.5379.

[42] A. Aguilar et al. (LSND Collaboration), *Evidence for neutrino oscillations from the observation of $\overline{\nu}_e$ appearance in a $\overline{\nu}_\mu$ beam*, Phys. Rev. D **64**, 112007 (2001), arXiv:hep-ex/0104049.

[43] A. A. Aguilar-Arevalo et al. (MiniBooNE Collaboration), *Event Excess in the MiniBooNE Search for $\overline{\nu}_\mu \to \overline{\nu}_e$ Oscillations*, Phys. Rev. Lett. **105**, 181801 (2010), arXiv:1007.1150.

[44] G. Mention et al., *The Reactor Antineutrino Anomaly*, Phys.Rev. **D83**, 073006 (2011), arXiv:1101.2755.

[45] B. Armbruster et al. (KARMEN Collaboration), *Upper limits for neutrino oscillations muon-anti-neutrino to electron-anti-neutrino from muon decay at rest*, Phys.Rev. **D65**, 112001 (2002), arXiv:hep-ex/0203021.

[46] L. Wolfenstein, *Neutrino Oscillations in Matter*, Phys.Rev. **D17**, 2369 (1978).

[47] S. Mikheev et al., *Resonance Amplification of Oscillations in Matter and Spectroscopy of Solar Neutrinos*, Sov.J.Nucl.Phys. **42**, 913 (1985).

[48] C. Giunti and C. W. Kim, *Fundamentals of neutrino physics and astrophysics* (Oxford university press, 2007).

[49] K. Hagiwara et al., *The earth matter effects in neutrino oscillation experiments from Tokai to Kamioka and Korea*, JHEP **1109**, 082 (2011), arXiv:1107.5857.

[50] B. Aharmim et al. (SNO Collaboration), *Low-energy-threshold analysis of the Phase I and Phase II data sets of the Sudbury Neutrino Observatory*, Phys. Rev. C **81**, 055504 (2010), arXiv:0910.2984.

[51] J. N. Bahcall et al., *New solar opacities, abundances, helioseismology, and neutrino fluxes*, Astrophys.J. **621**, L85 (2005), arXiv:astro-ph/0412440.

[52] A. Gando et al. (KamLAND Collaboration), *Constraints on θ_{13} from A Three-Flavor Oscillation Analysis of Reactor Antineutrinos at KamLAND*, Phys.Rev. **D83**, 052002 (2011), arXiv:1009.4771.

[53] Y. Ashie et al. (Super-Kamiokande Collaboration), *Measurement of atmospheric neutrino oscillation parameters by Super-Kamiokande I*, Phys. Rev. D **71**, 112005 (2005), arXiv:hep-ex/0501064.

[54] P. Adamson et al. (MINOS Collaboration), *Measurement of Neutrino Oscillations with the MINOS Detectors in the NuMI Beam*, Phys. Rev. Lett. **101**, 131802 (2008), arXiv:0806.2237.

[55] M. Apollonio et al. (CHOOZ Collaboration), *Search for neutrino oscillations on a long baseline at the CHOOZ nuclear power station*, Eur.Phys.J. **C27**, 331 (2003), arXiv:hep-ex/0301017.

[56] G. Mention et al., *A Unified analysis of the reactor neutrino program towards the measurement of the theta(13) mixing angle*, J.Phys.Conf.Ser. **110**, 082013 (2008), arXiv:0704.0498.

[57] Y. Abe et al. (DOUBLE-CHOOZ Collaboration), *Indication for the disappearance of reactor electron antineutrinos in the Double Chooz experiment*, Phys.Rev.Lett. **108**, 131801 (2012), arXiv:1112.6353.

[58] F. P. An et al. (Daya-Bay Collaboration), *Observation of Electron-Antineutrino Disappearance at Daya Bay*, Phys. Rev. Lett. **108**, 171803 (2012), arXiv:1203.1669.

[59] J. Ahn et al. (RENO collaboration), *Observation of Reactor Electron Antineutrino Disappearance in the RENO Experiment*, Phys.Rev.Lett. **108**, 191802 (2012), arXiv:1204.0626.

[60] K. Abe et al. (T2K Collaboration), *First muon-neutrino disappearance study with an off-axis beam*, Phys. Rev. D **85**, 031103 (2012), arXiv:1201.1386.

[61] Y. Itow et al. (T2K Collaboration), *The JHF-Kamioka neutrino project*, pp. 239–248 (2001), arXiv:hep-ex/0106019.

[62] *Accelerator facilities at J-PARC*, URL http://j-parc.jp/researcher/Acc/en/index.html.

[63] N. Abgrall et al. (NA61/SHINE Collaboration), *Measurements of Cross Sections and Charged Pion Spectra in Proton-Carbon Interactions at 31 GeV/c*, Phys.Rev. **C84**, 034604 (2011), arXiv:1102.0983.

[64] C. Bronner, Ph.D. thesis, Laboratoire Leprince-Ringuet, École Polytechnique (2011), available at the SUDOC catalogue.

[65] K. Abe et al. (T2K Collaboration), *Measurements of the T2K neutrino beam properties using the INGRID on-axis near detector* (2011), arXiv:1111.3119.

[66] K. Abe et al. (T2K Collaboration), *The T2K Experiment*, Nucl.Instrum.Meth. **A659**, 106 (2011), arXiv:1106.1238.

[67] P.-A. Amaudruz et al. (T2K ND280 FGD Collaboration), *The T2K Fine-Grained Detectors* (2012), arXiv:1204.3666.

[68] Y. Fukuda et al. (Super-Kamiokande Collaboration), *The Super-Kamiokande detector*, Nucl.Instrum.Meth. **A501**, 418 (2003), available at the SK website.

[69] J. B. Albert, Ph.D. thesis, Duke University (2012), available at the T2K website.

[70] *Hough transform*, URL http://planetmath.org/HoughTransform.html.

[71] C. Bronner et al., *Update of SK ν_e systematic error for 2012a oscillation analysis* (2012), T2K-TN-107 (T2K internal technical note).

[72] C. Giganti et al., *Study of neutrino charge current interactions in the ND280 tracker* (2011), T2K-TN-015 (T2K internal technical note).

[73] N. Abgrall et al., *Beam update for 2010a nue analysis using Run I+II data* (2011), T2K-TN-054 (T2K internal technical note).

[74] P. de Perio et al., *NEUT Systematic Studies for 2010a Analysis* (2011), T2K-TN-032 (T2K internal technical note).

[75] F. James et al. (CERN), *Minuit user's guide*, URL http://seal.cern.ch/documents/minuit/mnusersguide.pdf.

[76] R. C. Fernow, *Introduction to experimental particle physics* (Cambridge university press, 1986).

Appendix A

Details on the calculation of the oscillation probability

A.1 Oscillation probability expression

Using the definition of $|\nu_\alpha, t\rangle$ given by (1.3) we can calculate the oscillation probability :

$$\begin{aligned} P(\nu_\alpha \to \nu_\beta, t) &= ||\langle \nu_\beta | \nu_\alpha, t\rangle||^2 = \left|\left|\sum_{j,k} U_{\beta k} U^*_{\alpha j} e^{-iE_j t} \langle \nu_k | \nu_j \rangle\right|\right|^2 \\ &= \left|\left|\sum_{j} U_{\beta j} U^*_{\alpha j} e^{-iE_j t}\right|\right|^2 = \sum_{j,k} U_{\beta j} U^*_{\alpha j} e^{-iE_j t} U^*_{\beta k} U_{\alpha k} e^{iE_k t} \\ &= \sum_{j,k} U_{\beta j} U^*_{\alpha j} U^*_{\beta k} U_{\alpha k} e^{-i(E_j - E_k)t} \end{aligned}$$

The obtained expression is the same as shown in equation (1.4).

A.2 Change on the oscillation probability by multiplying the rotation matrix by a diagonal matrix

Let's assume that $U = D_1 U' D_2$ where D_1 and D_2 are diagonal matrices. Let's also write $U = \{u_{ij}\}$, $U' = \{u'_{ij}\}$ and

$$D_1 = \begin{pmatrix} d_1 & 0 & \cdots \\ 0 & d_2 & \\ \vdots & & \ddots \end{pmatrix} \quad D_2 = \begin{pmatrix} \delta_1 & 0 & \cdots \\ 0 & \delta_2 & \\ \vdots & & \ddots \end{pmatrix}$$

Let's also assume that $|d_i| = 1 = |\delta_i|, \forall i$

We have then that $u_{ij} = d_i u'_{ij} \delta_j$. We can then replace U in the oscillation probability

formula (1.4) :

$$\begin{aligned} P(\overline{\nu_\alpha} \to \overline{\nu_\beta}, t) &= \sum_{j,k} u_{\beta j} u^*_{\alpha j} u^*_{\beta k} u_{\alpha k} e^{-i(E_j - E_k)t} \\ &= \sum_{j,k} d_\beta u'_{\beta j} \delta_j d^*_\alpha u'^*_{\alpha j} \delta^*_j d^*_\beta u'^*_{\beta k} \delta^*_k d_\alpha u'_{\alpha k} \delta_k e^{-i(E_j - E_k)t} \\ &= \sum_{j,k} u'_{\beta j} u'^*_{\alpha j} u'^*_{\beta k} u'_{\alpha k} e^{-i(E_j - E_k)t} \end{aligned}$$

which is the oscillation probability obtained using the matrix U'.

In the given case we can simply ignore the diagonal matrices D_1 and D_2 as they do not affect the oscillation probability.

A.3 2-flavour oscillation matrix

We can write a generic 2×2 complex matrix U as

$$U = \begin{pmatrix} a_{11} e^{i\phi_{11}} & a_{12} e^{i\phi_{12}} \\ a_{21} e^{i\phi_{21}} & a_{22} e^{i\phi_{22}} \end{pmatrix} \qquad a_{ij}, \phi_{ij} \in \mathbb{R}$$

As $UU^\dagger = \mathbb{1}$ we have

$$\begin{cases} a_{11}^2 + a_{12}^2 = 1 \\ a_{21}^2 + a_{22}^2 = 1 \\ a_{11}^2 a_{21}^2 e^{i(\phi_{21} - \phi_{11})} + a_{12}^2 a_{22}^2 e^{i(\phi_{22} - \phi_{12})} = 0 \end{cases}$$

The first two equations imply that a_{ij} have the form :

$$\begin{cases} a_{11} = \cos\theta_1 \\ a_{12} = \sin\theta_1 \\ a_{21} = \sin\theta_2 \\ a_{22} = \cos\theta_2 \end{cases}$$

From the last equation we obtain :

$$\begin{cases} \cos\theta_1 \sin\theta_2 \cos(\phi_{21} - \phi_{11}) + \sin\theta_1 \cos\theta_2 \cos(\phi_{22} - \phi_{12}) = 0 \\ \cos\theta_1 \sin\theta_2 \sin(\phi_{21} - \phi_{11}) + \sin\theta_1 \cos\theta_2 \sin(\phi_{22} - \phi_{12}) = 0 \end{cases}$$

If we take either $\theta_1 = k\pi/2, k \in \mathbb{N}$ or $\theta_2 = k\pi/2, k \in \mathbb{N}$ we obtain that U is a diagonal or anti-diagonal matrix, thus there are no oscillations. In the following considerations this case will not be studied and we have that $\sin\theta_i \neq 0 \neq \cos\theta_i, i = \{1, 2\}$. We can then write that

$$\begin{aligned} &\frac{\cos\theta_1 \sin\theta_2}{\sin\theta_1 \cos\theta_2} = -\frac{\cos(\phi_{22} - \phi_{12})}{\cos(\phi_{21} - \phi_{11})}, \text{ for } \cos(\phi_{21} - \phi_{11}) \neq 0 \\ &\Rightarrow \tan(\phi_{22} - \phi_{12}) = \tan(\phi_{21} - \phi_{11}) \\ &\Rightarrow \phi_{22} - \phi_{12} = \phi_{21} - \phi_{11} + k_1\pi = \delta + k_1\pi \end{aligned}$$

Note that the case $\cos(\phi_{21} - \phi_{11}) = 0$ implies $\cos(\phi_{22} - \phi_{12}) = 0$, which also yields $\phi_{22} - \phi_{12} = \phi_{21} - \phi_{11} + k_1\pi = \delta + k_1\pi$.

By replacing this result again on the equation

$$\cos\theta_1 \sin\theta_2 e^{i(\phi_{21}-\phi_{11})} + \sin\theta_1 \cos\theta_2 e^{i(\phi_{22}-\phi_{12})} = 0$$

we obtain

$$\begin{aligned}
&\cos\theta_1 \sin\theta_2 e^{i(\phi_{21}-\phi_{11})} + \sin\theta_1 \cos\theta_2 e^{i(\phi_{21}-\phi_{11}-k_1\pi)} = 0 \\
\Rightarrow &\cos\theta_1 \sin\theta_2 + (-1)^{k_1} \sin\theta_1 \cos\theta_2 = 0 \\
\Rightarrow &\sin(\theta_2 + (-1)^{k_1}\theta_1) = 0 \\
\Rightarrow &\theta_2 + (-1)^{k_1}\theta_1 = k_2\pi \qquad k_2 \mathbb{N} \\
\Rightarrow &\theta = -\theta_2 = (-1)^{k_1}\theta_1 - k_2\pi
\end{aligned}$$

We can then rewrite the U matrix using all information we have :

$$\begin{aligned}
U &= \begin{pmatrix} \cos\theta(-1)^{k_2} e^{i\phi_{11}} & \sin\theta(-1)^{k_1+k_2} e^{i(\phi_{22}-\delta-k_1\pi)} \\ -\sin\theta e^{i(\phi_{11}+\delta)} & \cos\theta e^{i\phi_{22}} \end{pmatrix} \\
\Rightarrow U &= \begin{pmatrix} (-1)^{k_2} & 0 \\ 0 & 1 \end{pmatrix} \times \begin{pmatrix} \cos\theta & \sin\theta e^{-i\delta} \\ -\sin\theta e^{i\delta} & \cos\theta \end{pmatrix} \times \begin{pmatrix} e^{i\phi_{11}} & 0 \\ 0 & e^{i\phi_{22}} \end{pmatrix}
\end{aligned}$$

Note that by posing $\delta = \delta' - \phi_{11} + \phi_{22}$ we can write

$$U = \begin{pmatrix} (-1)^{k_2} e^{i\phi_{11}} & 0 \\ 0 & e^{i\phi_{22}} \end{pmatrix} \times \begin{pmatrix} \cos\theta & \sin\theta e^{-i\delta'} \\ -\sin\theta e^{i\delta'} & \cos\theta \end{pmatrix}$$

and by posing $\delta = \delta'' - k_2\pi$

$$U = \begin{pmatrix} \cos\theta & \sin\theta e^{-i\delta''} \\ -\sin\theta e^{i\delta''} & \cos\theta \end{pmatrix} \times \begin{pmatrix} (-1)^{k_2} e^{i\phi_{11}} & 0 \\ 0 & e^{i\phi_{22}} \end{pmatrix}$$

As $|e^{i\phi_{11}}| = |e^{i\phi_{22}}| = |(-1)^{k_2}| = 1$ we can use the result shown on the appendix A.2 and simply write U without the diagonal matrices

$$\begin{pmatrix} (-1)^{k_2} & 0 \\ 0 & 1 \end{pmatrix} \quad , \quad \begin{pmatrix} e^{i\phi_{11}} & 0 \\ 0 & e^{i\phi_{22}} \end{pmatrix}$$

as they do not change the oscillation probability. We have then

$$\begin{aligned}
U &= \begin{pmatrix} \cos\theta & \sin\theta e^{-i\delta} \\ -\sin\theta e^{i\delta} & \cos\theta \end{pmatrix} \\
&= \begin{pmatrix} e^{-i\delta} & 0 \\ 0 & 1 \end{pmatrix} \times \begin{pmatrix} \cos\theta & \sin\theta \\ -\sin\theta & \cos\theta \end{pmatrix} \times \begin{pmatrix} e^{i\delta} & 0 \\ 0 & 1 \end{pmatrix} \\
&= \begin{pmatrix} 1 & 0 \\ 0 & e^{i\delta} \end{pmatrix} \times \begin{pmatrix} \cos\theta & \sin\theta \\ -\sin\theta & \cos\theta \end{pmatrix} \times \begin{pmatrix} 1 & 0 \\ 0 & e^{-i\delta} \end{pmatrix}
\end{aligned}$$

which is the complex U matrix given on section 1.2.2 “2-flavour case”.

A.4 Complex phases on 3-flavour oscillation probability

We will assume here that the 3×3 matrix U has the form of the product of 3 matrices, where each is the same as a 2×2 complex rotation matrix between two different rows :

$$\begin{aligned} U &= \begin{pmatrix} 1 & 0 & 0 \\ 0 & (-1)^{k_{23}} e^{i\phi_{23}} & 0 \\ 0 & 0 & e^{i\psi_{23}} \end{pmatrix} \times \begin{pmatrix} 1 & 0 & 0 \\ 0 & c_{23} & s_{23} e^{-i\delta_{23}} \\ 0 & -s_{23} e^{i\delta_{23}} & c_{23} \end{pmatrix} \times \\ & \begin{pmatrix} (-1)^{k_{13}} e^{i\phi_{13}} & 0 & 0 \\ 0 & 1 & 0 \\ 0 & 0 & e^{i\psi_{13}} \end{pmatrix} \times \begin{pmatrix} c_{13} & 0 & s_{13} e^{-i\delta_{13}} \\ 0 & 1 & 0 \\ -s_{13} e^{i\delta_{13}} & 0 & c_{13} \end{pmatrix} \times \\ & \begin{pmatrix} c_{12} & s_{12} e^{-i\delta_{12}} & 0 \\ -s_{12} e^{i\delta_{12}} & c_{12} & 0 \\ 0 & 0 & 1 \end{pmatrix} \times \begin{pmatrix} (-1)^{k_{12}} e^{i\phi_{12}} & 0 & 0 \\ 0 & e^{i\psi_{12}} & 0 \\ 0 & 0 & 1 \end{pmatrix} \end{aligned}$$

where $c_{ij} = \cos\theta_{ij}$ and $s_{ij} = \sin\theta_{ij}$, with θ_{ij} mixing angles, δ_{ij} are a CP violating phases, and $k_{ij}, \phi_{ij}, \psi_{ij}$ are other constants obtained in the calculation of the 2×2 matrix.

By replacing $\delta_{23} \to \delta_{23} + \psi_{13}$ and removing the diagonal terms that we have demonstrated in section A.2 do not change the oscillation probability we obtain :

$$U = \begin{pmatrix} 1 & 0 & 0 \\ 0 & c_{23} & s_{23} e^{-i\delta_{23}} \\ 0 & -s_{23} e^{i\delta_{23}} & c_{23} \end{pmatrix} \times \begin{pmatrix} c_{13} & 0 & s_{13} e^{-i\delta_{13}} \\ 0 & 1 & 0 \\ -s_{13} e^{i\delta_{13}} & 0 & c_{13} \end{pmatrix} \times \begin{pmatrix} c_{12} & s_{12} e^{-i\delta_{12}} & 0 \\ -s_{12} e^{i\delta_{12}} & c_{12} & 0 \\ 0 & 0 & 1 \end{pmatrix}$$

We can then rewrite this U separating the complex phases δ_{23} and δ_{12} from the matrices at the sides and removing the diagonal terms that do not change the oscillation probability to obtain

$$\begin{aligned} U &= \begin{pmatrix} 1 & 0 & 0 \\ 0 & c_{23} & s_{23} \\ 0 & -s_{23} & c_{23} \end{pmatrix} \times \begin{pmatrix} 1 & 0 & 0 \\ 0 & 1 & 0 \\ 0 & 0 & e^{-i\delta_{23}} \end{pmatrix} \times \begin{pmatrix} c_{13} & 0 & s_{13} e^{-i\delta_{13}} \\ 0 & 1 & 0 \\ -s_{13} e^{i\delta_{13}} & 0 & c_{13} \end{pmatrix} \times \\ & \begin{pmatrix} e^{-i\delta_{12}} & 0 & 0 \\ 0 & 1 & 0 \\ 0 & 0 & 1 \end{pmatrix} \times \begin{pmatrix} c_{12} & s_{12} & 0 \\ -s_{12} & c_{12} & 0 \\ 0 & 0 & 1 \end{pmatrix} \\ &= \begin{pmatrix} e^{-i\delta_{12}} & 0 & 0 \\ 0 & 1 & 0 \\ 0 & 0 & 1 \end{pmatrix} \times \begin{pmatrix} 1 & 0 & 0 \\ 0 & c_{23} & s_{23} \\ 0 & -s_{23} & c_{23} \end{pmatrix} \times \begin{pmatrix} c_{13} & 0 & s_{13} e^{-i\delta} \\ 0 & 1 & 0 \\ -s_{13} e^{i\delta} & 0 & c_{13} \end{pmatrix} \times \\ & \begin{pmatrix} c_{12} & s_{12} & 0 \\ -s_{12} & c_{12} & 0 \\ 0 & 0 & 1 \end{pmatrix} \times \begin{pmatrix} 1 & 0 & 0 \\ 0 & 1 & 0 \\ 0 & 0 & e^{-i\delta_{23}} \end{pmatrix} \end{aligned}$$

where $\delta = \delta_{13} - \delta_{12} - \delta_{23}$.

We apply again the result shown on the appendix A.2 and simply write U without the diagonal matrices and obtain the expression for U previously given on section 1.2.2

"3-flavour case" :

$$\begin{aligned} U &= \begin{pmatrix} 1 & 0 & 0 \\ 0 & c_{23} & s_{23} \\ 0 & -s_{23} & c_{23} \end{pmatrix} \times \begin{pmatrix} c_{13} & 0 & s_{13}e^{-i\delta} \\ 0 & 1 & 0 \\ -s_{13}e^{i\delta} & 0 & c_{13} \end{pmatrix} \times \begin{pmatrix} c_{12} & s_{12} & 0 \\ -s_{12} & c_{12} & 0 \\ 0 & 0 & 1 \end{pmatrix} \\ &= \begin{pmatrix} c_{12}c_{13} & s_{12}c_{13} & s_{13}e^{-i\delta} \\ -s_{12}c_{23} - c_{12}s_{23}s_{13}e^{i\delta} & c_{12}c_{23} - s_{12}s_{23}s_{13}e^{i\delta} & s_{23}c_{13} \\ s_{12}s_{23} - c_{12}c_{23}s_{13}e^{i\delta} & -c_{12}s_{23} - s_{12}c_{23}s_{13}e^{i\delta} & c_{23}c_{13} \end{pmatrix} \end{aligned}$$

In order to understand the conditions needed to observe CP violation on the leptonic sector we need to evaluate when the oscillation probability changes when we replace U by U^*.

The oscillation probability, as shown in (1.4), depends on $W_{\alpha\beta jk} = U_{\beta j}U^*_{\alpha j}U^*_{\beta k}U_{\alpha k}$, with $\alpha, \beta \in \{e, \mu, \tau\}$ and $j, k \in \{1, 2, 3\}$. We should notice that $W_{\alpha\beta jk} = W^*_{\beta\alpha jk} = W^*_{\alpha\beta kj} = W_{\beta\alpha kj}$. We will consider now the value of this term for each (α, β, j, k):

- When $\alpha = \beta, \forall j, k$ we have $W_{\alpha\beta jk} = W^*_{\alpha\beta jk}, \forall j, k$
- When $j = k$ we also have $W_{\alpha\beta jk} = W^*_{\alpha\beta jk}, \forall \alpha, \beta$
- When $\alpha \neq \beta$ and $i \neq j$ we have the following cases :
  - $W_{e\mu 12} = W^*_{e\mu 21} = W^*_{\mu e12} = W_{\mu e21} = s_{12}c_{12}c^2_{13}\left(c_{12}c_{23} - s_{12}s_{23}s_{13}e^{-i\delta}\right)\left(-s_{12}c_{23} - c_{12}s_{23}s_{13}e^{i\delta}\right)$
  - $W_{e\tau 12} = W^*_{e\tau 21} = W^*_{\tau e12} = W_{\tau e21} = s_{12}c_{12}c^2_{13}\left(s_{12}s_{23} - c_{12}c_{23}s_{13}e^{i\delta}\right)\left(-c_{12}s_{23} - s_{12}c_{23}s_{13}e^{-i\delta}\right)$
  - $W_{\mu\tau 12} = W^*_{\mu\tau 21} = W^*_{\tau\mu 12} = W_{\tau\mu 21} = \left(s_{12}s_{23} - c_{12}c_{23}s_{13}e^{i\delta}\right)\left(c_{12}c_{23} - s_{12}s_{23}s_{13}e^{i\delta}\right)\left(-s_{12}c_{23} - c_{12}s_{23}s_{13}e^{-i\delta}\right)\left(-c_{12}s_{23} - s_{12}c_{23}s_{13}e^{-i\delta}\right)$
  - $W_{e\mu 13} = W^*_{e\mu 31} = W^*_{\mu e13} = W_{\mu e31} = c_{12}s_{13}c^2_{13}s_{23}\left(-s_{12}c_{23}e^{-i\delta} - c_{12}s_{23}s_{13}\right)$
  - $W_{e\tau 13} = W^*_{e\tau 31} = W^*_{\tau e13} = W_{\tau e31} = c_{12}s_{13}c^2_{13}c_{23}\left(s_{12}s_{23}e^{-i\delta} - c_{12}c_{23}s_{13}\right)$
  - $W_{\mu\tau 13} = W^*_{\mu\tau 31} = W^*_{\tau\mu 13} = W_{\tau\mu 31} = s_{23}c_{23}c^2_{13}\left(-s_{12}c_{23} - c_{12}s_{23}s_{13}e^{-i\delta}\right)\left(s_{12}s_{23} - c_{12}c_{23}s_{13}e^{i\delta}\right)$
  - $W_{e\mu 23} = W^*_{e\mu 32} = W^*_{\mu e23} = W_{\mu e32} = s_{23}s_{13}c^2_{13}s_{12}\left(-s_{12}c_{23}e^{-i\delta} - c_{12}s_{23}s_{13}\right)$
  - $W_{e\tau 23} = W^*_{e\tau 32} = W^*_{\tau e23} = W_{\tau e32} = c_{23}s_{13}c^2_{13}s_{12}\left(-c_{12}s_{23}e^{-i\delta} - s_{12}c_{23}s_{13}\right)$
  - $W_{\mu\tau 23} = W^*_{\mu\tau 32} = W^*_{\tau\mu 23} = W_{\tau\mu 32} = s_{23}c_{23}c^2_{13}\left(c_{12}c_{23} - s_{12}s_{23}s_{13}e^{-i\delta}\right)\left(-c_{12}s_{23} - s_{12}c_{23}s_{13}e^{i\delta}\right)$

By further developing the $W_{\alpha\beta jk}$ when $\alpha \neq \beta$ and $j \neq k$ the $e^{\pm i\delta}$ term has always $s_{13}s_{12}s_{23}$ as coefficient, thus if any of the θ_{ij} is 0 we cannot have CP violation as $W_{\alpha\beta jk} = W^*_{\alpha\beta jk} \forall \alpha, \beta, j, k$.

A.5 3-flavour oscillation probability calculation

Before we calculate the 3-flavour oscillation probability, it is useful to obtain some results :

$$\begin{aligned}
U_{\beta 1}U^*_{\alpha 1}U^*_{\beta 1}U_{\alpha 1} &= |U_{\beta 1}U_{\alpha 1}|^2 \\
&= (\delta_{\alpha\beta} - U_{\beta 2}U^*_{\alpha 2} - U_{\beta 3}U^*_{\alpha 3})\left(\delta_{\alpha\beta} - U^*_{\beta 2}U_{\alpha 2} - U^*_{\beta 3}U_{\alpha 3}\right) \\
&= \delta_{\alpha\beta}\left(1 - 2|U_{\beta 2}|^2 - 2|U_{\beta 3}|^2\right) + |U_{\beta 2}U_{\alpha 2}|^2 + |U_{\beta 3}U_{\alpha 3}|^2 + \\
&\quad U_{\beta 2}U^*_{\alpha 2}U^*_{\beta 3}U_{\alpha 3} + U_{\beta 3}U^*_{\alpha 3}U^*_{\beta 2}U_{\alpha 2} \\
&= \delta_{\alpha\beta}\left(1 - 2|U_{\beta 2}|^2 - 2|U_{\beta 3}|^2\right) + |U_{\beta 2}U_{\alpha 2}|^2 + |U_{\beta 3}U_{\alpha 3}|^2 + \Lambda_{23}
\end{aligned}$$

where we define $\Lambda_{jk} = U_{\beta j}U^*_{\alpha j}U^*_{\beta k}U_{\alpha k} + U_{\beta k}U^*_{\alpha k}U^*_{\beta j}U_{\alpha j}$. We do the same calculation for $|U_{\beta 2}U_{\alpha 2}|^2$ and $|U_{\beta 3}U_{\alpha 3}|^2$ which yields the same result as previously by replacing $1 \leftrightarrow 2$ and $1 \leftrightarrow 3$ respectively. Given these results we can calculate the $\sum_j |U_{\beta j}U_{\alpha j}|^2$:

$$\begin{aligned}
&\sum_j |U_{\beta j}U_{\alpha j}|^2 = \delta_{\alpha\beta}\left(3 - 4|U_{\beta 1}|^2 - 4|U_{\beta 2}|^2 - 4|U_{\beta 3}|^2\right) + 2\sum_j |U_{\beta j}U_{\alpha j}|^2 + \Lambda_{23} + \Lambda_{13} + \Lambda_{12} \\
\Rightarrow &\sum_j |U_{\beta j}U_{\alpha j}|^2 = \delta_{\alpha\beta} - \Lambda_{23} - \Lambda_{13} - \Lambda_{12}
\end{aligned}$$

We calculate then the 3-flavour oscillation probability :

$$\begin{aligned}
P(\nu_\alpha \to \nu_\beta) &= \sum_{j,k} U_{\beta j}U^*_{\alpha j}U^*_{\beta k}U_{\alpha k}e^{-i\Delta m^2_{jk}\frac{L}{2p}} \\
&= |U_{\beta 1}U^*_{\alpha 1}|^2 + |U_{\beta 2}U^*_{\alpha 2}|^2 + |U_{\beta 3}U^*_{\alpha 3}|^2 + \\
&\quad U_{\beta 1}U^*_{\alpha 1}U^*_{\beta 2}U_{\alpha 2}e^{i\Delta m^2_{21}\frac{L}{2p}} + U_{\beta 2}U^*_{\alpha 2}U^*_{\beta 1}U_{\alpha 1}e^{-i\Delta m^2_{21}\frac{L}{2p}} + \\
&\quad U_{\beta 1}U^*_{\alpha 1}U^*_{\beta 3}U_{\alpha 3}e^{i\Delta m^2_{31}\frac{L}{2p}} + U_{\beta 3}U^*_{\alpha 3}U^*_{\beta 1}U_{\alpha 1}e^{-i\Delta m^2_{31}\frac{L}{2p}} + \\
&\quad U_{\beta 2}U^*_{\alpha 2}U^*_{\beta 3}U_{\alpha 3}e^{i\Delta m^2_{32}\frac{L}{2p}} + U_{\beta 3}U^*_{\alpha 3}U^*_{\beta 2}U_{\alpha 2}e^{-i\Delta m^2_{32}\frac{L}{2p}} \\
&= \delta_{\alpha\beta} + U_{\beta 1}U^*_{\alpha 1}U^*_{\beta 2}U_{\alpha 2}\left(e^{i\Delta m^2_{21}\frac{L}{2p}} - 1\right) + U_{\beta 2}U^*_{\alpha 2}U^*_{\beta 1}U_{\alpha 1}\left(e^{-i\Delta m^2_{21}\frac{L}{2p}} - 1\right) + \\
&\qquad U_{\beta 1}U^*_{\alpha 1}U^*_{\beta 3}U_{\alpha 3}\left(e^{i\Delta m^2_{31}\frac{L}{2p}} - 1\right) + U_{\beta 3}U^*_{\alpha 3}U^*_{\beta 1}U_{\alpha 1}\left(e^{-i\Delta m^2_{31}\frac{L}{2p}} - 1\right) + \\
&\qquad U_{\beta 2}U^*_{\alpha 2}U^*_{\beta 3}U_{\alpha 3}\left(e^{i\Delta m^2_{32}\frac{L}{2p}} - 1\right) + U_{\beta 3}U^*_{\alpha 3}U^*_{\beta 2}U_{\alpha 2}\left(e^{-i\Delta m^2_{32}\frac{L}{2p}} - 1\right) \\
&= \delta_{\alpha\beta} + W_{\alpha\beta 12}\left(e^{i\Delta m^2_{21}\frac{L}{2p}} - 1\right) + W^*_{\alpha\beta 12}\left(e^{-i\Delta m^2_{21}\frac{L}{2p}} - 1\right) + \\
&\qquad W_{\alpha\beta 13}\left(e^{i\Delta m^2_{31}\frac{L}{2p}} - 1\right) + W^*_{\alpha\beta 13}\left(e^{-i\Delta m^2_{31}\frac{L}{2p}} - 1\right) + \\
&\qquad W_{\alpha\beta 23}\left(e^{i\Delta m^2_{32}\frac{L}{2p}} - 1\right) + W^*_{\alpha\beta 23}\left(e^{-i\Delta m^2_{32}\frac{L}{2p}} - 1\right)
\end{aligned}$$

where $W_{\alpha\beta jk}$ is defined as in the appendix A.4.

A.6 2-flavour approximation of 3-flavour oscillation probability calculation

In this section we assume $|\Delta m^2_{21}| \ll |\Delta m^2_{32}|$. We will then calculate the oscillation probability for $\Delta m^2_{21}\frac{L}{2p} \approx 0$ and $\Delta m^2 = \Delta m^2_{32} \approx \Delta m^2_{31}$

$$
\begin{aligned}
P(\nu_\alpha \to \nu_\beta) &= \sum_{j,k} U_{\beta j} U^*_{\alpha j} U^*_{\beta k} U_{\alpha k} e^{-i\Delta m^2_{jk} \frac{L}{2p}} \\
&= (U_{\beta 1} U^*_{\alpha 1} + U_{\beta 2} U^*_{\alpha 2})(U^*_{\beta 1} U_{\alpha 1} + U^*_{\beta 2} U_{\alpha 2}) + U_{\beta 3} U^*_{\alpha 3} U^*_{\beta 3} U_{\alpha 3} + \\
&\quad (U_{\beta 1} U^*_{\alpha 1} + U_{\beta 2} U^*_{\alpha 2}) U^*_{\beta 3} U_{\alpha 3} e^{i\Delta m^2 L/2p} + \\
&\quad U_{\beta 3} U^*_{\alpha 3} (U^*_{\beta 1} U_{\alpha 1} + U^*_{\beta 2} U_{\alpha 2}) e^{-i\Delta m^2 L/2p} \\
&= (\delta_{\alpha\beta} - U_{\beta 3} U^*_{\alpha 3})(\delta_{\alpha\beta} - U^*_{\beta 3} U_{\alpha 3}) + |U_{\beta 3}|^2 |U_{\alpha 3}|^2 + \\
&\quad (\delta_{\alpha\beta} - U_{\beta 3} U^*_{\alpha 3}) U^*_{\beta 3} U_{\alpha 3} e^{i\Delta m^2 L/2p} + U_{\beta 3} U^*_{\alpha 3} (\delta_{\alpha\beta} - U^*_{\beta 3} U_{\alpha 3}) e^{-i\Delta m^2 L/2p} \\
&= \delta_{\alpha\beta} \left(1 + U_{\beta 3} U^*_{\alpha 3} \left(e^{-i\Delta m^2 L/2p} - 1\right) + U^*_{\beta 3} U_{\alpha 3} \left(e^{i\Delta m^2 L/2p} - 1\right)\right) + \\
&\quad |U_{\beta 3}|^2 |U_{\alpha 3}|^2 \left(2 - e^{i\Delta m^2 L/2p} - e^{-i\Delta m^2 L/2p}\right) \\
&= \delta_{\alpha\beta} \left(1 + |U_{\alpha 3}|^2 \left(e^{-i\Delta m^2 L/2p} + e^{i\Delta m^2 L/2p} - 2\right)\right) + \\
&\quad 2|U_{\beta 3}|^2 |U_{\alpha 3}|^2 \left(1 - \cos \Delta m^2 L/2p\right) \\
&= \delta_{\alpha\beta} \left(1 + 2|U_{\alpha 3}|^2 \left(\cos \Delta m^2 L/2p - 1\right)\right) + 2|U_{\beta 3}|^2 |U_{\alpha 3}|^2 \left(1 - \cos \Delta m^2 L/2p\right)
\end{aligned}
$$

To obtain the usual formulas for the 2-flavour approximation of 3-flavour oscillation we use the relation $\cos 2\phi = 1 - 2\sin^2 \phi$ on the previous expression to obtain :

$$
\begin{cases}
P(\nu_\alpha \to \nu_\alpha) &= 1 - 4|U_{\alpha 3}|^2 \left(1 - |U_{\alpha 3}|^2\right) \sin^2 \left(\Delta m^2 \frac{L}{4p}\right) \\
P(\nu_\alpha \to \nu_\beta) &= 4|U_{\alpha 3} U_{\beta 3}|^2 \sin^2 \left(\Delta m^2 \frac{L}{4p}\right)
\end{cases}
$$

with $\alpha \neq \beta$ in this case. Furthermore the argument of the sinus in this case is given in natural units, thus we need to add a constant factor to convert it to the international system $\Delta m^2 \frac{L}{4p} \to \frac{c^3}{4\hbar} \Delta m^2 \frac{L}{E}$:

$$
\begin{cases}
P(\nu_\alpha \to \nu_\alpha) &= 1 - 4|U_{\alpha 3}|^2 \left(1 - |U_{\alpha 3}|^2\right) \sin^2 \left(\frac{c^3}{4\hbar} \Delta m^2 \frac{L}{E}\right) \\
P(\nu_\alpha \to \nu_\beta) &= 4|U_{\alpha 3} U_{\beta 3}|^2 \sin^2 \left(\frac{c^3}{4\hbar} \Delta m^2 \frac{L}{E}\right)
\end{cases}
$$

Appendix B

Off-axis beam

B.1 Neutrino energy selection by an "off-axis beam"

A classical neutrino beam is produced by the following decay :

$$\pi^+ \rightarrow \mu^+ + \nu_\mu$$

Therefore we can write :

$$P_{\pi^+} = P_{\mu^+} + P_{\nu_\mu}$$

where $P = (E, \boldsymbol{p})$ is the 4-momentum, E is the energy and $\boldsymbol{p}$ the 3-momentum.

Because we want to know the energy dependence of the ν_μ with respect to its angle in the laboratory referential we need to calculate $P_{\pi^+} \cdot P_{\nu_\mu} = E_{\pi^+}E_{\nu_\mu} - \boldsymbol{p}_{\pi^+} \cdot \boldsymbol{p}_{\nu_\mu}$ with $\boldsymbol{p}_{\pi^+} \cdot \boldsymbol{p}_{\nu_\mu} = |\boldsymbol{p}_{\pi^+}||\boldsymbol{p}_{\nu_\mu}| \cos\theta_{\pi\nu}$ where $\theta_{\pi\nu}$ is the angle between the π^+ and the ν_μ directions.

By using the 4-momentum relation given previously we have :

$$\begin{aligned}
&P_{\mu^+} = P_{\pi^+} - P_{\nu_\mu} \\
\Rightarrow &P_{\mu^+}^2 = \left(P_{\pi^+} - P_{\nu_\mu}\right)^2 \\
\Rightarrow &m_{\mu^+}^2 = m_{\pi^+}^2 + m_{\nu_\mu}^2 - 2P_{\pi^+} \cdot P_{\nu_\mu} \\
\Rightarrow &m_{\pi^+}^2 - m_{\mu^+}^2 + m_{\nu_\mu}^2 = 2\left(E_{\pi^+}E_{\nu_\mu} - |\boldsymbol{p}_{\pi^+}||\boldsymbol{p}_{\nu_\mu}| \cos\theta_{\pi\nu}\right)
\end{aligned}$$

we will suppose here that the ν_μ mass is zero, given that $m_{\nu_\mu} \ll m_{\pi^+}, m_{\mu^+}, |\boldsymbol{p}_{\nu_\mu}|$:

$$\begin{aligned}
\Rightarrow &m_{\pi^+}^2 - m_{\mu^+}^2 = 2E_{\nu_\mu}\left(E_{\pi^+} - |\boldsymbol{p}_{\pi^+}| \cos\theta_{\pi\nu}\right) \\
\Rightarrow &E_{\nu_\mu} = \frac{m_{\pi^+}^2 - m_{\mu^+}^2}{2\left(E_{\pi^+} - |\boldsymbol{p}_{\pi^+}| \cos\theta_{\pi\nu}\right)}
\end{aligned}$$

We can observe here that for $\theta_{\pi\nu} = 0°$ and $|\boldsymbol{p}_{\pi^+}| \gg m_{\pi^+}$ the neutrino energy can be simplified by the approximation $E_{\pi^+} \approx |\boldsymbol{p}_{\pi^+}| + \frac{m_{\pi^+}^2}{2|\boldsymbol{p}_{\pi^+}|}$ which results in a linear relation between the neutrino energy and the pion momentum :

$$E_{\nu_\mu} = |\boldsymbol{p}_{\pi^+}| \frac{m_{\pi^+}^2 - m_{\mu^+}^2}{m_{\pi^+}^2}$$

In the "off-axis beam" case, however, $\theta_{\pi\nu} \neq 0°$, therefore the same approximation as previously used will result in :

$$E_{\nu_\mu} = \frac{m_{\pi^+}^2 - m_{\mu^+}^2}{2|\boldsymbol{p}_{\pi^+}|(1 - \cos\theta_{\pi\nu}) + \frac{m_{\pi^+}^2}{|\boldsymbol{p}_{\pi^+}|}} \tag{B.1}$$

which has the same behaviour as the "on-axis" beam for $|\boldsymbol{p}_{\pi^+}| \ll \frac{m_{\pi^+}}{\sqrt{2(1-\cos\theta_{\pi\nu})}}$, and as $|\boldsymbol{p}_{\pi^+}| \to \infty$ the neutrino energy tends to 0. In figure B.1 is shown the neutrino energy distribution in function of the π^+ momentum for an "on-axis beam" and for an "off-axis beam" that is the same as the T2K off-axis angle, that is 2.5°.

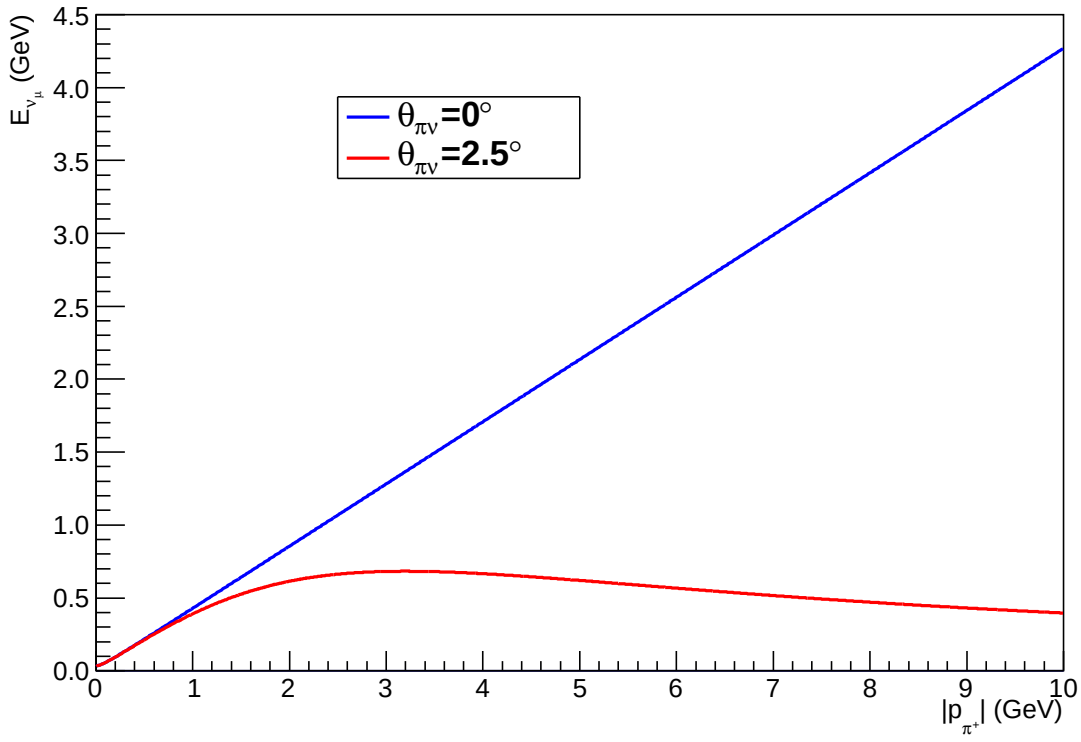

Figure B.1: Effect of "off-axis" beam on neutrino energy in function of the pion momentum in the $\pi^+ \to \mu^+ + \nu_\mu$ decay. In blue is shown the neutrino energy in an "on-axis beam" and in red is shown the neutrino energy in an "off-axis beam" with the same angle as T2K.

B.2 "Off-axis beam" effect on the contamination of a classic ν_μ beam from ν_e

Before taking into account the contamination of ν_e in a classic ν_μ beam it is useful to list how the ν_e beam could be generated, as shown in table 2.1. The ν_e component of a classical ν_μ beam is generated from kaons and muons decay. Because these decays are three body decays the equation (B.1) is not applicable and it is therefore essential to perform a Monte-Carlo study to compute the effect of the off-axis angle. In figures B.2 and B.3 are shown the neutrino fluxes at SK with no oscillation, and from which particles they were generated, as given by the T2K beam simulation (JNUBEAM version 10d). These figures show that typically the muon and kaon peaks are broader than the pion peak and that the average energy of the neutrinos produced via kaon decay is higher than that of neutrinos produced by pion decay.

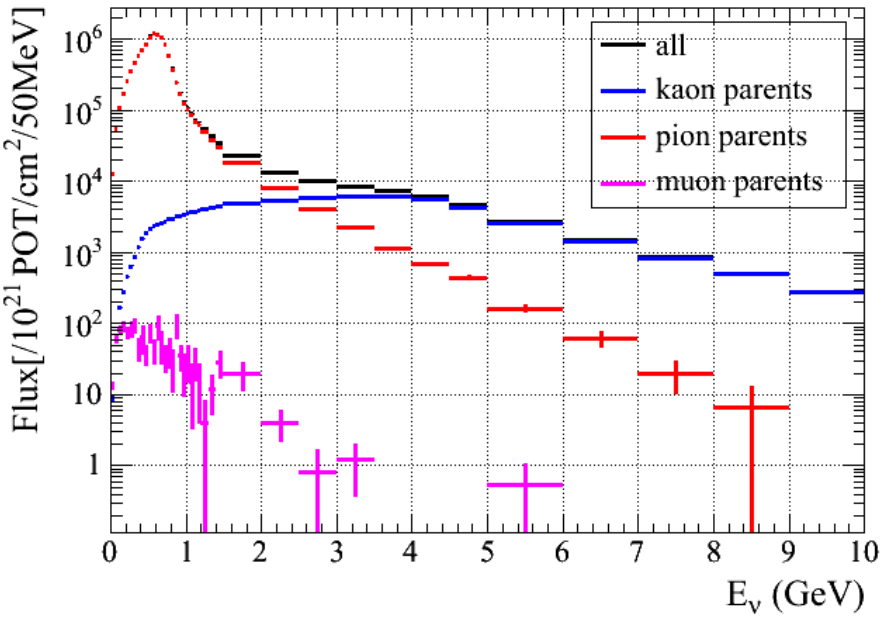

Figure B.2: ν_μ flux at Super Kamiokande (SK) in function of the neutrino energy assuming there is no neutrino oscillation. The parent particle that produced the ν_μ is also shown. These spectra were obtained from a simulation of the T2K using JNUBEAM 10d version. Note that the "muon parents" here comes from μ^- decay which was unfocused by the horns.

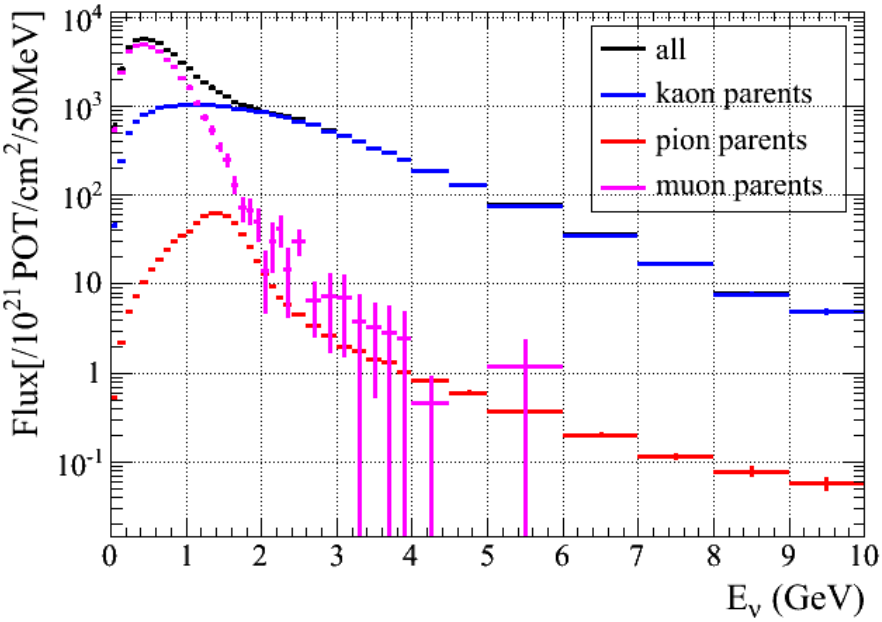

Figure B.3: ν_e flux at Super Kamiokande (SK) in function of the neutrino energy assuming there is no neutrino oscillation. The parent particle that produced the ν_e is also shown. These spectra were obtained from a simulation of the T2K using JNUBEAM 10d version.

For T2K, we are mainly interested in ν_e beam contamination on the supposedly pure ν_μ beam at the energy for which the oscillation probability is maximal, given the distance between J-PARC and Super Kamiokande, that is typically for $E_\nu < 1.2$ GeV. Figures B.2 and B.3 shows that, for this neutrino energy range, the ν_μ beam is composed mainly of the $\pi^+ \to \mu^+ + \nu_\mu$ decays, and the ν_e beam is composed mainly of the $\mu^+ \to e^+ + \nu_e + \overline{\nu_\mu}$ decay. These figures also show the ν_e contamination to the ν_μ beam is about 0.5% for $E_\nu < 1.2$ GeV.

To understand the effect of the "off-axis" angle in the ν_e contamination of the beam it is essential to estimate the angular dependency on the neutrino flux. We will consider a decay of a parent particle P into several different N daughter particles D_i, among which one of them is a ν (for simplicity we define the first daughter particle to be the ν), that is $P \to \nu + D_2 + \ldots + D_N$. We define the angle between the P momentum ($\boldsymbol{p}_P$) and the ν momentum ($\boldsymbol{p}_\nu$) to be θ, in the laboratory reference frame, which is boosted by $\boldsymbol{\beta}$ from the P reference frame. In the P reference frame we define the angle between the boost $\boldsymbol{\beta}$ and the ν momentum ($\boldsymbol{p}^*_\nu$) to be θ^*. We also define the energy of P and of the ν to be E_P and $E_\nu = |\boldsymbol{p}_\nu|$ in the laboratory reference frame and the energy of the ν to be $E^*_\nu = |\boldsymbol{p}^*_\nu|$ in the P reference frame. In this case the boost $\boldsymbol{\beta}$ defines θ as a function of θ^* by equation (B.2). The boost $\boldsymbol{\beta}$ is given by the P momentum and energy in the laboratory reference frame : $\boldsymbol{\beta} = \boldsymbol{p}_P / E_P$.

$$
\begin{aligned}
&\begin{cases} E_\nu & = \gamma E^*_\nu + \gamma |\boldsymbol{\beta}| |\boldsymbol{p}^*_\nu| \cos\theta^* \\ |\boldsymbol{p}_\nu| \cos\theta & = \gamma |\boldsymbol{\beta}| E^*_\nu + \gamma |\boldsymbol{p}^*_\nu| \cos\theta^* \end{cases} \\
\Rightarrow &\begin{cases} |\boldsymbol{p}_\nu| & = \gamma |\boldsymbol{p}^*_\nu| \left(1 + |\boldsymbol{\beta}| \cos\theta^*\right) \\ |\boldsymbol{p}_\nu| \cos\theta & = \gamma |\boldsymbol{p}^*_\nu| \left(|\boldsymbol{\beta}| + \cos\theta^*\right) \end{cases} \\
\Rightarrow &\cos\theta = \frac{\gamma |\boldsymbol{p}^*_\nu| \left(|\boldsymbol{\beta}| + \cos\theta^*\right)}{\gamma |\boldsymbol{p}^*_\nu| \left(1 + |\boldsymbol{\beta}| \cos\theta^*\right)} = \frac{|\boldsymbol{\beta}| + \cos\theta^*}{1 + |\boldsymbol{\beta}| \cos\theta^*}
\end{aligned}
\tag{B.2}
$$

In the P reference frame the ν direction is random, and therefore the θ^* distribution is flat, assuming we compare fluxes for the same solid angles. The θ distribution for a 3 GeV μ^+, π^+ and K^+ decays are shown in figure B.4. For a given off-axis angle of 2.5° we observe that the μ^+ intensity decreases much faster than the π^+ intensity, therefore the fraction of ν_e from μ^+ decays is reduced in relation to the fraction of ν_μ from π^+ decays, for particles decaying with the same energy. Furthermore, the K^+ flux is almost constant and almost no change is produced in the ν_e or ν_μ flux from kaons.

Taking these considerations into account, even though with this simplistic calculation, we obtain that the ν_e contamination of a classical ν_μ beam should be reduced with the increase of the "off-axis angle" where the measurement of the beam is performed.

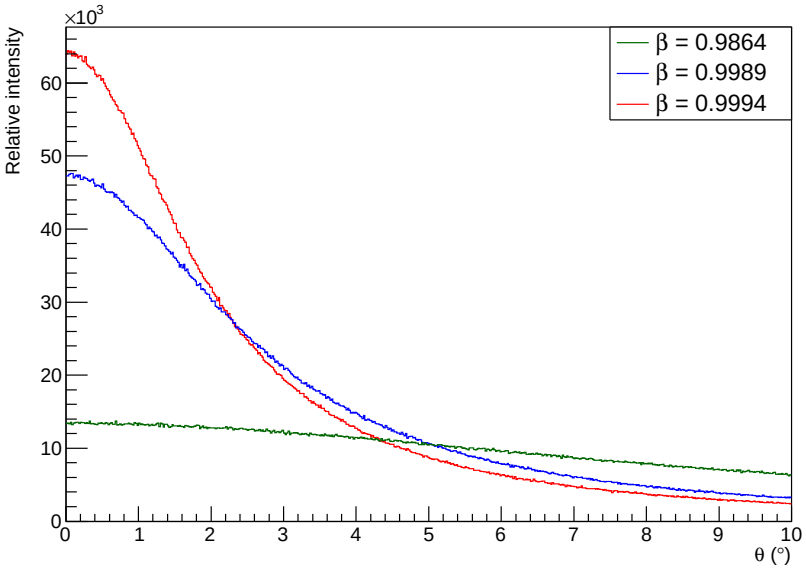

Figure B.4: Angular distribution of the opening angle (θ) between the parent particle P and the ν produced by its decay for 3 GeV μ^+ ($\beta = 0.9994$, in red), 3 GeV π^+ ($\beta = 0.9989$, in blue) and 3 GeV K^+ ($\beta = 0.9864$, in green).

Appendix C

Cerenkov radiation on water

C.1 The Cerenkov effect

The Cerenkov effect occurs when a charged particle travels through a medium with velocity larger than that of the light in the medium. This effect is the equivalent for light of the sonic boom, which happens when an object travels at a speed higher than the speed of the sound in the medium.

The light emitted though Cerenkov effect, called the Cerenkov radiation, is generated through a disruption of the electromagnetic field in the medium due to the passage of the particle. Even though such disruption happens for any charged particle passing through the medium, only in the case where the charge particle has speed greater than of light in the medium there is a constructive interference which intensifies the radiation intensity. This happens at a given angle θ from the direction the particle propagates with speed $\boldsymbol{\beta}c$ in a medium where the speed of light is c/n, with n the refraction index of light in the medium. The wavefront of the Cerenkov radiation is conical, as shown in figure C.1, with angle θ defined by equation (C.1) [76].

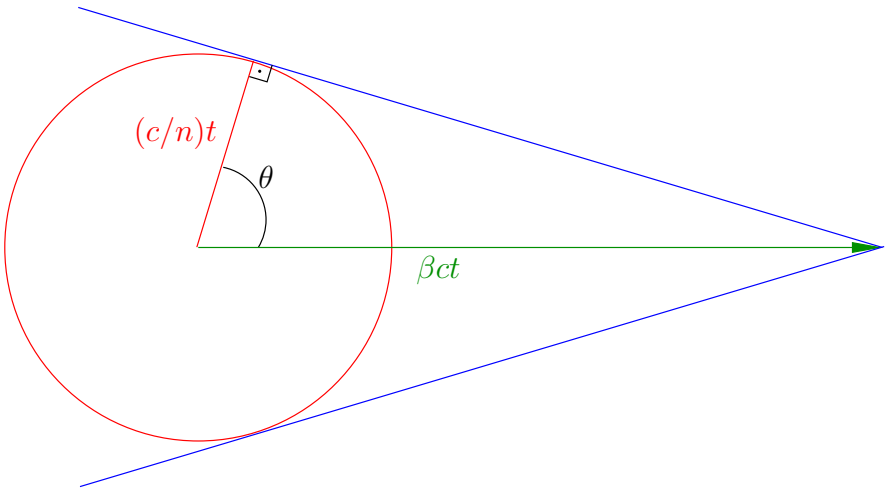

Figure C.1: Schema of a Cerenkov radiation emission by propagation of a charged particle (in green) with speed βc in a medium with refractive index n after a time t. The electromagnetic waves generated by the particle from a given point (in red) will propagate at the speed of light in the medium. This creates a constructive interference that will generate a conical wavefront of light (blue) defined by the Cerenkov opening angle θ.

$$\cos\theta = \frac{1}{\beta n} \tag{C.1}$$

For mediums where the refraction coefficient is constant, and for a singly charged particle, the number of photons emitted by Cerenkov effect between wavelength λ_1 and λ_2 is given by equation (C.2), where α is the fine structure constant [76]. From this equation we should note that a larger number of photons is emitted at smaller wavelengths which gives the blueish tint to the Cerenkov radiation observed at the core of nuclear reactors.

$$\frac{\mathrm{d}N}{\mathrm{d}x} = 2\pi\alpha \sin^2\theta \left(\frac{1}{\lambda_1} - \frac{1}{\lambda_2}\right) \tag{C.2}$$

Another property of the Cerenkov radiation is that it is linearly polarized in the plane containing the charged particle direction and the direction of the photons composing the Cerenkov radiation [14].

C.2 Cerenkov radiation in water

For practical purposes, we want to evaluate more specifically the Cerenkov radiation in water ($n = 1.34$), given that the Super Kamiokande detector uses the Cerenkov effect in water to detect neutrino interactions.

For a ultra-relativistic ($\beta \sim 1$) singly charged particle[1] we deduce the Cerenkov opening angle θ to be about 42°. The number of photons emitted by Cerenkov radiation is of about 270 photons/cm, assuming the wavelength interval for PMT response to be between 300-500 nm, region where the SK PMTs quantum efficiency is higher as shown in figure C.2. This corresponds to the energy emission for the given wavelength band per unit length of roughly 600-1000 eV/cm.

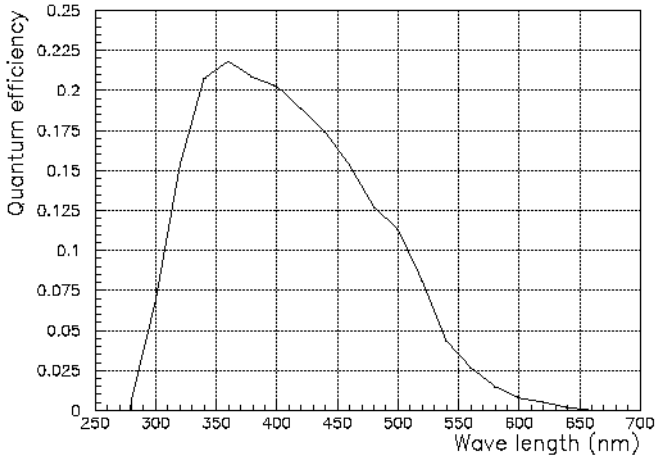

Figure C.2: The quantum efficiency of the PMTs used in Super Kamiokande as a function of the wavelength of incident light. Extracted from `http://www-sk.icrr.u-tokyo.ac.jp/sk/ykphd/chap3-6.html`.

[1] Typically this condition is satisfied for all electrons used for the T2K ν_e search.

The Cerenkov radiation energy loss is small compared to, for example, the ∼2 MeV/cm energy loss from ionization of the medium [76], and therefore does not explain the energy loss of electrons and muons in the detector.

For muons with momentum between 100 MeV/c and 10 GeV/c, which is typically the case for T2K, the energy loss is mainly due to ionization, which is about constant [14]. This is also the case for several other heavy particles such as $\pi^{\pm}$ and p. The ionization process will not change the trajectory of the particles and therefore a sharp edged ring is emitted, as shown in figure C.3.

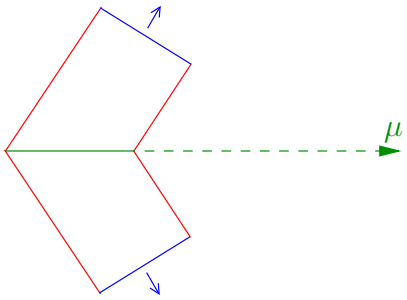

Figure C.3: Schema of a Cerenkov radiation emission for a μ (in green). The Cerenkov radiation (in red) emitted while the μ is above Cerenkov threshold (solid line) will create conical wavefront of light (blue). Once the μ is below Cerenkov threshold (dashed line) there is no longer Cerenkov radiation emission. The wavefront created by Cerenkov radiation will therefore create a ring when projected to the wall of the Super Kamiokande detector, for example. Note that if the μ leaves the detector while emitting Cerenkov radiation the actual shape will not be a ring but a full circle.

On the other hand, for electrons with energy higher than a few tens of MeV, which is also typically the case for T2K, the energy loss process is mainly due to bremsstrahlung [14]. Given the electron mass is rather small in comparison to other particles in the medium, from the interaction between the electron and the medium there is a rather large probability that the electron will change trajectory during its propagation, that is it will suffer multiple scattering. As consequence of these frequent changes in the electron trajectory, the ring from Cerenkov radiation produced by an electron will have a fuzzier edge than the rings from Cerenkov radiation produced by a muon. This is the reason for the difference in the charge pattern in the event displays from electrons and muons shown in figure 2.15.

Finally, even though photons are not charged particles, the high energy photons (with energy above a few MeV) will also emit Cerenkov radiation indirectly and therefore will also be visible in the Super Kamiokande detector. More precisely, the high energy photons will go through e^+e^- pair production after a certain conversion length, which will then generate Cerenkov radiation. For these photons pair production is the main process responsible for energy loss [14]. Given that the Cerenkov radiation is produced from the electrons and positrons from the γ pair production, the characteristics of a γ and an electron ring at Super Kamiokande are similar, except for the conversion length that is required before the γ will start emitting Cerenkov radiation.

Appendix D

Generic calculation to obtain remarkable results

D.1 Properties of the π^0 decay

D.1.1 π^0 mass from $\gamma\gamma$ decay

The $\pi^0 \to \gamma\gamma$ decay has a branching ratio of 98.8% [14] and is the π^0 decay mode we have studied here. It is necessary to calculate the π^0 mass from the observed properties of the two γ in order to check if the two reconstructed γ really correspond to a π^0.

By calculating the 4 momenta of the $\pi^0 \to \gamma\gamma$ decay we obtain :

$$\begin{aligned} & P_{\pi^0} = P_{\gamma_1} + P_{\gamma_2} \\ \Rightarrow & P_{\pi^0}^2 = P_{\gamma_1}^2 + P_{\gamma_2}^2 + 2P_{\gamma_1}P_{\gamma_2} \\ \Rightarrow & m_{\pi^0}^2 = 2|\boldsymbol{p}_{\gamma_1}||\boldsymbol{p}_{\gamma_2}|\,(1-\cos\phi_{12}) \\ \Rightarrow & m_{\pi^0} = \sqrt{2|\boldsymbol{p}_{\gamma_1}||\boldsymbol{p}_{\gamma_2}|\,(1-\cos\phi_{12})} \end{aligned} \tag{D.1}$$

where ϕ_{12} is the angle between the two γ.

D.1.2 Lower limit of the momentum of the highest energy γ from a π^0 decay

From the equation (D.1) we can easily calculate the momentum of each γ in the π^0 rest frame of reference, where we know by momentum conservation that $|\boldsymbol{p}_{\gamma}^{CM}| = |\boldsymbol{p}_{\gamma_1}^{CM}| = |\boldsymbol{p}_{\gamma_2}^{CM}|$ and $\phi_{12} = 180°$, therefore $|\boldsymbol{p}_{\gamma}^{CM}| = m_{\pi^0}/2$.

Now we define which γ is the first or second γ by imposing $|\boldsymbol{p}_{\gamma_1}| \geq |\boldsymbol{p}_{\gamma_2}|$ in the laboratory frame of reference, which is boosted from the π^0 rest frame by $\boldsymbol{\beta} = \boldsymbol{p_{\pi^0}}/E_{\pi^0}$ given in the laboratory frame of reference.

Given that in the π^0 rest frame the γ are produced back to back, when they are boosted by $\boldsymbol{\beta}$ we have that $|\boldsymbol{p}_{\gamma_1}| \geq |\boldsymbol{p}_{\gamma}^{CM}|$ where γ_1 has $\boldsymbol{p}_{\gamma_1}^{CM} \cdot \boldsymbol{p}_{\pi^0} \geq 0$, given the definitions previously given. Therefore $|\boldsymbol{p}_{\gamma_1}| \geq m_{\pi^0}/2 \approx 67.5$ MeV, in natural units (where $c = 1$).

D.2 Reconstructed neutrino energy for CCQE events

We will obtain in this section the reconstructed neutrino energy of a neutrino that interacts through CCQE interaction, where the produced lepton momentum and direction is

measured.

The CCQE interaction can simply be written as :

$$\nu_l + n \rightarrow l^- + p$$

Therefore we can write the following identity, where P_i is the 4-momentum vector of i :

$$\begin{aligned} & P_{\nu_l} + P_n = P_l + P_p \\ \Rightarrow & P_p = P_{\nu_l} + P_n - P_l \\ \Rightarrow & P_p^2 = P_{\nu_l}^2 + P_n^2 + P_l^2 + 2P_{\nu_l}P_n - 2P_{\nu_l}P_l - 2P_nP_l \end{aligned}$$

In order to expand this expression it is useful to make a few approximations :

- $m_{\nu_l} = 0$, therefore $|\boldsymbol{p}_{\nu_l}| = E_{\nu_l}$
- $\boldsymbol{p}_n = \overrightarrow{0}$, where $\boldsymbol{p}_n$ is the 3-momentum vector of the neutron in the laboratory referential, therefore $E_n = m_n$.

$$\begin{aligned} \Rightarrow & m_p^2 = m_n^2 + m_l^2 + 2E_{\nu_l}m_n - 2m_nE_l - 2(E_{\nu_l}E_l - \boldsymbol{p}_{\nu_l} \cdot \boldsymbol{p}_l) \\ \Rightarrow & m_p^2 = m_n^2 + m_l^2 - 2m_nE_l + 2E_{\nu_l}(m_n - E_l + |\boldsymbol{p}_l| \cos\vartheta_{\nu l}) \end{aligned}$$

$$\Rightarrow E_{\nu_l} = \frac{2m_nE_l - m_l^2 - m_n^2 + m_p^2}{2(m_n - E_l + |\boldsymbol{p}_l| \cos\vartheta_{\nu l})} \tag{D.2}$$

where $\vartheta_{\nu l}$ is the angle between the ν_l and the l directions.

The expression of the neutrino reconstructed energy given by (D.2) is similar to the one given by (2.1). The difference between these two expressions comes from the fact that the neutron here was assumed to be a free neutron, while at the equation (2.1) it was considered to be a bound neutron in an atom.

We can obtain the equation (D.3) from (D.2) if we replace the m_n by $(m_n - V)$, that is we say that the effective neutron mass available for the CCQE interaction is not the neutron mass, but the neutron mass in the bounded atom that is reduced by a V potential from the nucleus. The equation (D.3) is the same as equation (2.1).

$$E_\nu = \frac{2(m_n - V)E_l - m_l^2 - (m_n - V)^2 + m_p^2}{2(m_n - V - E_l + p_l \cos\vartheta_{\nu l})} \tag{D.3}$$

We should also note that when T2K will start running on $\overline{\nu}$ beam mode the corresponding CCQE interaction will be written as $\overline{\nu_l} + p \rightarrow l^+ + n$, and by making the same approximations as previously while swapping the role of the p and n on the previous calculation we obtain the similar expressions as (D.2) and (D.3), with m_n and m_p swapped.

Appendix E

Estimation of systematic error set that maximizes the probability of a given oscillation parameter set assuming a simple Gaussian error on number of expected events at SK

In this appendix we will use the same notations defined in chapter 5.

We want to calculate here the value of $P(O_i|M,\varepsilon)$ when $P(\varepsilon_j|O_i)$ is a Gaussian. Since $P(O_i|M,\varepsilon)$ is defined to be the maximum for any realization ε_j of $P(O_i|M,\varepsilon_j)$ we need to study the derivative of this probability with respect to ε_j.

The expression of $P(O_i|M,\varepsilon_j)$ is :

$$P(O_i|M,\varepsilon_j) = \kappa(M,O_i)P(M|O_i,\varepsilon_j)P(\varepsilon_j|O_i)$$

where κ is a product of probabilities independent of ε_j. Developing the terms depending on ε_j we obtain :

$$\begin{aligned} P(O_i|M,\varepsilon_j) &= \kappa(M,O_i)\left(\frac{(n_{exp})_i(1+\varepsilon_j)}{n_{obs}}\right)^{n_{obs}} \exp\left[n_{obs} - (n_{exp})_i(1+\varepsilon_j) - 0.5\left(\frac{\varepsilon_j}{\sigma_{SE}}\right)^2\right] \\ &= \kappa'(M,O_i)\,(1+\varepsilon_j)^{n_{obs}} \exp\left[-(n_{exp})_i(1+\varepsilon_j) - 0.5\left(\frac{\varepsilon_j}{\sigma_{SE}}\right)^2\right] \end{aligned}$$

where $\kappa'(M,O_i)$ is a factor that does not depend on ε_j.

The $P(O_i|M,\varepsilon_j)$ derivative with respect to ε_j is :

$$\begin{aligned} \frac{\mathrm{d}\,P(O_i|M,\varepsilon_j)}{\mathrm{d}\,\varepsilon_j} = \kappa'(M,O_i)\Bigg\{ & n_{obs}\,(1+\varepsilon_j)^{n_{obs}-1} + (1+\varepsilon_j)^{n_{obs}}\left[-(n_{exp})_i - \frac{\varepsilon_j}{\sigma_{SE}^2}\right]\Bigg\} \\ & \exp\left[-(n_{exp})_i(1+\varepsilon_j) - 0.5\left(\frac{\varepsilon_j}{\sigma_{SE}}\right)^2\right] \end{aligned}$$

At the maximum $\frac{\mathrm{d}\,P(O_i|M,\varepsilon_j)}{\mathrm{d}\,\varepsilon_j} = 0$, and we obtain the condition :

$$n_{obs}\,(1+\varepsilon_j)^{n_{obs}-1} + (1+\varepsilon_j)^{n_{obs}}\left[-(n_{exp})_i - \frac{\varepsilon_j}{\sigma^2_{SE}}\right] = 0$$

one possible solution is $\varepsilon_j = -1$. To find remaining solutions we can further simplify the problem by solving :

$$\begin{aligned}
&n_{obs} + (1+\varepsilon_j)\left[-(n_{exp})_i - \frac{\varepsilon_j}{\sigma^2_{SE}}\right] = 0\\
&\varepsilon_j^2 + \left(1 + (n_{exp})_i\sigma^2_{SE}\right)\varepsilon_j + \left((n_{exp})_i - n_{obs}\right)\sigma^2_{SE} = 0\\
\Rightarrow &\varepsilon_j = \frac{-\left(1+(n_{exp})_i\sigma^2_{SE}\right) \pm \sqrt{\left(1+(n_{exp})_i\sigma^2_{SE}\right)^2 - 4\left((n_{exp})_i - n_{obs}\right)\sigma^2_{SE}}}{2}\\
\Rightarrow &\varepsilon_j = \frac{-\left(1+(n_{exp})_i\sigma^2_{SE}\right) \pm \sqrt{\left(1-(n_{exp})_i\sigma^2_{SE}\right)^2 + 4n_{obs}\sigma^2_{SE}}}{2}
\end{aligned}$$

There are 3 possible solutions for ε_j that could maximize $P(O_i|M,\varepsilon_j)$. The first solution we will consider it the "$-$" solution of the second degree equation. In this case

$$\varepsilon_j = -\frac{1+(n_{exp})_i\sigma^2_{SE} + \sqrt{\left(1-(n_{exp})_i\sigma^2_{SE}\right)^2 + 4n_{obs}\sigma^2_{SE}}}{2}$$

and given that $\sqrt{\left(1-(n_{exp})_i\sigma^2_{SE}\right)^2 + 4n_{obs}\sigma^2_{SE}} \geq \sqrt{\left(1-(n_{exp})_i\sigma^2_{SE}\right)^2} = |1-(n_{exp})_i\sigma^2_{SE}|$,

$$\varepsilon_j < -\frac{1+(n_{exp})_i\sigma^2_{SE} + |1-(n_{exp})_i\sigma^2_{SE}|}{2} \leq -1$$

since it is not reasonable to consider the number of expected events to be negative, that is $\varepsilon_j \geq -1$, the proposed solution is not physical, and therefore refused. Note that the boundary condition case $\varepsilon_j = -1$ is one of the possible solutions mentioned previously.

The second solution to be considered is $\varepsilon_j = -1$. For $\varepsilon_j = -1$, the $P(O_i|M,\varepsilon_j)$ is 0 unless n_{obs} is 0, which is assumed to be the case from the definitions given. Given that the P function is bound between 0 and 1 we can safely conclude that $\varepsilon_j = -1$ is not a maximum, and therefore not the solution we are searching for.

The remaining solution, which is used in chapter 5 and given in equation (5.14), is

$$\varepsilon_j = \frac{-\left(1+(n_{exp})_i\sigma^2_{SE}\right) + \sqrt{\left(1-(n_{exp})_i\sigma^2_{SE}\right)^2 + 4n_{obs}\sigma^2_{SE}}}{2}$$

which, if $\varepsilon_j > -1$, maximizes $P(O_i|M,\varepsilon_j)$, since $\frac{\mathrm{d}^2\,P(O_i|M,\varepsilon_j)}{\mathrm{d}\,\varepsilon_j^2} < 0$.